NASA Technical Memorandum 87801

Geodynamics Branch Annual Report 1985

OCTOBER 1986

NASA

NASA Technical Memorandum 87801

Geodynamics Branch Annual Report—1985

Edited by
W. D. Kahn, S. C. Cohen
and B. S. Boccucci
Goddard Space Flight Center
Greenbelt, Maryland

National Aeronautics and
Space Administration

**Scientific and Technical
Information Branch**

1986

GEODYNAMICS BRANCH STAFF

CODE 621

David E. Smith, Branch Head
Ph.D., 1966, University of London, Satellite Geodesy
Beatrice Sidotti Boccucci, Secretary
Mary A. Melissa Harper, Secretary

William B. Boyer, A.A., 1957, Montgomery Community College, Electronic Technology
Benjamin F. Chao, Ph.D., 1981, University of California (San Diego), Earth Sciences
Demosthenes C. Christodoulidis, Ph.D., 1976, Ohio State University, Satellite Geodesy
Thomas A. Clark, Ph.D., 1967, University of Colorado, Radio Astronomy
Steven C. Cohen, Ph.D., 1973, University of Maryland, Physics
Theodore L. Felsentreger, M.A., 1961, University of Maryland, Mathematics
Werner D. Kahn, M.S., 1955, University of Illinois, Mathematics
Chester J. Koblinsky, Ph.D., 1979, Oregon State University, Physical Oceanography
Ronald Kolenkiewicz, M.S., 1965, Catholic University, Space Science and Applied Physics
Francis J. Lerch, M.S., 1950, University of Delaware, Mathematics
Han-Shou Liu, Ph.D., 1963, Cornell University, Physics
Chopo Ma, Ph.D., 1978, University of Maryland, Physics
James G. Marsh, M.S., 1963, West Virginia University, Physics
Patrick H. McClain, M.S., 1959, Howard University, Mathematics
Carole M. Nethery, M.A., 1965, University of Denver, Mathematics
Barbara H. Putney, B.S., 1960, Brooklyn College, Mathematics
David P. Rubincam, Ph.D., 1973, University of Maryland, Physics
James W. Ryan, M.S., 1968, George Washington University, Mathematics
Braulio V. Sanchez, Ph.D., 1975, University of Texas, Aerospace Engineering
Frederick G. Schamann, B.S., 1967, City College of New York, Mathematics
Jean E. Welker, M.A., 1980, University of Maryland, Physical Geography/History
William T. Wildes, B.A., 1967, Northeastern University, Boston, Mathematics
George H. Wyatt, B.S., 1962, North Carolina State College, Mathematics

Resident Research Associates

William P. O'Connor, Ph.D., 1984, University of Wisconsin, Meteorology
Maria T. Zuber, Ph.D., 1985, Brown University, Geophysics

TABLE OF CONTENTS

TABLE OF CONTENTS (continued)

TABLE OF CONTENTS (continued)

INTRODUCTION

This report is the fourth of a series of reports which summarizes the research activities of the Geodynamics Branch. The branch is located within the Laboratory for Terrestrial Physics of the Space and Earth Sciences Directorate of the Goddard Space Flight Center. The branch's major research activites focus on solid-earth dynamics including crustal movements, ocean topography and dynamics, and planetology. For the solid-earth, research is conducted in tectonic plate motion, lithospheric structure and dynamics, regional scale crustal deformation, polar motion, earth orientation and rotation, and gravity field modeling. Satellite laser ranging and very long baseline interferometric data provide much of the observational information used in studying these topics. For the oceans, research is conducted in ocean topography and circulation, and mesoscale variability and structure. Analysis of satellite altimeter data, ocean geoid modeling, and precision orbit determination are fundamental for performing this research. Planetology studies are of recent interest to the branch and consist of geodetic and geodynamic analyses. Impetus was given to this research by the future Mars Observer Space Mission in which the branch plans to play a key role.

The NASA programs which are supported by the work described in this document, include the Geodynamics and Ocean Programs, the Crustal Dynamics Project, the Ocean Topographic Experiment (TOPEX) and the Mars Observer Mission. The report highlights the investigations conducted by the Geodynamics Branch Staff and its on-site contractors during calendar year 1985. The individual papers, are grouped into the chapters: Tectonophysics, Sea Surface Topography, Geodesy and Geopotential Field, Planetology, and Geophysical Techniques. More detailed information on the activities of the branch or the particular research efforts described herein, can be obtained through the branch office or from individual staff members.

CHAPTER I

TECTONOPHYSICS

OVERVIEW

For the past two decades, the theory of plate tectonics has provided a framework for studying a variety of geodynamic processes. Foremost among these is the motion of the plates themselves. Measurements using space techniques are particularly well-suited to the direct determination of tectonic plate kinematics. In fact, measurements using satellite laser ranging and very long baseline interferometry have matured to the point where three-dimensional descriptions of individual site locations are being determined. This new information supplements the interesting, but more limited, determinations of intersite baselines which have been obtained for several years. Currently, changes in site positions and baseline lengths are being studied from sites situated on most of the major tectonic plates. This year's reports concentrate on measurements involving plate motion and deformation in the western United States and the Pacific. Particularly interesting are the comparisons between the currently observed rates and those deduced from the geological record. In many cases the contemporary and geologic rates closely agree, but the remaining differences are quite intriguing. The continued monitoring of these motions will address the questions of whether temporal variations exist in the motions, how deformations occur near plate boundaries, and whether current models of plate motion are adequate. The kinematic descriptions of the tectonic plate motion provides input for dynamical models of the associated driving processes. Howevever, the kinematic description of plate tectonics can be determined directly by space measurements, while the determination of driving forces associated with geodynamical processes requires a merging of observational data and geophysical models. Accordingly several studies conducted within the Geodynamics Branch involve analytical and numerical modeling of the dynamics of tectonic phenomena. During the past year, models have been developed of the lithospheric deformation associated with continental collisions, the deformation associated with folding in the Indian Ocean, the stresses associated with the Tibetan and Himalayan uplifts, and the changes in earth rotation, polar motion and the gravity field induced by earthquakes.

The dynamical processes that are responsible for some of the tectonophysics phenomena discussed in this section are intimately related to those discussed in subsequent chapters of this report on Geodesy and Geopotential and on Planetology. The interested reader is referred to these sections for additional reports on the earth and planetary physics studies being conducted within the Geodynamics Branch.

Contributors to this chapter are: B. Fong Chao, Demosthenes C. Christodoulidis, Thomas A. Clark, Steven C. Cohen, David Gordon, Richard S. Gross, Han-Shou Liu, Chopo Ma, James W. Ryan, David E. Smith, and Maria T. Zuber.

TECTONIC MOTIONS IN WESTERN USA FROM SLR

Demosthenes C. Christodoulidis
David E. Smith

OBJECTIVE

The objective of this work is to derive tectonic motion vectors for tracking sites in the western United States from analysis of LAGEOS satellite laser tracking data.

BACKGROUND

The analysis of laser satellite tracking data utilizes principles from dynamic satellite geodesy. Products of this type of analysis are precise three-dimensional laser tracking coordinates. Dynamic analyses have been performed on data accumulated over a 6-year period (1979-1984) resulting in precise annual tracking station positions. During this 6-year period, laser systems and data consistency have reached advanced levels of maturity yielding a strong network geometry and better network resolution than in previous years. The analysis of the data at GSFC yielded the SL6 solution consisting of improved Earth rotation, station coordinates and geodetic constants. In this work, the original SL6 solution was iterated with the introduction of better nutation and ocean tide models. Annual geodesic lengths were computed from the precise final annual station positions in our new SL6 system.

RECENT ACCOMPLISHMENTS

Absolute velocity vectors for the laser tracking stations in the western United States have been computed via a least-squares adjustment model. "Absolute" in this context means that the velocities are referenced with respect to mantle intrusions into the Earth's crust, known as hotspots. In this model, two types of stations are defined: "external" stations which have their absolute plate motion defined by a geologic plate motion model (these are shown in Figure 1); and "internal" stations for which the absolute motion is sought (shown in Figure 2). The Minster and Jordan (1978) AM1-2 model was adopted to describe the absolute motion of the external stations for two reasons. First, it agrees well with the SLR observed rates for these stations, and secondly it provides the means to relate the computed velocity vectors to the mantle-based reference frame. All the "external" stations

have dense tracking data sets and the SLR derived relative rates for these stations are within one standard deviation from the relative rates implied by the geologic model. The methodology developed in this work begins by fitting a slope to the time series of geodesics between all pairs of stations which have in common at least two annual geodesic lengths. These slopes, or geodesic rates, assumed constant are then processed simultaneously in a least-squares algorithm to yield absolute velocity vectors for the "internal" station network. The errors in the station positions, as approximated by the error in the height of the station, are propagated throughout the system. The uncertainties in the geodesic rates are used as "observational" weights in the simultaneous solution.

Details of this work are described in Christodoulidis et al. (1986).

SIGNIFICANCE

Satellite laser ranging has advanced to the point of providing the capability to monitor tectonic motions. The analysis made in this work guarantees self-consistency in the solution for absolute motion since all of the constructable geodesic rates enter into the set of simultaneous equations. This is a considerable improvement over the previous methods of analyzing the results in a baseline-by-baseline manner. The resulting tectonic motion model, the SL6 Tectonic Model, has been compared with the geologic models of Minster and Jordan (1978) and Chase (1978). The SL6 computed absolute motions are listed in Table 1 along with motions implied by the geologic models. The modeled geodesic rates which traverse the San Andreas Fault indicate that the rate of change (shortening) over these lines has slowed considerably in the last 3 years. The best estimate for the period 1982-84 is -2.56 cm/year. The slower northwesterly absolute motion for the Monument Peak site is largely responsible for this behavior. The current results indicate that the motion along the SAFE line (San Andreas Fault Experiment line, Momument Peak [7110] to Quincy [7051 & 7109] now agrees with the rate obtained from the local ground survey networks. This significant change in the rate of the SAFE line raises the question whether Monument Peak is located on the Pacific Plate or is on some California platelet. Implementation of dense regional observation networks and continuous analysis of SLR and VLBI data are necessary for furthering our understanding of the dynamic behavior of this entire region.

FUTURE EMPHASIS

The accuracy and reliability of SLR Tectonic Motion Models will be improved as additional data are acquired and processed. The

least-squares algorithm is being improved to propagate full covariance information and the analysis portions are being supplemented to better locate aberrant data. With these improvements, it is expected that these results will have considerable impact among the tectonophysics community.

REFERENCES

Chase, C.G., "Plate Kinematics: The Americas, East Africa, and the Rest of the World," Earth & Plan. Sci. Letters, Vol. 37, pp 355-368, 1978.

Christodoulidis, D.C., D.E. Smith, S.M. Klosko and J.W. Robbins, "Tectonic Motion in Western U.S.A. from Satellite Laser Ranging," Proc. of AAPG Memoir Workshop, Corvallis, Oregon, in press, 1986.

Minster, J.B. and T.H. Jordan, "Present-Day Plate Motions," J. Geophys. Res., Vol. 83, pp 5331-5354, 1978.

Table 1. A Comparison of Absoluted Station Motions From Differing Models

	MAGNITUDE (CM/YR)			AZIMUTH (DEG)		
	MINJOR	CHASE	SL6	MINJOR	CHASE	SL6
7210	9.68	9.10	9.68	300.40	297.14	300.40
7090	7.97	7.24	7.97	21.71	29.11	21.71
7907	3.12	2.34	3.12	265.76	288.42	265.76
7105	2.69	2.71	2.69	251.53	264.95	251.53
7086	2.67	2.69	2.95	241.14	242.82	239.86
7051	2.41	2.79	3.86	233.86	232.01	229.63
7062	6.38	6.50	4.98	296.64	296.37	307.53
7109	2.41	2.79	1.19	233.86	232.01	251.66
7110	6.31	6.44	4.50	296.62	296.38	301.14
7112	2.55	2.77	3.12	239.39	243.17	346.89
7114	2.49	2.79	3.30	235.46	233.66	174.31
7122	2.72	2.61	4.15	241.06	239.91	201.74

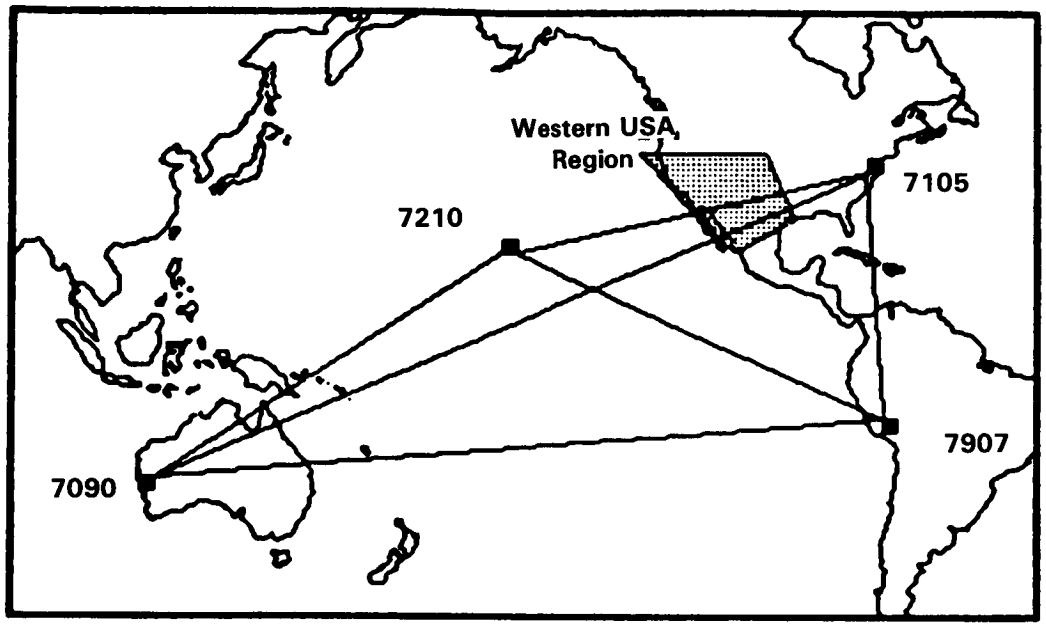

Figure 1. "External" SLR network.

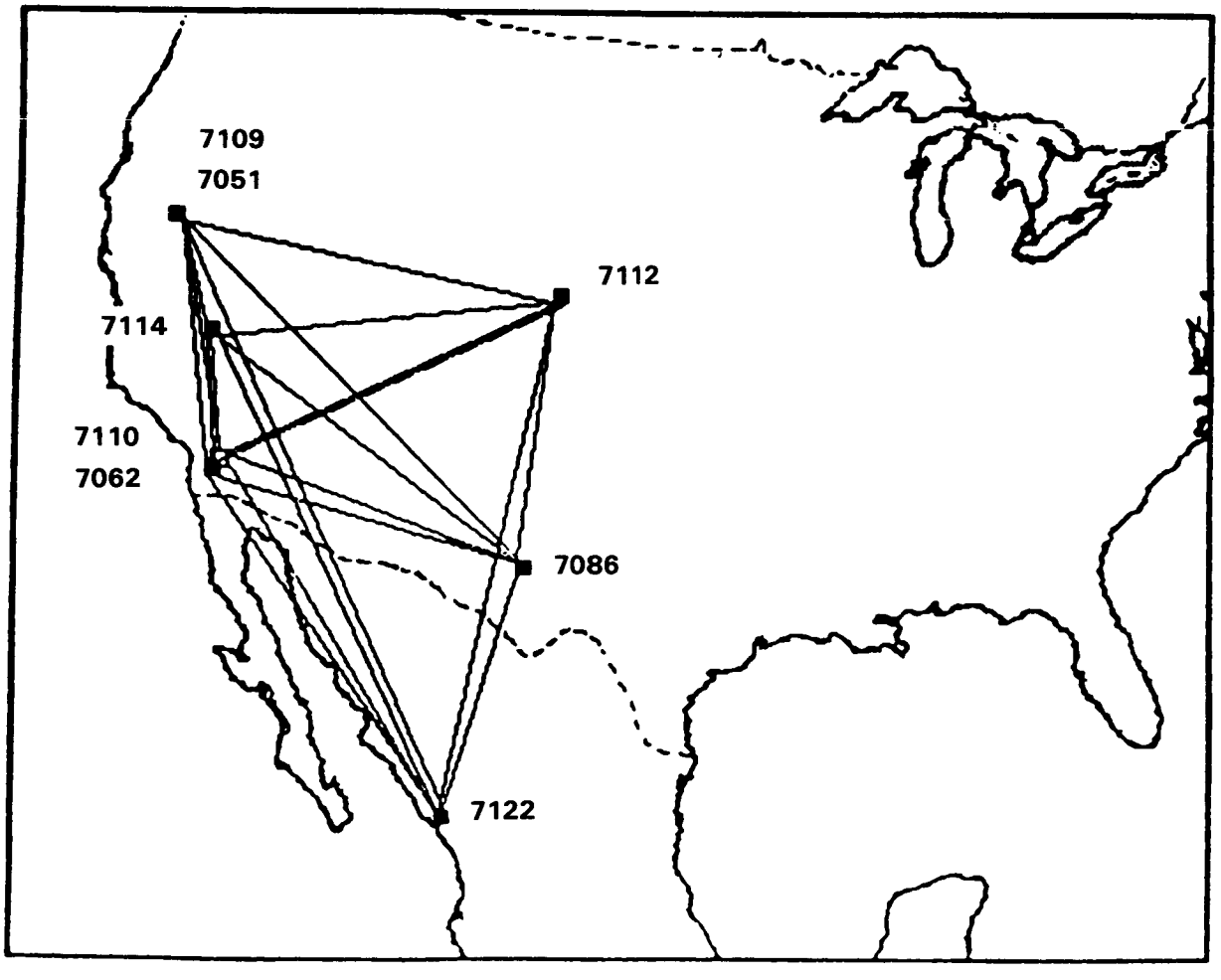

Figure 2. "Internal" SLR network.

DETERMINATION OF SITE MOTIONS IN THE WESTERN UNITED STATES FROM MARK III VLBI MEASUREMENTS

David Gordon
Thomas A. Clark

OBJECTIVE

The objective of the work reported here is to determine site motions at 14 fixed and mobile VLBI sites in the western continental United States using a large data set of Mark III VLBI measurements.

BACKGROUND

For several years NASA's Crustal Dynamics Project (CDP) has used the Mark III VLBI system to study crustal deformations and movements in the western United States. Several dozen sites, mostly in California, have been visited repeatedly by 3 mobile VLBI units. Additionally, 4 fixed sites in this region have been repeatedly used in conjunction with the mobile sites. The CDP is currently performing some 2 dozen experiments yearly involving these sites. VLBI data involving some 3 years of mobile and some 5 years of fixed station baseline measurements to sites in the western U.S. have been analyzed. Sufficient data now exist to begin assembling a detailed picture of the plate motions in this region.

For a VLBI geodetic experiment, the quantity of interest is the baseline vector between the two antennas and how this vector changes with time. (For the mobile systems, the baseline vector is transposed to a fixed geodetic marker). The standard technique is to define an a priori baseline, as measured at some reference epoch, and to monitor changes in that baseline each time it is remeasured. Baseline changes can be broken up into three orthogonal components: length, transverse and vertical. The rates of change in these three directions are simply the length, transverse, and vertical velocities. Length changes are simply increases (positive) or decreases (negative) in the length of the baseline. The transverse component is perpendicular to the baseline vector and directed along the horizon at either site. Positive transverse motion is defined as a clockwise rotation of the baseline as seen from above. The vertical component is perpendicular to both the length and transverse components, and is directed towards the vertical at the midpoint of the baseline. A positive vertical change means either an increase in height at station #1 or a decrease at station #2.

Measurements of transverse and vertical components are strongly affected by errors in the determination of the Earth's pole position and UT1. The vertical component also suffers strongly by uncertainties in the tropospheric delay calibration. The length component, however, is essentially unaffected by errors in the Earth orientation, and length errors due to tropospheric delay calibration errors can generally be held small (to about the 1 cm level for the baseline lengths studied here) through the consistent use of surface meteorology measurements. Until recently, only the length components of baseline velocities have been useful in attempts at resolving individual site motions. The use of the transverse component requires the availability of a highly accurate and homogeneous Earth orientation series. Until recently, no such series were available; BIH Circular D is not accurate enough and other, more accurate series were not homogeneous.

RECENT ACCOMPLISHMENTS

Since late December, 1983, the National Geodetic Survey has been conducting program IRIS, utilizing a 4 station (Westford, Ft. Davis, Richmond and Wettzell) VLBI network to very accurately determine pole position and UT1 at 5-day intervals. The GSFC VLBI group has compiled and regularly updates an Earth orientation series based on these IRIS measurements. (NGS also maintains an IRIS Earth orientation series. The two series differ slightly mainly in the use of different a priori site and source positions). This series, which is continuous since the beginning of 1984, is homogeneous and appears to be highly accurate. During the past year, software has been developed to map the Earth orientation parameters from this IRIS series into data bases at the time of analysis. Using this technique, errors in the transverse baseline component are limited to the 1 - 2 cm level for baselines in the western U.S. This has allowed accurate determination of transverse velocities using data from 1984 and 1985.

A data set comprised of baseline measurements between 14 mobile and fixed VLBI sites in the western continental U.S. plus measurements from Westford and Gilmore Creek (Fairbanks) to these sites has been compiled for this study. This data set contains some 500 individual baseline measurements (not counting several hundred measurements of Westford to Ft. Davis as part of the IRIS and POLARIS programs) on some 57 individual baselines. For each baseline, a length and transverse velocity was computed using a simple linear least squares fitting program. The transverse velocities were computed using only data from 1984 and 1985 (about 360 individual baseline measurements) since the IRIS series does not exist before this. Table 1 lists, for each baseline, the length and transverse velocities in mm/year along with their computed standard deviation. In

order to get a more realistic estimate of the standard deviation, 1 cm of noise was added to each length measurement and 2 cm of noise was added to each transverse measurement. As an example of the data, in Figure 1 plots of the length and transverse data for the Mojave to Monument Peak baseline are shown.

Software has been developed to perform a least squares analysis of this set of length and transverse velocities and determine individual site motions. In the analysis performed, the velocities were weighted by the inverse of their standard deviations. It was necessary to hold two stations fixed to define a reference frame. Westford, included because it helps to resolve the motion at Ft. Davis, was held fixed as one of the anchor points. OVRO was chosen as the other anchor point; its motion was restricted to less than 1 mm/year. OVRO was chosen because it is well east of the San Andreas fault and because there exists a long history of VLBI between Westford and OVRO showing no significant motion. Fairbanks was included because it helps to resolve the northward motions in California. The program allowed specifying a priori first guess site motions as well as restricting a site to a specified a priori value with varying degrees of rigidity. The final solution obtained is thus not unique. However, various solutions with different constraints seem to differ at only the few mm/year level in terms of site motions. Table 2 gives the results of the final solution. Site speed in mm/year and azimuthal direction in degrees are given. Graphically, the results are presented on a map of the western U.S. in Figure 2 (Clark, 1986). The arrows from each site indicate its direction of motion and relative speed. Figure 2 also shows error ellipses. These are estimates based on an examination of the data and are not computed by the least squares fitting program.

SIGNIFICANCE

This work yields the most detailed picture yet of crustal motions in the western U.S. from space geodetic techniques. Seven sites situated near or west of the San Andreas fault show large, significant motions. They are Monument Peak, Vandenberg, JPL (Pasadena), Pearblossom, Fort Ord, Presidio (San Francisco), and Pt. Reyes. While a detailed analysis of these motions is not attempted here, a few points are worth noting. The direction of motion as one moves northward through these sites (except Presidio) rotates to follow the direction of the San Andreas fault. The Presidio site, in San Francisco, appears anomalous. It is just east of the San Andreas and shows westward motion towards the fault, motion which is not understood at this time. At Monument Peak, only about 60% of the full motion of the Pacific Plate relative to the North American is

seen, indicating that the other 40% is taken up in offshore faults. However, Vandenberg and Fort Ord show motion of some 4 - 6 cm/year, which accounts for most of, if not all, the Pacific Plate motion and indicates that little if any slippage is occurring in the faults offshore of these regions. Thus some 4 - 6 cm/year of slippage and/or strain accumulation must be occurring in the region from Vandenberg/Fort Ord eastward to the San Andreas. This could be occurring among the many faults of the Hosgri and San Gregorio fault systems or along the San Andreas or a combination of these.

Additionally, Ft. Davis shows clear eastward motion of about 7 mm/year, in general agreement with earlier findings. There seems to be motion at Platteville and Quincy but it is very uncertain at this time. Also, the southward motion of Fairbanks relative to eastern California is not considered significant.

FUTURE EMPHASIS

During the next year, additional measurements are planned to Vandenberg, Monument Peak, Yuma, Platteville, JPL, and Quincy, as well as the fixed sites Hatcreek, OVRO, Mojave, and Ft. Davis. These can be expected to strengthen the site motion determinations at these sites. Also four sites which have been visited before, Pinyon Flats, Flagstaff, Ely and Blackbutte will be revisited and enough data should then be obtained to include them in a site motion solution. Additional measurements from Fairbanks to Mojave, OVRO and Hatcreek in 1986 should help to clarify the relation between Alaska and eastern California.

REFERENCE

Clark, Thomas A., "Plate Deformation Measurements Using VLBI in the Western U.S.," Report presented to the CDP Investigators Meeting, JPL, Pasadena, California, March 27, 1986.

Table 1. Baseline Motion Information

Baseline		Rate of Change of Baseline Length (mm/year)		Number of Data Sets	Solution Residual	Normalized Solution Residual
		Value	Sigma		(mm/year)	(unitless)
Mojave	to Vandenberg	37	12	8	17	1.4
Mojave	to Gilcreek	−20	10	17	−2	0.2
Mojave	to Kauai	28	11	13	6	0.5
Mojave	to Kwajalein	−14	28	11	−6	0.2
Mojave	to Kashima	−5	25	15	−5	0.2
Vandenberg	to Gilcreek	−72	13	16	17	1.3
Vandenberg	to Kauai	−7	16	9	−5	0.3
Gilcreek	to Kauai	−34	16	12	3	0.2
Gilcreek	to Kwajalein	−35	16	10	8	0.5
Gilcreek	to Kashima	−7	20	12	−19	1.0
Kauai	to Kwajalein	−2	17	11	30	1.8
Kauai	to Kashima	−69	25	10	−15	0.6
Kwajalein	to Kashima	−87	17	8	−17	1.0

Table 2. Site Motion Solution

STATION	Motion (mm/yr.)	Azimuth (degrees)
MOJAVE12	0.	—
KASHIMA	0.	—
VNDNBERG	62.	326.
GILCREEK	19.	136.
KAUAI	61.	308.
KWAJAL26	76.	333.

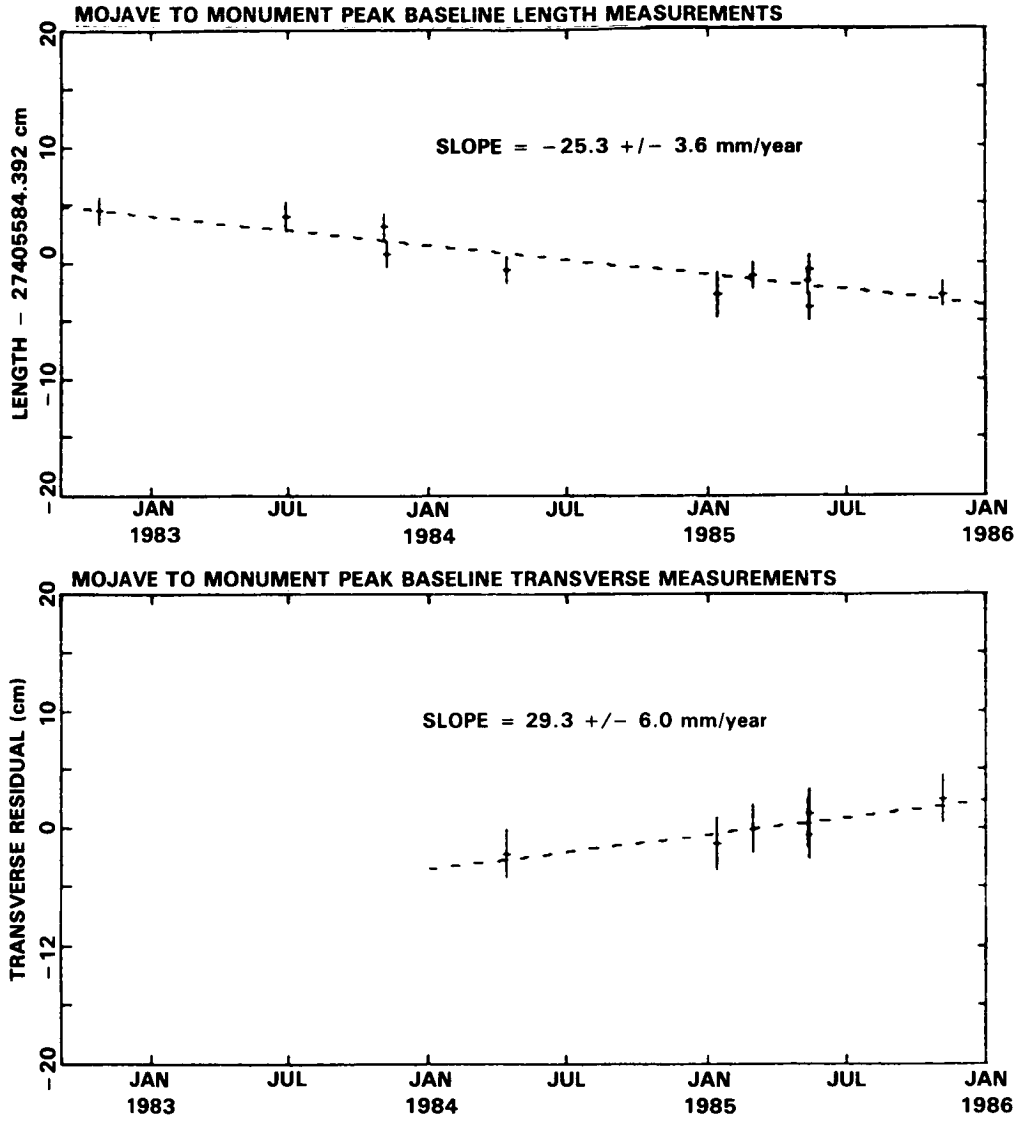

Figure 1. Baseline length and transverse data versus time for the baseline from Mojave to Monument Peak as measured by Mark III VLBI. The vertical line for each point represents the error bar for each individual baseline measurement, where 1 cm of noise was added to each length standard deviation and 2 cm of noise was added to each transverse standard deviation. The least squares fit and its slope for each plot represent the length and transverse velocities of this baseline.

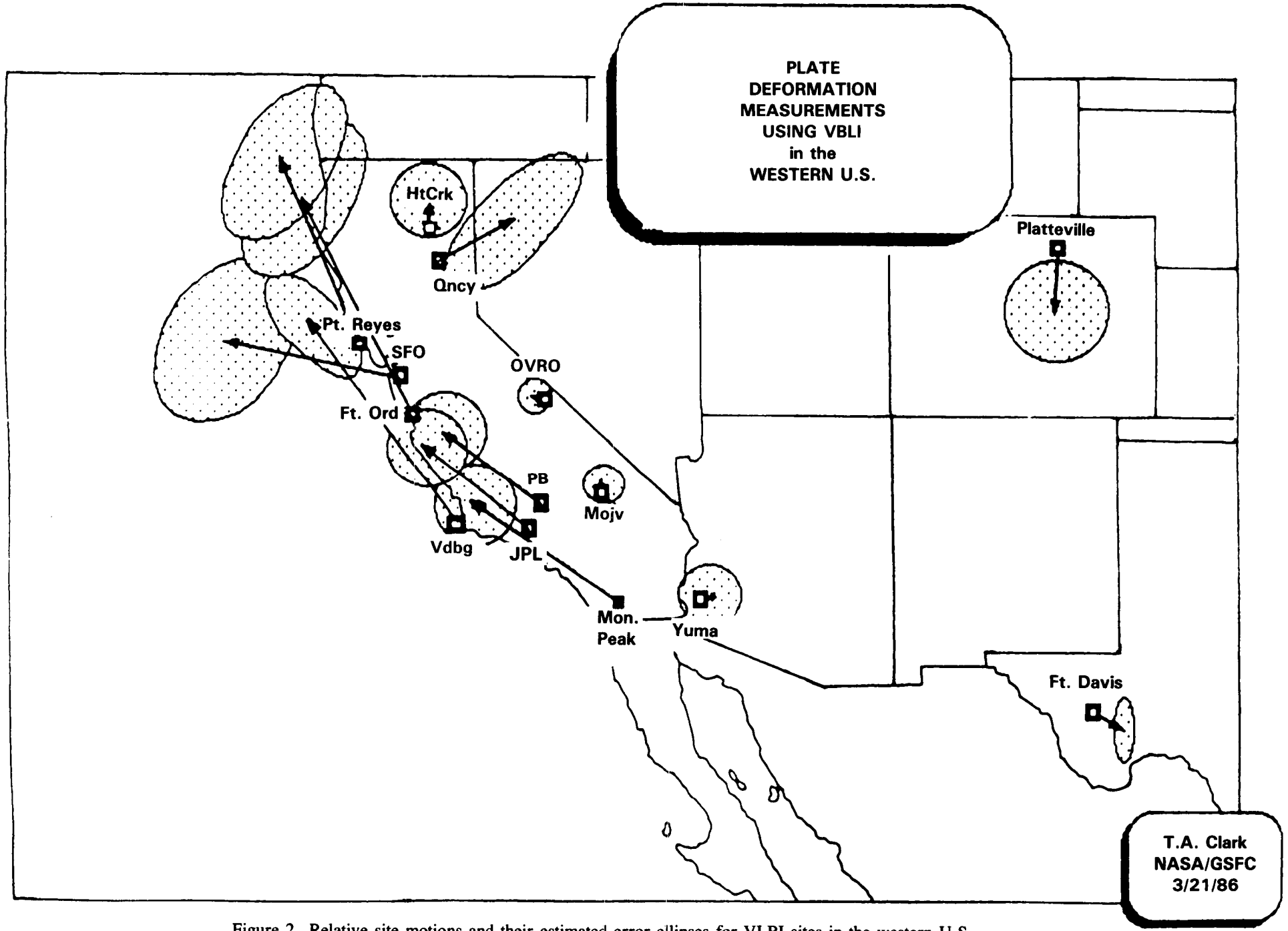

Figure 2. Relative site motions and their estimated error ellipses for VLBI sites in the western U.S.

PACIFIC PLATE MOTION OBSERVED WITH MARK III VLBI

James W. Ryan
Chopo Ma

OBJECTIVE

A primary objective of the NASA Crustal Dynamics Project (CDP) is to make contemporary measurements of the large-scale motions of the Earth's crust. These data are then the basis from which models of the current dynamics of the Earth can be made. Because of its seismicity, one area of great interest is the rim of the Pacific.

BACKGROUND

As a part of its program to monitor global-scale tectonic plate motions the CDP in early 1984 began a series of VLBI experiments to measure the motions of sites on the Pacific plate relative to sites on the Pacific rim. The Pacific plate sites, called here Kauai, Kwajalein, and Vandenberg, are located in the Hawaiian and Marshall Islands (3700 kilometers west Hawaii) and at Point Arguello in California, respectively. The Pacific rim sites, called Mojave, Gilcreek, and Kashima, are located in California's Mojave desert, in central Alaska, and in Japan, respectively.

The first two experiments in the Pacific motion series took place in January and February 1984 between Mojave and Kashima and were largely engineering tests of the new Japanese-built K-3 VLBI data acquisition system. In the summers of 1984 and 1985 there were two series of six experiments each using various subsets of the sites mentioned above. Vandenberg also participated with Gilcreek in a series of Alaskan regional experiments in 1984 and 1985. Table 1 shows the number of data sets for the various baselines. Some experiments produced two data sets.

RECENT ACCOMPLISHMENTS

These data were analyzed as a part of a large least-squares adjustment of all the CDP and IRIS Mark III VLBI data acquired in 1984 and 1985. (IRIS is the operational Earth rotation monitoring program of the National Geodetic Survey which uses Mark III VLBI). In all there were 167 data sets. The parameters estimated in this solution were experiment-dependent site positions, globally

estimated radio source coordinates, experiment-dependent offsets to the nutations in obliquity and longitude, and time and station-dependent clock and atmosphere parameters. Since the site coordinates were estimated in this solution for each epoch independently, any tectonic effects which might have occurred during the 2-year period could be accommodated. The results of this solution were condensed in the form of tables of baseline length during the time interval. Errors in the a priori values of pole position and UT1 from the B.I.H. do not affect these length histories since they affect only the orientation of the networks in the VLBI coordinate system. From each of these baseline histories a length and rate of change of length were determined. Table 1 shows the rates of change of baseline length with their formal standard error from the least-squares fits. The rates of change reflect possible plate motion effects.

In order to test whether these observed motions are consistent with a simple model of Pacific plate motion relative to the North American plate, the 13 rates-of-change given in Table 1 were used to estimate by weighted least-squares the motions of Kwajalein, Kauai, Vandenberg, and Gilcreek. For each station the local north and east components of the station velocity were estimated in a coordinate frame in which Mojave and Kashima were held fixed. This is an ad hoc constraint. However, there are valid geophysical reasons (not discussed here) for assuming that Kashima and Mojave have no relative motion, and the direct baseline measurements between these sites are consistent with no motion. In any case some such constraint is needed to anchor the coordinate frame. Table 2 presents the results of this estimation as the total station motion in the horizontal plate and the azimuth of the motion. The uncertainties are not tabulated. Since this data set spans only 1.5 years with only 13 data points to estimate 6 parameters, the uncertainties produced by the estimator are not meaningful. The justification for the correctness of this solution is intuitive and rests on its ability to fit the observed motions.

SIGNIFICANCE

The last two columns in Table 1 present the differences between the observed and computed motions and these differences normalized by the corresponding rate-of-change sigma. Three baseline velocities, Mojave to Vandenberg, Vandenberg to Gilcreek and Kauai to Kwajalein, have large normalized residuals indicating that these velocities and sigmas are not entirely consistent with the other data. Except for these three values the residuals are 1 sigma or less and eight are at the level of 0.5 sigma or less. Table 2 shows that Vandenberg, Kauai and Kwajalein are all moving with a velocity of 60-70 mm/year in a northwesterly direction. This is entirely

consistent with current models for the motion between the Pacific and North American plates. The solution also indicates a relative motion of approximately 15 mm/year between Kauai and Kwajalein and motion of Gilcreek towards Mojave at a rate of 19 mm/year. Neither of these smaller motions is consistent with current plate motion models.

In summary, a motion of the Pacific plate relative to the North American plate of approximately 65 mm/year in a northwesterly direction appears to have been detected. The solution also indicates that there are intraplate motions at the level of 20 mm/year, which are at variance with current plate motion models.

FUTURE EMPHASIS

Experiments involving the current Pacific stations planned for the summer of 1986 will nearly double the time span of the data sets on these baselines. This will significantly improve the precision of the observed motions and provide the basis for a statistically significant estimation of the motion of the stations. During a trip made by the second author to China and Japan in 1985, discussions were held with researchers at the Shanghai Observatory, the Yunnan Observatory, the Research Institute of Mapping and Surveying in Beijing, and the Kashima Space Research Center about future VLBI programs which could extend the baselines around the Pacific into the Asian mainland. An exploratory VLBI experiment has been performed between Shanghai and Kashima. The Shanghai Observatory has acquired Mark III VLBI equipment, and its new 25-m antenna is planned to be operational by 1986.

Table 1.

Baseline	LENGTH VELOCITY mm/yr	TRANSVERSE VELOCITY mm/yr
WESTFORD — FT. DAVIS	−9. +/− 2.	—
WESTFORD — OVRO	2. +/− 2.	—
WESTFORD — FAIRBANKS	5. +/− 5.	—
FT. DAVIS — PLATTVIL	−13. +/− 8.	−7. +/− 10.
FT. DAVIS — YUMA	11. +/− 4.	0. +/− 100
FT. DAVIS — MON PEAK	39. +/− 5.	20. +/− 10.
FT. DAVIS — MOJAVE	5. +/− 2.	7. +/− 4.
FT. DAVIS — OVRO	8. +/− 2.	4. +/− 5.
FT. DAVIS — VNDNBERG	47. +/− 7.	55. +/− 16.
FT. DAVIS — QUINCY	−0. +/− 9.	37. +/− 10.
FT. DAVIS — HATCREEK	15. +/− 4.	2. +/− 10.
FT. DAVIS — FAIRBANKS	0. +/− 22.	31. +/− 20.
PLATTVIL — MOJAVE	−9. +/− 8.	10. +/− 10.
PLATTVIL — OVRO	−1. +/− 8.	23. +/− 10.
PLATTVIL — HATCREEK	−3. +/− 7.	.6 +/− 10.
YUMA — MON PEAK	32. +/− 8.	16. +/− 100
YUMA — MOJAVE	5. +/− 5.	1. +/− 8.
YUMA — OVRO	8. +/− 10.	0. +/− 100
YUMA — VNDNBERG	44. +/− 11.	19. +/− 13.
MON PEAK — MOJAVE	−25. +/− 4.	29. +/− 5.
MON PEAK — OVRO	−31. +/− 4.	22. +/− 5.
MON PEAK — VNDNBERG	15. +/− 6.	34. +/− 7.
MON PEAK — QUINCY	−35. +/− 7.	36. +/− 22.
MON PEAK — HATCREEK	−22. +/− 6.	20. +/− 6.
MOJAVE — PBLOSSOM	9. +/− 3.	27. +/− 5.
MOJAVE — PASADENA	10. +/− 6.	31. +/− 6.
MOJAVE — OVRO	−2. +/− 2.	−0. +/− 2.
MOJAVE — VNDNBERG	18. +/− 3.	29. +/− 4.
MOJAVE — QUINCY	−2. +/− 4.	19. +/− 6.
MOJAVE — HATCREEK	5. +/− 3.	2. +/− 4.
MOJAVE — FORT ORD	31. +/− 6.	35. +/− 6.
MOJAVE — PRESIDIO	28. +/− 4.	−11. +/− 5.
MOJAVE — PT REYES	29. +/− 6.	22. +/− 7.
MOJAVE — FAIRBANKS	−10. +/− 5.	0. +/− 10.
PBLOSSOM — PASADENA	−2. +/− 6.	−4. +/− 10.
PBLOSSOM — OVRO	−7. +/− 3.	19. +/− 5.
PBLOSSOM — VNDNBERG	13. +/− 4.	7. +/− 8.
PASADENA — OVRO	−17. +/− 6.	19. +/− 8.
PASADENA — VNDNBERG	19. +/− 10.	−6. +/− 10.
OVRO — VNDNBERG	−10. +/− 3.	53. +/− 4.
OVRO — QUINCY	−4. +/− 4.	19. +/− 7.
OVRO — HATCREEK	5. +/− 3.	5. +/− 4.
OVRO — FORT ORD	13. +/− 4.	53. +/− 8.
OVRO — PRESIDIO	25. +/− 6.	10. +/− 7.
OVRO — PT REYES	29. +/− 6.	39. +/− 8.
VNDNBERG — QUINCY	−44. +/− 17.	52. +/− 28.

Table 1. (Con't)

Baseline	LENGTH VELOCITY mm/yr	TRANSVERSE VELOCITY mm/yr
VNDNBERG — HATCREEK	−28. +/− 4.	34. +/− 5.
VNDNBERG — FORT ORD	8. +/− 5.	22. +/− 6.
VNDNBERG — PRESIDIO	−1. +/− 6.	−23. +/− 7.
VNDNBERG — PT REYES	2. +/− 9.	9. +/− 8.
VNDNBERG — FAIRBANKS	−70. +/− 6.	10. +/− 20.
QUINCY — HATCREEK	3. +/− 10.	−11. +/− 6.
HATCREEK — FORT ORD	−25. +/− 5.	34. +/− 6.
HATCREEK — PRESIDIO	33. +/− 8.	39. +/− 9.
HATCREEK — PT REYES	−23. +/− 8.	18. +/− 9.
FORT ORD — PRESIDIO	−9. +/− 11.	−40. +/− 115
PRESIDIO — PT REYES	−4. +/− 9.	23. +/− 20.

Table 2.

STATION	MOTION (mm/yr)	AZIMUTH (degrees)
WESTFORD	0.	0.
FT. DAVIS	7.	132.
PLATTVILLE	13.	183.
YUMA	2.	71.
MONUMENT PEAK	35.	304.
MOJAVE	2.	359.
PEARBLOSSOM	24.	308.
JPL (PASADENA)	27.	318.
OVRO	0.	210.
VANDENBERG	50.	325.
QUINCY	19.	61.
HATCREEK	5.	9.
FORT ORD	48.	334.
PRESIDIO (SFO)	36.	288.
PT. REYES	40.	338.
FAIRBANKS	8.	176.

CHANGES IN THE EARTH'S ROTATION AND LOW-DEGREE GRAVITATIONAL FIELD INDUCED BY EARTHQUAKES

B. Fong Chao

Richard S. Gross

OBJECTIVE

The two objectives of this work are: (1) To compute the changes in the Earth's rotation parameters (polar motion and length-of-day) and in low-degree gravitational field caused by major earthquakes during the period 1977-1985, and (2) To conduct statistical analyses on these changes to reveal their geophysical significance.

BACKGROUND

The Earth's gravitational field is not static. Instead, it is constantly subject to minute changes caused by geophysical variations in the density distribution of the Earth's material. These density variations also cause the Earth's rotation to fluctuate--they excite the polar motion and change the length-of-day (LOD).

This study investigates the geodetic and gravitational effect of earthquakes as a mechanism by which the Earth changes its density distribution. The study of gravitational effect of earthquakes has been restricted only to the polar motion, although it has been studied many times over in the past (e.g. Lambeck, 1980). No conclusive evidence of a significant effect has yet been found. Two reasons stand out: (1) inadequacies in accuracy and temporal resolution of the conventional polar motion data, and (2) lack of truly great earthquakes since the 1964 Alaskan event. However, modern techniques, such as satellite laser ranging and very-long-baseline-interferometry, have demonstrated the ability to yield highly accurate polar motion and LOD data, as well as the ability to detect changes in J_2 (e.g. Rubincam, 1984) and other gravitational coefficients. While these techniques are improving, future space geodetic missions (such as the proposed Geopotential Research Mission) may prove to be useful tools to observe the temporal changes in the gravitational field (Wagner and McAdoo, 1986).

RECENT ACCOMPLISHMENTS

The theoretical formulation is achieved using a normal mode summation scheme based on Gilbert (1973) and Gilbert and Dziewonski (1975). [The same scheme has been employed by O'Connell and

Dziewonski (1976) in computing seismically-induced changes in polar motion and LOD, but no complete account of their procedure has been published.] Thus we derived our basic formula which turns out to be particularly simple both in a mathematical and computational sense:

$$\Delta C_{\ell m} + i\Delta S_{\ell m} = \Sigma \; I_{n\ell} \; M : \varepsilon_{n\ell m}(r_o) \qquad (1)$$

where the symbol : indicates a tensor contraction.

The left-hand side is the change in the gravitational-field harmonic coefficient (the "Stokes Coefficient") of degree ℓ and order m. On the right-hand side, $I_{n\ell}$ is an integral involving the spheroidal eigenelements of the (spherically symmetric) Earth with overtone number n and degree ℓ ; M is the moment tensor of the earthquake; and $\varepsilon_{n\ell m}\ (r_o)$ is the elastic strain tensor at the source r_o associated with the (n, ℓ, m)th spheroidal normal mode. The eigenelements and the strain tensor are obtained from the earth model 1066B from Gilbert and Dziewonski (1975). The seismic moment tensors M are taken from those published regularly by the Harvard Group since 1977 (some 2000 events, see Dziewonski et al., 1985). The summation in (1) (over n) is found to converge rapidly. We have thus computed the seismically induced changes in some low-degree Stokes coefficients. Of particular interest are the J_ℓ (m=0) coefficients and the polar motion excitation (ℓ=2, m=1). In addition, a formula similar and complementary to (1) gives the changes in the length-of-day.

Major findings are: (1) The earthquake-induced changes we computed are in general two orders of magnitude smaller than the observed values that are available. (2) Most of these changes show strong evidences of non-randomness either in their polarity or in their directions. (3) The parameters that show the strongest non-randomness are the dynamic oblateness J_2, the total principal moment of inertia, the length-of-day, and the sum of as well as the difference between the two equatorial principal moments of inertia. They are all inclined toward negative changes, indicating the tendency of earthquakes to make the Earth rounder, and to pull in mass toward the center of the Earth. (4) The earthquakes continue to make the rotational pole drift toward a preferred direction of ~150°E. This direction is roughly the opposite to that inferred from observations. (5) The earthquake-induced changes in the polar principal moment of inertia are considerably larger than those in its two equatorial counterparts combined. (6) The earthquake-induced changes in the zonal harmonics J_3, J_4, J_5 (and perhaps higher terms) are much smaller than that in J_2; and they show little sign of non-randomness. (7) The above behaviors appear to be independent of time and the size of the earthquake causing the changes.

Further investigation will be made on the statistics of the seismic excitation of polar motion. The results will be interpreted in the hope that light can be shed on the Earth's internal dynamics. On the other hand, any great earthquakes in the future will be subjected to the study outlined here on an individual basis. The predicted geodetic and gravitational changes will be compared to observations in search of any possible correlation.

REFERENCES

Dziewonski, A.M., J.E. Franzen, and J.H. Woodhouse, Centroid-moment tensor solutions for January - March 1985, Phys. Earth Planet. Int., 40, 249-258, 1985.

Gilbert, F., Excitation of the normal modes of the Earth by earthquake sources, Geophys. J. R. Astro. Soc., 22, 223-226, 1970.

Gilbert, F., and A.M. Dziewonski, An application of normal mode theory to the retrieval of structural parameters and source mechanisms from seismic spectra, Phil. Trans. R. Soc. Lond., A-278, 187-269, 1975.

Lambeck, K., The Earth's Variable Rotation, Cambridge Univ. Press, New York, 1980.

O'Connell, R.J., and A.M. Dziewonski, Excitation of the Chandler wobble by large earthquakes, Nature 262, 259-262, 1976.

Rubincam, D.P., Postglacial rebound observed by LAGEOS and the effective viscosity of the lower mantle, J. Geophys. Res., 89, 1077-1087, 1984.

Wagner, C.A., and D.C. McAdoo, Time variations in the Earth's gravity field detectable with GRM intersatellite tracking, in preparation, 1986.

FEATURES OF COMPRESSIONAL STRAINING IN CONTINENTAL COLLISIONS

Steven C. Cohen

OBJECTIVE

Continental collisions result in considerable intraplate deformation, a geophysical phenomenon that is not well-incorporated into the rigid plate formulation of plate tectonics. The manner in which strain and stress are transmitted into the plate interior from the plate boundary is an important aspect of this phenomenon. The objective of this work is to develop numerical models that explain the intraplate deformation and strain propagation in terms of the rheological properties of the earth and mechanisms of plate interactions.

BACKGROUND

Among the many manifestations of continental collisions are a variety of lithospheric and crustal deformations that can extend very deep into continental interiors. Mountain building, plateau uplift, block rotations, and thrust, strike-slip, and normal faulting have all been related to the convergence between two lithospheric plates having large continental masses. Much of the research on continental collisions has focused on the India-Eurasia collision; however there are several other examples on continental collision which are ongoing today or have occurred in the past. Several models have been proposed to account for some or all of the features of continental collision. Frequently one of the colliding continents is more deformable than the other. A viscous sheet/rigid punch model has enjoyed considerable success in accounting for many of the tectonic features for this case. For example, Tapponnier and Molnar (1977) applied this model in Asia to explain the extensive left lateral strike-slip motion that results in an eastward extrusion of a portion of China away from the collisional front. The model is also consistent with the right lateral fault motion observed in Southeast Asia, the compression observed north of Himalayas, the crustal thickening in the Tibet, and perhaps even the extensional deformation observed in Shansi graben and Baikal rift zones. England and McKenzie (1982) and Vilotte et al. (1982) have derived mathematical representations of this model and have done extensive numerical experiments to elicit the dependence of

the deformation on model parameters. Their results and those of Cohen and Morgan (1986) show that the critical model parameters are the stress exponent and multiplicative constant of the stress-strain rate constitutive law, the parameters expressing the relative magnitude of the horizontal tectonic and isostatically induced stresses, and the boundary conditions placed on the plate edges. In this study a finite element realization of the England and McKenzie (1982) model was used to study the modes of compression predicted to occur as a consequence of continental collision.

RECENT ACCOMPLISHMENTS AND SIGNIFICANCE

Figure 1 shows the essential features of the viscous sheet-rigid punch model. The lithosphere of the deformable continental plate is represented by a thin, incompressible viscous sheet governed by a nonlinear power law constitutive relation:

$$r_{ij} = BE^{(1/n-1)}e_{ij} \qquad (1)$$

where r and e are the deviatoric stress and strain rate tensors, E is the second invariant of the strain rate tensor, and B and n are numerical parameters. A single constitutive law is used for the entire lithosphere but the division of the lithosphere into crust and mantle layers is accounted for in vertically averaging the deformation. During the collision a portion of the southern boundary of the deformable sheet is moved northward at a prescribed rate in order to represent the advance of a rigid punch or nondeforming continental plate. As a consequence both horizontal deformations and crustal and mantle thickness changes occur in the sheet. Local isostasy is maintained by assuming Airy compensation against a crustless oceanic plate. Conservation of crustal mass is also maintained through an incompressibility condition. Figure 2 shows an example of the deformation of a finite element mesh that is used to model the lithosphere. Symmetry is assumed about the Y-axis so that only the right-hand side of the deforming sheet needs to be shown.

The major feature examined in this report is the contraction rate observed in front of the punch; particular emphasis is placed on its spatial and temporal dependence. Specifically e_{yy} is plotted as a function of distance from the punch at various times along the axis X=0. A moving coordinate system is used where the value Y=0 is located on the boundary between the advancing punch and deforming plate. There are two classes of patterns for e_{yy}. When the horizontal stresses are sufficiently large that they dominate the isostatic relaxation, the deformation pattern shows very

little time-dependence. For a linear rheology, the peak value of the strain rate occurs not on the punch boundary but at a considerable distance into the plate interior. Conversely when the B value of the constitutive law is sufficiently small that the tectonic and isostatic stresses can be of comparable magnitude, the strain rate field can propagate ahead of the advancing punch. This propagation is more efficient for a nonlinear rheology with typical values being few cm/yr. Some specific examples of these two types of behavior are presented below.

Figure 3 shows the dependence of the strain rate on distance from the punch for two difference times for a linear rheology with B equal to 1. x 10^{24} Pa sec (corresponding to a viscosity of 5. x 10^{23} Pa sec). The peak value of the strain rate occurs not at the punch boundary, but at about 1000 km from the punch, a value determined primarily by the punch width. The strain rate field is very broad. The value of the strain rate at the northern boundary of the sheet (Y=3600 km) at t=0 is still about 50 percent of the peak value. The broadness of the strain rate field for the linear rheology makes the results somewhat sensitive to the choice of distant boundary conditions (for these results, the northern boundary of the sheet is held fixed). Additionally, the strain rate field shows only minor changes with time. This general behavior persists with decreasing viscosity until the viscosity is smaller than that suggested by various geophysical measurements. However with a viscosity of 5. x 10^{21} Pa sec the differences between the strain rates at the two times shown on Figure 4 are more substantial. Following the buildup of topography and crustal thickening, isostatic effects reduce the strain rate near the collisional boundary and increase them farther away. Still, the position of the peak strain rate advances only very slowly away from its initial position relative to the boundary. The results for a nonlinear rheologies are quite different. In Figure 5, for example, the values n=3 and B=5 x 10^{13}(cgs units) were used which correspond to the experimentally-determined values for typical lithospheric rocks. With the nonlinear rheology, the effective viscosity can be very small in the contact region and larger at a distance. As a consequence when the initial contact occurs between the plates, the strain rate is a maximum closer to the boundary than for the linear rheology. As the crust thickens with time, the stresses associated with the isostatic process increase and become comparable to the stresses due to the collision. When this condition is achieved, further thickening of the region is resisted. Instead the crustal material is extruded northward (and eastward) resulting in an increase in the strain rate and crustal thickening in front of the punch. The position of the strain rate maximum propagates northward. The rate of propagation is the time derivative of the extremum position. For the parameters used in this

calculation, the propagation velocity reaches approximately 3 cm/yr. The calculation can be repeated for a nonlinear rheology with a higher B value or with no density contrast between the mantle and crust. These results are shown in Figure 6 which illustrates a case where the propagation effect has been eliminated with this change in parameter values. Two general conclusions can be reached by comparing these results. First, the propagation of the strain field is much more pronounced for n=3 than n=1, and second, the propagation results from an interaction of the tectonic and isostatic stresses and disappears when the gravitational effects vanish.

FUTURE EMPHASIS

The deformation features associated with continental collision are influenced both by the compressive and shear stresses generated by the collision and by the extensional stresses generated by the induced isostatic response. A fully satisfactory treatment of this problem requires a three-dimensional analysis where stress and strain rate can vary with depth. Future work will be directed toward the development of a complete three-dimensional finite element model capable of analyzing both the horizontal and vertical deformations.

REFERENCES

Cohen, S.C., and R.C. Morgan, "Intraplate Deformation Due to Continental Collisions: A Numerical Study of Deformation in a Thin Viscous Sheet," Tectonophysics (in press), 1986.

England, P., and D.P. McKenzie, "A Thin Viscous Sheet Model for Continental Deformation," Geophys. J.R. Astron. Soc., 70, 295-321, 1982. (Correction: Geophys. J.R. Astron. Soc., 73, 523-532, 1983.

Tapponier, P., and P. Molnar, "Active Faulting and Tectonics in China," J. Geophys. Res., 82, 2905-2930, 1977.

Vilotte, J.P., M. Daignieres, and R. Madariaga, "Numerical Models of Intraplate Deformation," J. Geophys. Res., 87, 10709-10728, 1982.

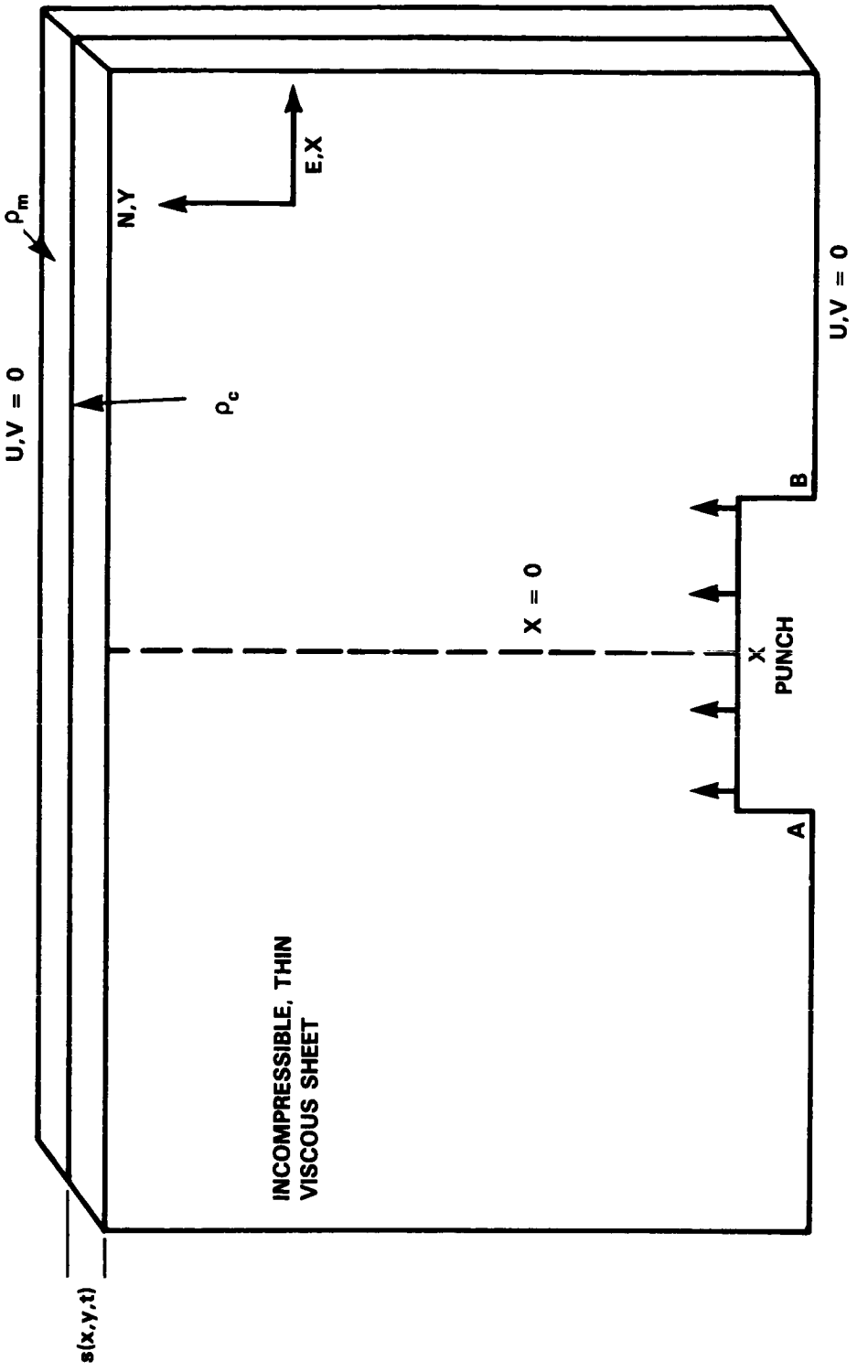

Figure 1. Viscous sheet/rigid punch model of continental deformation. The sheet is an incompressible viscous fluid governed by a single linear or nonlinear constitutive relationship but with crustal and mantle material. A thin layer approximation is used with depth averaging of deformation and stress. In the finite element realization of this model the effects of the rigid punch are modeled by imposing northward motion on a portion of the southern boundary.

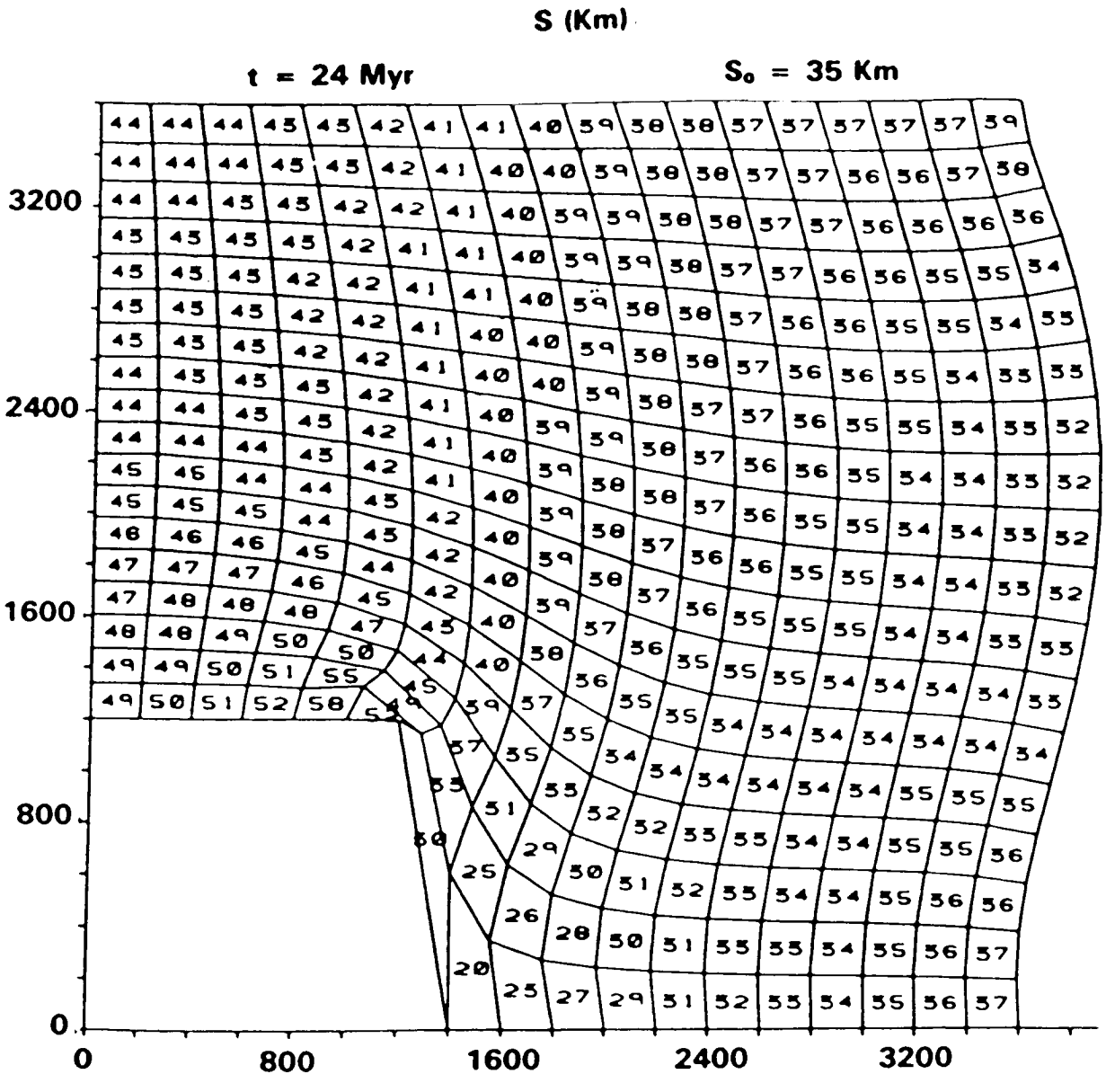

Figure 2. Deformation of the finite element mesh 24 million years subsequent to collision initiation. The grid contains nodes initially separated by 200 km. The punch half width is 1200 km; its northward velocity is 5 cm/yr. The numbers are crustal thicknesses in kilometers, with the initial crustal thickness equal to 35 km. The rheological law is the same as used in Figure 3a.

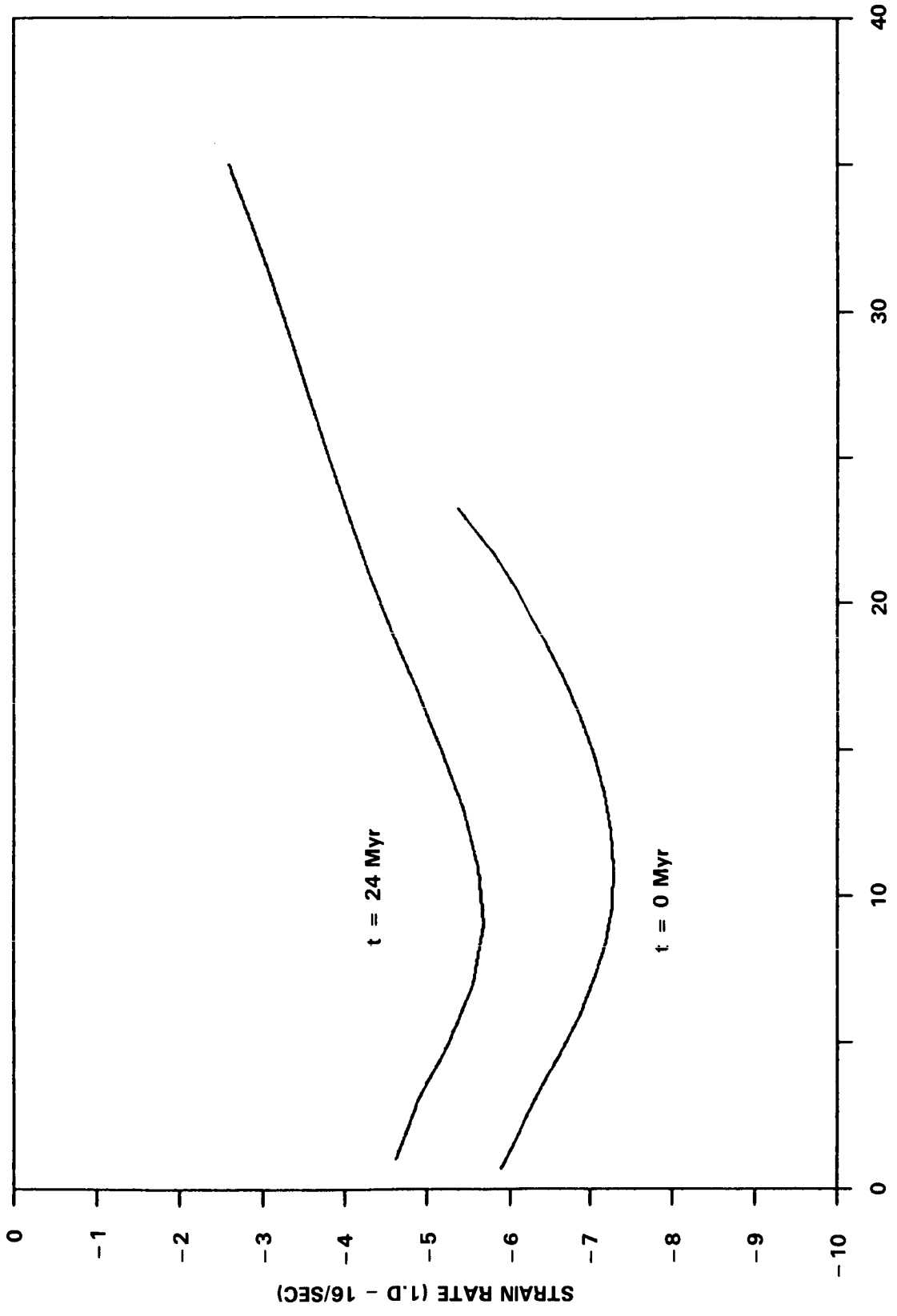

Figure 3. Strain rate versus distance from punch at collision initiation and after 24 million years. Linear rheology (n = 1).

a) B = 1. × 10^{24} Pa sec.
b) B = 1. × 10^{22} Pa sec.

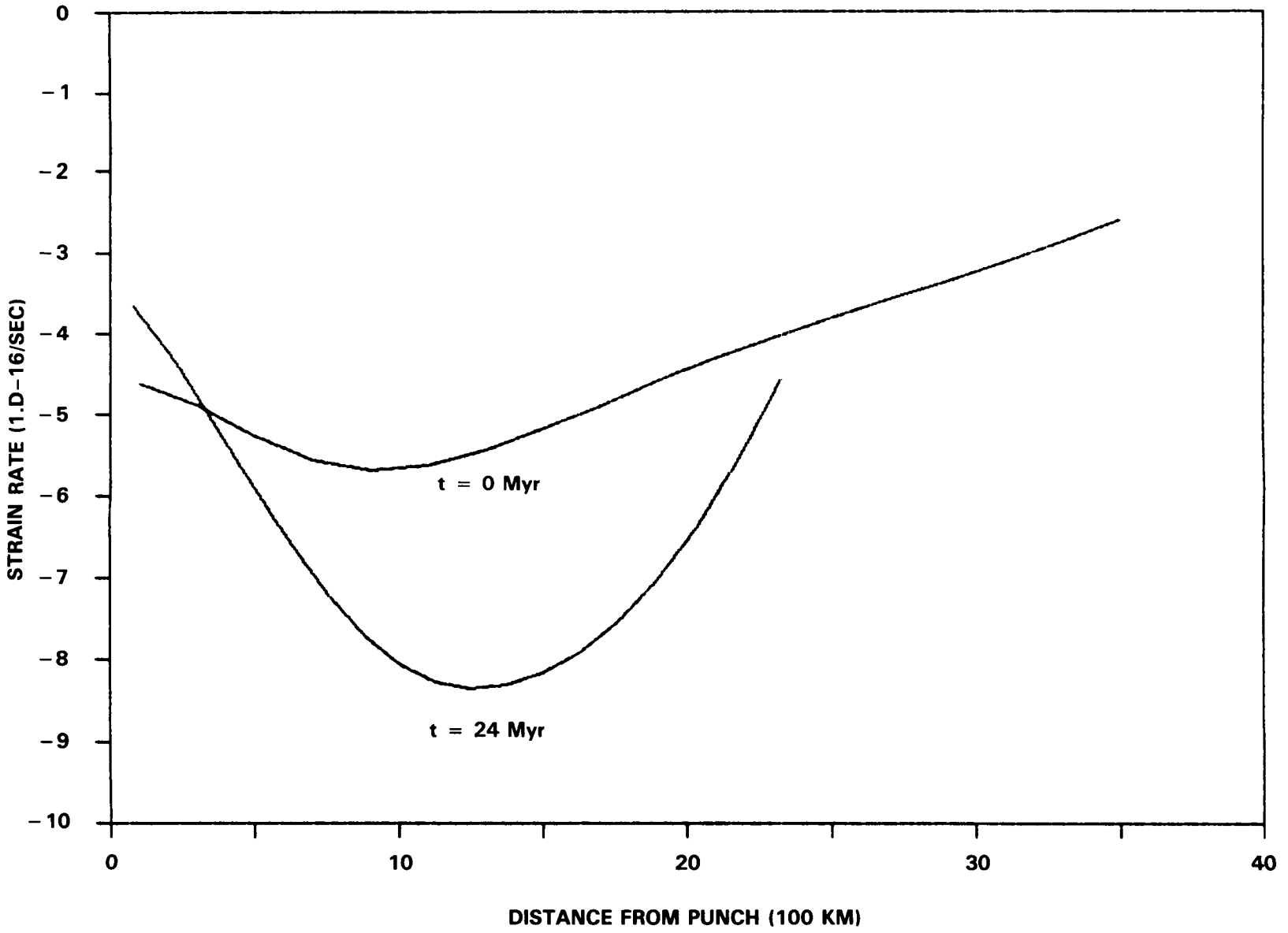

Figure 4. Strain rate versus distance from punch at collision initiation and after 24 million years. Linear rheology (n=1). B=1. × 10^2 Pa sec.

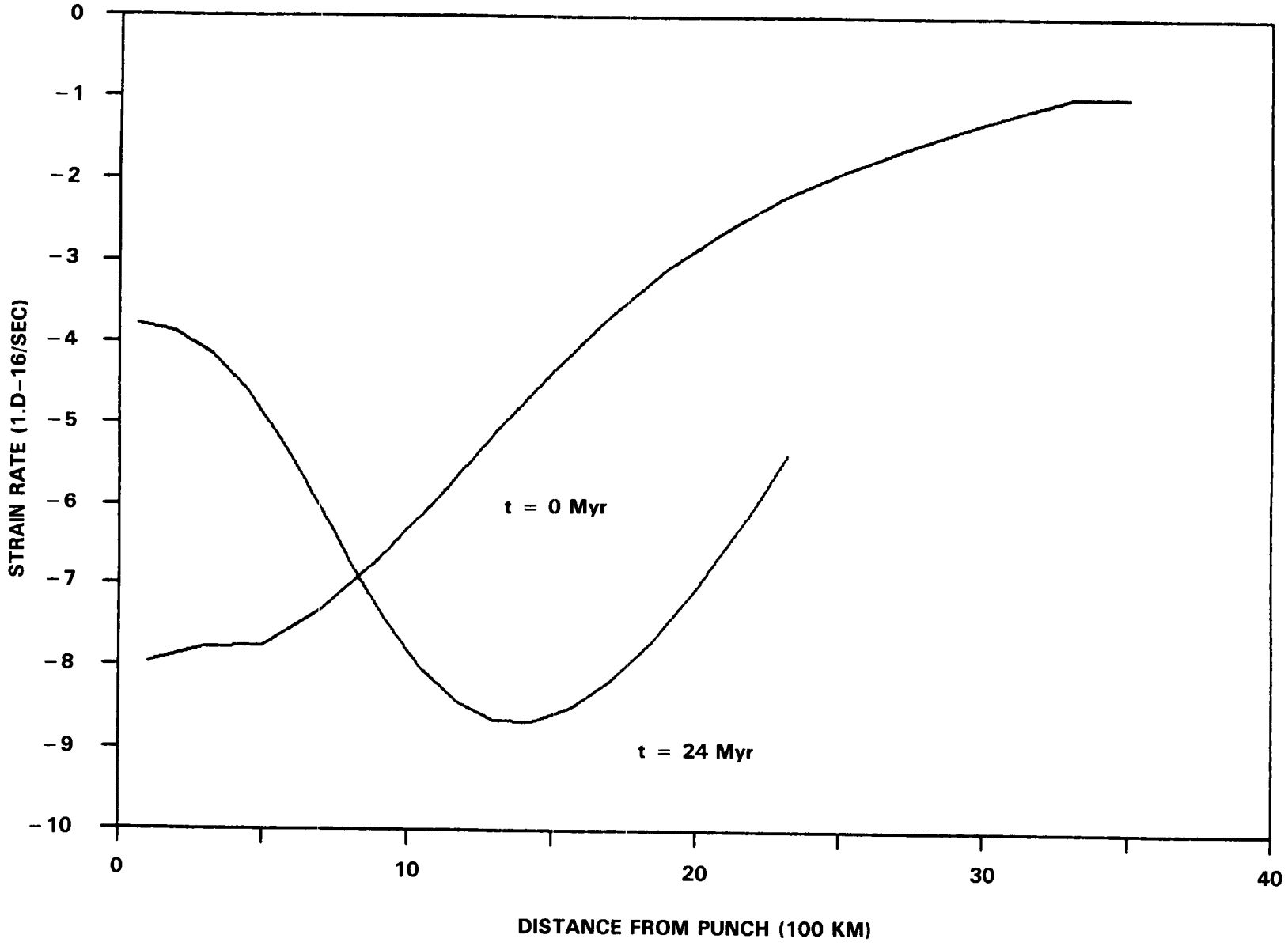

Figure 5. Strain rate versus distance from punch at collision initiation and after 24 million years. Nonlinear rheology (n=3). B=5. $\times 10^{13}$ (cgs units)

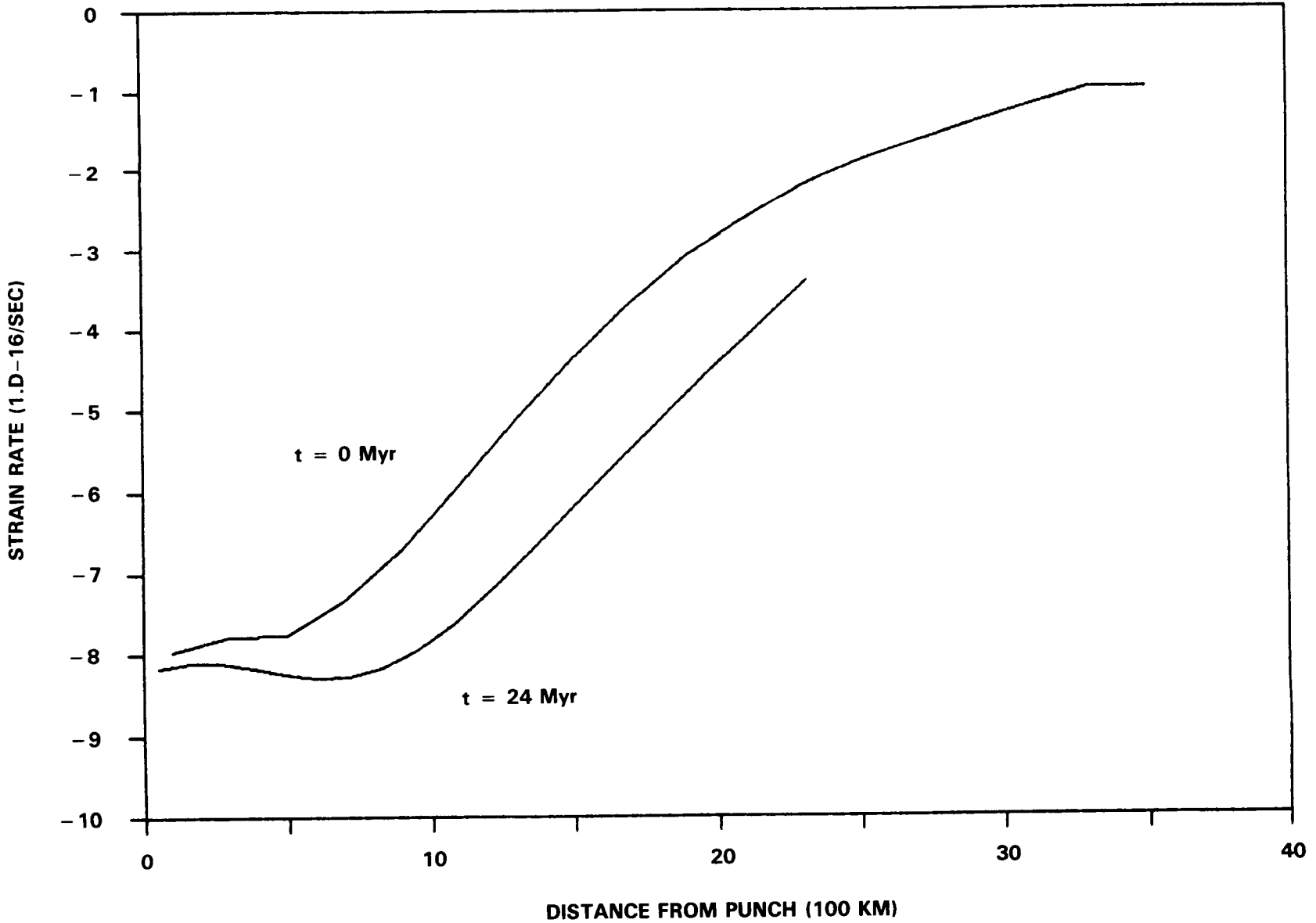

Figure 6. Strain rate versus distance from punch at collision initiation and after 24 million years. Nonlinear rheology (n=3). B is very large or crustal and mantle densities are equal.

ANALYSIS OF INTRAPLATE DEFORMATION IN THE CENTRAL INDIAN BASIN

Maria T. Zuber

OBJECTIVE

Compressional intraplate deformation of oceanic lithosphere is more clearly developed in the Central Indian Basin than anywhere else on the seafloor. This deformation violates the fundamental assumption in plate tectonics that lithospheric plates behave rigidly, deforming only along their boundaries. As most global dynamic and kinematic tectonic models are formulated on the basis of the rigid plate hypothesis, it is of obvious importance to characterize and understand those areas which are deforming internally. The purpose of this work is to investigate the nature of intraplate deformation of oceanic lithosphere using models of a compressing density and strength (viscosity) stratified medium. Model results are compared to the observed geophysical and structural signature of the intraplate deformation in order to constrain the level of stress and style of sub-surface deformation in this part of the Indo-Australian plate.

BACKGROUND

Intraplate deformation in the Central Indian Basin, in the vicinity of the Ninetyeast Ridge, consists of approximately east-west trending topographic undulations with an amplitude of 1-3 km and with a regular spacing of about 200 km (Weissel et al., 1980). The basement undulations are oriented approximately normal to the direction of maximum compressive stress in the Indian plate, which suggests that the deformation is related to forces resulting from the collision of India and Eurasia to form the Himalayas. Associated with the topography are large gravity and geoid anomalies, extensive seismicity, and high heat flow. A map illustrating the east-west trending anomalies in the marine geoid as derived from the Seasat and GEOS-3 altimeter data is shown in Figure 1.

To better understand the nature of the intraplate deformation, models such as shown in Figure 2 have been developed (Zuber et al., 1985a,b) in which the oceanic lithosphere is treated as a strong viscous or plastic layer of uniform strength and thickness h overlying a viscous substrate in which strength decreases with depth. This simple rheological representation, which approximates a

lithosphere in which deformation is accommodated by brittle fracture near the surface and thermally-activated ductile flow at greater depths, has been successfully applied to describe length scales of continental tectonic deformation (e.g., Fletcher and Hallet, 1983). The model lithosphere is assumed to be in a state of uniform horizontal compression.

Two mechanisms are considered to explain the regular spacing of the seafloor topography, namely, flexural buckling of a thin plate and the hydrodynamic growth of compressional instabilities in a layered medium. In both models periodic deformation develops at a dominant wavelength (λ_d), defined by the wave number $k_d(=2\pi/\lambda_d)$ at which viscous resistance to deformation is minimized. The dominant wavelength is a function of the physical properties of the model lithosphere, in particular the layer thickness and the density and strength stratification of the medium. The dominant wavelength is determined from the solution for the instantaneous flow in the compressing layer and substrate. The model results, combined with the observed wavelength of deformation in the Indian Ocean, other geophysical observations, and experimental results on rock rheology, provide constraints on the mechanical and compositional structure of the oceanic lithosphere.

RECENT ACCOMPLISHMENTS

For a range of possible models, three modes of intraplate deformation are possible. These are illustrated in Figure 3 for representative values of the dimensionless parameter S, which relates the buoyancy force due to topographic variations to the vertically averaged strength of the layer. For S=0.1 deformation occurs by flexural folding, in which the strong layer of the lithosphere and the crust (which composes a fraction of the strong layer) retain approximately constant relative thickness. For S=1 deformation occurs by folding accompanied by thickening of the crust and layer in the vicinity of topographic highs. For S=10 deformation occurs in a pinch and swell mode. In the hydrodynamic instability model for a viscous layer, all three modes of deformation are possible, while if the layer is plastic, only the pinch and swell mode can occur. For the viscous buckling model, only the flexural folding mode of deformation is allowed. A comparison of the layer strengths and strong layer thicknesses associated with each model to the depths of intraplate seismicity and experimental results for rock rheology indicate that the S=0.1 and S=1.0 modes of deformation are possible in the Central Indian Basin. Thus, on the basis of present data, either the hydrodynamic growth of instabilities or flexural buckling of a viscous layer may explain the internal deformation of the Indian plate.

FUTURE EMPHASIS

To distinguish between the flexural folding (S=0.1) and layer thickening (S=1) modes of deformation requires measurements of crustal thickness associated with topographic highs and lows within the region of intraplate deformation. Seismic refraction profiling, which will allow the determination of crustal thickness, as well as the collection of more gravity and heat flow data in the Central Indian Basin are planned for the coming year.

REFERENCES

Fletcher, R.D., and B. Hallet, "Unstable Extension of the Lithosphere: A Mechanical Model for Basin and Range Structure, J. Geophys. Res., 88, 7457-7466, 1983.

Marsh, J.G., C.J. Koblinsky, A. Brenner, B. Beckley, and T. Martin, "Global Mean Sea Surface Computations Based Upon a Combination of SEASAT and GEOS-3 Satellite Altimeter Data," EOS Trans. Am. Geophys. Un., 65, 857, 1984.

Weissel, J.K., R.N. Anderson, and C.A. Geller, "Deformation of the Indo-Australian Plate," Nature, 287, 284-291, 1980.

Zuber, M.T. and E.M. Parmentier, "Compression of Oceanic Lithosphere: A Model for Intraplate Deformation in the Central Indian Ocean," EOS Trans. Am. Geophys. Un., 66, 360, 1985a.

Zuber, M.T. and E.M. Parmentier, "Unstable Compression of Oceanic Lithosphere: Application to Intraplate Deformation in the Central Indian Ocean," EOS Trans. Am. Geophys. Un., 66, 1098, 1985b.

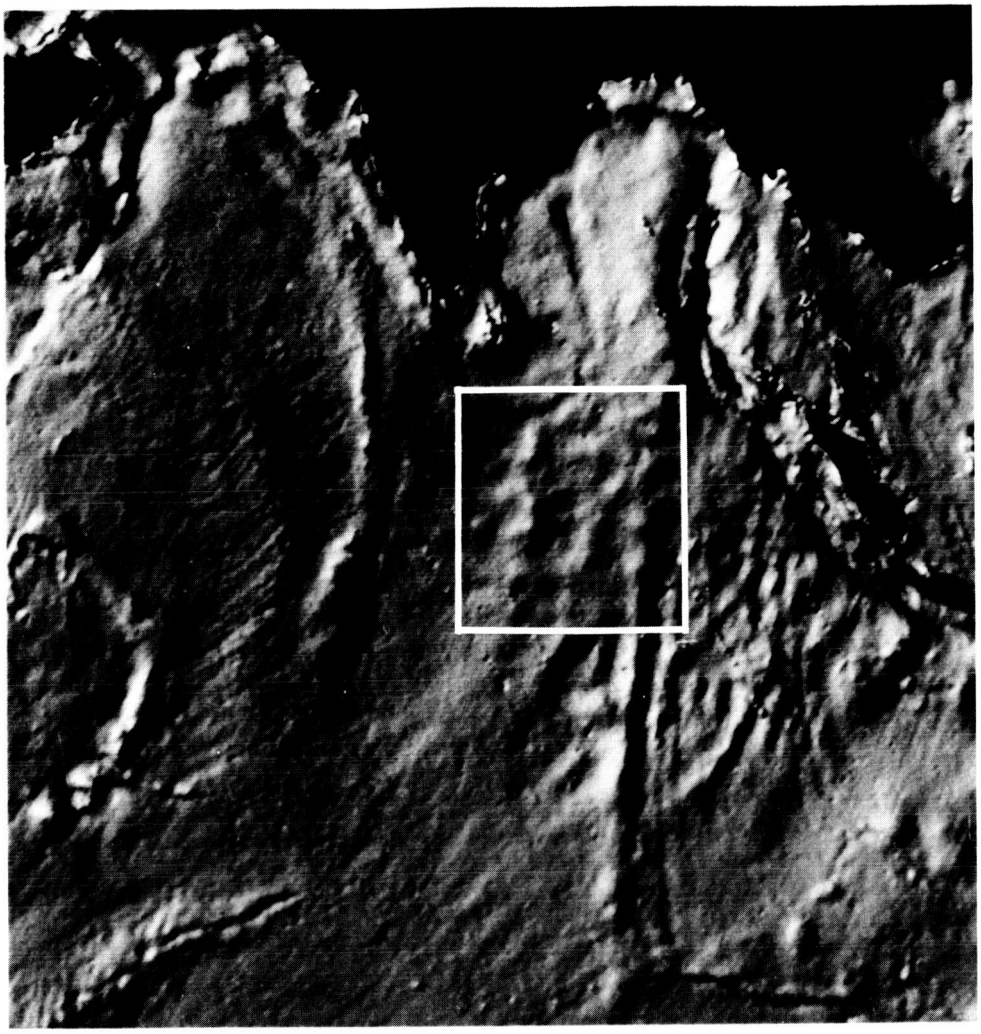

Figure 1. Shaded relief map showing east-west trending geoid anomalies correlated with seafloor deformation. The mean sea surface was derived from Seasat and GEOS-3 altimeter data (Marsh et al., 1984).

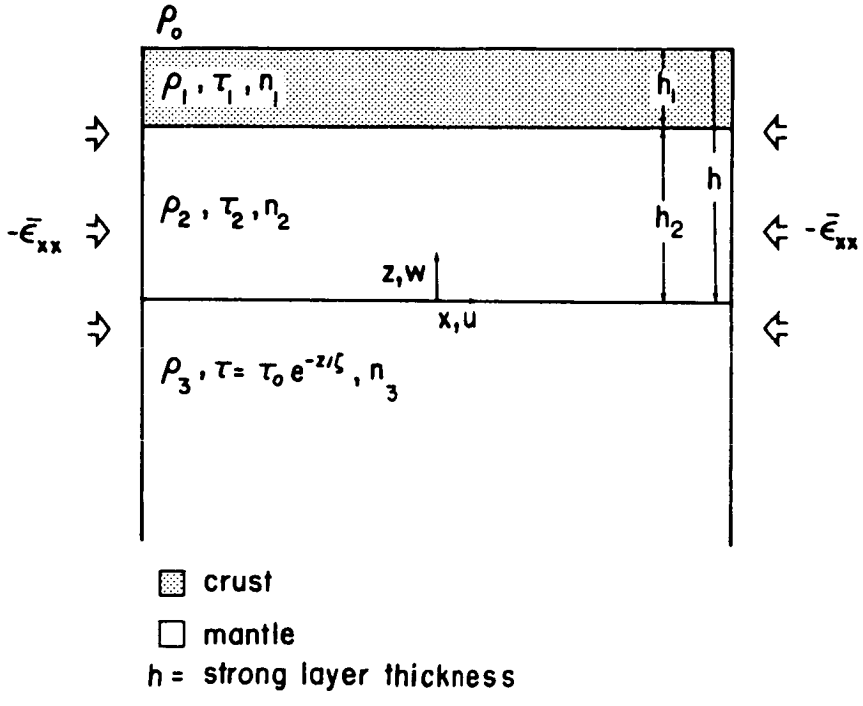

Figure 2. Model of compressing oceanic lithosphere with strong viscous or plastic layer of thickness h overlying weaker viscous substrate with decay depth ζ. The strong layer is composed of the crust and that part of the upper mantle which makes the greatest contribution to lithosphere strength. ϵ_{xx} is the mean horizontal strain rate, and ρ, τ, and n are the density, strength, and stress exponent in the steady state flow law relating stress and strain rate.

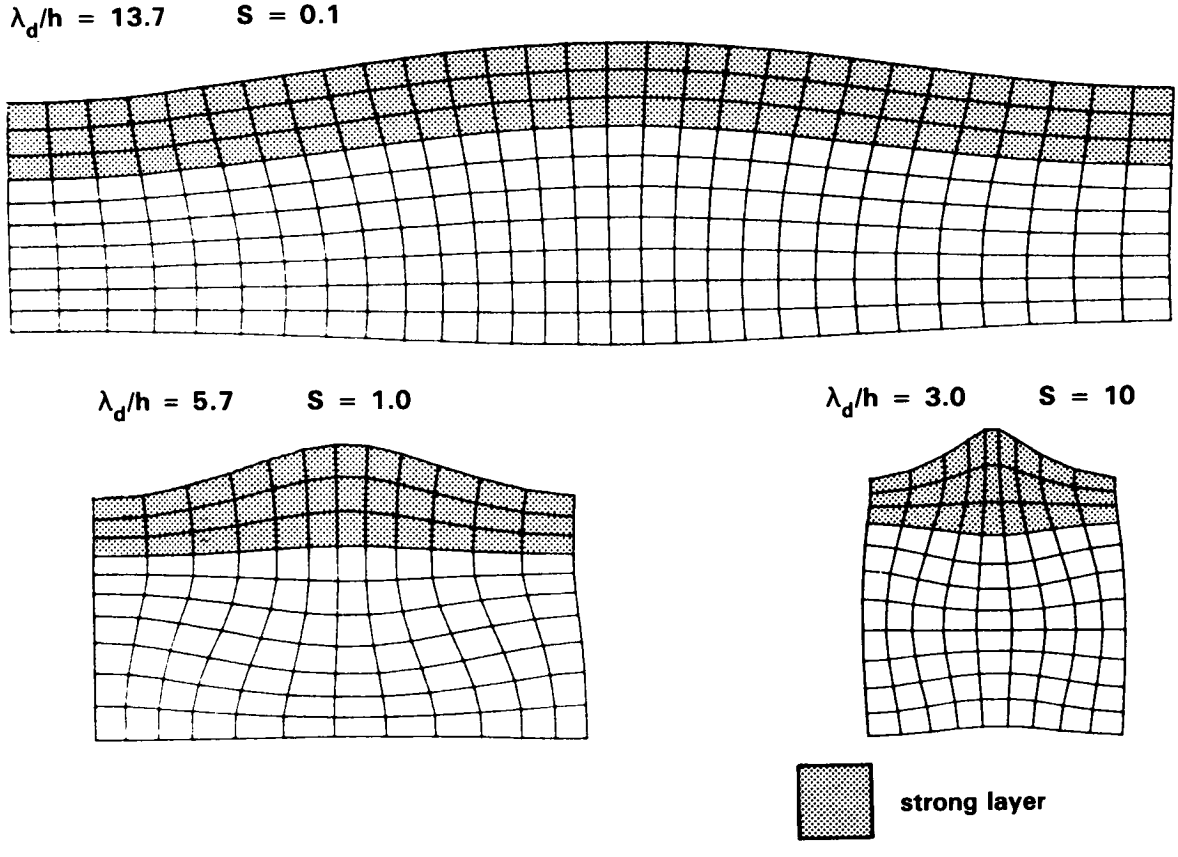

Figure 3. Instantaneous displacement fields illustrating three possible modes of intraplate deformation. For deformation by the hydrodynamic growth of compressional instabilities all three modes are possible, while for deformation by viscous buckling of a thin plate only the S = 0.1 mode is allowed. The S = 0.1 and =1 modes are consistent with Indian Ocean intraplate seismicity and experimental rheological results.

CRUSTAL DEFORMATION UNDER THE TIBETAN PLATEAU AND THE HIMALAYAN RANGE

Han-Shou Liu

OBJECTIVE

The purpose of this paper is to calculate the crustal stresses under the Tibetan Plateau and the Himalayan Range from plate tectonics and satellite-derived gravity data. Our intent is to use this crustal stress model as a geodynamical basis for interpreting seismotectonic characteristics and integrating the satellite-derived gravity data into the framework of plate tectonics.

BACKGROUND

Since Argand (1924) presented his ideas on the tectonics of Asia, Tibet has emerged as a symbol of continental collision. Today, within the framework of plate tectonics, there is little doubt that the massive plateau which maintains an elevation of 4.5 km, over 600 x 1000 km^2 north of the Himalayas, is anything but a direct consequence of the most spectacular India-Eurasia plate collision which has resulted from global plate motions. The forces that have pushed up this immense region must produce a crustal stress field in Tibet. Because a number of tectonic plates on the Earth move in a rather complicated way, the critical problem is how to derive the crustal stress field under Tibet from the stress functions of the global plate boundaries. In this paper mathematical methods for calculation of the stress field in the crust caused by global plate motions are developed.

The methods of stress calculation developed in this paper are based on three fundamental premises: (1) Kelvin's theory for the deformation of spherical shells is correct; (2) Runcorn's theory for the geoid and mantle convection is correct; and (3) The rates of crustal creation and destruction along the global plate boundaries and the satellite-derived gravity data are correct. Given these premises, this study relates the geophysical theories to satellite observations.

Despite decades of research by geoscientists, the crustal deformation of the Tibetan Plateau and the Himalayan Range remains enigmatic. In this paper, a relatively underexploited approach to the study of stress fields which lead to crustal deformation is

presented. The exploration of the stress environment in the crust inferred from plate tectonics and satellite-derived gravity data would provide geophysical explanations for geological field observations and seismological dislocations in Tibet (Liu, 1985).

RECENT ACCOMPLISHMENTS

This paper uses plate tectonics and satellite-derived gravity data to further discussion of crustal deformation under the Tibetan Plateau. The first of three contributions is a spherical harmonic analysis of the global plate boundary system. A distribution of 470 Dirac delta functions is applied to describe the generating forces according to the rates of crustal creation and destruction on the plate boundaries. Analysis of the extensional and compressional forces in the spreading and subducting zones shows that the present global plate motion causes compressional stresses in the N-S direction under the Tibetan Plateau (Fig. 1 and 2). The second contribution is the calculation of the crustal stresses in Tibet as inferred from satellite gravity data. By applying solutions to the problem of the spherical shells, the satellite-determined stresses indicate that the upwelling mantle material under Tibet induces N-S and E-W extension (Fig. 3). Finally, a superimposed stress system is constructed. This stress system shows that the present crustal deformation in Tibet does not produce N-S shortening but generates E-W extension (Fig. 4).

The results of this paper have provided geophysical explanations for geological field observations in Tibet and fault plane solutions of earthquakes in the Tibetan side of the India-Eurasia collision. The stress patterns reveal that the cold downwelling mantle convection flow beneath southern Tibet pulls the Indian plate down but applies a bending moment on the end of the plate to uplift and support the mass of the Himalayas.

SIGNIFICANCE

(1) Interpretation of crustal deformation

Crustal deformation is one of the most puzzling aspects of plate tectonics. The geophysics governing crustal deformation are not yet known. At present there are two theoretical points of view. One is that deformations may be described by the motion of a number of tectonic plates moving in a rather complicated way. The other is that intraplate deformations are caused by the convection-generated subcrustal stress systems. These descriptions are now sufficiently precise to allow analyses to be carried out with

mathematical rigor. Therefore, the relationship of crustal deformations to the combined stress field caused by the global plate motions and mantle convection should be clear.

If the momentum involved in crustal deformation under the Tibetan Plateau can be neglected, all crustal deformation in this region must be caused by forces now acting. There are two possible forces which could in principle maintain the observed deformation: force due to plate motion and force on the base of the crust which is generated by mantle convection. The analysis of stresses caused by the motion of a number of tectonic plates moving in a rather complicated way shows that the Tibetan crust is under N-S compression. The calculation of the crustal stresses caused by the subcrustal stress field as inferred from the satellite-derived gravity data shows that this region is under N-S and E-W extension. Therefore, crustal deformation under the Tibetan Plateau could be formed by the superposition of these two force systems, the N-S compression associated with the global plate motions plus the N-S and E-W extension caused by the upwelling mantle convection cell. In this case, the E-W component of the tensional stresses from mantle convection would produce E-W crustal extension and the N-S component of the tensional stresses from mantle convection just cancels the N-S compression associated with plate motion. The combined force system shows that the present crustal deformation in Tibet does not produce N-S shortening but generates E-W extension (See Fig. 4).

The validity of these theoretical results is subject to observational tests. The most important observational tests which verify this deformation model are: (1) fault plane solutions from earthquakes in Tibet and (2) geological results from field expeditions in Tibet.

Fault plane solutions for all crustal and intermediate depths events beneath the highest parts of the Tibetan Plateau show combinations of normal and strike-slip faulting with tensional stresses oriented approximately in the E-W direction (Molnar and Tapponnier, 1978; Molnar and Chen, 1983). None of these fault plane solutions from earthquakes exhibit components of thrust faulting. Therefore, seismic data confirm that active tectonics in Tibet are dominated by E-W extension.

Tibet has been much studied by geologists in China. Important results of their studies have been extended by the 1980 French-Chinese joint study of the geological structure, formation and evolution fo the Earth crust and upper mantle of this region (Tapponnier et al., 1981a). The most surprising field observations were the comparatively small or no amount of N-S shortening and

deformation. A pure E-W extension in Tibet seems to reflect a particular state of stress in the crust and upper mantle, where the upwelling mantle material as inferred from the satellite-derived gravity data can be the main driving force. Microtectonic observations by Tapponnier et al. (1981b) support this inference.

(2) Uplift of the Himalayas

Figure 3 shows an upwelling mantle convection cell of lenticular shape under the Tibetan Plateau. The general geological setting and continental subduction along the Himalayan Range are outlined in Figs. 5 and 6. Figures 5 and 6 show that the Main Central Thrust (MCT), the Main Boundary Thrust (MBT) and the Boundary Thrust Fault (BTF) (Gansser, 1964; Seeber et al., 1981) are in the compressional stress zone generated by mantle convection.

By assuming that the topography of the Himalaya is supported by the Indian plate, Lyon-Caen and Molnar (1983) discussed the subduction of the Indian plate beneath the Himalayan Range. They have concluded that regardless of flexural rigidity of the plate, the weight of the material in the Greater Himalaya depresses the Moho too much to fit the observed gravity anomalies unless a large bending moment is applied to the north end of the plate. The origin of such a bending moment is unknown.

The possible source of a large bending moment may be the torque applied to the Indian plate by the downwelling mantle flow which is relatively cold and dense under the range. If the under-thrusted Indian plate extends north of the Indus suture and is pushed for bending by the convective downwelling of the lower lithosphere, the force acting on the north end of the plate will apply a torque to the portion of the plate beneath the Himalaya.

A cross section PT of the mantle convection pattern beneath the Himalaya as inferred from satellite gravity data is shown in Fig. 7. Figure 7 shows that there is cold and dense downwelling material beneath southern Tibet that pulls the Indian plate down slightly, but exerts a torque to the end of the plate so as to apply a bending moment. Therefore, the mantle convection cell of a lenticular shape under the Tibetan Plateau applies a bending moment on the end of the Indian plate to uplift and support the mass of the Himalayas.

FUTURE EMPHASIS

The superimposed stress system based on plate tectonics and the satellite-derived gravity data seems to provide a geophysical basis for iterpreting the complicated deformation of the Himalayan Range and the Tibetan Plateau. Future work will concentrate on identifying more planetary tectonic stress regimes such as the Ishtar Terra on Venus and the Tharsis Plateau on Mars.

REFERENCES

Argand, T., 1924. Proc. 13th Int. Geol. Cong. 1, Part 5, 171-372.

Gansser, A., 1964. Geology of the Himalayas, Interscience, New York 289 pp.

Liu, H.S., 1985. Geophysical Basis for Crustal Deformation Under the Tibetan Plateau. Phys. Earth Planet. Inter. 41, 170-185. (This paper is selected from Symposium S10, "Physics of the Earth's Interior," from the Regional Assembly of the IASPEI at Hyderabad, India on November 2, 1984.

Lyon-Caen, H. and P. Molnar, 1983. "Constraints on the Structure of the Himalaya from an Analysis of Gravity Anomalies and a Flexural Model of the Lithosphere," J. Geophys. Res., 88, 8171-8191.

Molnar, P. and W.P. Chen, 1983. "Focal Depths and Fault Plane Solutions of Earthquakes Under the Tibetan Plateau," J. Geophys. Res., 88, 1180-1195.

Molnar, P. and P. Tapponnier, 1978. "Active Tectonics of Tibet," J. Geophys. Res., 83, 5361-5375.

Seeber, L., J.G. Armbruster and R.C. Quittmeyer, 1981. "Seismicity and Continental Subduction in the Himalayan Arc," In: H.K. Gupta and F.M. Delany (Editors), Zagros Hindu Kush, Himalaya-Geodynamics Evolution, Geodyn Ser., Vol. 3, pp 215-242.

Tapponnier, P., J.L. Mercier, F. Proust, J. Andrieux, R. Armijo, J.P. Bassoullet, M. Brunel, J.P. Burg, M. Colchen, B. Dupre, J. Girardeau, J. Marcoux, G. Mascle, P. Matte, A. Nicolas, T.D. Li, X.C. Xiao, C.F. Chang, P.Y. Lin, G.C. Li, N.W. Wang, G.M. Chen, T.L. Han, X.B. Wang, W.M. Den, H.X. Zhen, H.B. Sheng, Y.G. Cao, J. Zhou and H.G. Qiu, 1981a. "The Tibetan Side of the India-Eurasia Collision," Nature, 294, 405-410.

Tapponnier, P., J.L. Mercier, R. Armijo, T. Han and J. Zhou, 1981b. "Field Evidence for Active Normal Faulting in Tibet," Nature, 294, 410-414.

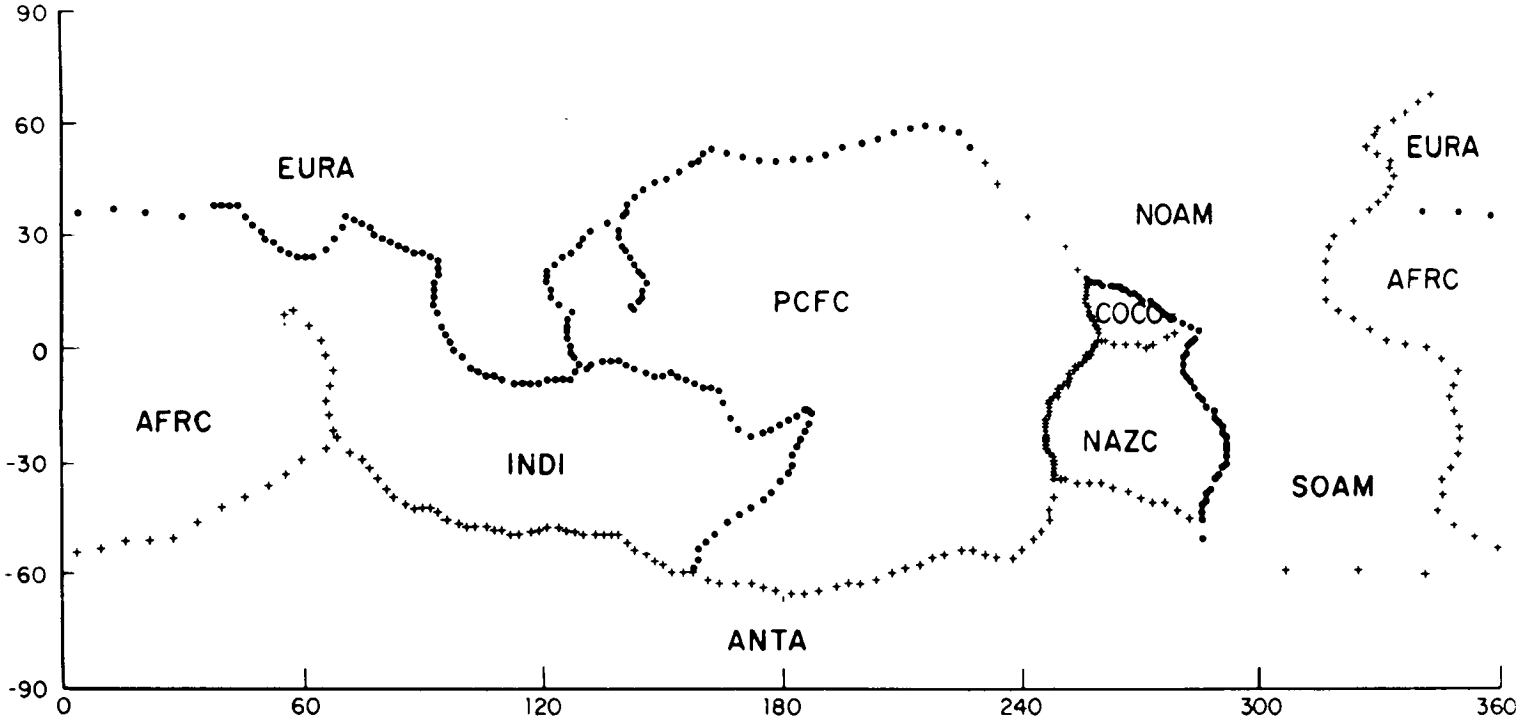

Figure 1. Distribution of .470 forcing functions along plate boundaries. + and • represent points of positive and negative delta functions in the spreading and subducting zones respectively.

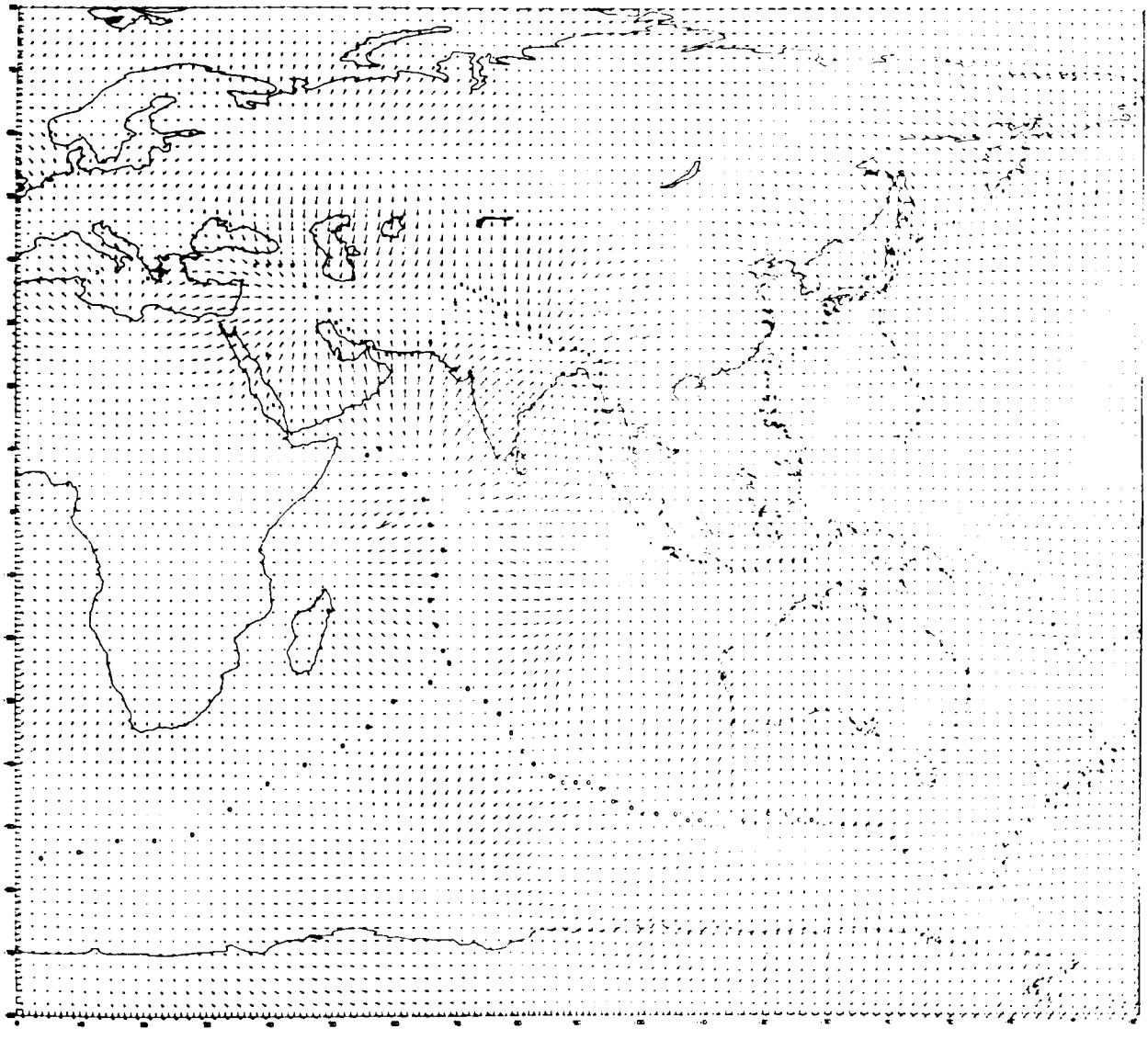

Figure 2. Crustal stresses derived from the stress functions for the plate boundaries synthesized to the degree and order of 10.

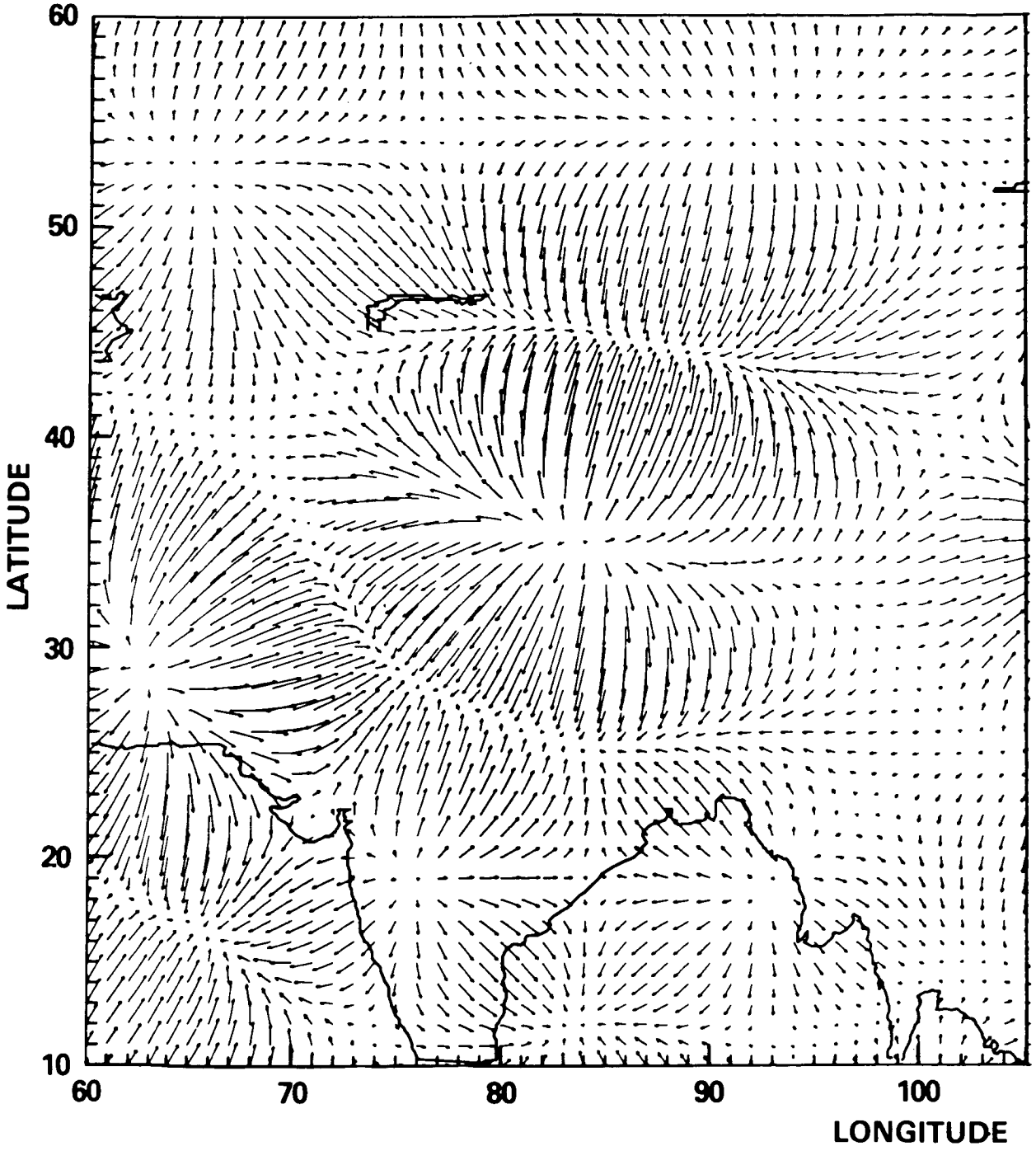

Figure 3. Subcrustal stress system under Tibet generated by mantle convection.

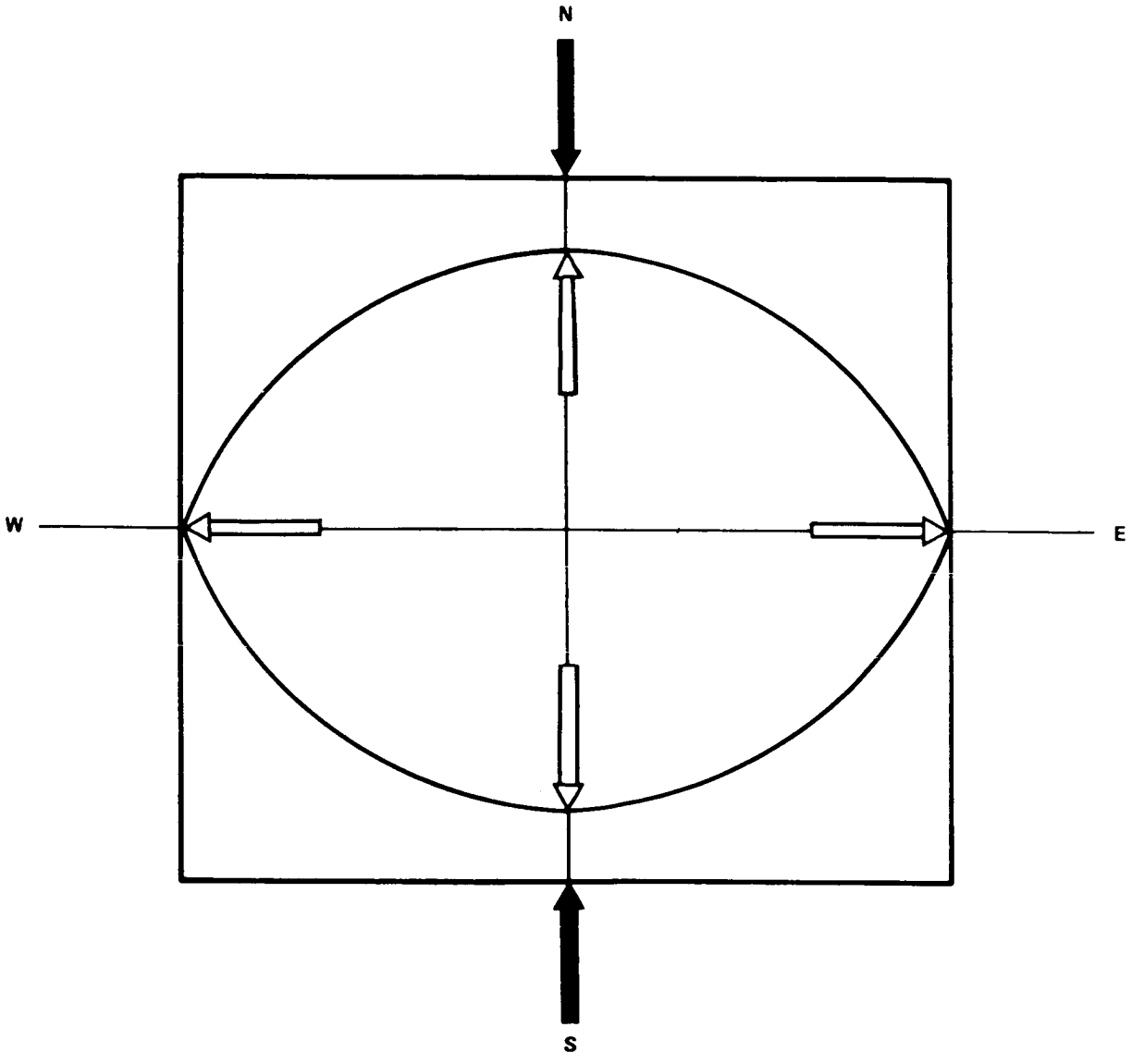

Figure 4. Force diagram for the Tibetan crust. (Black arrows indicate compression due to plate motion and blank arrows indicate extension due to mantle convection).

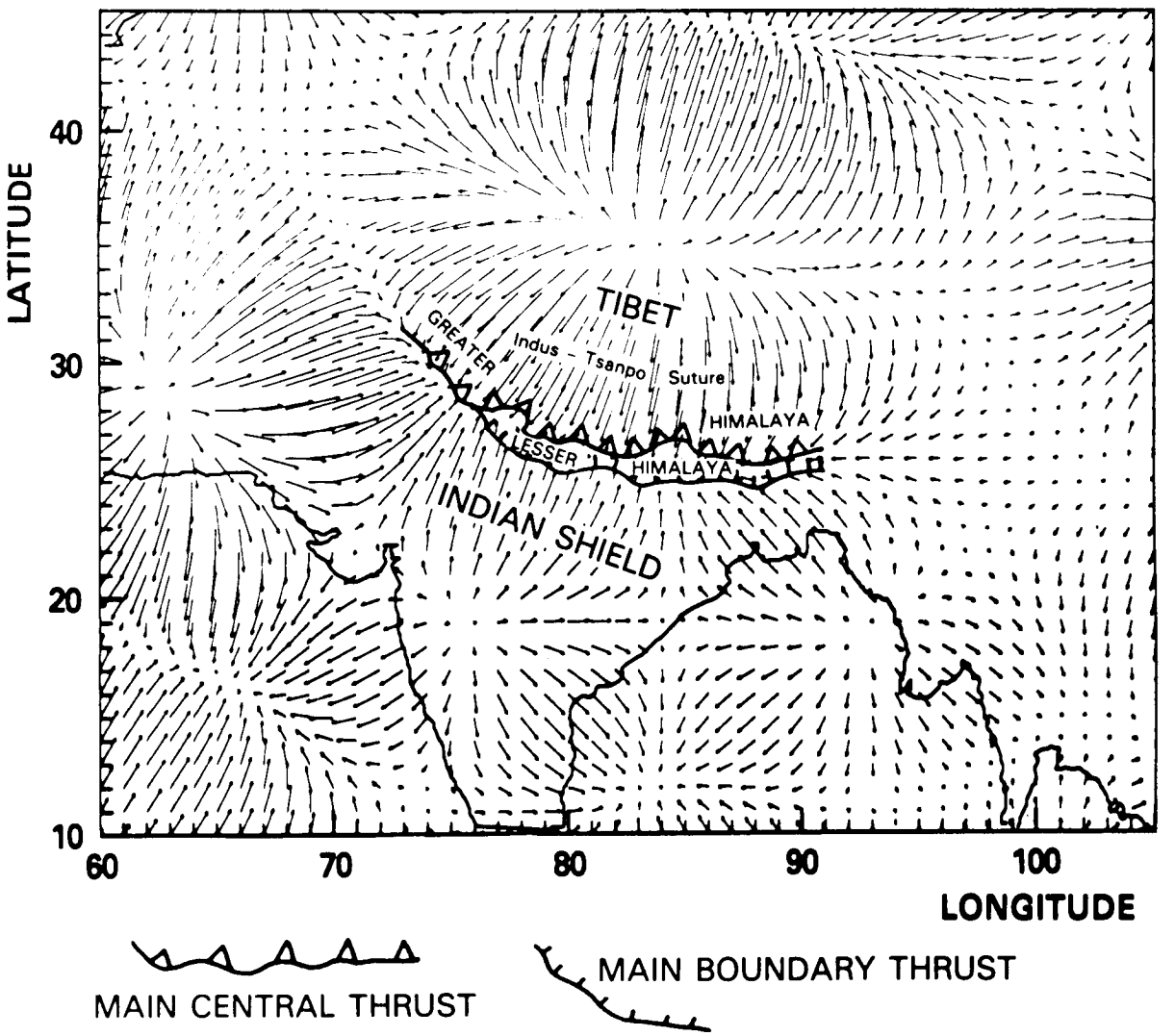

Figure 5. Mantle convection pattern and the general geological setting of the Himalayan region.

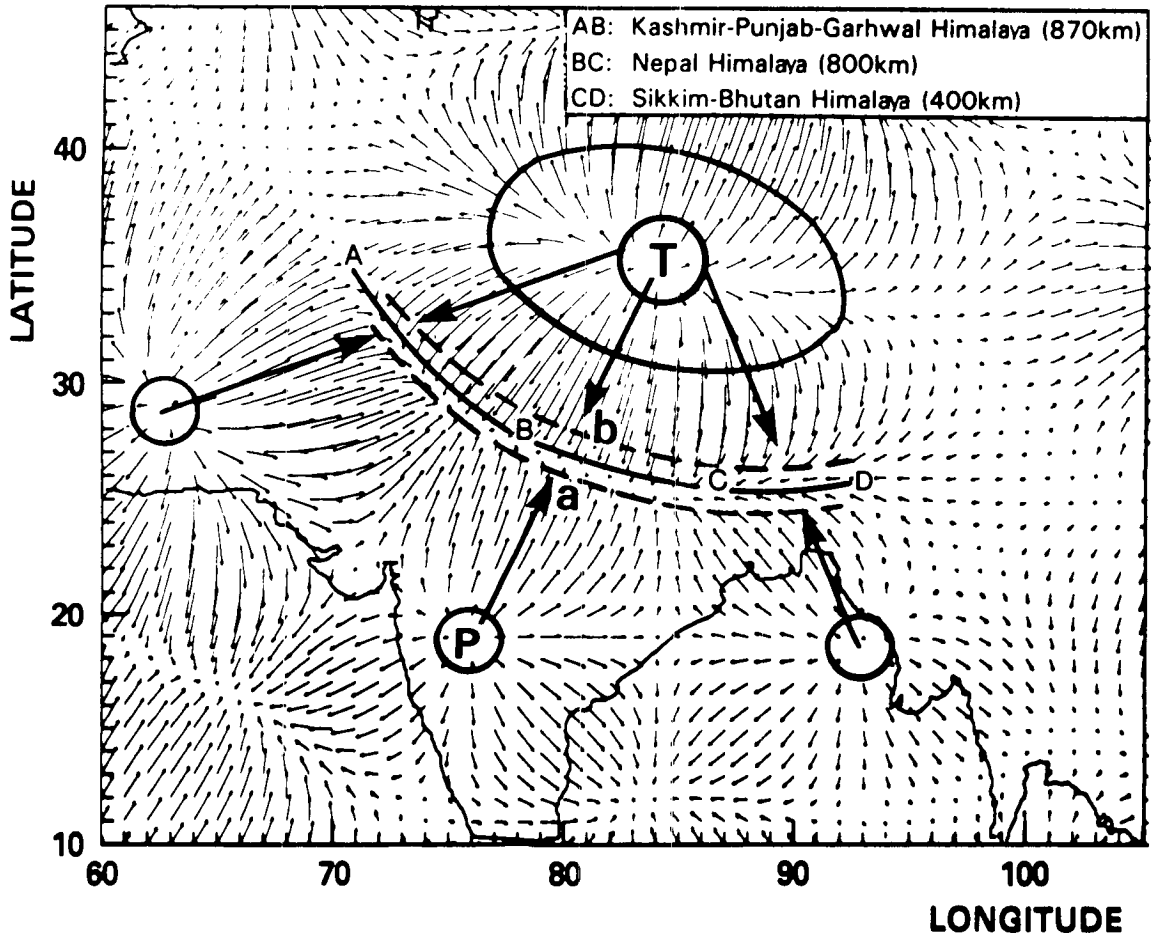

Ellipse and circles represent upwelling mantle convection cells. Dashed lines indicate stress free. AD is the trace of the Boundary Thrust Fault (BTF) of Seeker et al. (1981). BTF is in the compressional stress zone generated by mantle convection.

Figure 6. Mantle convection pattern and continental subduction under the Himalayan arc.

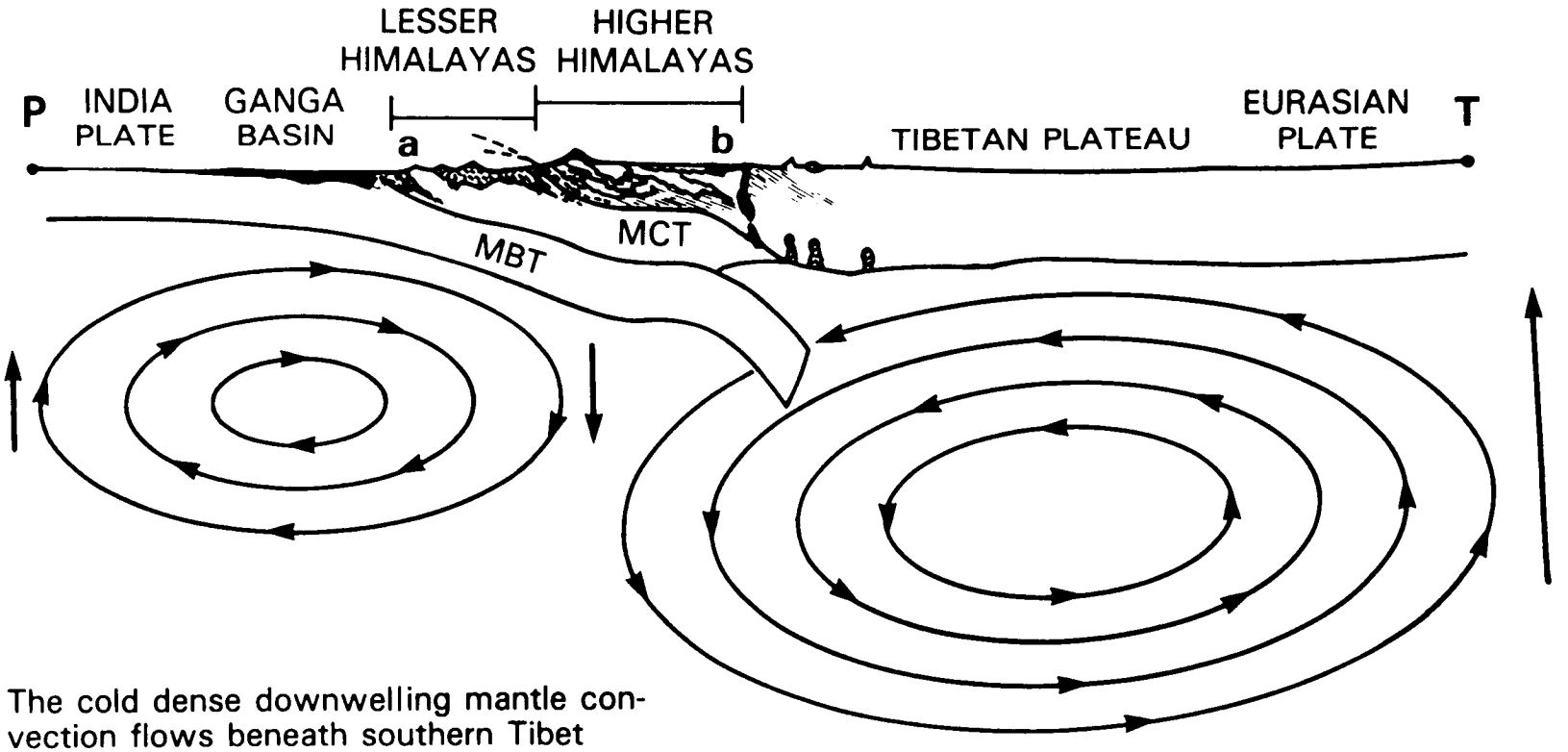

Figure 7. Deformation of the Himalayas: Constraints from space geodynamics.

CHAPTER II

SEA SURFACE TOPOGRAPHY AND OCEAN/SOLID-EARTH INTERACTION

OVERVIEW

The oceans have a fundamental role in regulating major processes occurring on the earth's surface. Weather and climate are profoundly influenced by the heat energy stored and transported by the oceans, and the oceans are the primary source of water that reaches the continents as rain and snow. The immense importance of ocean transport is self-evident, and timely information and predictions of ocean surface conditions and currents are also important to both marine shipping and population concentrations along coasts. A basic element in understanding these practical aspects of oceanography is ocean dynamics which embraces the general ocean circulation, tides, current systems, the air-sea interface, sea state, storm surges, etc. An essential source of information is the topography of the ocean surface. Ocean currents have a topographic signature--a slope of the sea surface perpendicular to the flow caused by the interaction of the current with the Coriolis force. For example, the Gulf Stream has a rise of approximately 1 meter over a distance 50 km. Satellite altimeters measure the distance between the satellite and the ocean surface and thus can obtain information on the topography of the ocean surface along the subsatellite track. Recovery of the sea-surface topography requires knowledge of the satellite orbit. In order to recover oceanographic and meteorological information, it is necessary to separate the mean sea surface topography (geoid undulations) from the measured topography obtained with satellite altimetry. The overall objective of the research described in this chapter is to apply remote sensing data exemplified by satellite altimetry, satellite laser ranging, orbit perturbation, and gravity data as the basic data types used to perform studies of dynamic ocean and earth processes. Research programs are underway in the following areas, to analyze and interpret altimetry data, spaceborne radiometer data, and satellite laser ranging data from Lageos: (1) The computation of a global mean sea surface based upon a combination of GEOS-3 and Seasat altimeter data. (2) Examination of large scale circulation of the world's oceans utilizing remotely-sensed satellite-borne radiometer in conjunction with in situ data. (3) Development of mathematical models and computational algorithms for the computation of any tide constituent and its esimated error from the major tides and their associated errors. (4) Develop and test an interpretation technique which allows accurate extrapolation of tidal height fields in the ocean basins. (5) Develop numerical modeling to examine the effect of the wind-driven oceans on the rotation of the earth. (6) Study the effects of the 13-month pole tide on the earth's rotation. (7) Review and validate the Seasat altimeter height calibration technique.

Contributors to this chapter are: Demosthenes C. Christodoulidis, Ronald Kolenkiewicz, Chester J. Koblinsky, James G. Marsh, William P. O'Connor, Braulio V. Sanchez and Daniel J. Steinberg.

GLOBAL MEAN SEA SURFACE BASED UPON A COMBINATION OF GEOS-3 AND SEASAT ALTIMETER DATA

James G. Marsh

OBJECTIVE

The objective of this work has been the computation of a global mean sea surface map based upon the GEOS-3 and SEASAT altimeter data sets. The dominant error source in the satellite altimeter data is the radial orbit error. This error is primarily due to earth gravity model errors. These errors are long wavelength in nature, primarily once per revolution. In order to minimize the effects of the radial orbit error, a combination of crossing-arc techniques and accurate reference orbits have been used.

BACKGROUND

The mean sea surface provides a reference surface for the detection of mesoscale ocean circulation features, global ocean circulation patterns and detailed information over the oceans on the internal structure of the earth.

The GEOS-3 and SEASAT altimeter experiments have provided important sets of data for the computation of a mean sea surface. The precision of the GEOS-3 data is about 30 cm and the precision of the SEASAT data is 5-10 cm for length scales of a few thousand kilometers. The dominant frequency of the gravity model errors in the radial position of the satellite is once per orbital revolution and can thus be well-represented by a linear function of time over distances of a few thousand kilometers. In the present analyses crossing-arc adjustment techniques were used to solve for linear trend parameters in order to absorb radial orbit errors. The linear trend parameters also tend to absorb other errors, e.g., tropospheric and ionospheric refraction errors, and tidal model errors. Any geographically correlated gravity model errors cannot be removed by this procedure and thus absolute errors of a few decimeters over ocean basin scales may still exist in the mean sea surface.

RECENT ACCOMPLISHMENTS

Previous mean sea surface maps had been computed at GSFC on grid spacings of 0.25°x0.25° and 0.5°x0.5°. Detailed analyses indicated that the along-track data density and the cross-track spacing supported a further reduction in the grid spacing. In the present analyses a grid spacing of 1/8° was used. The limiting factors in the computations are now due to the mesoscale ocean height variability due to the major current systems. In the oceanic quiet areas, the rms crossovers were usually less than 10 cm, while over the major Western Boundary Current systems residuals of 20 cm to 30 cm were observed.

The data analysis technique consisted of: the computation of 65 regional crossover solutions which covered the global set of altimeter data; the adjustment of these regional solutions into a global reference grid, and the subsequent adjustment of the GEOS-3 data set on a pass-by-pass basis into this SEASAT reference grid. A bi-quadratic local surface fitting function was used to determine a sea height value representative of the sea surface heights at each grid location. A grid spacing of 0.125° was used for the computations.

This gridded data set has been analyzed using image processing techniques to enhance the short wavelength topographic features which are present in the map. The map is presented in the figure at the end of this section. Such features as the mid-Atlantic Ridge and the detailed fracture zone system, fracture zones in the Pacific (e.g., Mendocino, Murray and Clipperton and others), sea mount chains and other bathymetric features are clearly shown. In order to emphasize the short wavelength features, a long wavelength geoid corresponding to the GEM 10B (12,12) model has been removed from the mean sea surface.

SIGNIFICANCE

The shaded relief maps such as the one shown in the figure provide an important new basis for the definition of ocean circulation processes. In addition, an important basis for the interpretation of geophysical features over the oceans has been provided.

FUTURE EMPHASIS

Significant progress is being made in the refinement of the geodetic models for the earth gravity model, the reference coordinate system, earth and ocean tides and other parameters. These new models are expected to provide a major reduction in the radial orbit errors

for SEASAT. These new models will be used in combination with the SEASAT Doppler tracking data in order to form a more accurate reference network for the adjustment of the altimeter data.

Negotiations are underway for the acquisition of the GEOSAT altimeter and tracking data. The higher quality of these data and more favorable area to mass ratio versus SEASAT are expected to provide a significant improvement in the overall accuracy of the mean sea surface. It is anticipated that the amplitude of the geographically correlated gravity model errors can be reduced when the new TOPEX gravity model is used.

ACKNOWLEDGMENTS

This work is the result of a team effort involving Chet Koblinsky of the Geodynamics Branch, Tom Martin and Brian Beckley of the Washington Analytical Services Center, Inc., EG&G. The image processed versions of the maps have been computed by Carole Nethery, of the Geodynamics Branch and Karen Settle, of the University of Maryland.

BIBLIOGRAPHY

Marsh, J.G., A.C. Brenner, B.D. Beckley, and T.V. Martin, "Global Mean Sea Surface Based Upon the SEASAT Altimeter Data," J. Geophys. Res., 91, B3, 3501-3506, 1986.

Figure 1. Mean sea surface based upon SEASAT and GEOS-3 satellite altimeter data

OCEAN CIRCULATION STUDIES

Chester J. Koblinsky

OBJECTIVE

The purpose of these studies is to utilize remotely-sensed signatures of ocean surface characteristics from active and passive satelliteborne radiometers in conjunction with in situ data to examine the large scale low frequency circulation of the world's oceans.

BACKGROUND

For the past several years oceanographers have been able to study the ocean using a variety of passive and active radars in space on such missions as GEOS, NIMBUS, TIROS, and SEASAT. It is now possible to usefully measure a number of sea surface variables from space including temperature, winds, and dynamic topography. Such measurements complement observations of the ocean interior to significantly improve the understanding of marine physics including the dynamics of mesoscale processes, the momentum exchange between atmosphere and ocean, and the general circulation.

Mesoscale processes are ubiquitous in the ocean. They have length scales of approximately 10 to 1000 km and time scales of days to months. In the deep ocean, isolated vortices or eddies such as western boundary current rings are an important mesoscale process. These features can have a dynamic topography anomaly of 25 to 100 dyn cm that is observable with a satellite altimeter and can align the sea surface temperature field such that the eddy can be 'seen' with a satellite radiometer. Eddies can rotate rapidly, up to one revolution in a few days, and move about, typically 5 kilometers a day so that large scale rapid sampling from satellites provides a unique synoptic view of these processes.

Direct forcing of the ocean by the atmosphere through the stress of the wind on the sea surface provides an important exchange of global angular momentum. Direct observations of low frequency deep-ocean currents have now been made that demonstrate the ocean's response to wind forcing (Niiler and Koblinsky, 1985). Low frequency wind-driven deep-ocean currents are thought to provide a background level of eddy kinetic energy and drive the general circulation.

On climatological scales the general circulation of the ocean and its variability is important to an understanding of the global heat and momentum balance and biogeochemical processes. The capability of satellite altimetry to observe the global sea surface dynamic topography now allows one to significantly improve the kowledge of the general circulation. Furthermore, the large scale ocean circulation must provide a couple between the atmosphere and solid-earth that may affect polar motion, earth rotation, and satellite orbits.

RECENT ACCOMPLISHMENTS AND SIGNIFICANCE

Two studies have been submitted which examine mesoscale processes in the California Current System with in situ and satellite observations (Simpson, et al., 1986; Haury, et al., 1986). These papers utilize a long time series (3 years) of west coast imagery from the NIMBUS-7 Coastal Zone Color Scanner (CZCS) and the NOAA Advanced Very High Resolution Radiometer (AVHRR) to study time changes of sea surface pigment and temperature. Over 30 years of hydrographic and biological samples from the California Cooperative Fisheries Investigations were used to examine long term change of physical, chemical, and biological in the upper 500 meters of the ocean and relate them to surface changes from the satellite imagery. In addition, comparisons were made with a very intensive ship survey made in January 1981. It is demonstrated that the offshore eddies in the California Current play a major role in the offshore movement and mixing of coastal waters.

Work is continuing on studies of the wind-forced circulation of the North Pacific. One study is exploring the geographic variability of the mesoscale wind-forced response of the ocean from over 30 current meter moorings, each extending from 1 to 3 years in duration (Koblinsky, Niiler, and Schmitz, 1986). This study clearly shows a strong ocean response in the winter months because of the intensification of the North Pacific winter winds. A second study with J. Price (WHOI) and P. Niiler (SIO) is examining the generation of inertial/internal waves by large scale, intense storms that frequent the eastern North Pacific in the winter.

FUTURE EMPHASIS

A. Mesoscale Processes

Research will continue on the merger of several different ocean remote sensing measurements with shipboard observations to understand ocean mesoscale processes.

1) An effort to understand the quantitative description of mesoscale ocean eddy fields by satellite altimeters has been initiated using eddy resolving ocean numerical models.

2) J. Marsh (Geodynamics Branch), F. Sciremammano (RIT) and the author are continuing to study mesoscale variability in the SEASAT and GEOS-3 altimeter data sets. Techniques have been developed by Sciremammano to extract mesoscale features according to wave number. Comparative studies of individual features in eddy intense regions of the ocean are in progress. Techniques for extracting larger scale variability are being pursued using the long time series of altimetry data in the western North Atlantic.

B. Atmospheric-Ocean-Solid Earth Momentum Exchange

1) A joint research project is being coordinated in an attempt to measure the mesoscale wind-forced response of the North Pacific using satellite altimeter data from the GEOSAT mission. These measurements will be compared/assimilated with in situ measurements of bottom pressure, currents and accoustic tomography being carried out by investigators at Scripps Institution of Oceanography.

2) The numerical ocean general circulation model of Cox and Bryan has been obtained from NOAA/GFDL and implemented on the GSFC Cyber 205 by Dan Steinberg, NASA Graduate Fellow. This model is being used to study the wind-forced circulation of the global ocean using estimates of the wind field over the past 10 years obtained from the National Meteorological Center.

3) Maps of the global intensity and variation of mesoscale wind-forced ocean currents using a model function derived from direct observations and winds from the SEASAT scatterometer and the National Meteorological Center are being produced.

BIBLIOGRAPHY

Haury, L.R., J. Pelaez, J.J. Simpson, and C.J. Koblinsky, "The biological consequences of a recurrent eddy off Point Conception, California," J. Geophys. Res., submitted, 1986.

Koblinsky, C.J., P.P. Niiler, and W.J. Schmitz, Jr., "Direct observations of mesoscale wind-forced deep ocean currents in the North Pacific," in preparation, 1986.

Niiler, P.P., and C.J. Koblinsky, "A local time dependent Sverdrup balance in the eastern North Pacific," Science, 229, 754-6.

Schmitz, W.J., Jr., P.P. Niiler, and C.J. Koblinsky, "A summary of moored instrument observations along 152E in the western North Pacific," J. Physical Oceanography, submitted 1986.

Simpson, J.J., C.J. Koblinsky, J. Pelaez, L.R. Haury, and D. Wiesenhahn, "Temperature - plant pigment - optical relations in a recurrent offshore eddy off Point Conception, Califonria," J. Geophys. Res., submitted, 1986.

PREDICTION OF MINOR OCEAN TIDE CONSTITUENTS

Demosthenes C. Christodoulidis

OBJECTIVE

The most comprehensive models for ocean tides currently available represent only the major tides. Whereas these constituents account for over 90% of the global tidal amplitude, the remaining minor constituents can have significant perturbing effects on a satellite's orbit. The major tides have been determined by others through accurate numerical solutions of the Laplace Tide Equations, requiring a heavy computational burden. A simple predictive algorithm was developed for the computation of any tide constituent and its estimated error from the major tides and their associated errors. This process provides oceanographically reasonable a priori estimates of the minor tides and corresponding estimates of their errors which are necessary for the TOPEX gravity model improvement and for related precision orbit determination error analyses.

BACKGROUND

Modeling ocean tides has been a significant problem for precision satellite geodesy and geodynamics since the late 1960's. The effects on satellite orbits are often at the meter level and can reach tens-of-meters in satellite position. For the TOPEX/POSEIDON mission, which is expected to be launched in February of 1991, a major goal is to map the global ocean topography to an accuracy of better than a decimeter--the total error budget is a decimeter in satellite radial position. The oceanic tides must be accounted for, both in their effect on the satellite orbit and in their effect on the altimetric measurement of the sea surface.

Table 1 shows the estimated radial perturbation amplitude due to the major ocean tide constituents on the proposed TOPEX orbit and on the GEOS-3 orbit. This analysis was based upon a Kaula type first order linear orbit perturbation theory. More than half of the constituents have effects which exceed 1 decimeter radially. These terms must be modeled. It is probable that the associated minor tides for some of these also must be modeled if the minor tide response is proportional to the tide raising potential of the major tide.

The pervasiveness of the ocean tide effect on satellites is readily shown. A crude estimate of the effect of the ocean tide is about 10% of the body tide. A set of 53 satellite orbits was evaluated for their nominal ocean tide perturbations of 230 tidal frequencies. These 53 orbits represent a variety of orbital inclinations and altitudes, and all have reasonable tracking data histories. Figure 1 shows the number of satellites having effects over .001 arcsec in the inclination as a function of tidal frequency. Satellites were also included if the principal third degree terms from an ocean tide decomposition produced a perturbation in the orbit eccentricity greater than 1 ppm. In this analysis, the amplitude of the ocean tide coefficients was assumed to be 1 cm. Note that the criterion of 1 ppm perturbation in the eccentricity is equivalent to the criterion of a .001 arcsec perturbation in the inclination.

Of the 230 tidal frequencies, significant perturbations can be anticipated for about 150 of them. Numerical tide models are available only for the major tides, shown by the shaded bars, but not for any of the sideband or minor tide constituents. Thus, there are possibly about 140 minor tide constituents for which models are required in precision computations. Because of possible commensurabilities between the orbital periodicities of a satellite and the periods of the tides at the surface of the Earth, these minor tides may actually produce the larger perturbation of the satellite orbit.

The ocean tide effects are thus an important concern for precision orbit calculations and also for geodynamic parameter recovery from analyses of satellite tracking data. Neglect of these effects may have significant impact on gravity model determination because the time varying potential of the tides has a similar form to that of the long wavelength geopotential. The best gravity field model available prior to the TOPEX modeling efforts is estimated to produce radial rms errors on TOPEX of 54 cm (GEM-L2 evaluation by Rosborough, 1985). Among the known modeling deficiencies in the development of GEM-L2 is that no comprehensive tide modeling was available. TOPEX requires a major improvement in the knowledge of the geopotential. Proper modeling the ocean tides is anticipated to make a major contribution to this goal.

Solutions of the Laplace Tidal Equations require a large computational burden. Oceanographic numerical models such as those of Schwiderski or Parke exist for the major tide constituents only. It was therefore necessary to develop a method which would provide reasonable estimates for the minor tides and corresponding estimates of their errors from the available major tide constituent models.

RECENT ACCOMPLISHMENTS

A method has been developed for predicting minor ocean tide constituents. This method has been used to derive models and error estimates for some 36 minor tides. The method is based upon interpolating the admittance of each desired minor tide from the admittances of the major tides. The use of the admittance was motivated by the study of Munk and Cartwright (1966). The Schwiderski tide models from the Naval Surface Weaspons Center (NSWC), which are the most complete set available, were adopted for this effort. Minor constituent models are generated on a 1 degree global grid matching that of Schwiderski and have also been converted to spherical harmonics for subsequent satellite studies.

The semidiurnal, diurnal, and long period tidal bands are separately analyzed so that the range of frequencies for interpolation is limited. The procedure assumes that the tidal response is locally linear, i.e., within each band at each latitude, longitude point on the Earth's surface. This linearity assumption was adopted because global nonlinearities are expected to be small, and also for the practical reason that there are at best four points to interpolate over (or extrapolate from) in each tidal band. The fit is weighted according to the nominal errors in each tide at the given location. The nominal errors in the diurnal and semidiurnal band were global values supplied by Schwiderski. Nominal errors for the long period band were estimated as being proportionally as well determined relative to the equilibrium tide as M2, i.e. 12.8%. Note that the NSWC Mm and Mf tide amplitudes are smaller by a factor of 3 or 4 compared to their nominal equilibrium values. This suggests a conflict with the assumption of linearity of response across the long period tidal band. Proportionally, there is a much greater span of frequency variation in the long period band than in the diurnal or semidiurnal band. However, only three long period tides are availale so this frequency band cannot be further segmented to reduce the range of interpolation.

Table 2 shows the global statistics associated with the local linear fits for each of the major tides. With the exception of O1 and M2, the rms global fit in each of the semidiurnal and diurnal bands shows that the linear model disagrees with the NSWC input by approximately the estimated error in NSWC. M2, the worst case, has a weighted rms disagreement of 7 cm out of a total 30 cm, which is an error in power of less than 5%. The fits in the long period band show that the long period tides are probably not adequately modeled with this procedure, in that the weighted rms residual amplitude is of the order of the entire NSWC rms tide amplitude. The standard deviations of unit weight given in Table 2 provide the factors by which the NSWC rms amplitude errors need to be adjusted in order to map the weighted residuals into the unit normal

distribution. The semidiurnal and diurnal bands are near unity, but the long period band is off by a factor of 2.5. Thus the linear model is not inconsistent with the semidiurnal and diurnal data, but it is inconsistent for the long period tides assuming the projected error estimates for these tides are correct. However, rms fits are still less than 40% of the equilibrium amplitude for these long period tides, and are only about twice the estimated nominal error in these tides.

Figure 2 compares the global amplitude of the M2 tide of NSWC with that from the numerical method used. Figure 3 shows the amplitude of the total error (vector magnitude) as a function of latitude and longitude and also the corresponding percent relative error. The models are qualitatively the same, which indicates that this tide was not seriously corrupted by the procedure used. This is so for all of the semidiurnal and diurnal tides. Similar comparisons for the long period tides are less successful as is expected from the above discussion. These tides show regions of over 100% differences.

FUTURE EMPHASIS

An extensive comparison for each of the major tides in terms of amplitude, phase, admittance, and estimated errors is in preparation. Future emphasis will be in terms of using these models as error models for satellite precision orbit determination studies and for comparisons with spherical harmonic tide models recovered as part of the TOPEX gravity field improvement effort.

ACKNOWLEDGMENT

The author wishes to acknowledge the contribution provided to this report by Ron Williamson, of EG&G/WASC, Inc., and Doug Chin and Ron Estes of SAR.

REFERENCES

Christodoulidis, D., R. Williamson, D. Chinn, and R. Estes, "On the Prediction of Ocean Tides for Minor Constituents," 10th International Symposium on Earth Tides, 1985.

Munk, W.H., and D.E. Cartwright, "Tidal Spectroscopy and Prediction," Phil. Trans. Roy. Soc., Lond, Ser. A, 259, pp 533-581.

Rosborough, G., "Geopotential Covariance Analyses Results," TOPEX Gravity Model Improvement Meeting No. 4, Minutes, James Marsh and George Born, Ed., NASA Conference Publication 2380.

Schwiderski, E.W., "Ocean Tides, Part I: Global Ocean Tide Equations," Marine Geodesy, 3, No. 1-4, pp 161-217.

Schwiderski, E.W., "Ocean Tides, Part II: Hydrodynamical Interpolation Model," Marine Geodesy, 3, No. 1-4, pp 219-255.

Table 1. Ocean Tide Radial Perturbation Amplitudes on Satellite Orbits

	Schwiderski Tide Model	Tide Frequency (cycles/day)	GEOS-3 Amplitude (cm)	TOPEX Amplitude (cm)
LONG-PERIOD	S_{sa}	0.005	10	6
	M_m	0.036	1	1
	M_f	0.073	1	1
DIURNAL	Q_1	0.083	2	2
	O_1	0.930	13	—
	P_1	0.997	24	24
	K_1	1.003	125	116
SEMI-DIURNAL	N_2	1.896	3	2
	M_2	1.932	3	13
	S_2	2.000	29	70
	K_2	2.005	13	13

Table 2. Summary of Amplitudes and Errors

Band i	Tide j	Equilibrium Tide Amplitude K_β (cm)	NSWC RMS Ampl. (cm) $\bar{a}_{ij}$	NSWC RMS Ampl. Err. (cm) $\bar{\sigma}_{a_{ij}}$	RMS Residual Mod. Admittance $\delta\bar{M}_{ij}$	RMS Residual Amplitude (cm) $\delta\bar{a}_{ij}$	Stand. Dev. of Unit Wt. $\hat{\sigma}_{o_1}$	Estimated RMS Ampl. Error (cm) $\hat{\sigma}_{o_1} * \hat{\sigma}_{a_{ij}}$
o	S_{sa}	1.9	1.6	0.2*	0.27	0.5	2.5	0.5
	M_m	2.2	0.8	0.3*	0.37	0.8		0.8
	M_f	4.2	1.0	0.5*	0.16	0.7		1.3
1	Q_1	1.9	1.7	0.1	0.05	0.1	1.1	0.1
	Q_1	10.1	7.9	0.6	0.12	1.2		0.7
	P_1	4.7	3.5	0.2	0.03	0.2		0.2
	K_1	14.1	10.9	0.9	0.06	0.9		1.0
2	N_2	4.6	6.5	0.5	0.18	0.8	1.3	0.7
	M_2	24.2	30.0	3.1	0.29	7.0		4.0
	S_2	11.3	12.2	1.3	0.13	1.5		1.7
	K_2	3.1	3.4	0.2	0.07	0.2		0.3

*Estimated

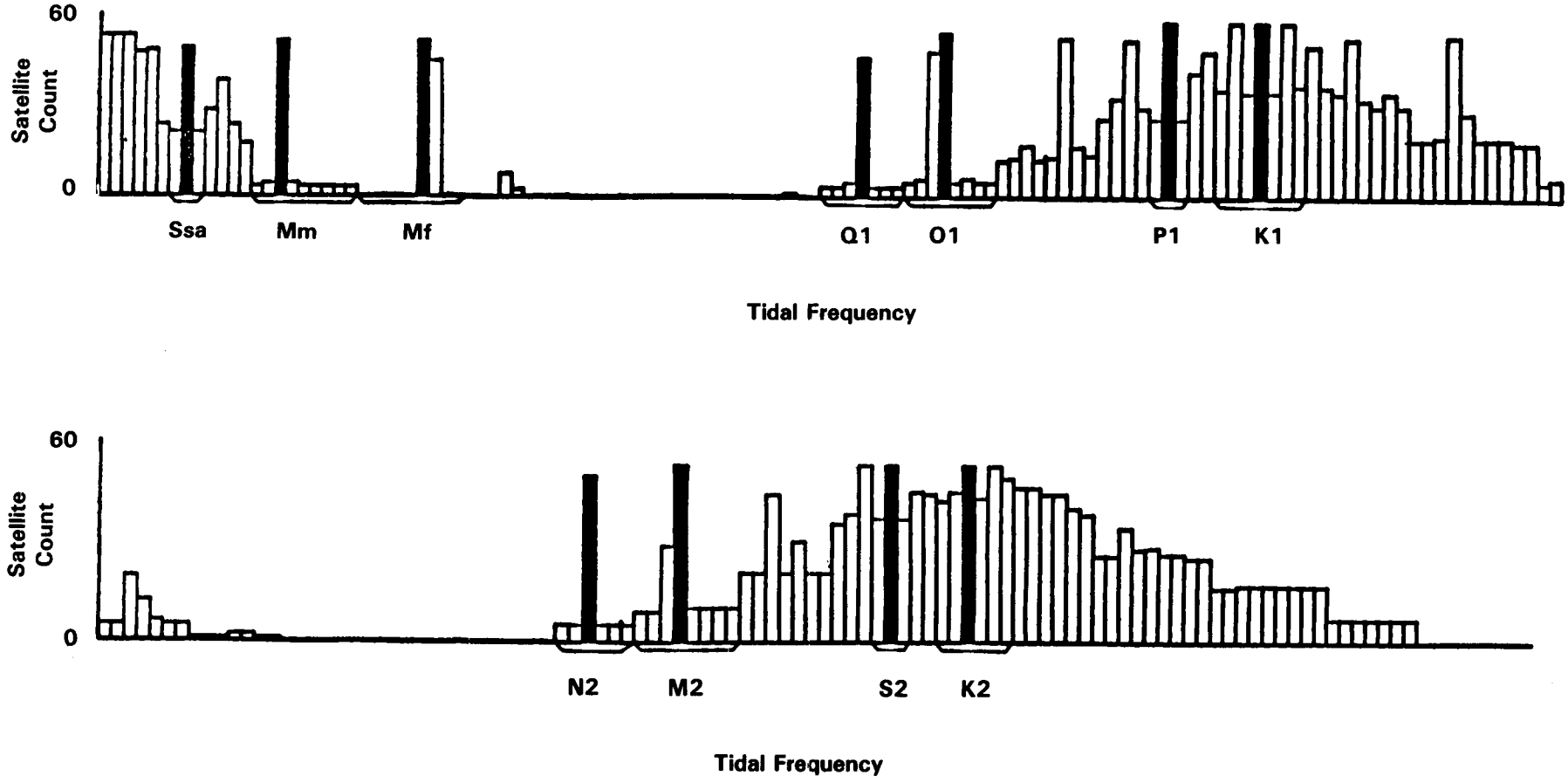

Figure 1. Histogram of the number of satellites with strong sensitivity to various tidal frequencies. The tidal frequency axis is not linear. The 11 major constituent tidal families are marked by brackets. Numerical tide models exist only for the principal tidal frequency of each family shown by the black bars.

Schwiderski M_2 Tide — Amplitude in cm.

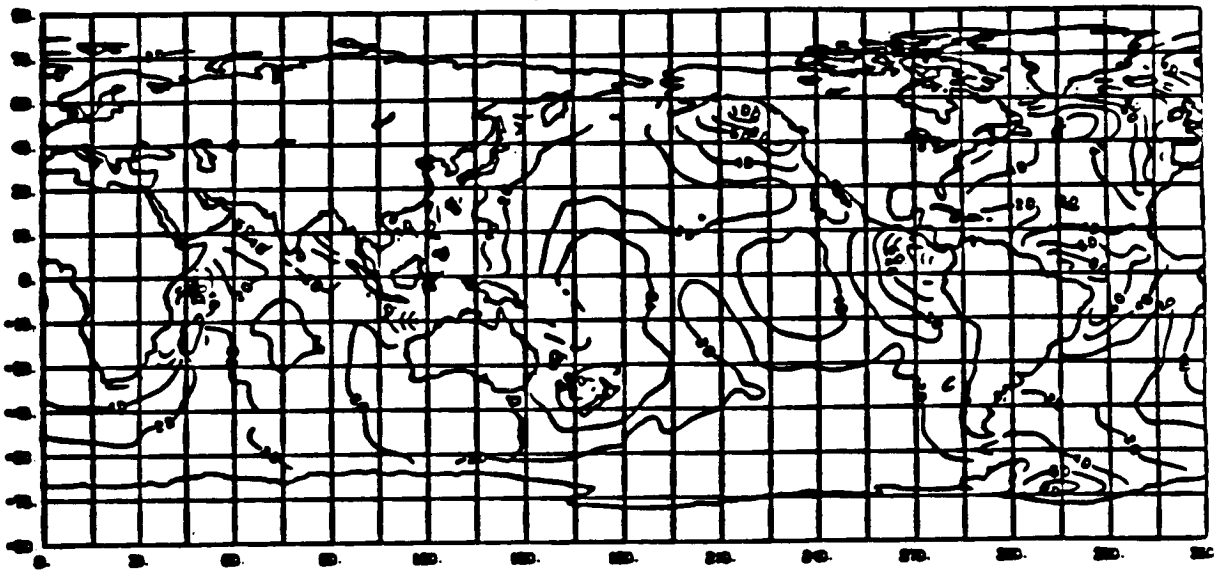

Interpolated M_2 Tide — Amplitude in cm.

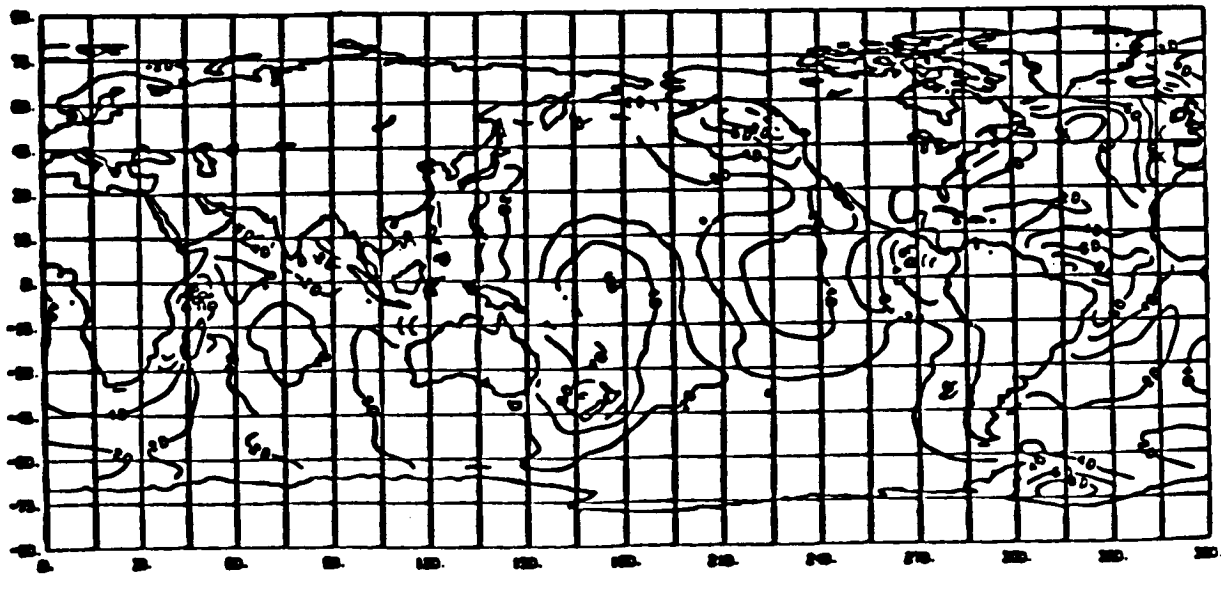

Figure 2. Comparison of M_2 Tide Amplitudes

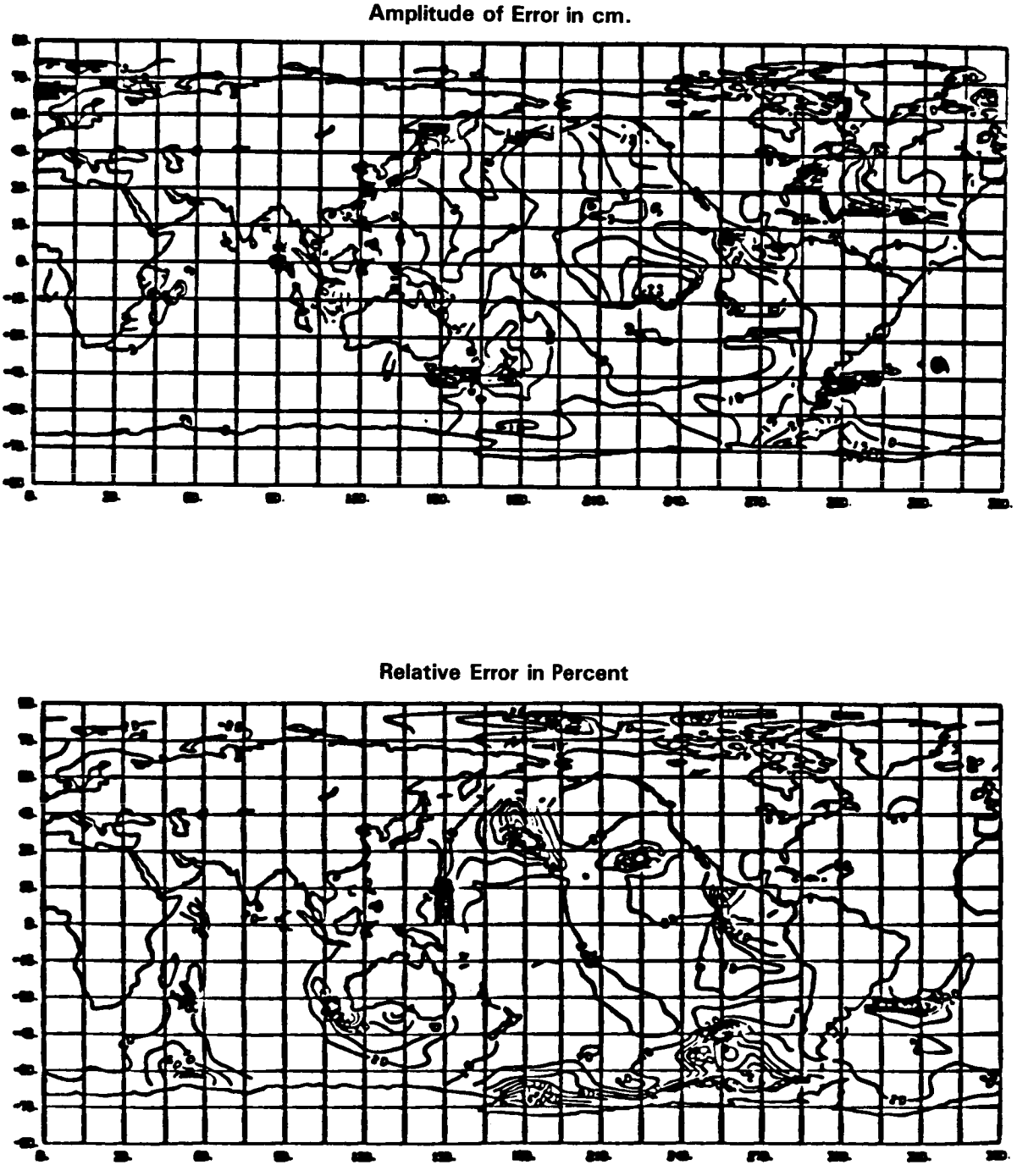

Figure 3. Error in Interpolated M_2 Tide

AN OBJECTIVE ANALYSIS TECHNIQUE FOR EXTRAPOLATING TIDAL FIELDS

Braulio V. Sanchez

OBJECTIVE

This work develops and tests an interpolation technique which allows accurate extrapolation of tidal height fields in the ocean basins by making use of selected satellite altimetry measurements and/or conventional gauge measurements.

BACKGROUND

The theoretical foundation of the method used in the calculations is based on Proudman's theory (1918) as reformulated by D.B. Rao (1966). The theory provides a formulation for calculation of gravitational normal modes and rotational normal modes of irregularly shaped basins with realistic bathymetry. The objective analysis uses orthogonal functions which form the basis to represent the water level fluctuation field. The method has been applied successfully to compute the M2 tide in Lake Superior by Sanchez, Rao and Wolfson (1983).

RECENT ACCOMPLISHMENTS

A normal mode solution for the Atlantic and Indian Oceans has been obtained by means of 3°x3° finite difference grid. There are 1915 velocity potential and 1717 stream function points in the grid. An eigenvalue solution was obtained for both fields. The normal mode solution was obtained by including 150 eigenfunctions from each field (velocity potential and stream function) into the Laplace tidal equations, a third eigenvalue solution is then obtained which yields the normal modes. The normal modes were used to obtain the coefficients for the forced solution and to compute power spectrums for the tidal components M2 and K1. Table 1 below gives a list of the first 20 gravitational modes in order of decreasing period, for each mode the ratio of energies is given as well as the percentage of the total power which that mode contributes to the M2 and K1 tidal components. The three most powerful modes in the M2 spectrum are the ones with periods of 12.68 hours (7.73%), 11.10 hours (5.76%) and 11.55 hours (5.23%). Correspondingly the three most powerful modes in the K1 spectrum have periods of 22.89 hours (10.47%), 19.13 hours (6.88%) and 20.61 hours (6.57%).

The coefficients for the forced solutions yield the tidal amplitudes and phases when used in conjunction with the velocity potential eigenfunctions previously computed. These functions are linearly

combined to obtain the amplitude and phase. The computation of the forced solution includes the effects of the yielding of the solid earth to the tide generating forces through the Love numbers k_2 and h_2; the effects of self-attraction of the tide, tidal loading and bottom friction have not been incorporated in the theoretical simulation at this point. The amplitudes and phases have been computed at the velocity potential points defined in the 3°x3° grid. Figures 1 and 2 below give the structure for the M2 and K1 tides in the Atlantic-Indian Oceans. The investigators involved are B.V. Sanchez, D.B. Rao and S. Steenrod.

SIGNIFICANCE AND FUTURE EMPHASIS

A method has been developed to objective analyze tidal amplitudes and phases to map the tidal constituents over an entire basin. The method allows the computation of the normal modes of the basin as well as a theoretical forced solution for each of the tidal components. The method has been applied to the Lake Superior basin (1983) and to the Atlantic-Indian and Pacific basins using a 6°x6° grid (1983,1984).

The future emphasis will lie in the development of a 3°x3° solution in the Pacific Ocean and the application of the objective analysis using the 3°x3° solutions.

REFERENCES

Proudman, J., 1918. On the Dynamical Equations of the Tides, Proc. of the Lond. Math. Soc. 18, 1-68.

Rao, D.B., 1966. Free Gravitational Oscillations in Rotating Rectangular Basins, J. Fluid Mechanics 25, 523-555.

Sanchez, B.V., D.B. Rao and P.G. Wolfson, 1983. Objective Analysis for Tides in a Closed Basin, Marine Geodesy, Vol. 9, NO. 1, 71-93, 1985.

Geodynamics Branch Annual Report - 1983, NASA TM 86123.

Geodynamics Branch Annual Report - 1984, NASA TM 86223.

Table 1. Normal modes and power spectrum for the M2 and Kl components. Atlantic-Indian, 3° × 3° grid.

Period (hours)	Energy Ratio K/P	Power % M2	Power % K1
68.14	1.66	0.15	2.53
43.99	0.93	0.30	1.27
31.16	0.79	0.04	1.81
29.20	0.94	0.01	2.06
28.20	0.94	0.39	2.09
22.89	0.90	1.13	10.47
20.61	0.87	1.70	6.57
19.13	1.20	0.36	6.88
17.59	0.99	1.16	4.43
16.21	0.92	1.09	4.41
15.51	1.05	1.03	1.42
14.79	0.89	2.10	0.76
13.68	0.98	1.88	4.50
12.85	1.05	1.90	4.12
12.68	1.05	7.73	1.41
12.05	1.15	1.94	2.42
11.88	1.03	2.97	0.88
11.55	1.03	5.23	2.01
11.10	1.01	5.76	1.12
10.96	1.11	5.08	2.47

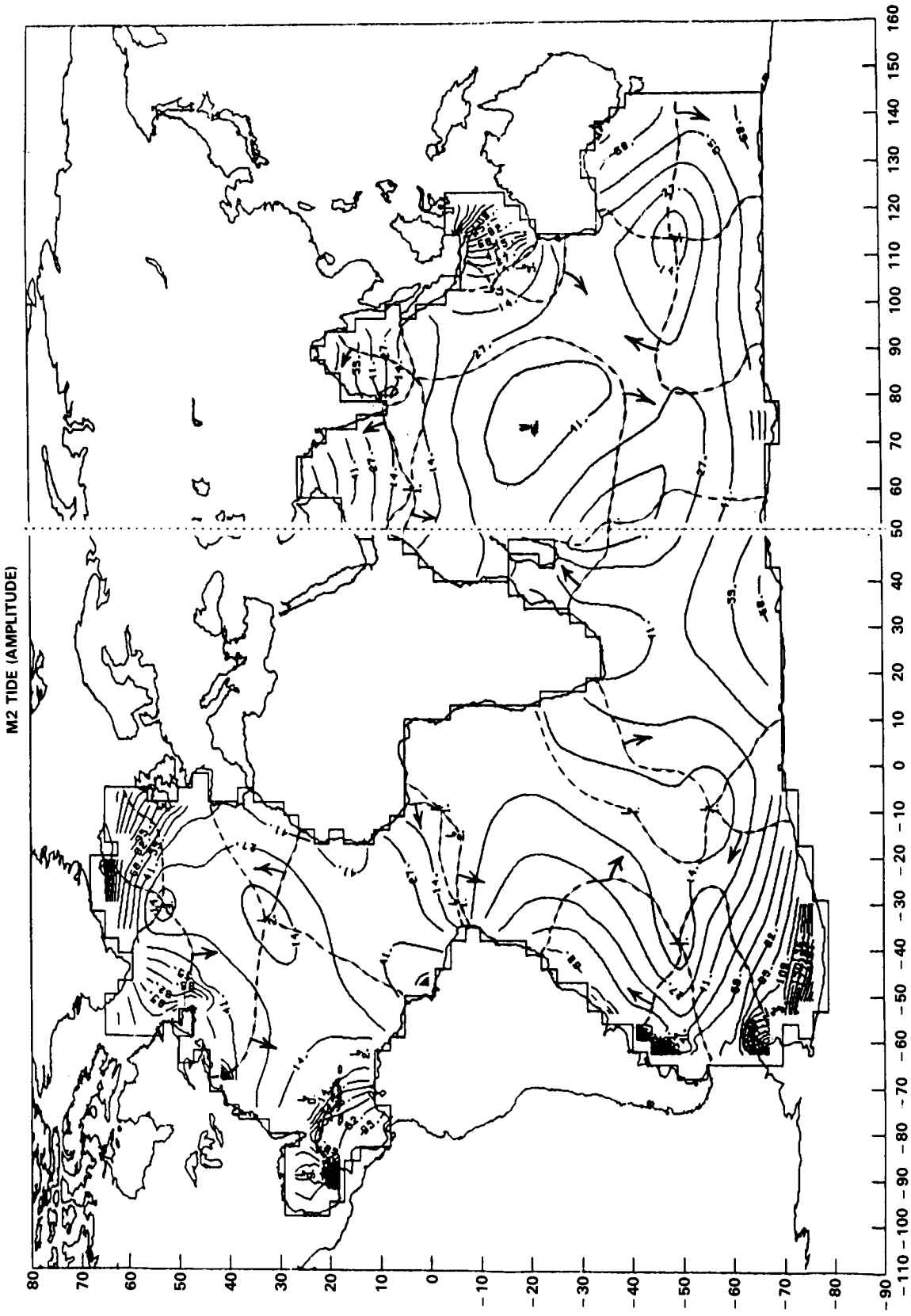

Figure 1. M2 tide (amplitude)

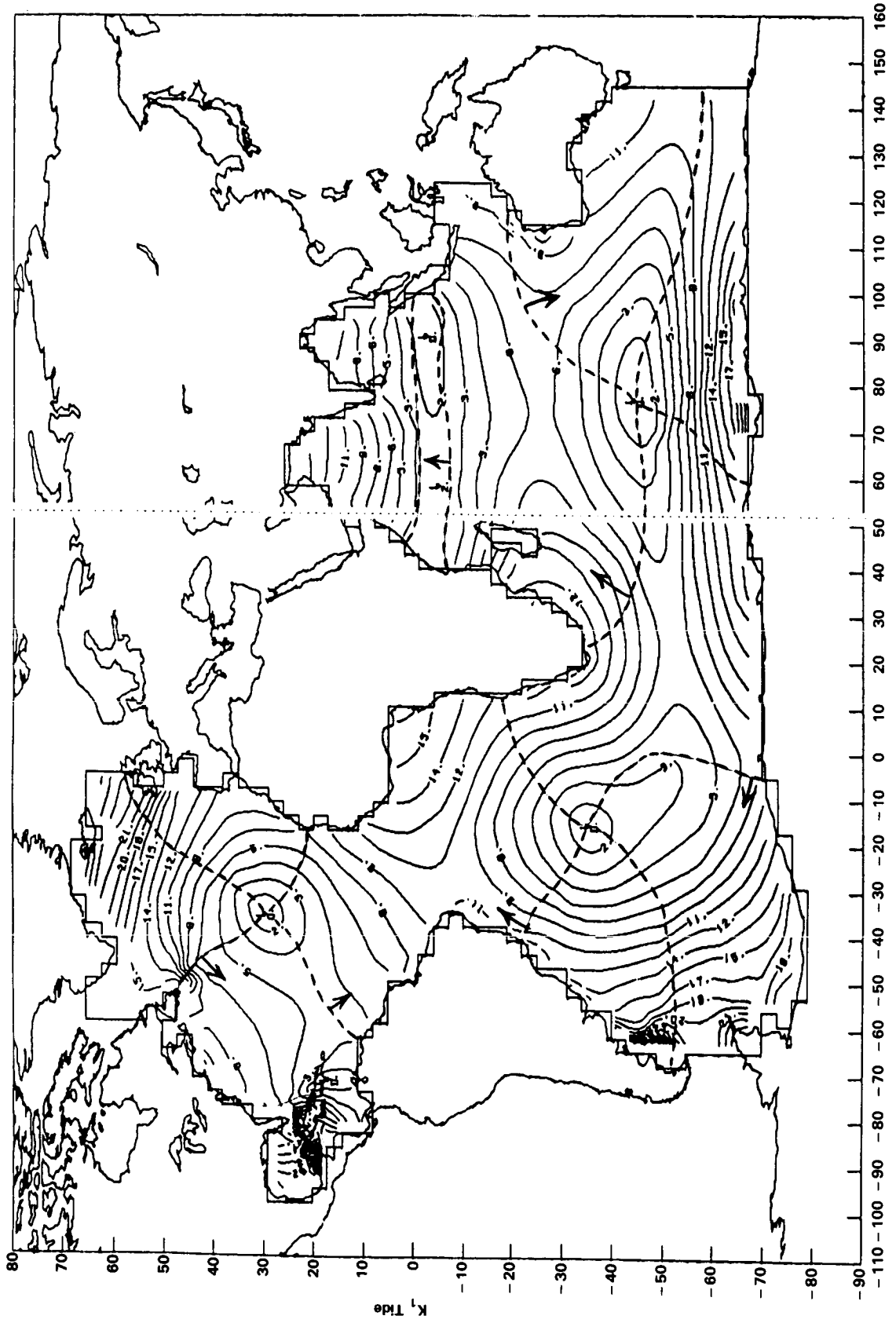

Figure 2. K_1 tide (amplitude)

OCEANIC EXCITATION OF THE EARTH'S ROTATION DURING EL NINO

Daniel J. Steinberg
Chester J. Koblinsky

OBJECTIVE

This work will utilize numerical modeling to examine the effect of the wind-driven oceans on the rotation of the earth.

BACKGROUND

The Chandler wobble is the earth's natural wobble. As a result of dynamic response of the oceans as well as the anelastic behavior of the mantle, the Chandler wobble should, eventually, be damped out. However, it has been observed continuously for many years, at times even increasing in magnitude rather than decreasing, indicating a recurrent source of excitation. The wobble can be excited by torques exerted on the solid earth externally or from deformations and motions within the earth. The most popular candidates for excitation are earthquakes and atmospheric forcing, but neither has been shown to have the necessary magnitude to match the observed excitation of the wobble. The oceans have been studied as a possible excitation source using simple numerical ocean models (Wahr, 1983). The authors propose to extend this research using a numerical general circulation model forced by observed global wind fields.

Recent studies have shown a correlation between Southern Oscillation/El Nino phenomena and the polar motion (e.g., Chao, 1985). The 1982-83 El Nino was the strongest observed in this century. It was responsible for large changes in the length-of-day (e.g., Rosen and Salstein, 1984). This correlation was due largely to the change in atmospheric angular momentum associated with the Southern Oscillation. The wind speeds and, therefore, the wind stress in the Pacific were enhanced during the 1982-83 El Nino (Wyrtki, 1984). This may have had a large effect on the ocean circulation. Such circulation must be modeled since data to establish it are very sparse. This significant event in the short term climate will be the focus of this study.

RECENT ACCOMPLISHMENTS AND SIGNIFICANCE

The Cox and Bryan (1983) model has been obtained from NOAA/GFDL and implemented on the SESCC CYBER 205. Successful preliminary comparisons have been made between the Cox and Bryan model, a Sverdrup model and simple analytical models of wind drive circulation. Studies of variable wind forcing are now in progress using climatological wind fields.

FUTURE EMPHASIS

Ocean models will be subject to the observed winds during the 1982-1983 El Nino period. The authors will be trying to determine how large the angular momentum and mass redistributions of a model ocean are when subject to realistic wind stress. In addition, how large an effect, such a wind-driven ocean can have on the length-of-day and on the Chandler wobble will be studied. The latter will be accomplished by a correlation between the excitation function derived from the model and an astronomical excitation function derived from LAGEOS polar motion data.

BIBLIOGRAPHY

Chao, B.F., "Excitation of the Earth's Chandler Wobble by Southern Oscillation/El Nino, 1900-1979," Private Communication, 1985.

Cox, M.D., "A Primitive Equation, 3-Dimensional Model of the Ocean," Private Communication, 1983.

Rosen, R.D. and D.A. Salstein, "An El Nino Signal in Atmospheric Angular Momentum and Earth Rotation," Science, 225, 411-414, 1984.

Wahr, J.M., "The Effects of the Atmosphere and Oceans on the Earth's Wobble and on the Seasonal Variations in the Length of Day," Geophys. Journ. of R.A.S., 74, 451-487.

Wyrtki, K., "The Slope of Sea Level Along the Equator During the 1982/1983 El Nino," J. Geophys. Res., 89, 10419-10424, 1984.

THE POLE TIDE AND THE EARTH'S ROTATION

William P. O'Connor

OBJECTIVE

The objective of the research is to explain why the 14-month pole tide is enhanced above its equilibrium value in some coastal regions, especially along the Dutch and Danish coasts of the North Sea.

BACKGROUND

The 14-month Chandler wobble of the earth sets up the associated pole tide in the ocean, which has a maximum amplitude of a half centimeter in mid-latitudes. Theoretical work with Laplace's tidal equations has shown that the global structure of the pole tide should be very close to the equilibrium tide value determined by the wobble forcing potential, even when the effects of ocean boundaries are considered (O'Connor and Starr, 1983; O'Connor, 1986). Since the amplitude of the pole tide is so small, with most of the data taken at coastal stations, it is difficult to determine the global structure of the pole tide from observations. The statistical analysis of long period sea level data records detects the pole tide signal, and shows that in some coastal regions the tide height is several times that value which would be predicted by equilibrium theory alone. This is especially true in the North and Baltic Seas. In particular there is a steep gradient of the observed pole tide height along the Dutch and Danish coasts, increasing northwards to a value five times that predicted by equilibrium theory.

It is important to find an explanation for any significant deviation of the tide from equilibrium. One important question of geodynamics concerns the possibility of damping of the earth's Chandler wobble energy, and whether this could take place in the oceans. This damping can only occur when the pole tide departs significantly from equilibrium over a large part of the ocean basins (Lambeck, 1980; Smith and Dahlen, 1981). Although these large deviations of the pole tide from equilibrium in coastal regions are not likely to result from large scale deviations of the tide from equilibrium over the ocean basins, it is certainly desirable to find an explanation for them.

The analysis done so far on the pole tide in the North Sea (Wunsch, 1974) has shown that the slope of the bottom topography, deepening to the north, causes an eastward intensification of the flow regime and tide height. However, this effect alone is not sufficient to explain the large gradient in the tide height along the Danish coast. It is assumed that since the area of the North Sea is small compared to the global scale tidal potential, the direct effect of the tidal forcing on this sea is negligible, and so the Laplace's tidal equations contain no tidal forcing terms. Then the tidal forcing in the North Sea appears only as the boundary condition at the northern opening to the deep ocean. This has been shown to be an acceptable assumption in modeling the effects of the diurnal tides in the North Sea.

ACCOMPLISHMENTS AND SIGNIFICANCE

The work now in progress departs from previous works in that other non-tidal forcing mechanisms are considered. It is known that the North Atlantic and North European regions have a 14-month oscillation in sea level pressure on the order of a few tenths of a millibar. These oscillations may or may not be an effect of the earth's Chandler wobble on the atmosphere-ocean system, but whatever their origin, they have been detected in data records. These long period pressure oscillations must in turn give rise to low level atmospheric motion through the geostropic relationship giving a balance between the horizontal pressure gradient and coriolis forces. Then the wind stress at the air-ocean interface transfers horizontal momentum from the atmosphere to the ocean, and forces motion at least in the uppermost layers of the ocean. The effect of an explicit wind stress forcing term is included in the Laplace's equations of motion for a North Sea model.

The wind stress forcing pattern at this low frequency must be obtained. An indirect approach is to use the atmospheric pressure data showing this small oscillation at the Chandler frequency (Bryson and Starr, 1977), and then compute the wind stress by the geostrophic relationship and momentum transfer equations. Historically, most of the published wind stress data over the oceans has been given as monthly means over the course of an average annual cycle. Recently, however, Hellerman and Rosenstein (1983) have compiled a time series of monthly mean wind stresses over the oceans, and the analysis in progress seeks to determine directly the 14-month oscillation in wind stress over the North Sea.

The atmospheric momentum transferred to the oceans is proportional to the square of the wind speed. Then the oscillation in momentum transfer from air to ocean is proportional to the difference of the squares (as opposed to the square of the difference) of the oscillating wind speed from the average. Thus a small wind stress oscillation can transfer significant momentum to the sea, and drive a circultion in a shallow sea. It is this circulation that could cause the observed deviations of the pole tide from equilibrium.

FUTURE EMPHASIS

Work will continue on the low frequency dynamics of the ocean and the earth's rotation. This includes further work on low frequency meteorological forcing of the oceans. When these effects on sea level are better understood, it may be possible to determine whether the pole tide is in equilibrium over most of the oceans.

REFERENCES

Bryson, R., and T. Starr, 1977. Chandler Tides in the Atmosphere, J. Atmos. Sci., 34, 1975-1986.

Hellerman, S., and M. Rosenstein, 1983. Normal Monthly Wind Stresses over the World Ocean with Error Estimates, J. Phys. Ocean., 13, 1093-1104.

Lambeck, K., 1980. The Earth's Variable Rotation, Geophysical Causes and Consequences, Cambridge University Press, 449 pp.

O'Connor W., 1986. On the Application of Asymptotic Analysis to the Dynamical Theory of the Pole Tide, Geophys. J. Roy. Astr. Soc., in press.

O'Connor, W. and T. Starr, 1983. Approximate Particular Solutions for the Pole Tide in a Global Ocean, Geophys. J. Roy. Astr. Soc., 75, 397-405.

Smith, M., and F. Dahlen, 1981. The Period and Q of the Chandler Wobble, Geophys. J. Roy Astr. Soc., 64, 223-281.

Wunsch, C., 1974. Dynamics of the Pole Tide and the Damping of the Chandler Wobble, Geophys. J. Roy. Astr. Soc., 39, 539-550.

REEVALUATION OF THE SEASAT ALTIMETER HEIGHT CALIBRATION

Ronald Kolenkiewicz

OBJECTIVE

The objective of this work is to review the SEASAT altimeter height calibration performed by NASA/GSFC (Kolenkiewicz and Martin, 1982) and to verify that the results are valid. These results are to be conveyed to NASA Headquarters Oceans Branch, the SEASAT and the TOPEX Project Offices at Jet Propulsion Lab (JPL), Naval Surface Weapons Center (NSWC) Dahlgren, VA, and Defense Mapping Agency Aerospace Center (DMAAC).

BACKGROUND

During the summer of 1984 DMAAC (based on the analysis of their new World Geodetic System (WGS 84) results) concluded that the NSWC SEASAT-derived geoid was in error by about 2 meters. In an attempt to explain this discrepancy, NSWC found three potential error sources (Duke 1984):

1. A NSWC software error--amounting to 71 to 80 cm.

2. Neglect of the altimeter feedhorn-antenna separation distance in calculating the altimeter correction--amounting to 74 cm.

3. A speculation of aerodynamic lift from the SAR antenna--amounting to 54 cm.

Since the original NSWC SEASAT geoid had presumably been in agreement with the NASA/GSFC SEASAT geoid, the application of the above three corrections would lead to a 2 meter discrepancy between NSWC and NASA SEASAT geoids (although agreeing with DMAAC). Bill Townsend, of NASA Headquarters, asked for a resolution of this discrepancy and, in particular, why the Bermuda calibration, performed with the aid of NASA laser systems, did not detect the antenna-feedhorn separation problem.

ANALYSIS AND RESOLUTION

For the corrections listed above to the NSWC geoid the following assessments have been made:

1. The Software Problem. There is no reason to question that NSWC found a software problem in their analysis program.

2. The antenna-feedhorn separation. Indeed the preprocessing of the SEASAT altimeter data did neglect the antenna feedhorn path length of ~74 cm (MacArthur 1978, Lorell 1979).

3. The speculation of an aerodynamic lift from the SAR Antenna. As has been found by the NASA/GSFC Geodynamics Group and the Geodynamics Corporation (Santa Barbara, CA), the calculated lift was in error by several orders of magnitude. It was later confirmed by NSWC that their calculation was in error by the spacecraft mass (a factor of 2000).

The following questions have been addressed in these analyses:

1. Should the DMAAC reference geoids be regarded as an accurate reference for comparison?

   It has been determined that the 2 meter error found by DMAAC was based on a comparison of the NSWC geoid with geoid heights of coastal tracking stations obtained from WGS 84. It is NASA's assessment that, even if the tracking station heights were absolutely correct (and current estimates indicate they may be systematically in error by some 40 cm), geoid slopes in coastal regions are sufficiently great as to make this test of very limited validity.

2. Why did the Bermuda calibration show the altimeter to have a zero bias when the antenna-feedhorn separation had been neglected?

   A thorough review of the Bermuda calibration process (Kolenkiewicz and Martin, 1982; Marsh and Martin, 1982; Martin and Kolenkiewicz 1981 and Marsh et al., 1982) found no problems, either in concept or performance. The calibration used data processed the same as that to be operationally distributed (with corrections made for altimeter instrument delay and for the altimeter offset from the spacecraft center-of-mass). The instrument delay applied by JPL was the (APL recommended) average of two prelaunch calibrations, three were actually made (MacArthur, 1978). Recently, APL has both changed their recommended instrument calibration and recomputed the antenna-feedhorn offset, with a net change of 58 cm from what was applied to the SEASAT data (Kolenkiewicz 1985). As far as the inflight calibration is concerned, what was determined was the correction to the data as it was actucally preprocessed. The conclusion is that the Bermuda calibration did exactly as it was purported to do: Calibrate the SEASAT Altimeter. No further corrections are necessary to alter the geoid height obtained using this calibration, regardless of the number of errors that may have been made in processing the altimeter data (Kolenkiewicz 1985).

FUTURE ANALYSIS

NASA Personnel are convinced that there is no problem with the Bermuda inflight calibration or with SEASAT altimeter data processing. This conclusion implies the current state of affairs:

1. The DMAAC WGS 84 geoid, containing no SEASAT altimetry data is 2 meters above the NASA/GSFC SEASAT (and GEOS-3) altimetry only geoid.

2. The NSWC SEASAT geoid is 71 to 85 cm above the NASA/GSFC SEASAT geoid.

As requested by NASA Headquarters, offers have been made to assist NSWC in resolving any problems with SEASAT data. Specifically, NASA has requested NSWC processed SEASAT altimeter data (Kolenkiewicz 1985), which will then be compared with NASA processed data. To date, (June 1, 1986), none of the NSWC data have been supplied to NASA.

ACKNOWLEDGEMENTS

The author would like to acknowledge C.F. Martin of EG&G Washington Analytical Services Center and Mary Abresch of RMS Technologies, Inc. for their support in the preparation of this document.

REFERENCES

C.W. Duke, Jr., "Recently Discovered Errors in Reduction of SEASAT Radar Altimeter Data to Ocean Geoid Heights," Naval Surface Weapons Center, Dahlgren, Virginia, 13300 K12-SLS, October 23, 1984, private communication.

R. Kolenkiewicz and C. F. Martin, "SEASAT Altimeter Height Calibration," J. Geophys. Res., Vol. 87, No. C5, April 30, 1982.

J. L. MacArthur, "SEASAT-A Radar Altimeter Design Description," JHU/APL SDO5232, November 1978.

J. Lorell, "Algorithm Development Facility Altimeter Sensor Algorithm Specifications," NASA/JPL, 622-202, June 1979.

C.F. Martin and R. Kolenkiewicz, "Calibration Validation for the GEOS-3 Altimeter," J. Geophys. Res., Vol. 87, No. C5, April 1982.

J.G. Marsh, T.V. Martin and J.J. McCarthy, "Global Mean Sea Surface from GEOS-3 Altimeter Data," J. Geophys. Res., vol. 87, No. B13, December 1982.

R. Kolenkiewicz, "Summary Conclusions, and Recommendations of the SEASAT Meeting of February 13, 1985, unpublished, February 1985.

CHAPTER III

GEODESY AND GEOPOTENTIAL

OVERVIEW

The development of techniques for determining satellite orbits to high precision and accuracy is basic to the extraction of geodynamic, oceanographic, gravitational, and other geophysical information from observations on satellites. Indeed the development of global gravity models is largely dependent on high precision observations to near-earth satellites; the gravity field in turn has become a basic data set for understanding the internal structure and dynamics of the earth. Similarly, the extraction of polar motion and tectonic plate motion from satellite laser ranging observations has depended on high accuracy orbit determination. Time variations in the orbital elements of Lageos and other satellites can be related to gravity field and tidal effects, and forcing due to interactions of the satellite with electromagnetic radiation, charged and neutral particle, and other phenomena. Altimetric measurements of the height of a satellite above the surface are used for determining the shape of mean sea level (the geoid) and the sea surface topography. Such data are then used in studies of ocean dynamics. The papers in this chapter focus on these elements of geodesy and orbit determintaion. The topics discussed include the theoretical formulation of the gravitational perturbation problem for near-circular orbits, the Lageos orbit, and Lageos orbit perturbations due to various radiative and thermal effects. Additionally, several papers are devoted to the ongoing geopotential model development for the TOPEX satellite (planned for launch in the early 1990's). This oceanographic satellite will be equipped with a high precision radar altimeter which will be used to make precise measurements on the sea surface height. The measurements are to be used for studying the dynamics of oceanic processes and ocean-atmosphere interactions. To properly interpret the data, the TOPEX orbit must be known with a radial error of 10 cm or less. Such a precise orbit can be obtained only with an enhanced and improved global gravity field over that which is currently available. The relevant papers in this chapter are devoted to a discussion of the derivation of this precise gravity field through the analysis of high quality satellite observations, particularly those involving laser ranging. Finally, an analysis of altimetric data over inland sea is presented as an example of the utility of radar height determinations to the study of tectonophysics processes.

The problems in geodesy, geopotential field modeling, and satellite orbit determination are strongly coupled to those in Tectonophysics and Sea Surface Topography. The interested reader is referred to the other chapters of this report for further discussions of these topics.

Contributors to this chapter are: Theodore L. Felsentreger, Francis J. Lerch, James G. Marsh, David P. Rubincam, Braulio V. Sanchez, David E. Smith, and Jean E. Welker

LAGEOS ORBIT DETERMINATION

David E. Smith

OBJECTIVE

The orbit of the Lageos satellite has been re-analyzed for the period 1983-1985 using improved orbital and earth models, and the new Geodyn 2 software system. The analysis was conducted in preparation for the next global analysis of Lageos data for the determination of tectonic plate motion and crustal deformation.

BACKGROUND

Lageos was launched into a high altitude circular orbit in 1976 and has been tracked regularly by laser ranging systems ever since. Since launch the quality of the tracking has steadily improved from the decimeter level to the present day few centimeter level for most of the international laser tracking network. Our knowledge of and ability to model the many perturbing forces acting on Lageos, particularly the earth's gravity field and the ocean tides, has also significantly improved over this time. We are now able to compute the orbit of Lageos to a much greater precision (and probably accuracy) than we could only one or two years ago. Data in the period, January 1983 through December 1985, has recently been re-analysed in preparation for a new global station coordinate solution using our most up-to-date models and software systems.

RECENT ACCOMPLISHMENTS AND RESULTS

Thirty-six orbital arcs, each one month in length, have been determined and analyzed for the period January 1983 to December 1985. Each monthly orbital arc contained all the presently available Lageos laser data from the international global tracking network. The apriori parameter values and models are shown in Table 1. The solution to each orbital arc included the orbit, the position of the pole and Universal Time (UT), an estimate for the value of GM (the product of the earth's mass and gravitational constant), and the coordinates of the tracking stations.

Table 2 summarizes the preliminary solution for each arc. Of particular interest in Table 2 are the rms deviations of the observations (normal points) from the orbit, which are averaging in the 5 to 8 centimeter range, with a few exceptions above 10 centimeters. These orbital fits are on average several centimeters better than were obtained in the SL 6 solution for the same orbital arc and reflect the improved models being used in the new SL 7.

Because of the adjustments that are made to the station coordinate in each arc the rms deviations are indication of overall data precision.

The values obtained for GM are slightly larger in this new solution, averaging around 398600.442 km**3sec**-2 for the 36 month period, compared to 398600.436 +/- .002 from the 9-year SL 6 solution. At the present time it is not known why there has been this small but systematic difference from SL 6 but it may be caused by the enlarged ocean tidal model used in the new SL 7 solution increasing the energy of the system. The new value presently being obtained is more consistent with the value of GM being obtained from Lageos long orbital arc analyses at the University of Texas at Austin, and also from the analyses of lunar laser data at NASA/JPL; both of whom are recovering values in the 398600.440 to 398600.410 km**3sec**-2 range. Table 3 shows the values of GM obtained from the three annual solutions for the station coordinates.

Two accelerations of the spacecraft were recovered in each orbital arc; each acceleration covering a 15 day period. In previous solutions only one acceleration had been recovered for the full 30 day period. The improvement in the orbital fit (rms) as a result of increasing the number of accelerations from 1 to 2 per arc was very small, less than a centimeter in most cases. However, the values of the acclerations that were obtained appeared to be well determined, providing a historical variation over the three year period very similar to that obtained from earlier solutions. In addition, the Lageos along-track acceleration accumulates to about 5 meters (on average) in along-track position in 15 days and it was felt that this should be easily recoverable and would improve the overall accuracy of the orbit computation.

FUTURE EMPHASIS

The purpose of this analysis has been to prepare for the next (SL7) solution for global plate motions. The data set described here will, over the next few months, be extended back to 1976 and forward to include the early months of 1986. At the present time the Lageos orbital studies appear to be substantially better in the new analyses than earlier ones. In addition, there is clear evidence of the steady and continued improvement in the quality of the data throughout the 3 year period.

Table 1. Nominal Parameter Values and Models of SL 7

Lageos:	
Area	0.28274 m^2
Mass	406.965 kg
Earth Models:	
Gravity field	GEM L2 (PGS 1715C) (CS(2,1) ≡ 0)
Earth tides	Wahr
Ocean tides	Schwiderski, expanded by Christodoulidis to approx. 600 terms out to degree 6 and order 2.
Body tides	$h_2 = 0.609$, $l_2 = 0.0852$
Gravity tide	$k_2 = 0.30$, $k_3 = 0$; phases zero
Earth rotation	Lageos, SL6 polar motion; BIH Universal time
Planets	Gravity fields of Venus, Mars, Jupiter, Saturn
GM	398600.4359×10^9 $m^3 sec^{-2}$
A_e	6378137.0 meters
Flattening	1/298.257
Station Coordinates	SL 6, rotated to be consistent with BIH mean pole of 1980–84, epoch 1983.0, with tectonic motion model AM 1-2 of Minster, Jordan
Orbit Models:	
Data:	2 minute normal points, Herstmonceux definition
Arc length:	30 or 35 days
Acceleration:	2 per arc (one for each 15 days)
Solar Radiation Parameter:	1 per arc
Albedo:	None
Relativity:	None
Software System:	Geodyn II E Version 8601.6 Geodyn II S Version 8601.4 TDF Version 8601.0 Solve Version 8604.4

Table 2.

	# N. POINTS	RMS	GM	SOLRAD	ACCEL1	ACCEL2
JAN 1983	2156	.0871	.436103	1.1280	−3.4728	−1.9100
FEB 1983	1854	.0938	.436039	1.1187	−1.2659	−1.0149
MAR 1983	2360	.1163	.447487	1.1358	−0.3659	−0.3357
APR 1983	2650	.1153	.446485	1.1581	−0.3486	−0.5177
MAY 1983	2628	.1101	.442030	1.1747	−0.6822	−3.3470
JUN 1983	2750	.0892	.438976	1.1754	−2.9646	−3.0004
JUL 1983	2504	.0850	.440372	1.1710	−3.1163	−2.7362
AUG 1983	2358	.0719	.437685	1.1615	−3.3236	−3.1336
SEP 1983	3679	.0832	.440812	1.1490	−3.3022	−3.2352
OCT 1983	5042	.0863	.438748	1.1342	−3.5701	−3.3510
NOV 1983	3817	.0660	.440942	1.1360	−3.9255	−3.7097
DEC 1983	3136	.0851	.439168	1.1344	−3.8881	−3.7083
JAN 1984	3754	.0830	.440461	1.1381	−4.2159	−4.1993
FEB 1984	3428	.0824	.447869*	1.1391	−3.9027	−3.9029
MAR 1984	3030	.0895	.442593	1.1449	−4.3083	−3.6693
APR 1984	5003	.1149*	.447785*	1.1165*	−3.6012	−3.7488
MAY 1984	5612	.0957	.443547	1.0884*	−3.4054	−3.5003
JUN 1984	6007	.1019*	.442965	1.1393	−3.6195	−3.5948
JUL 1984	6269	.0991	.447069*	1.1357	−3.6474	−3.7233
AUG 1984	6915	.0876	.442681	1.1290	−3.2606	−2.9631
SEP 1984	6159	.0783	.441776	1.1298	−2.4225	−2.6875
OCT 1984	5343	.0675	.441947	1.1274	−2.2271	−2.2892
NOV 1984	4197	.0805	.441734	1.1269	−3.8781	−3.8518
DEC 1984	3420	.0808	.441107	1.1338	−3.9171	−3.9094
JAN 1985	2726	.0588	.443669	1.1274	−4.0738	−3.3464
FEB 1985	2519	.0689	.443165	1.1633*	−4.4251	−3.3776
MAR 1985	3125	.0744	.440077	1.1462	−3.9302	−3.7261
APR 1985	4012	.0822	.443068	1.1443	−3.2980	−2.3004
MAY 1985	3223	.0636	.440662	1.1416	−5.1747	−6.8523
JUN 1985	5074	.0669	.439999	1.1405	−5.4280	−5.1037
JUL 1985	5542	.0698	.440364	1.1406	−4.7332	−4.7977
AUG 1985	5654	.0627	.441228	1.1357	−4.0265	−4.0593
SEP 1985	7036	.0642	.437719	1.1324	−3.8560	−4.2805
OCT 1985	5027	.0608	.437251	1.1342	−3.9852	−4.7499
NOV 1985	4283	.0540	.442727	1.1364	−3.3935	−3.6056
DEC 1985	2628	.0559	.439182	1.1363	−3.4028	−3.3641

Table 3.

	Orbital RMS	GM
1983	9.9 cm	$398600.4405 \pm .0010\ km^3sec^{-2}$
1984	8.2 cm	$398600.4440 \pm .0008\ km^3sec^{-2}$
1985	7.1 cm	$398600.4417 \pm .0008\ km^3sec^{-2}$

GRAVITATIONAL PERTURBATION OF RADIAL POSITION AND VELOCITY FOR THE NEAR-CIRCULAR SATELLITE ORBIT

Francis J. Lerch

OBJECTIVE

A new method is developed to derive the radial position and velocity spectrum of gravitational perturbations for a near-circular orbit. These results are compared with those currently obtained from linear perturbations of Kepler variables which are near-singular for orbits with small eccentricity.

BACKGROUND

The radial position and velocity spectrum of gravitational harmonics for near-circular orbits are respectively useful in the analysis of altimeter missions (Tapley and Rosborough, 1985; Wagner, 1985) and the NASA planned Geopotential Research Mission (Kaula, 1983; Colombo 1984; Wagner, 1983).

Orbits of small eccentricity ($e \doteq .003$) give rise to non-linear Kepler perturbations because e occurs as a divisor in the Kepler elements of mean anomaly (M) and argument of perigee (ω). Kozai (1961) and Izsak (1961) derived radial perturbations for leading zonal terms of the potential using non-singular variables ($e\cos\omega$ $e\sin\omega$). Using these same variables Cook (1966) showed how the non-linear effects of long period in e and ω may be stabilized (frozen orbit), but short period effects due to J_2 remain. Kaula (1983) also suggested to employ these non-singular variables due to the small e divisor in GRM orbits. Colombo (1985) used Hill's equations to avoid the singularity problem of small e and used the extensive zonal field as a reference orbit for GRM analysis.

ACCOMPLISHMENTS

In the present analysis non-singular variables

$$\begin{aligned} u &= e\cos M \\ w &= e\sin M \end{aligned} \tag{1}$$

are employed which are directly related to the radial distance (r) and velocity ($\dot{r}$) as follows:

$$\begin{aligned} r &= a(1-e\cos E) = a(1-e\cos M) + O(e^2) \\ \dot{r} &= \frac{a^2}{r}\, e\, n \sin E = aen\sin M + O(e^2)\,. \end{aligned} \tag{2}$$

where dominant effects of the perturbations are carried out through first order in eccentricity. The variational equations from (1) are related to the Kepler form as

$$\dot{u} = \dot{e} \cos M - e\dot{M} \sin M$$
$$\dot{w} = \dot{e} \sin M + e\dot{M} \cos M \tag{3}$$

where $\dot{e}$ and $\dot{M}$ are given by the Lagrangian equations, as in the Theory of Satellite Geodesy (TSG 3.38) by Kaula (1966), namely

$$\dot{e} = \frac{1 - e^2}{na^2e} \frac{\partial R}{\partial M} - \frac{(1-e^2)}{na^2e} \frac{\partial R}{\partial \omega}$$
$$\dot{M} = n - \frac{1 - e^2}{na^2e} \frac{\partial R}{\partial e} - \frac{2}{na} \frac{\partial R}{\partial a} \tag{4}$$

where e and M are retained for convenience but are understood by (1) to be

$$e = (u^2 + w^2)^{1/2}$$
$$M = \tan^{-1} w/u \tag{5}$$

The other non-singular Kepler variables are $\omega + M$, a, i, and Ω.

The disturbance potential R is represented in a Fourier series in Table 1 with angular arguments Ψ and amplitudes R.

Perturbations, $\Delta u = u - u_0$ and $\Delta w = w - w_0$, use a mean reference orbit (TSG 3.74) which is a secularly moving ellipse with angular rates ($\dot{\omega}_0$, $\dot{\Omega}_0$, n_0) and mean elements (a_0, e_0, i_0, $\bar{\Omega}_0$, $\bar{\omega}_0$, $\bar{M}_0$) as follows:

$$u_o = e_o \cos M_o \qquad w_o = e_o \sin M_o$$
$$M_o = n_o t + \bar{M}_o, \; \Omega_o = \dot{\Omega}_o t + \bar{\Omega}_o, \; \omega_o = \dot{\omega}_o t + \bar{\omega}_o \tag{6}$$

Perturbative derivatives, $\Delta\dot{u}$ and $\Delta\dot{w}$, are obtained from (3) thru (6) to the desired accuracy in e as follows:

$$\Delta\dot{u} = -n_o \Delta w + u'$$
$$\Delta\dot{w} = n_o \Delta u + w' \tag{7}$$

$$\begin{bmatrix} w' \\ u' \end{bmatrix} = \begin{bmatrix} \cos M & \sin M \\ -\sin M & \cos M \end{bmatrix} \begin{bmatrix} eM' \\ \dot{e} \end{bmatrix} \tag{8}$$

where $M' = \dot{M} - n_0$,

$$\begin{bmatrix} eM' \\ \dot{e} \end{bmatrix} = \frac{1}{na^2} \begin{bmatrix} -\frac{\partial R}{\partial e} \\ \frac{1}{e} \left(\frac{\partial R}{\partial M} - \frac{\partial R}{\partial \omega} \right) \end{bmatrix} \tag{9}$$

The eccentricity function of the disturbance R (Table 1) is approximated for dominant terms in eccentricity as

$$G_{\ell pq}(e) = G_{\ell pq}(0) + e\, G'_{\ell pq}(0)$$

$$G_{\ell po}(e) = 1 + 0(e^2) \qquad \text{for } q = 0 \tag{10}$$

$$G_{\ell pq}(e) = \frac{e}{2}\,[\ell + 2q\,(\ell - 2p) + 1] + 0(e^3) \text{ for } q = \pm 1.$$

The Fourier components of (9) from Table 1 are zero for q=0, and for $q = \pm 1$

$$\begin{bmatrix} eM' \\ e \end{bmatrix}_{\ell mpq} = \frac{\overline{R}'_{\ell mpq}}{na^2} \begin{bmatrix} -Sq \\ qS'q \end{bmatrix} \tag{11}$$

where $S_q = S_{\ell mpq}$ denote the Fourier terms with arguments

$$\psi_{\ell mpq} = (\ell - 2p)\,(\omega + M) + qM + m(\Omega - \Theta) \tag{12}$$

and where $S'_q = \dfrac{dS_q}{d\psi}$, $\overline{R}'_{\ell mpq} = \dfrac{\mu}{a}\left(\dfrac{a_e}{a}\right)^{\ell} F_{\ell mp}(i)\, G'_{\ell pq}(0)$.

Since

$$S_q = [\cos \Psi_{\ell mpq} \sin_{\ell mpq}] \begin{bmatrix} C_{\ell m} \\ S_{\ell m} \end{bmatrix}_{\substack{\ell - m \\ \text{even}}} \text{ or } \begin{bmatrix} -S_{\ell m} \\ C_{\ell m} \end{bmatrix}_{\substack{\ell - m \\ \text{odd}}}$$

then

$$\begin{bmatrix} Sq \\ S'_q \end{bmatrix} = \begin{bmatrix} \cos qM & \sin qM \\ -\sin qM & \cos qM \end{bmatrix} \begin{bmatrix} S_o \\ S_o' \end{bmatrix} \tag{13}$$

Using (11) and (13) with (8) the near-singular variable M may be eliminated as follows:

$$\begin{bmatrix} w' \\ u' \end{bmatrix}_{\ell mpq} = A \begin{bmatrix} \cos M & \sin M \\ -\sin M & \cos M \end{bmatrix} \begin{bmatrix} -1 & 0 \\ 0 & q \end{bmatrix} \begin{bmatrix} \cos qM & \sin qM \\ -\sin qM & \cos qM \end{bmatrix} \begin{bmatrix} S_o \\ S'_o \end{bmatrix}$$

$$= A \begin{bmatrix} -S_o \\ qS'_o \end{bmatrix} \qquad \text{for } q = \pm 1 \tag{14}$$

where $A = R'_{\ell mpq}/na^2$, $S_o = S_{\ell mpo}$.

Equation (14) shows that q is eliminated from the arguments in (12) where $\Psi_{\ell mpq}$ becomes $\Psi_{\ell mpo}$.

From equations (11) and (14) the near-singular variables M and e are both eliminated from (8) and thus (7) may now be integrated (term by term) by evaluating the Fourier components on the reference orbit (6) with the mean elements. Here the amplitudes (19) are constant and the arguments from (6) and (12) are secular as follows:

$$\begin{aligned} \Psi o &= \psi_{\ell mpo} = \dot{\psi}_o t + \overline{\psi}_o \\ \dot{\Psi} o &= \dot{\psi}_{\ell mpo} = (\ell - 2p)(\dot{\omega}_o + n_o) + m(\dot{\Omega}_o - \dot{\Theta}) \\ \overline{\dot{\Psi}} o &= \overline{\dot{\psi}}_{\ell mpo} = (\ell - 2p)(\overline{\omega}_o + \overline{M}_o) + m(\overline{\Omega}_o - \overline{\Theta}_o) . \end{aligned} \tag{15}$$

The simultaneous system (7) may be integrated for a particular solution since the homogeneous solution is given by the reference terms (6) for u_o and w_o. Perturbational derivatives from (12) are of the following form where a and b are constants representing coefficient values ($C_{\ell m}$, $S_{\ell m}$), namely

$$\begin{bmatrix} w' \\ u' \end{bmatrix}_{\ell mpq} = \begin{bmatrix} -A\, H_o \\ qA\ \ H'_o \end{bmatrix} \qquad \begin{bmatrix} H_o \\ H'_o \end{bmatrix} = \begin{bmatrix} a \cos \psi_o + b \sin \psi_o \\ \dfrac{d\, H_o}{d\, \psi_o} \end{bmatrix}$$

and the perturbations have a solution from (7) for $q = \pm 1$ as

$$\begin{bmatrix} \Delta w \\ \Delta u \end{bmatrix}_{\ell mpq} = \frac{A}{\dot{\psi}_o^2 - n_o^2} \begin{bmatrix} (\dot{\psi}_o - n_o q)\, H'_o \\ (q\dot{\psi}_o - n_o)\ \ H_o \end{bmatrix} \tag{16}$$

where $\dot{\psi}_o$ is given in (15) above.

C-2

RESULTS AND SIGNIFICANCE

Following equation (16) the solutions for the perturbations Δu and Δw for ℓmpq components are given in Table 2. From (1) and (2) the dominant perturbations in eccentricity for radial position and velocity are respectively.

$$\Delta r_{\ell mpq} = \int \Delta \dot{r}_{\ell mpq}\, dt \tag{17}$$

$$\Delta \dot{r}_{\ell mpq} = a n_o\, \Delta w_{\ell mpq} \tag{18}$$

for $q = \pm 1$.

A special point of significance is that equation (14) gives the same result when derived from linear perturbations for Δe and ΔM (TSG 3.76) and when (14) is evaluated on the reference orbit. This is because the near-singular variable M (including non-linear effects) vanishes from the equation as a separate variable, at least for this case where only the dominant effects in eccentricity are being treated. Wagner (1983 and 1985) applied linear perturbations ($\Delta e, \Delta M$) to obtain Δr and $\Delta \dot{r}$ and his results agree with those derived in this report. These results are shown directly from the formal solution to (7) and (8) with use of (11) through (14) as follows:

for ℓmpq components with $q = \pm 1$:

$$\begin{bmatrix} \Delta w \\ \Delta u \end{bmatrix} = \begin{bmatrix} \cos M_o & \sin M_o \\ -\sin M_o & \cos M_o \end{bmatrix} \begin{bmatrix} \bar{w} \\ \bar{u} \end{bmatrix}$$

where on the reference orbit

$$\begin{bmatrix} \dot{\bar{w}} \\ \dot{\bar{u}} \end{bmatrix}_o = \begin{bmatrix} \cos M_o & \sin M_o \\ -\sin M_o & \cos M_o \end{bmatrix}^{-1} \begin{bmatrix} w' \\ u' \end{bmatrix}_o = \begin{bmatrix} e_o M' \\ \Delta e \end{bmatrix},$$

hence

$$\begin{bmatrix} \bar{w} \\ \bar{u} \end{bmatrix} = \begin{bmatrix} e_o \Delta M \\ \Delta e \end{bmatrix}.$$

FUTURE EMPHASIS

The accuracy of the position and velocity gravitational perturbations may be improved by extending the theory to include higher order terms in eccentricity.

REFERENCES

Colombo, O.L., "The Global Mapping of Gravity with Two Satellites," Netherlands Geodetic Commission Publications on Geodesy, New Series, Vol. 7, No. 3, 1984.

Cook, G.E., "Perturbations of Near-Circular Orbits by the Earth's Gravitational Potential," Planet. Space Sci., 14, 433-444, 1966.

Izsak, I.G., "On Satellite Orbits with Very Small Eccentricities," Astronom. J. 66, 129-131, 1961.

Kaula, W.M., "Inference of Variations in the Gravity Field from Satellite-to-Satellite Range Rate," J. Geophys. Res., 88, 8345-8349, 1983.

Kaula, W.M., Theory of Satellite Geodesy, Blaisdell Press, Waltham, Mass., 1966.

Kozai, Y., "Note on the Motion of a Close Earth Satellite with a Small Eccentricity," Astronom. J. 66, 132-134, 1961.

Tapley, B.D., and G.W. Rosborough, "Geographically Correlated Orbit Error and Its Effect on Satellite Altimetry Missions," J. Geophys. Res., 90, 11817-11831, 1985.

Wagner, C.A., "Direct Determination of Gravitational Harmonics from Low-Low Gravsat Data," J. Geophys. Res., 88, 10209-10321, 1983.

Wagner, C.A., "Radial Variations of a Satellite Orbit Due to Gravitational Errors: Implications for Satellite Altimetry," J. Geophys. Res., 90, 3027-3036, 1985.

Table 1. Disturbance Potential R* in Orbital Coordinates With Fourier Components and Related Derivatives

$$R = \sum_{\ell=2}^{\infty} \sum_{m=0}^{\ell} R_{\ell m}$$

$$R_{\ell m} = \frac{\mu a^{\ell}}{a^{l+1}} \sum_{p-o}^{\ell} F_{\ell mp}(i) \sum_{q--\infty}^{\infty} G_{\ell pq}(e) S_{\ell mpq}(\omega, M, \Omega, \theta).$$

where

$$S_{\ell mpq} = \begin{bmatrix} C_{\ell m} \\ -S_{\ell m} \end{bmatrix}_{\ell-m \text{ odd}}^{\ell-m \text{ even}} \cos[(\ell-2p)\omega + (\ell-2p+q)M + m(\Omega-\theta)]$$

$$+ \begin{bmatrix} S_{\ell m} \\ C_{\ell m} \end{bmatrix}_{\ell-m \text{ odd}}^{\ell-m \text{ even}} \sin[(\ell-2p)\omega + (\ell-2p+q)M + m(\Omega-\theta)].$$

$$\bar{R}_{\ell mpq} = \frac{\mu}{a} \left(\frac{a_e}{a}\right)^{\ell} F_{\ell mp}(i)\, G_{\ell pq}(e)$$

$$R_{\ell mpq} = \bar{R}_{\ell mpq}\, S_{\ell mpq}$$

$$\begin{bmatrix} \dfrac{\partial R}{\partial e} \\ \dfrac{\partial R}{\partial m} - \dfrac{\partial R}{\partial \omega} \end{bmatrix}_{\ell mpq} = \begin{bmatrix} \bar{R}'_{\ell mpq}\, S_{\ell mpq} \\ q\bar{R}_{\ell mpq}\, S'_{\ell mpq} \end{bmatrix}$$

where

$$\bar{R}'_{\ell mpq} = \frac{\mu}{a} \left(\frac{a_e}{a}\right)^{\ell} F_{\ell mp}(i)\, G'_{\ell pq}(e)$$

$$S'_{\ell mpq} = \frac{d}{d\psi} S_{\ell mpq} \quad (\psi \text{ is argument of } S_{\ell mpq})$$

*TSG 3.70

Table 2. Radial Position (Δr) and Velocity ($\Delta \dot{r}$) Spectrum of Gravitational Perturbations from Non-singular Variable.

For $q = \pm 1$

$$\begin{bmatrix} \Delta w \\ \Delta u \end{bmatrix}_{\ell mpq} = \frac{A}{(\dot{\psi}_o^2 - n_o^2)} \begin{bmatrix} (\psi_o - n_o q)\, S'_{\ell mpo} \\ (q_o - n_o)\, S_{\ell mpo} \end{bmatrix}$$

$$A = n_o \left(\frac{a_e}{a}\right)^{\ell} F_{\ell mp}(i)\, G'_{\ell pq}(0)$$

$$G'_{\ell pq}(0) = [\ell + 2q\,(-2p) + 1]\,/2$$

$$\Delta \dot{r}_{\ell mpq} = a n_o\, \Delta w_{\ell mpo}$$

$$\Delta r_{\ell mpq} = \frac{a n_o\, A\, (\dot{\psi}_o - n_o q)\, S_{\ell mpo}}{\dot{\psi}_o\, (\dot{\psi}_o^2 - n_o^2)}$$

THE YARKOVSKY EFFECT, THE SCHACH EFFECT, AND LAGEOS

David P. Rubincam

OBJECTIVE

The objective of this study is to find whether the Yarkovsky effect or the Schach effect accelerate Lageos at the 10^{-12} ms^{-2} level.

BACKGROUND

The Lageos satellite was launched in 1976 to determine tectonic plate motion, polar motion, and length-of-day. Lageos is a spherical, completely passive satellite. Its aluminum shell is studded with fused silica retroreflectors to permit laser tracking. Inside Lageos is a cylindrical beryllium copper core. The orbit is nearly circular and inclined to the earth's equator by 110 degrees. The altitude is 5900 km.

Lageos is experiencing a fluctuating along-track acceleration of unknown origin of order 3×10^{-12} ms^{-2} (see Figure 1). It is important to understand the origin of the forces causing the acceleration, not only from the standpoint of scientific curiosity, but also to aid in the performance of Lageos' mission by modeling them. The Yarkovsky and Schach effects have heretofore not been examined in detail to assess their importance for Lageos (Rubincam 1982; Barlier et al., 1985). Both effects are radiation-reaction forces.

The Yarkovsky effect can be qualitatively understood as follows. The satellite spins while direct sunlight impinges on its surface, warming it up. Because the satellite has thermal inertia, the hottest spot on the satellite is not the subsolar point. There is delayed heating, so that the hottest spot is on the "afternoon" side of the satellite, just as the hottest time of day on earth is the afternoon, instead of noon.

Lageos emits infrared radiation due to the solar heating, and the radiation carries away momentum. There is a net momentum imbalance due to the asymmetric temperature distribution, so that Lageos feels a force. Moreover, the force is not along the sun-satellite line, due to the delayed heating mentioned above. This is the Yarkovsky effect (e.g., Opik, 1951; Burns et al., 1979; Rubincam, 1982; Barlier et al., 1985).

The Schach effect is more subtle; it operates only when the satellite enters the earth's shadow. There is an asymmetric north-south temperature distribution across Lageos' surface due to solar heating, which gives a force along the spin axis. The satellite cools off slightly as it enters the shadow, then heats up again as it exits. This causes the force to vary. Once again there is a thermal lag due to the satellite's thermal inertia, causing a net force when averaging over one revolution (Rubincam, 1982).

RECENT DEVELOPMENTS

The Yarkovsky and Schach effects for Lageos' aluminum have been modeled by assuming Lageos is a solid homogeneous sphere of radius R_L, density ρ, thermal conductivity K, and specific heat Cp and rotating at angular speed w. The sun was assumed to be infinitely far away. The temperature distribution T inside Lageos was found by solving the heat conduction equation

$$\rho C_p \frac{\partial T}{\partial t} = \nabla^2 T$$

in spherical harmonics (e.g., Merzbacher, 1970, pp. 194-198) subject to the boundary condition

$$\varepsilon \sigma T^4 + K \frac{\partial T}{\partial r} = (1-A)\, F$$

at the surface. Here ε is the infrared emissivity, F the irradiance, A the albedo, and σ the Stefan-Boltzmann constant. (The boundary condition was linearized by assuming $T=T_0 + \Delta T$, where T_0 is a constant and $T_0 >> \Delta T$. The only term contributing to the temperature asymmetry is the $\ell = 1$ term, where ℓ is the degree of the spherical harmonic (Rubincam and Weiss, 1986).

The results for the Yarkovsky effect were as follows. For the reasonable values R_L = 0.3 m, ρ = 3634 kg m^{-3}, K = 150 $Wm^{-1}K^{-1}$ C_p = 672 Jkg^{-1} K^{-1}, E = A = 0.3, and w = 1 rad s^{-1}, the amplitude of the temperature asymmetry was about 0.01K and the lag angle was about 45 degrees (the maximum lag angle). These give an acceleration of about 0.1 x 10^{-12} ms^{-2} for Lageos.

For the Schach effect the results were a maximum temperature difference of about 0.8K between the poles of Lageos, with a thermal lag angle of about 7.5 degrees. The net along-track acceleration is about 0.2 x 10^{-12} ms^{-2}.

SIGNIFICANCE AND FUTURE EMPHASIS

The Yarkovsky effect and the Schach effect both give along-track accelerations about an order of magnitude below those observed (Figure 1). Hence they cannot be the cause of the unmodeled along-track force, and the search should continue.

REFERENCES

Barlier, F., M. Carpino, P. Farinella, F. Mignard, A. Milani and A.M. Nobili, "Non-gravitational Perturbations on the Semimajor Axis of Lageos," Ann. Geophys., submitted, 1985.

Burns, J.A., P.L. Lamy, and S. Sofer, "Radiation forces on Small Particles in the Solar System," Icarus, 40, 1-48, 1979.

Merzbacher, E., Quantum Mechanics, 2nd ed., Wiley, New York, 1970.

Opik, E.J., "Collision probabilities with the Planets and the Distribution of Interplanetary Matter," Proc. Roy. Irish Acad., 54A, 165-199, 1951.

Rubincam, D.P., "On the Secular Decrease in the Semimajor Axis of Lageos' Orbit," Celest. Mech., 26, 361-382, 1982.

Rubincam, D.P., and N.R. Weiss, "Earth Albedo and the Orbit of Lageos," Celest. Mech., in press, 1986.

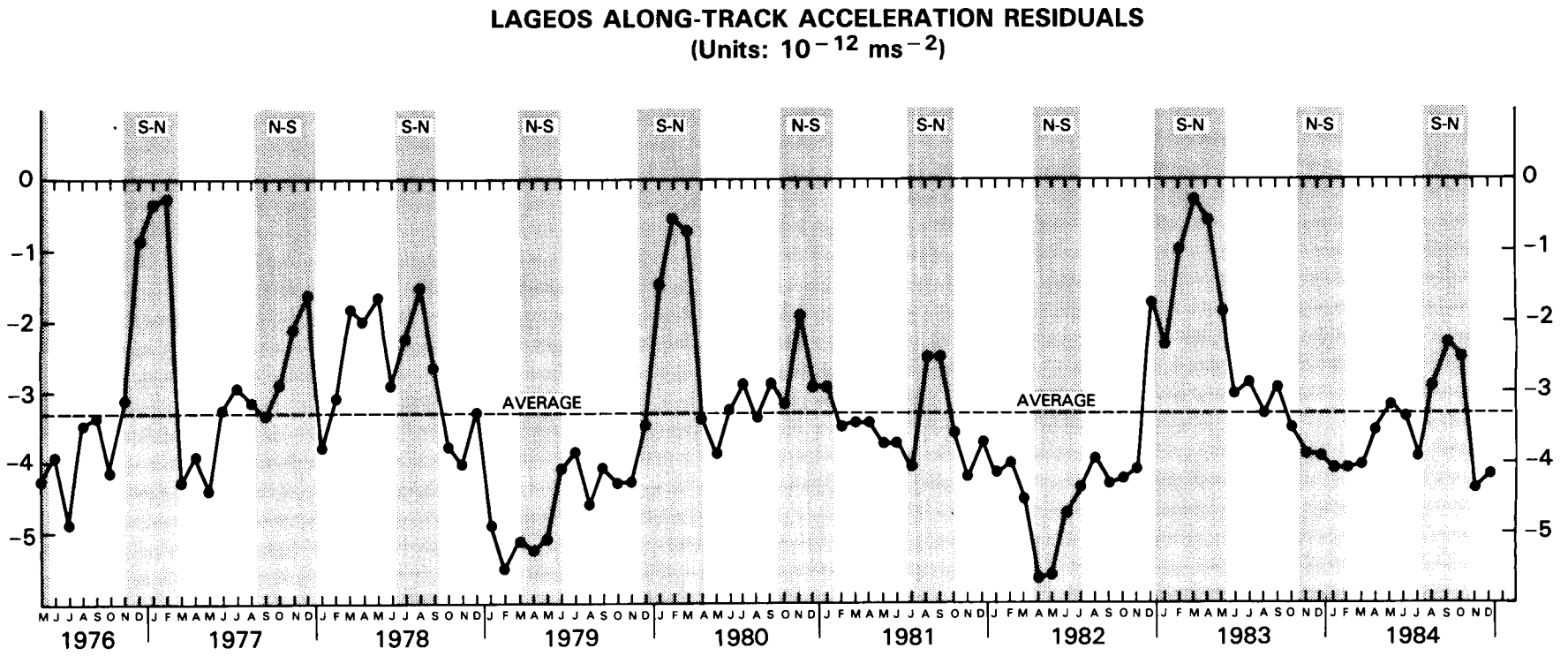

Figure 1. Lageos along-track acceleration residuals (Units: 10^{-12} ms^{-2})

PERTURBATIONS ON LAGEOS' ORBIT

DUE TO INFRARED RADIATION

David P. Rubincam

OBJECTIVE

The objective of this study is to find whether infrared radiation pressure from the earth gives long-period accelerations at the 10^{-12} ms^{-2} level.

BACKGROUND

The rationale for investigating the unknown forces on Lageos are given in "The Yarkovsky Effect, the Schach Effect, and Lageos' elsewhere in this issue.

The effect of reflected sunlight on Lageos' orbit when the earth reflects like Lambert's law is given by Rubincam and Weiss (1986). They found that perturbations of Lageos' orbit were negligible, in agreement with Barlier et al. (1985). The next logical step was to find the effect of the earth's infrared radiation pressure on the orbit. The effect was presumed to be even smaller than that due to reflected sunlight, due to the way infrared radiation varies smoothly across the earth's surface, in contrast to the reflected sunlight.

RECENT ACCOMPLISHMENTS

The formalism developed by Rubincam and Weiss (1986) has been modified to handle infrared radiation emission by the earth. The modifications are: all $d_\ell = 0$, except $d_0 = 1$; $F°_S(r°_S/r_S)^2 = 1$; and replace the A_{NKI} with E_{NKI}, where the E_{NKI} are the spherical harmonic coefficients of the earth's existence, so that $E_{001} = 232$ Wm^2, $E_{201} = -26.6$ Wm^{-2}, etc. These suffice to give the correct equations for infrared radiation, assuming the emission follows Lambert's law.

Only the accelerations for the N=0 and N=2, K=0 terms were found since these are the two dominant terms in the spherical harmonic expansion. The N=0 term provided a check on the modifications, since this term gives only a constant radial force. The formalism performed as expected, giving the radial force of correct magnitude and zero for the along-track and normal-to-orbit forces.

The N=2 or E_{201} term gave only short-period radial accelerations of order 14×10^{-12} m s^{-2}, and along-track accelerations of order 6×10^{-12} m s^{-2}. There were no long-period perturbations in the semi-major axis to order e in the eccentricity.

SIGNIFICANCE AND FUTURE EMPHASIS

Infrared radiation pressure from the earth cannot explain the fluctuations in along-track acceleration of order 3×10^{-12} m s^{-2} observed on Lageos. This was expected and agrees with Sehnal (1981). Hence the search for the origin of the unmodeled along-track forces must turn elsewhere.

REFERENCES

Barlier, F., M. Carpino, P. Farinella, F. Mignard, A. Milani, and A.M. Nobili, "Non-gravitational Perturbations on the Semimajor Axis of Lageos," Ann. Geophys., submitted, 1985.

Rubincam, D.P., and N.R. Weiss, "Earth Albedo and the Orbit of Lageos," Celest. Mech., in press, 1986.

Sehnal, L., "Effects of the Terrestrial Infrared Radiation Pressure on the Motion of an Artificial Satellite," Celest. Mech., 25, 169-179, 1981.

GEOPOTENTIAL MODEL DEVELOPMENT FOR TOPEX

James G. Marsh

OBJECTIVE

The TOPEX oceanographic satellite mission which is planned for the early 1990's will carry as a prime instrument a radar altimeter system. In order to use altimetric data for the mapping of the ocean surface, radial orbit information with an accuracy approaching a decimeter is required. To achieve this level of accuracy, at least a factor of 2 improvement in the modeling of the earth's gravity field is required. A major effort is underway in the Geodynamics Branch for the computation of a new earth gravity field model which will support the TOPEX precision orbit determination requirements.

BACKGROUND

Satellite altimeters measure the height of the satellite above the sea surface. When these measurements are combined with the satellite position information determined from the tracking observations of the satellite, the sea surface height with respect to a reference earth ellipsoid can be computed. The information on temporal and spatial variations in sea surface height will lead to a substantial improvement in our understanding of the ocean circulation and global ocean processes. The satellite altimeter hardware system planned for TOPEX will have an accuracy of about 2 cm and the total system error budget (including the radial orbit error) is on the order of 10 cm. In order to meet this stringent requirement, a significant improvement in the model of the earth's gravity field is required. In support of this research a comprehensive set of computer programs has been developed. Most of this software was developed for use on the IBM 360 series computers. The recent availability of the Cyber 205 Vector Processing Super Computer has provided a significant enhancement in the capability to perform such massive numerical computations. For example, in the actual least squares solution for the gravity coefficients, a factor of 30 improvement in speed has been achieved.

Significant improvements in the quality of laser tracking data have been achieved since the computation of the previous general GSFC gravity model GEM 10B. These new data form a major portion of the observational data base used for the new solution.

RECENT ACCOMPLISHMENTS

The basic objective of the TOPEX Gravity model activity within the Geodynamics Branch during the past year has been the computation of a preliminary gravity model solution based upon a set of the most important satellite tracking data.

The total observational data base available for analysis consists of observations on 60 satellites with a range of accuracies from tens-of-meters to a few cm. In order to establish an optimum data base for observations on the preliminary solution, a comprehensive satellite ranking system was established which considered such factors as unique orbit contribution, data accuracy, and non-conservative force model errors. A total of 11 satellites was selected. The recently acquired laser data on the geodetic spacecraft formed an important part of this data base. Orbital arcs, generally 5 to 7 days in length (30 days for Lageos) were selected. An extensive data validation effort resulted in a set of relatively error-free data arcs for each satellite. In this preliminary solution the coordinates of the tracking stations were derived using datum shifts based upon the best Lageos solution and were held fixed. Solid earth and ocean tides produce significant perturbations on the satellite orbits considered for the analyses. An extensive long wavelength earth and ocean tidal model has been implemented for the data reduction. In order to insure uniformity in the orbit computations for all 11 satellites a standard set of constants has been adopted.

The total software system for orbit and geodetic parameter estimation has been converted to the Cyber 205 Vector Processing Computer. Comprehensive data analysis and matrix generation procedures compatible with the Cyber resources have been created. The availability of the Cyber 205 computer system has permitted a far superior data analysis capability than was possible on the earlier IBM 360 system.

The analyses to date have resulted in the computation of a preliminary gravity model based upon over 500 arcs of data on the 11 satellites. The model is complete to degree and order 36 and is based upon the best available set of constants and force models. In addition, a version of the model has been produced which has permitted the adjustment of some 66 ocean tidal terms.

Accuracy checks of the model based upon rms fits to tracking data have demonstrated significant improvement for all satellites even when the results are compared with earlier "tailored" models. For example, on Starlette the rms fits were reduced from over 70 cm for an earlier Starlette tailored model (PGS-1331) to 30 cm for the new model.

SIGNIFICANCE

In order to meet the radial orbit accuracy requirement of the TOPEX Project, a factor of at least 2 improvement in the gravity field is required. The preliminary results computed to date are indicative that substantial progress can be made in the reduction of the gravity field errors. The overall gravity field improvement effort will be carried out over a time period of several years with the final model being available prior to the launch of the TOPEX satellite.

FUTURE EMPHASIS

Future emphasis will be directed toward the incorporation of additional data sets such as, altimetry, satellite-to-satellite tracking and a re-assessment of the value of the lower priority data sets. Surface gravity data will be incorporated in order to provide better definition of the higher degree and order coefficients. A calibrated set of statistics will be derived which accurately describe the errors in the new gravity field so that the performance for TOPEX orbit computations can be assessed.

ACKNOWLEDGMENTS

This work is the result of a major team effort involving: Demos Christodoulidis, Ted Felsentreger, Frank Lerch, James Marsh, Barbara Putney, Braulio Sanchez, and David Smith of the Geodynamics Branch; Neader Chandler, Oscar Colombo, Steve Klosko, Tom Martin, Erricos Pavlis, John Robbins and Ron Williamson of EG&G, Washington Analytical Services Corp.; Sushila Bhati and Girish Patel of Science Applications Research; Douglas Chin of Business and Technological Systems, Inc.; and Carl Wagner of NOAA, National Ocean Survey.

BIBLIOGRAPHY

"TOPEX Gravity Model Improvement and Precision Orbit Determination Meetings," Minutes edited by Bob Schutz and James G. Marsh, meeting held at the University of Texas, Austin, April 1986.

"TOPEX Gravity Model Improvement and Precision Orbit Determination Meetings," minutes edited by James G. Marsh and Byron D. Tapley, meeting held September 10-12, 1985 at the Goddard Space Flight Center.

"TOPEX Gravity Model Improvement Meeting No. 4... Minutes," edited by James G. Marsh and George H. Born, NASA Conference Publication 2380, Meeting held at the University of Texas, Austin, February 1985.

ANALYSIS OF GEOS-1 LASER RANGING DATA FOR TOPEX

Theodore L. Felsentreger

OBJECTIVE

The intent of this work is to prepare a 2-year set of GEOS-1 laser ranging data for inclusion in a data base which is to be used in a solution for the gravity field of the Earth. This new gravity field model is needed so that the orbit of the proposed TOPEX satellite can be determined accurately enough for the mission to be accomplished.

BACKGROUND

The TOPEX (Ocean TOPography EXperiment) is a dedicated satellite whose primary instrument will be an altimeter with an anticipated precision of 2 cm. This altimeter will be used to measure sea surface elevation to an expected accuracy of a few centimeters. This accuracy is necessary for worthwile information about ocean circulation to be obtained. Thus, the accuracy of the TOPEX orbit is critical, and this implies the use of an accurate gravity field model for the Earth in the orbit determination procedure.

A large data base of satellite tracking data exists at GSFC. An effort is underway to collect and process this data (consisting of Optical, Doppler and Laser) for use in the derivation of a model for the Earth's gravity field. Laser tracking data for the GEOS-1 satellite is part of this data base.

RECENT ACCOMPLISHMENTS

GEOS-1 laser data from the period January 20, 1977 to December 14, 1978 have been chosen for analysis. This time span more than covers one period of the argument of perigee, thus providing good global coverage. The data involves both SAO and NASA stations.

The first step in the procedure was to catalog the data and divide it into 5-day arcs, eliminating those time periods with little or no coverage. Attention was given to the number of passes and the number of stations involved in any 5-day period. A total of 104 arcs survived this scrutiny. Table 1 provides a summary of the satellite's orbit and the tracking data.

The NASA data was at a frequency of 1 measurement/sec., with 1 measurement/2.5 sec. for the SAO data. It was decided to choose every third NASA observation and every SAO observation to provide a more even weighting of the data. Then, using estimates of the position and velocity vectors of the satellite for the arc epochs, nominal values for air drag, solar radiation pressure and solid-earth tidal parameters, and the GEM-10B gravity field, the arcs were converged. In the convergence process, the position and velocity vectors, air drag and solar radiation pressure parameters were adjusted for each arc. The purpose of the convergence is twofold: (1) to obtain more accurate position and velocity vectors preparatory to the creation of the matrix of normal equtions ("E"-matrix) to be used in the gravity field solution, and (2) to identify and delete nonreliable measurements and/or passes. One air drag coefficient (C_D) for each day of a 5-day arc and one solar radiation pressure (C_R) coefficient for the whole arc were solved for. The data reduction was performed using the GEODYN computer program. A total of 53 arcs have been processed, covering the time period 2/1/78 - 12/14/78. The results are given in Table 2. An rms value for each 5-day arc has been computed--this provides an indication of the overall fit to the data for the arc. The rms values are generally in the 1-2 meter range--this is quite good, considering that there is a resonant effect on the orbit caused by the 12th order coefficients in the Earth's gravity field.

FUTURE EMPHASIS

Future activities will concentrate on processing the data for the rest of the arcs. Also, the effects of the ocean tides will be modeled and a more extensive solid-earth tide model will be used. Closer attention will be paid to eliminating nonreliable measurements from the data. Finally, the matrices of normal equations will be formed to be included in the solution for the gravity field.

ACKNOWLEDGMENTS

Thanks are given to Ms. Susan Blackwell of RMS Technologies, Inc., for cataloging the data, and to Ms. Barbara Putney for her help in setting up the GEODYN computer runs.

Table 1. Data Summary

- SATELLITE: GEOS-1
- ORBITAL ELEMENTS:

  Semimajor axis ≈ 8080 km Inclination = 59°.4
  Eccentricity = .07 Period of arg. perigee ≃ 540 days

- TIME PERIOD: 1/20/77 - 12/14/78
- ARC LENGTH: 5 Days
- DATA: SAO + NASA LASER
- NO. ARCS (INCL. NASA): 104 (60)
- NO. OBS.: ~ 155,000
- NO. PASSES (MIN-MAX): 2274 (13-33)

Table 2. GEOS-1 Orbit Determination Summary

	Arc Epoch YYMMDD	No. Obs.	RMS (m)	C_D	C_R	Arg. Per. Range (deg.)
	780201	1091	2.9030	2.373—4.188	1.020	189.3 - 193.3
*	209	1052	1.3375	2.296—2.959	1.269	194.8—198.9
*	217	1290	2.4337	0.852—2.203	1.690	200.7—203.5
*	222	1666	1.7366	2.320—3.290	0.780	203.5—207.2
*	308	876	1.1719	2.299—2.613	0.850	212.9—215.9
*	314	1031	1.3511	2.079—2.598	1.295	216.5—220.6
*	322	836	1.1865	2.242—2.451	1.259	222.4—225.3
*	330	935	1.1273	2.311—2.601	1.198	227.7—230.5
*	404	974	1.5250	1.664—2.328	1.686	230.5—234.0
	413	892	1.1264	2.286—2.663	1.009	236.7—239.9
	419	954	1.3172	2.391—3.144	1.360	240.8—244.1
	424	1512	1.2363	1.257—2.133	1.089	244.1—247.2
	429	977	1.5580	2.256—3.247	1.633	247.2—251.0
	504	1331	2.0774	2.474—4.522	1.586	251.0—253.5
	509	1832	1.1245	2.099—2.613	1.315	253.5—257.6
*	514	1055	1.5260	2.305—2.943	1.628	257.6—260.2
*	520	1085	1.5142	2.346—2.941	1.628	261.0—264.9
	528	1099	1.2058	2.251—2.668	1.394	266.5—269.9
	602	1468	1.2645	2.381—2.965	1.248	269.9—273.4
	607	1698	1.1120	1.805—2.258	1.316	273.4—276.5
*	613	1565	1.0501	1.426—2.241	1.377	277.4—280.3
*	620	1036	1.0907	1.795—2.302	1.712	281.5—285.4
*	625	1493	1.2779	1.780—3.288	1.512	285.4—288.3
*	630	1503	1.2411	2.332—3.374	1.284	288.3—291.8
*	705	1691	1.6425	1.114—2.339	1.397	291.8—295.2
*	710	1563	1.2306	2.117—2.720	1.277	295.2—298.6
*	715	1224	1.2703	2.282—2.887	1.138	298.6—301.8
*	720	1036	1.4015	1.997—2.293	1.396	301.8—304.9
*	725	962	1.6927	1.977—2.298	1.610	304.9—308.5
	730	1694	1.5088	2.261—2.586	1.114	308.5—311.2
	804	1397	1.5396	2.023—2.330	1.453	311.2—315.4
*	809	1016	1.8366	2.038—2.313	1.650	315.4—318.1
*	820	901	1.7908	2.304—2.488	0.805	322.7—325.3
*	825	1012	1.3705	2.243—2.373	1.287	315.3—329.0
*	830	1000	1.1439	1.931—2.284	1.258	329.0—331.7
*	906	814	0.9754	2.003—2.306	0.963	333.0—337.1
*	919	1802	1.2879	2.461—3.545	1.291	342.5—345.3
*	924	1339	1.0878	2.236—2.899	1.279	345.3—348.6
*	929	1474	0.8966	2.239—2.312	1.269	348.6—351.9
*	1004	1666	2.2681	2.406—4.418	1.508	351.9—354.6
*	1009	2041	1.4950	2.517—4.867	1.233	354.6—358.7
*	1014	1911	1.5439	2.840—5.302	1.342	358.7— 1.6
*	1019	1211	1.7310	2.629—4.126	1.696	1.6— 5.4
*	1024	2074	1.7677	2.434—4.895	1.829	5.4— 8.0
*	1029	1280	1.5958	2.387—3.889	1.676	8.0— 11.7
*	1105	1239	1.3640	2.330—3.365	1.481	12.9— 15.4
*	1110	1241	0.7669	2.130—2.632	1.393	15.4— 19.5
	1115	1391	1.0669	1.904—2.482	1.257	19.5— 22.3
*	1120	1588	1.1684	2.272—3.477	1.166	22.3— 26.3
*	1125	1009	0.9963	2.300—3.401	1.253	26.3— 28.9
*	1204	1378	1.0902	2.404—3.428	0.547	31.7— 34.8
*	1209	920	0.9503	2.317—2.644	0.929	34.8— 37.7

*Arc includes NASA data

GEOS-3 ORBIT DETERMINATION

Braulio V. Sanchez

OBJECTIVE

The objective of this work is to determine the epoch state vectors for 5-day arcs of laser range data for the GEOS-3 earth orbiting satellite. These arcs will be used as part of the data base leading to the derivation of a gravity field model for the TOPEX Project.

BACKGROUND

The Geodynamics Earth and Ocean Satellite, GEOS-3, was launched on April 9, 1975. The satellite characteristics and the nominal orbital parameters are the following:

Area:	1.4365 m^2
Mass:	345.909 kg
Eccentricity:	0.0014
Inclination:	115°
Perigee Height:	840 km
Apogee Height:	860 km
Orbital Period:	102 minutes
Argument of Perigee Period:	1039 days

The available data were obtained by both NASA and SAO laser tracking stations during the years 1975 and 1976. It is distributed as follows:

1975: 196916 meas.
1976: 193405 meas.

Total: 389421 meas. (SAO: 18%).

Past experience indicates that a 5 to 7 day arc length is optimum for geodetic satellites at 800 to 1000 km orbit heights. This time span provides strong dynamic content without incurring excessive nonconservative force effects such as atmospheric drag and solar radiation pressure. A 5-day arc for GEOS-3 covers approximately the period of the effect produced by the resonant 14th order coefficients of the Earth's gravitational field. This effect can reach magnitudes of 150 meters in the along-track component. The gravitational field used in the computations is the GEM-10B model full to degree and order 36, derived from satellite tracking data, surface gravity and altimetry. The atmospheric density is obtained from the Jacchia 1971 model.

The data reduction is performed by means of the GEODYN least squares parameter estimation and orbit determination system. The GEODYN system has the capability to estimate the state vector (position and velocity of the satellite) as well as many other kinematic and dynamic parameters including parameters appearing in the force models such a atmospheric drag coefficients (C_D) and solar radiation pressure coefficients (C_R).

RECENT ACCOMPLISHMENTS

A total of 41 arcs have been processed, covering the time period from May to December of 1975. At this point the only editing applied to the data has been the dynamic editing inherent in the iterative process of GEODYN. Besides the position and velocity of the satellite, epoch values for C_D and C_R have been estimated also. The trajectory generated using these estimated parameters is used to compute an rms value for each 5-day arc, which provides an indication of the overall fit to the data for each arc. The results are given in Table 1 below.

FUTURE EMPHASIS

Future activities will include the processing of the data available for 1976 as well as the incorporation of more sophisticated force models for the atmospheric drag. The data will be scrutinized more closely in order to eliminate nonreliable measurements. Also the effects of ocean tides will be modeled and a more extended earth tide model will be used; in generating the results up to now no ocean tide effects have been included and the earth tide effects have been modeled through k_2 and h_2 only.

The converged arcs will be used to compute the coefficients of the matrix appearing in the normal equations. Once the new gravity field has been computed, it will be used to process the data again and the results will be studied.

Table 1. GEOS-3 Orbit Determination Results

ARC EPOCH	NO. OF MEAS.	RMS (meters)	C_D	C_R
750511	2312	1.425	3.32	2.11
750519	1087	0.663	4.01	2.52
750524	1119	0.504	3.51	2.41
750603	1054	1.834	3.41	1.37
750609	1179	1.462	2.59	1.59
750614	3179	1.493	2.65	1.62
750619	2940	1.551	2.79	1.30
750624	2273	1.510	2.92	1.46
750629	3834	1.670	3.01	1.55
750704	3126	2.160	3.11	1.37
750709	4449	2.175	3.34	1.76
750714	2956	1.301	2.67	1.71
750719	4173	1.745	2.78	1.72
750724	3317	1.557	2.91	1.25
750729	3279	1.019	3.08	1.52
750803	4049	1.548	2.66	1.66
750808	2942	1.222	2.90	1.50
750813	2607	1.283	3.34	1.52
750818	3502	1.591	3.16	1.93
750823	4484	1.637	3.83	1.65
750828	5579	1.141	3.83	1.65
750902	3967	1.001	4.62	1.63
750907	4835	1.195	4.00	1.45
750912	1818	1.004	3.31	1.42
750919	1813	2.295	2.21	1.42
750924	1733	3.006	2.34	0.96
750929	1652	2.105	2.73	1.30
751004	1646	2.624	2.50	1.06
751009	1630	2.639	2.42	1.28
751014	1387	2.953	2.79	1.43
751019	1723	1.657	2.95	1.33
751029	2348	3.033	2.54	1.52
751103	2017	0.618	2.30	1.19
751108	1868	0.248	2.77	1.17
751113	1166	0.161	2.69	1.16
751118	2778	2.688	2.67	1.75
751123	2698	0.587	2.28	0.77
751202	2299	1.955	2.54	1.48
751209	2464	2.696	3.72	0.31
751216	6322	2.329	3.06	1.95
751227	1096	1.449	3.44	0.92

A SURFACE CONTOUR OF THE CASPIAN SEA FROM SATELLITE ALTIMETRY

Jean E. Welker

OBJECTIVES

There are two aspects of this work: 1) to combine a surface contour mapping of the Black and Aral Seas with the current Caspian Sea mapping for a regional tectonic analysis; 2) to modify and program some existing mathematical models in order to interpret the altimetric mapping data over these seas.

BACKGROUND

The northern and southern portions of the Caspian Sea have differences in their origins, and can be divided into two distinctly different tectonic zones. The boundary of this division has been defined by the shallow east-west zone which cuts across the Caspian Sea at the Apsheron Peninsula, forming the boundary between the northern and southern Caspian depressions. This shallow zone or boundary also lies along the projected path of the spine of the greater Caucasus, were it to continue and pass directly under the Caspian Sea. The formation of the northern Caspian depression has been linked to the Paleotethyan ocean closing. The southern Caspian depression has been related to an enlarged ocean basin resulting from motion along the fault system formed by the same Paleotethyan ocean closing (Sengor, 1984; Dercourt, et al., 1986). From a broader perspective, the region of the greater Cacasus (located between the Black and Caspian Seas) is part of the Alpine-Himalayan system of orogenic belts which formed from the double closing of the Paleotethys and Neo-tethys oceans beginning in the late Triassic. This region has a complex of active tectonic features as shown in Figure 1. In both the northern and southern portions of the Caspian Sea, linear tectonic features are either projected crossing the sea, or the same feature is shown on either side of the sea. The continuation of these features in easterly and westerly directions intersect the Black and Aral Seas, forming a complex of tectonic features which run into or through the three seas.

In order to shed some light on the tectonic features described above, a modified approach has been developed for processing altimetry records over inland seas to obtain surface contours for those sea surfaces (Zwally, 1983; Martin, 1983; Brenner, 1983).

Altimetry records from both the SEASAT and GEOS-3 satellites have been processed for all three seas in order to obtain surface contours. With these contours, inferences can be made about the type and shape of the tectonic structures beneath the seas.

In a separate but related effort, an existing two-dimensional gravity modeling program is being expanded to three dimensions. Inherent limitations in the application of certain boundary conditions, such as the length and depth dimensions of tectonic structures, are being investigated. The program in its final form will be used to model the tectonic configurations beneath the seas which have produced the anomalies in the sea surface contours.

RECENT ACCOMPLISHMENTS

In order to meet the mapping requirements, an investigation of the surface topography of the Caspian Sea was initiated. The satellite altimetry data from GEOS-3 and SEASAT provided a data base for the measurement of the surface height and structure of the Caspian. The concept of calculating surface contours from altimetry data had already yielded results in the open ocean areas (Marsh et al., 1980, Brown, et al, 1983), and over the continental ice sheets (Zwally et al., 1983). Because the reduction of the altimetry data over the Caspian Sea required many similar techniques to those developed for over the oceans and continental ice sheets, a contour mapping of the Caspian was possible. The basic technical obstacle to the contour mapping of an inland sea such as the Caspian was the smooth gridding and contouring of the unevenly distributed altimetry data, which was especially uneven near the water-land interface. A similar problem had occurred with the unevenly distributed altimetry data over the continental ice sheets. When the techniques developed for the ice sheets were applied to the Caspian Sea data, results were obtained near the shore without degrading the results in the central regions of this inland sea. The ground tracks from the SEASAT and GEOS-3 satellites and the contour map of the Caspian are shown in Figures 2 and 3, respectively. The surface contour of the Black Sea has also been completed, but has not been processed in its final form. The surface contouring of the Black Sea has been straight forward, and no major problems have been encountered. The number of crossover points from intersecting ascending and descending satellite groundtracks has been sufficient

to satisfy the surface contouring requirements. An initial paper describing the results of the contouring of the Caspian and Black Seas and interpretation is in preparation.

The Aral Sea has presented a problem because of the limited number of crossover points from the intersection of ascending and descending satellite groundtracks. Its general shape is roughly circular, with a diameter of approximately 250 km. Crossover intersections are scarce and some small islands in the sea have contributed to a further reduction in the crossovers. If a proper contour of the Aral Sea cannot be constructed, surface profiles for the individual satellite tracks will be drawn.

SIGNIFICANCE

The successful contour mapping of the Caspian and Black Seas to date has proven the viability of a new technique for the investigation of inland seas. The mapping of surface contours has provided insight in the relation of tectonic features bordering the Caspian and Black Seas to one another. With the successful development of models to utilize the surface contour data, additional insight into the underlying tectonic structure, and the origin and formation of these seas may be possible.

FUTURE EMPHASIS

A study of the region of the greater Caucasus will continue with the development of the model technique discussed above. Lake Baikal, in Central Soviet Siberia, is also under study. An assessment of other inland seas which can be contoured using SEASAT and GEOS-3 altimetry is continuing. These include the eastern Mediterranean, the Lake Victoria region in southeast Africa, and the Great Lakes region on the U.S.-Canadian border.

BIBLIOGRAPHY

Brenner, A.C., R.A. Bindschadler, R.H. Thomas, and H.J. Zwally, "Slope Induced Errors in Radar Altimetry over Continental Ice Sheets," J. Geophys. Res., 88, No. C3, 1617-1673, 1983.

Brown, R.D., W.D. Kahn, D.C. McAdoo, and W.E. Himwich, "Roughness of the Marine Geoid from SEASAT Altimetry," J. Geophys. Res., 88, No. C3, 1531-1540, 1983.

Dercourt, J., L. P. Zonenshain, L. E. Ricou, V. G. Kazmin, X. Le Pichon, A.L. Knipper, C. Grandjacquet, I.M. Sbortshikov, J. Geyssant, C. Lepvrier, D.H. Pechersky, J. Boulin, J.-C. Sibuet, L.A. Savostin, O. Sorokhtin, M. Westphal, M.L. Bazhenov, J.P. Lauer, and B. BijuDuval, "Geological Evolution of the Tethys Belt from the Atlantic to the Pamirs Since the Lias," Tectonophysics, 12, 1986.

Graber, K., The Evolution of the Caspian Sea, unpublished Master's Theseis, University of Houston, Houston, TX, May 4, 1984.

Marsh, J.G., T.V. Martin, J.J. McCarthy, and P.S. Chovitz, "Mean Sea Surface Computations Using GEOS-3 Altimeter Data," Marine Geodesy 3, 359-378, 1980.

Martin, T.V., H.J. Zwally, A.C. Brenner, and R.A. Bindschadler, "Analysis and Retracking of Continental Icea Sheet Radar Altimeter Waveforms," J. Geophys. Res., 88, No. C3, 1608-1616, 1983.

Menard, H.W., "Transitional Types of Crust Under Small Ocean Basins," J. Geophys. Res., 72, 3061-3073, 1967.

Sengor, A.M.C., "The Cimmeride Orogenic System and Tectonics of Eurasia," Geologic Society of America, Special Paper, 195, 1984.

Zwally, H.J., R.A. Bindschadler, A.C. Brenner, T.V. Martin, and R.H. Thomas, "Surface Elevation Contours of Greenland and Antartic Ice Sheets," J. Geophys. Res., 88, No. C3, pp. 1589-1596, 1983.

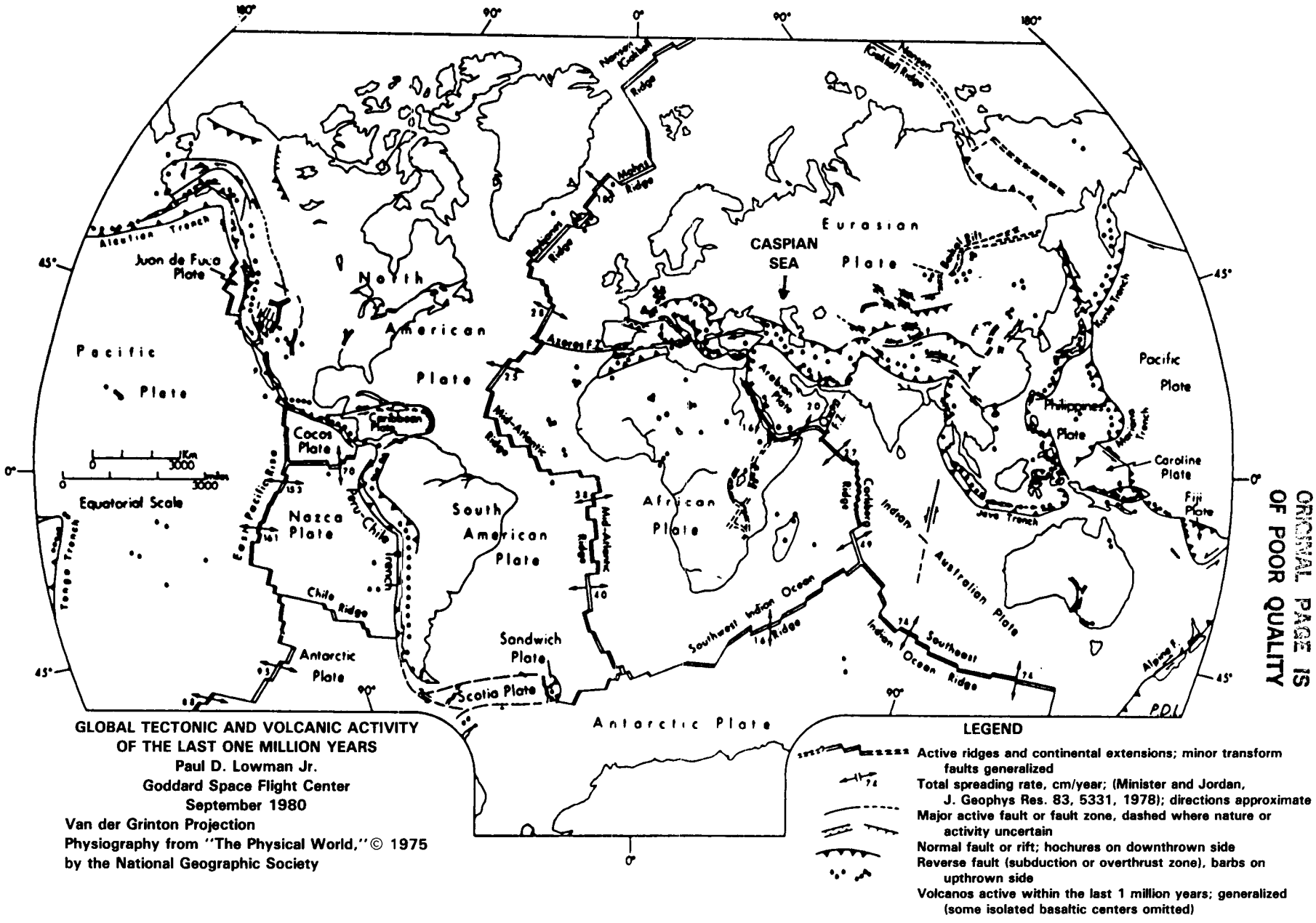

Figure 4. Map showing tectonic and volcanic features active within the last one million years. Drawn partly from satellite imagery (Lowman, 1981).

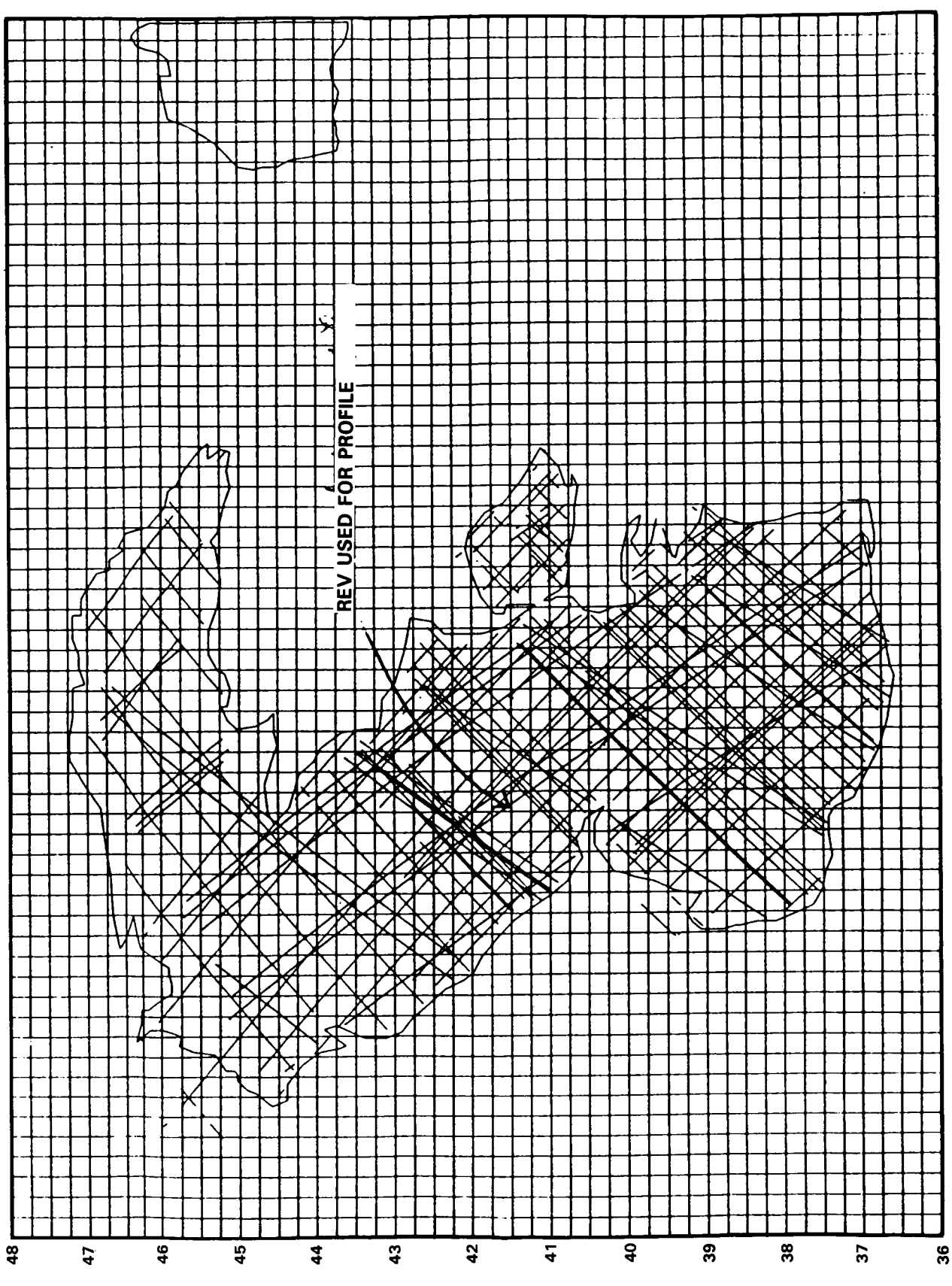

Figure 2. GEOS-3 & SEASAT Ground Tracks Used for Surface

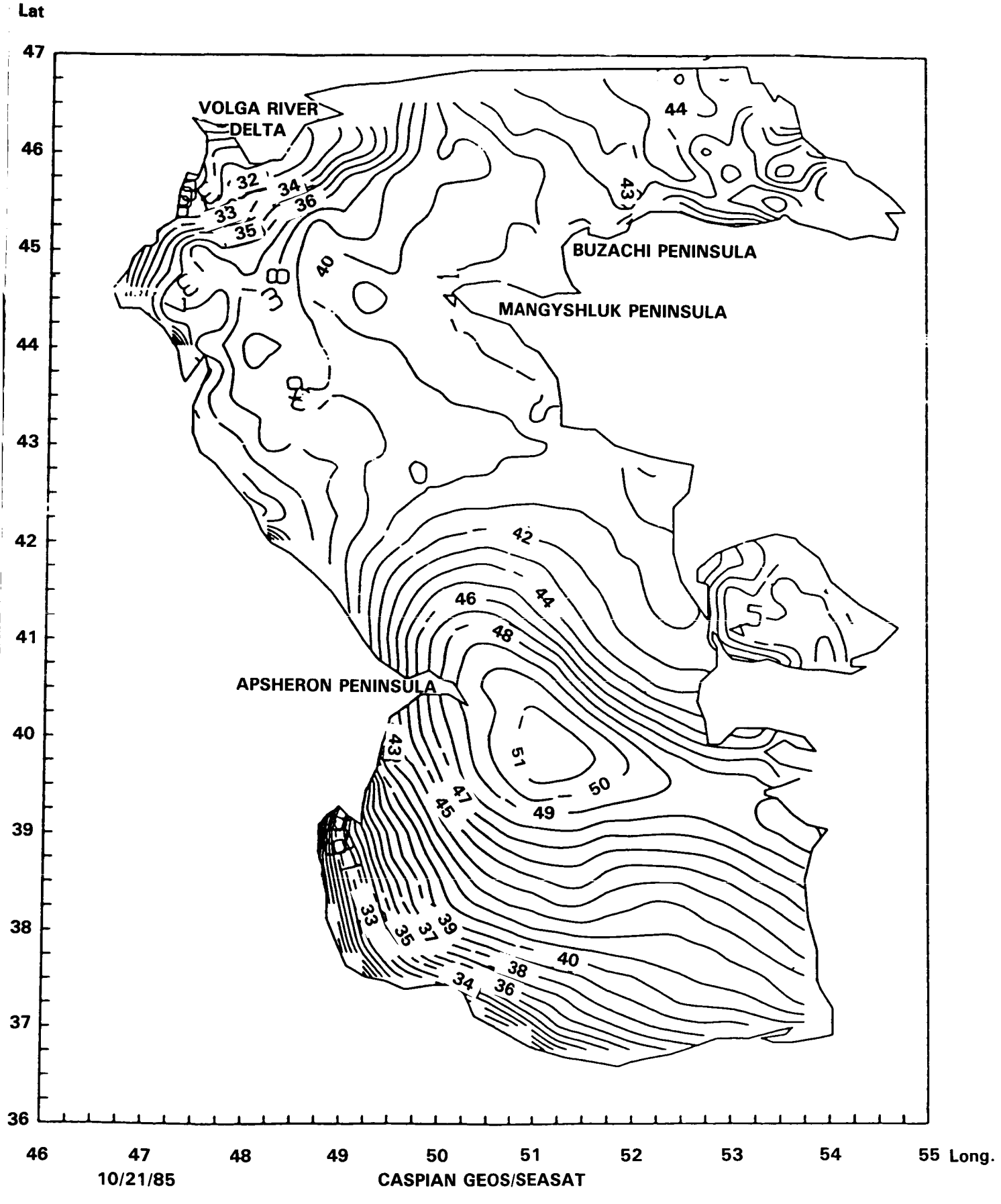

Figure 3. A Surface Contour of the Caspian Sea from Satellite Altimetry.

CHAPTER IV

PLANETOLOGY

OVERVIEW

Although individual members of the Geodynamics Branch have previously been interested in problems in planetology, 1985 marked the beginning of a concerted effort to establish a major planetary research program within the branch. Much of the effort is directed toward geodetic studies of the planet Mars through gravity field mapping and altimetric studies. The work is a direct extension of the well-established expertise and experience within the branch in developing gravity field models, performing orbit determinations, and analyzing altimetric data for earth satellites. The Mars Observer Mission, planned for the early 1990's gives new emphasis to these studies. The interest of branch personnel in planetology has been further heightened by the applicability of their geophysical models of lithospheric deformation and solid-earth dynamics to processes on other terrestrial-like planets.

Contributors to this chapter are: B. Fong Chao, Francis J. Lerch, David P. Rubincam and Maria T. Zuber.

ANALYSIS OF MARS GRAVITY FIELD FROM RADIO TRACKING OF MARS OBSERVER

Francis J. Lerch

OBJECTIVES

The objective of this work is to estimate the accuracy and resolution of the gravity spectrum from the Mars Observer (MO) mission with earthbased DSN Doppler tracking. A global potential of spherical harmonics is modeled with an a priori power spectrum based upon earlier DSN tracking of the Viking and Mariner missions. Gravity anomaly wavelength resolution is derived from the detailed MO accuracy spectrum of harmonics. This information is useful for understanding the physics (stress state, density contrasts, flexural response, lithospheric thickness, etc.) of the interior of Mars and its surface. In conjunction with existing topography and improved topography from the MO altimeter it will serve to determine bounds for theories and models of isostatic compensation of the Martian crust. Also the accuracy of the low degree field will indicate if temporal changes can be detected that correspond to seasonal variations in the Martian polar caps' and atmosphere.

BACKGROUND

The representation for the Martian (Ares) gravitational potential at the altitude of the MO spacecraft can be defined in spherical harmonics as follows:

$$V_a(\bar{r}) = \frac{GM_a}{r} \sum_{\ell=0}^{N} \sum_{m=0}^{\ell} \left(\frac{r_a}{r}\right)^{\ell} P_{\ell m}(\sin\phi)\,[C_{\ell m}\cos m\lambda + S_{\ell m}\sin m\lambda] \qquad (1)$$

where

- $\bar{r}$ - position vector of the satellite with coordinates $(r,\phi,\lambda,)$ Areocentric distance, latitude, and longitude
- GM_a - Areoidal central gravitational constant
- r_a - mean radius of the reference ellipsoid of Mars
- $P_{\ell m}$ - normalized associated Legendre functions of degree ℓ and order m
- $C_{\ell m}, S_{\ell m}$ - normalized spherical harmonic coefficients which are to be estimated to define the gravitational model
- N - maximum degree representing the size (resolution) of the field.

N is expected to be as high as 50, equivalent to a horizontal resolution of about 200 km.

Harmonic coefficients have been estimated (Balmino et al., 1982) from the previous Martian DSN data complete through only degree and order 18 (N=18). These coefficients have been shown (Balmino et al., 1982) to have an rms size per degree of

$$\sigma(C,S)_{\ell m} \approx 13 \times 10^{-5}/\ell^2 \qquad (2)$$

which is 13 times the size of the coefficients for the Earth as estimated by Kaula (1966). Balmino's rule (2) for the coefficient size will be used when estimating the harmonic perturbations in satellite position and velocity of MO.

The Mars Orbiter will be launched (1990 planned) in a near-circular orbit at 350 km altitude with a mission lifetime of 1 Martian year (687 earth days). Tracking data is scheduled from the earth-based Deep Space Network of NASA with accuracy of ±0.03 cm/sec over a 1 minute averaging interval as in the previous Mariner 9 mission (Balmino et al., 1982). Using this figure as a guide and Balmino's rule (2) for Mars, a spectrum of significant perturbations in the velocity of MO orbit can be seen in Figure 1 from the harmonics through degree 50.

Velocity component perturbations (radial, crosstrack, and along-track) of MO are summarized in Figure 2 for the same spectrum of harmonics. The MO Doppler signal of gravity would be composed of the projection of these components on the line of sight from the tracking station. Separability of the harmonics in the solution is discussed below. From Figure 1 the sensitivity to a single harmonic perturbation on MO is on averge about 0.01 cm/sec at degree 50, but for the root-sum-of-squares of all orders there is approximately 0.1 cm/sec, considerably higher than the noise level of the data.

ACCOMPLISHMENTS AND RESULTS

An error spectrum (Figure 3) was derived for an MO gravitational model of spherical harmonics complete through degree and order 50. The spectrum shows an order of magnitude improvement over current knowledge (Balmino et al., 1982). The analysis assumed DSN Doppler data of 0.3 cm/sec noise for 1 minute data intervals over 70 days of MO tracking. For simplicity, an average component (Figure 3) of alongtrack, radial, and crosstrack velocity was used to represent the DSN Doppler tracking coverage (described in Figure 5 of the Project Overview of Mars Observer Proposal Information Package, OSSA2-85, Volume IV). From the same reference the analysis employed

the "frozen orbit" geometry (ω fixed at -90°) of MO along with the repeating groundtrack of 56-day period of 30 km uniform spacing. These conditions remove the long-term perturbation effects and permit the gravitational signal to repeat itself. As a consequence, the cross terms of the normal matrix of the velocity components of the gravitational signal (Colombo, 1981; Wagner, 1983) nearly average to zero (barring small nonlinear effects) except for the terms of order m and the same degree parity. This allowed the matrix to be simplified to a sparse form of block diagonal terms corresponding to each order m. Employing the Fourier representation (Kaula, 1966) of the potential perturbations, the signal was averaged analytically over the span of the repeat cycle, thus simplifying point-by-point computations. Because of the occultation of the radial and velocity components as given in the Project Overview (Figure 13, Volume IV), crossterms will not completely vanish.

From Figure 3 of the error spectrum, the cross-track effects are more dominant in the solution than radial or along-track effects. Cross-track effects are not occulted by Mars when the orbital plane is normal to the line-of-sight. About 1.9 years of tracking coverage (687 days) are available and about 1/10 the quantity of data (70 days) is assumed for the solution. By calibrating the error spectrum from actual but spotty satellite tracking coverage from Earth satellites, the MO error spectrum (Figure 3) was degraded by a factor 6 from the ideal solution. Combining this degradation with that from the data ($\sqrt{10}$), a total reduction of a factor of 19 from the ideal value has been employed as a conservative estimate of the accuracy for the MO model. The solution also assumed use of a priori knowledge (Figure 3) for the gravitational field from previous Martian missions. If this a priori assumption is removed, there is essentially no change in the error spectrum, except at high degrees where the error curve departs along a tangential line at degree 30 and approaches closely to the a priori estimate at degree 50.

SIGNIFICANCE AND FUTURE EMPHASIS

The error spectrum of the harmonics was used to estimate the global rms mean gravity anomaly errors for various block sizes (half wavelength) as indicated in the table below. The results for the 400 km blocksize, showing a 6.9% error of total power, will be needed to estimate useful density contrasts in the Martian crust (e.g., basalt/granite). Wavelengths shorter than 1000 km (500 km half wavelength) are expected to show negligible flexural response (no compensation). Therefore, at these wavelengths, the gravity anomalies should result from the near-surface density contrasts in the crust.

MARS MEAN GRAVITY ANOMALY*

POWER SPECTRUM - $13X10^{-5}/\ell^2$ COEFF. MODEL
MO MODEL - 50X50, 70 DAYS DSN DATA, 0.03 cm/sec.

MEAN ANOMALY BLOCK SIZE (1/2 Wavelength)	TOTAL POWER*	MO MODEL COMMISSION ERROR*	MO MODEL TOTAL ERROR*	TOTAL PERCENT ERROR (%) Error/Power
1.0°	132.1 mgals	11.0 mgals	72.4 mgals	54.8
3.5° (200 km)	107.7	8.5	26.4	24.5
5.0° (300 km)	99.8	6.0	13.0	13.0
7.0° (400 km)	91.9	2.8	6.3	6.9
10.0°	82.9	1.3	4.7	5.7

*Gravity anomaly averaged over a block.

Density structure may be analyzed from the gravity model in conjunction with the topography obtained from the MO altimeter and will increase our understanding of the Martian lithosphere and its evolution.

Modeling of the MO orbit and gravitational signal from earth-based DSN tracking will be developed in order to recover the gravity field to the accuracy specified in Figure 3. This developmental program will be tested with existing DSN data from Viking and Mariner missions.

REFERENCES

Balmino, G., B. Moynot, N. Vales, "Gravity Field Model of Mars in Spherical Harmonics up to Degree and Order Eighteen," J. Geophys. Res., 87, 9735-9746.

Colombo, O.L., "Geoid Geopotential Modelling from Satellite-to-Satellite Tracking," Dept. of Geodetic Science and Surveying, Report No. 317, The Ohio State University, 1981.

Colombo, O.L., "The Global Mapping of Gravity with Two Satellites," Netherlands Geodetic Commission Publications on Geodesy, New Series, Vol. 7, No. 3, 1984.

Kaula, W.M., Theory of Satellite Geodesy, Blaisdell Press, Waltham, Mass., 1966.

Wagner, C.A., "Direct Determination of Gravitational Harmonics from Low-Low Gravsat Data," J. Geophys. Res., 88, 10309-10321, 1983.

Wagner, C.A., "Geopotential Orbit Variations: Applications of High Speed Satellite Geodesy," J. Geophys. Res., in publication.

HARMONIC PERTURBATIONS FOR MOM

ORBIT: 350 KM ALTITUDE ECCENTRICITY = 0 93 DEG INCLINATION
MARS POTENTIAL: $\sigma_{\ell m} = 13 \times 10^{-5/\ell^2}$

Total velocity perturbation
Units in 0.001 cm/sec.

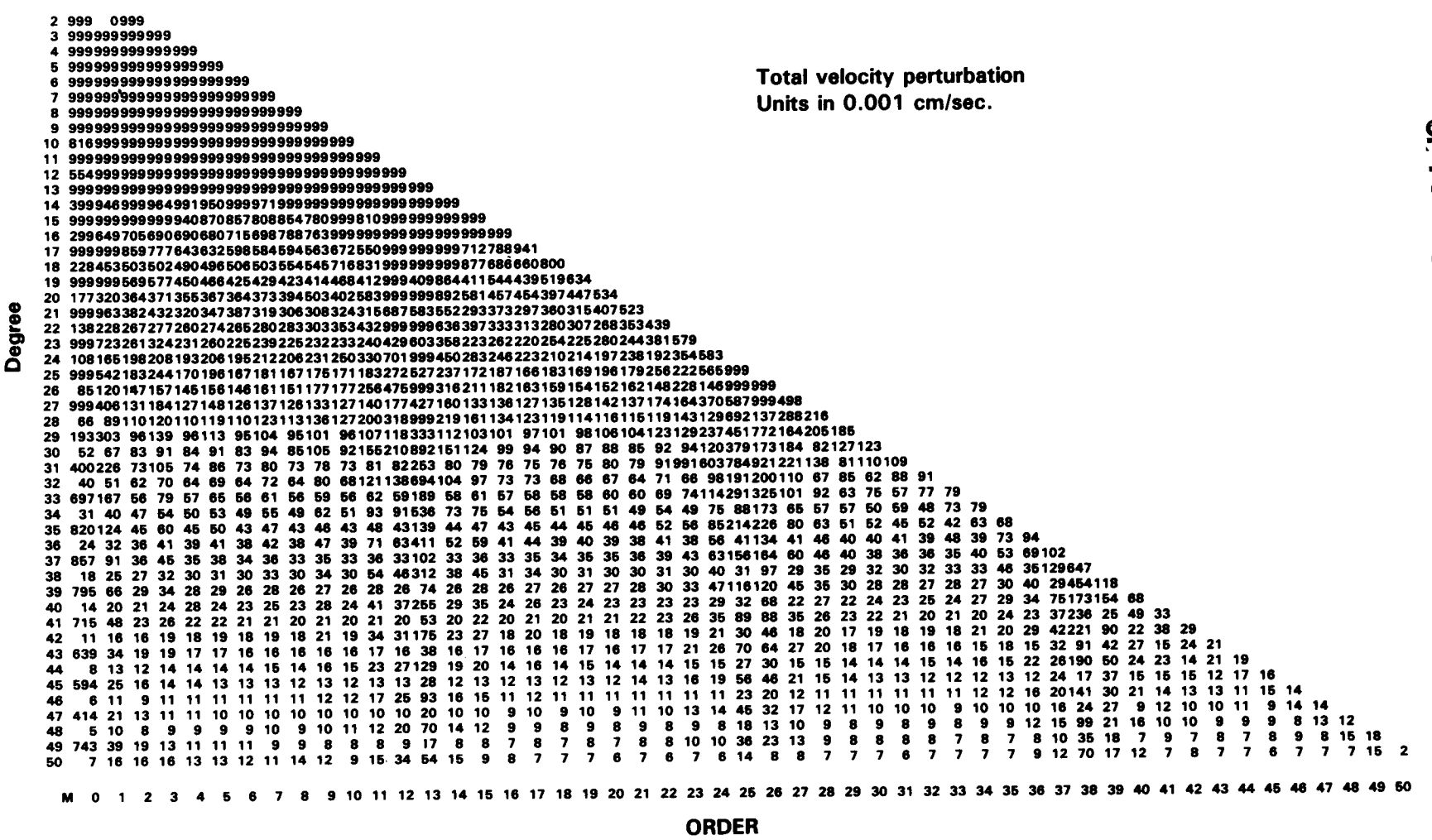

Fig. 1

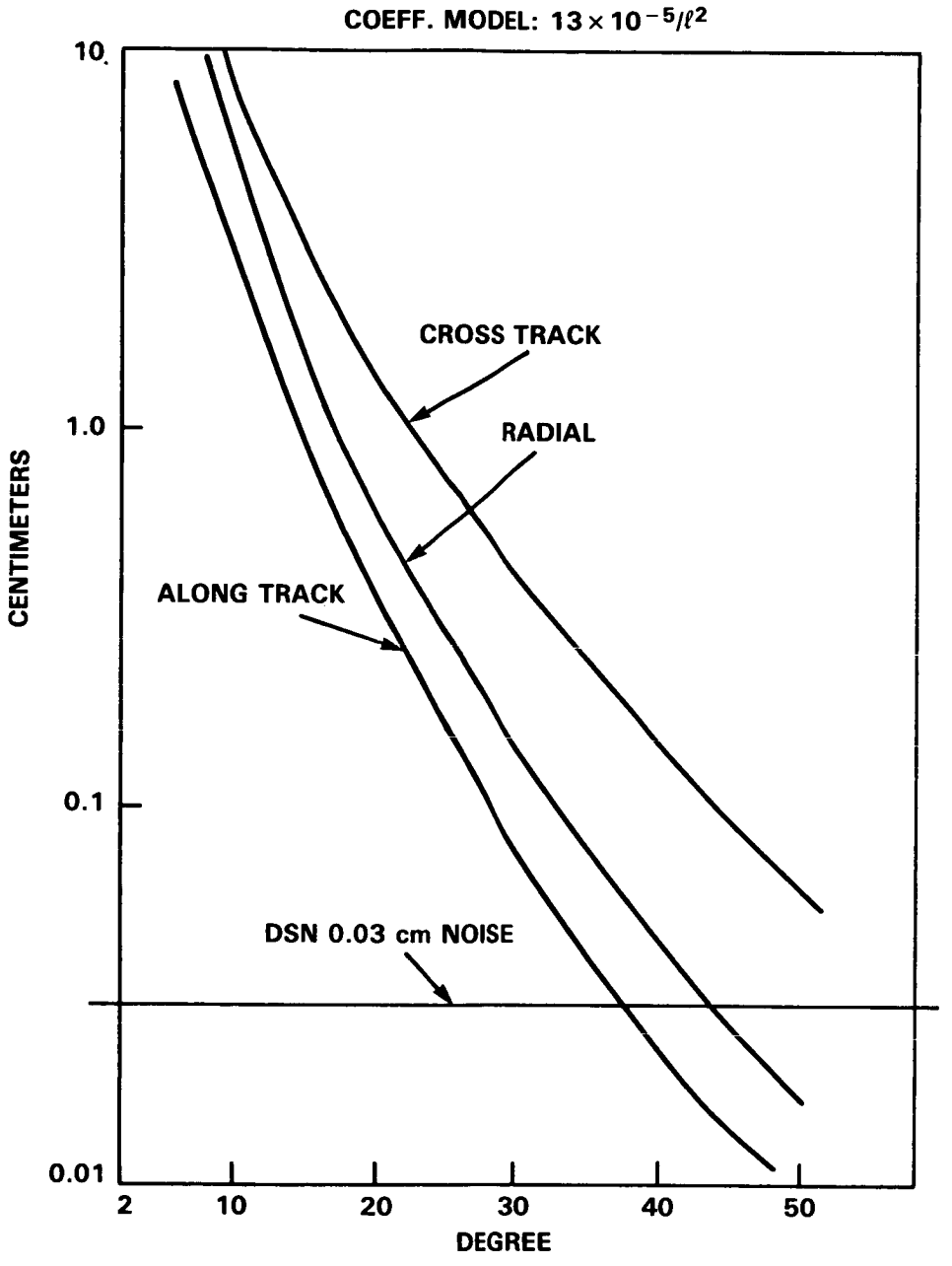

Figure 2. Harmonic Perturbation by Degree for Radial, Along, and Cross Velocity Components for MO

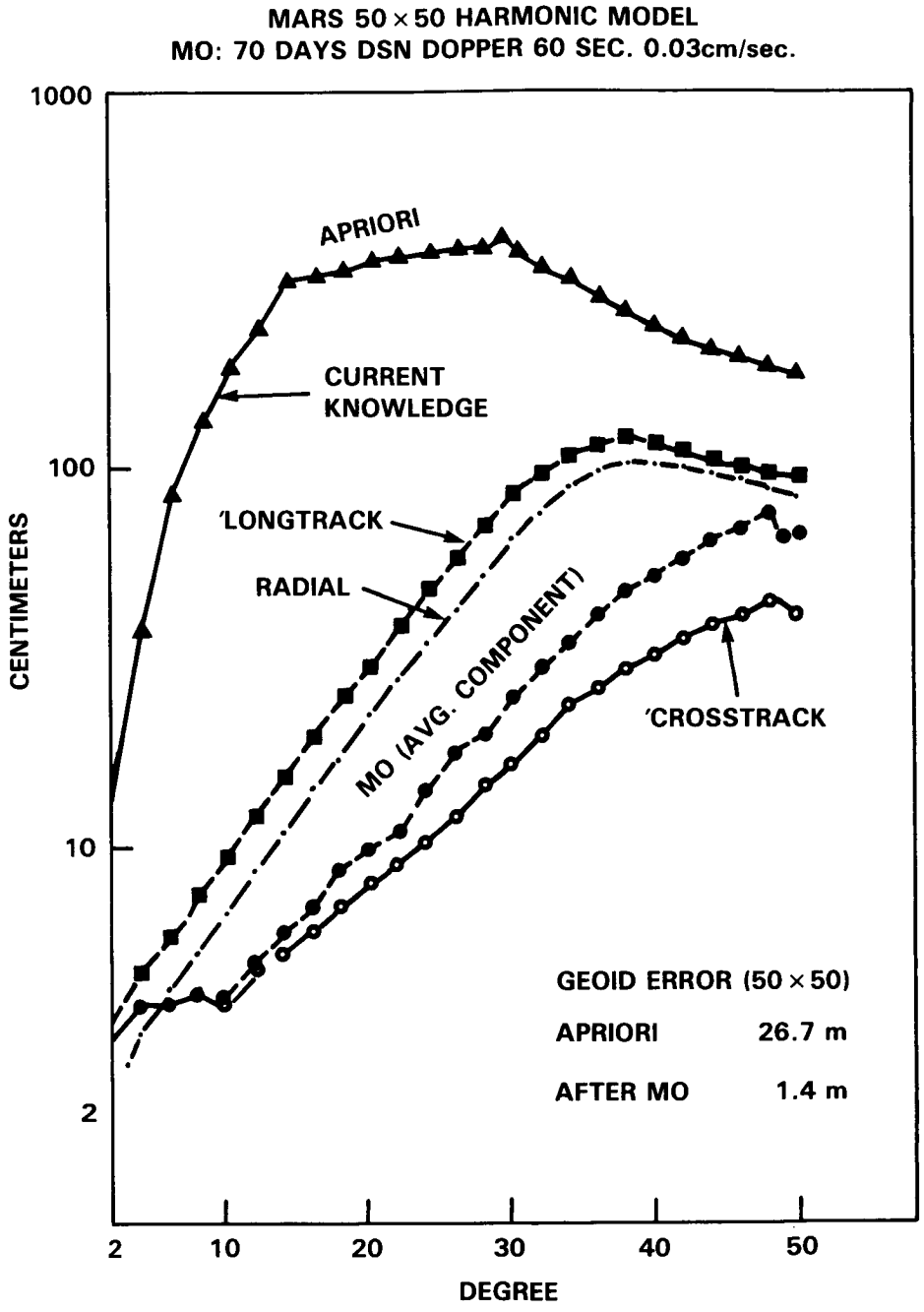

Figure 3. Error Spectra Per Degree

ON SEASONAL VARIATIONS OF MARS' GRAVITATIONAL FIELD

B. Fong Chao

David Parry Rubincam

OBJECTIVE

The objective of this work is to study, based on simplified models, the variation in Mars' gravitational field caused by the seasonal exchange of CO_2 mass between the Martian atmosphere and polar caps.

BACKGROUND

It is well-known that Mars has seasons like the Earth. However, the colder atmospheric temperature of Mars (some 80°K lower than the Earth's) and its predominantly CO_2 atmosphere (more than 95%) conspire to create a large exchange of CO_2 mass between the atmosphere and polar caps. The mass exchange occurs in seasonal cycles: a great quantity of CO_2 condenses to form (or add to) the polar caps in winter and sublimes into the atmosphere in summer. The mass involved is at least 8×10^{15} kg, which is about 25% of the total mass of the Martian atmosphere, or equivalent to a cap of solid CO_2 extending to 45° latitude changing its thickness by some 20 cm. In contrast, the Earth's atmosphere only varies seasonally by about 1×10^{15} kg (or about 0.02% of the total), primarily due to variation of water vapor content.

The CO_2 mass redistribution inevitably changes Mars' gravitational field. As an order-of-magnitude assessment, for the gravitational effect of any mass redistribution on a planetary scale, the deciding factor is the ratio of the net redistributed mass to the total mass of the planet. For the Martian CO_2-exchange effect, the ratio is $8 \times 10^{15} / 6.4 \times 10^{23}$, or about 10^{-8}. No geological or geophysical phenomenon on Earth is known to produce a relative mass redistribution of nearly that size in a year. The post-glacial rebound of the mantle, the strongest southern oscillation/El Nino events in the atmosphere and the ocean, and the greatest earthquakes are all at least 2 or 3 orders of magnitude smaller. Since even these geophysical phenomena are already being observed gravitationally by Earth satellites (e.g., Rubincam, 1984; Gross and Chao, 1985), we can expect the CO_2-exchange effect to be detectable from future Mars orbiter missions. If so, the observed gravitational field changes can provide gross constraints on the meteorological models for Mars.

RECENT ACCOMPLISHMENTS

Suppose the planet's surface is subject to a time-varying change in the surface density $\Delta\sigma(\Omega,t)$. The resultant change in the gravitational field, expressed in terms of its harmonic coefficients (or the "Stokes' coefficient") of degree ℓ and order m can be shown to be

$$\Delta[C_{lm}+iS_{lm}](t) = \frac{R^2}{(2l+1)M} \int \Delta\sigma(\Omega,t)\ Y_{lm}(\Omega)\ d\Omega \qquad (1)$$

where R is the radius, M the mass of the planet, $Y_{\ell m}$ is the normalized spherical harmonic function, and the integration is over the entire surface (with surface element $d\Omega$) in an Eulerian description. For convenience we shall also translate these changes into equivalent rms changes in the geoid height N using Bruns' formula

$$\Delta N_{lm}(t) = R\ |\ \Delta(C_{lm}+iS_{lm})(t)\ |. \qquad (2)$$

$\Delta N_{\ell m}(t)$ in millimeters provides a comfortable measure of the effect of $\Delta\sigma(\Omega,t)$ on the geoid. It can also be shown that the elastic yielding of Mars is small so that the solid Mars can be treated as a rigid body.

We follow the seasonal journey of the CO_2 mass and consider separately the contributions of two phases to equation (1): (i) the waxing and waning of the solid CO_2 in polar caps, and (ii) the geographical distribution of the gaseous CO_2 in the atmosphere. The two phenomena, of course, accompany each other inasmuch as the total CO_2 mass is constant. The total CO_2-exchange effect is just the sum of the two contributions.

(i) We assume that the seasonal condensation and sublimation are uniform on the polar caps, and that the caps are circular and symmetrical with respect to the poles. Equation (1) then gives

$$\Delta C_{l0}(t) = \left[\frac{1}{\sqrt{2l+1}(1-\cos\kappa)}\int_{\cos\kappa}^{1} P_l(\mu)\ d\mu\ \frac{\Delta M(t)}{M}\right]_n + (-1)^l\left[\ \text{same}\ \right]_s \qquad (3)$$

where P_ℓ is the ordinary Legendre function of degree ℓ, $\kappa=45°$ is the angular extent of the polar cap, ΔM is the total CO_2 mass accumulated on the cap at any given moment, and the subscripts n and s indicate the northern and southern hemisphere, respectively. Here we shall only consider a few of the lowest degree terms by evaluating their maximum amplitudes which occur at the peak of

formation of the southern cap ($t=t_0$). Thus substituting into equation (3) the value for ΔM, $\Delta M(t_0) = 8\times10^{15}$ kg, and R=3390 km, the result shows that the largest change is in J_2, which sees a maximum relative seasonal change of 3.8 ppm (parts per million). In comparison, the observed secular change in the Earth's J_2 (due to post-glacial rebound) is 0.024 ppm per year (Rubincam, 1984), which is two orders of magnitude smaller. The results are summarized in Table 1.

(ii) The Martian surface topography will influence the way the changing atmospheric CO_2 mass distributes itself geographically; that, in turn, will change the gravitational field. Its effect on the gravitational field can be shown to be

$$\Delta(C_{lm}+iS_{lm})(t) = -\frac{2-\delta_{m0}}{2l+1}\,\frac{RH_{lm}}{Z}\,\frac{\Delta M(t)}{M} \qquad (4)$$

where $H_{\ell m}$ is the "effective topography" defined as the departure of the true topography from the geoid; Z is the scale height of the Martian atmosphere. Again, the largest effect is on J_2. The results are summarized in Table 2.

SIGNIFICANCE AND FUTURE EMPHASIS

The variations in Mars' gravitational field due to the CO_2 mass exchange are generally very large compared with their terrestrial counterparts. Nevertheless, whether they can be observed by the upcoming MO (Mars Observer mission, due to be launched in 1990) is presently uncertain. A preliminary simulation (F. Lerch, private communication, 1985) has indicated that, using Doppler tracking data alone, the change in J_2 can be marginally detected, provided that all favorable conditions prevail throughout the MO lifetime (1 Martian year). However, if in addition the surface altimetry data (as differences at crossovers) are available, then the accuracy in the gravitational field determination is expected to be greatly improved. It may then be possible to detect changes not only in J_2 but in other components as well. A more realistic and more detailed simulation is currently underway (see Lerch, this issue). If the above analysis is confirmed, the observed changes in the gravitational parameters can place constraints on the meteorological models of Mars.

REFERENCES

Gross, R.S., and B.F. Chao (1985). Excitation study of the LAGEOS-derived Chandler wobble. J. Geophys. Res., 90, 9369-9380.

Rubincam, D.P. (1984). Postglacial rebound observed by LAGEOS and the effective viscosity of the lower mantle. J. Geophys. Res., 89, 1077-1087.

Table 1. Maximum Gravitational Effect of the Changing Polar Cap CO_2 (equation 3)

ℓ	$\Delta C_{\ell 0}(\times 10^{-8})$	$\Delta J_\ell(\times 10^8)$	$\Delta N_{\ell 0}$(mm)	Remarks
2	0.34	−0.75	11	Largest term.
3	−0.15	0.40	5.0	Progressively smaller.
4	0.031	−0.094	1.1	↓
5	0.030	−0.10	1.0	

Table 2. Maximum Gravitational Effect of the Changing Atmospheric CO_2 (equation 4)

ℓ	m	$\Delta C_{\ell m}(\times 10^8)$	$\Delta S_{\ell m}(\times 10^8)$	$\Delta J_\ell(\times 10^8)$	$\Delta N_{\ell m}$(mm)	Remarks
1	0	−0.053	—	0.092	1.8	Corresponding to 2.6 mm of shift in center of mass
1	1	−0.0023	0.056	—	1.9	
2	0	−0.080	—	0.18	2.7	Largest term, about 1/4 that of Table 1, but out of phase
2	1	0.012	−0.018	—	0.72	Corresponding to 50 cm of polar motion excitation
3	0	0.0051	—	−0.014	0.17	Small compared with Table 1
2	2	−0.034	−0.028	—	1.5	Large because of Tharsis
3	3	0.0093	−0.027	—	1.0	

CONSTRAINTS ON VENUS' LITHOSPHERE RHEOLOGY FROM TECTONIC FEATURES

Maria T. Zuber

OBJECTIVE

The geometries of tectonic surface features provide a direct indication of the rheological structure of the lithosphere at the time of deformation. Recent radar images of the surface of Venus reveal a variety of features which are interpreted to have formed in response to tectonic stresses. In this study, characteristics of these features are used to place constraints on theoretical models of the mechanical structure of the Venus lithosphere.

BACKGROUND

Radar images obtained from Pioneer Venus (Masursky et al., 1980, Pettengill et al., 1980) earth-based observations (Campbell et al., 1983, 1984), and the Venera 15/16 spacecrafts (Barsukov et al., 1986; Basilevsky et al., 1983) indicate that the Venus surface has undergone extensive tectonic activity. In particular, the highlands regions of Venus (radius > 6053 km; Masursky et al., 1980) contain numerous examples of both extensional and compressional deformation (Head, 1986). A conspicuous extensional feature, illustrated in Figure 1, is the Beta Regio Rift zone. As observed in high resolution Arecibo radar images (Campbell et al., 1984), the rift consists of a central depression and uplifted flanks with an average flank-to-flank width of 100-200 km. Within the central depression are alternating radar-bright lineations which are interpreted as faults (Campbell et al., 1984) with widths which range from 10 to 20 km. Figure 2 shows a group of prominent compressional features, termed ridge belts, which were revealed by Venera 15 and 16 imaging radar (Barsukov et al., 1986; Basilevsky et al., 1986). The ridge belts are north-south trending linear ridges which have a regular spacing perpendicular to strike of approximately 300 km (Zuber, 1986), within which are contained systems of sub-parallel trending ridges and grooves with widths of 10-20 km. The geometries of these features and others on the Venus surface illustrate that extensional and compressional deformation in many instances developed with two length scales, one of a few tens-of-km and another on the order of hundreds-of-km.

The parallel strikes and regular or characteristic spacings of tectonic features on Venus suggest that their length scales of deformation are controlled by a dominant wavelength arising from the growth of compressional and extensional instabilities in the lithosphere. Instability growth may occur in a horizontally-stressed medium which is stratified in viscosity (strength) or in which viscosity is continuous and decreases with depth (Biot, 1957; 1960). Deformation arises under conditions for which initial perturbations along free surfaces and/or interfaces between regions of high and low viscosity amplify with time. The style of deformation associated with instability growth is determined by the nature of the initial perturbations. In either an extending or compressing medium in which initial perturbations are distributed randomly, deformation develops periodically at the dominant wavelength, λ_d (e.g., Fletcher, 1974; Smith, 1975). In an extending layered medium in which an initial perturbation is localized, deformation consists of a central depression and uplifted flanks, and is morphologically analogous to a rift zone (Zuber and Parmentier, 1986). The dominant wavelength of the extensional instability controls the width of the rift. In both cases the dominant wavelength is a funcion of the mechanical structure of the medium, and in particular the thickness of the strong layer. Thus, instability growth may describe both the periodic spacings of extensional and compressional features and the width of an isolated rift.

In a study of deformation due to extensional instability applied to the Basin and Range Province of the western U.S., Zuber et al. (1986) have shown that two scales of deformation may arise if the lithosphere consists of two high viscosity layers separated by a weaker layer. For the earth's continental lithosphere, the strong layers are believed to correspond to the upper crust and a region of strength in the upper mantle, while the weak layer is thought to correspond to the ductile lower crust. It is suggested that the existence of two scales of deformation on Venus indicates that its lithosphere has also differentiated into a crust that is chemically distinct and weaker than the underlying mantle.

Figure 3 shows one possible strength stratification for the Venus lithosphere assuming that the thickness of the crust (shown by the dashed line) and the compositions of the crust and mantle are similar to those for terrestrial ocean basins. The regions in which strength increases linearly with depth correspond to the part of the lithosphere which deforms by brittle fracture. In other areas deformation occurs by ductile flow and strength decreases rapidly with increasing temperature (depth). The left and right sides of the diagram show the strength of the lithosphere, defined as the difference between the maximum and minimum principal effective stresses, for compression and extension, respectively. Note that for both extension and compression the upper crust and mantle are stronger than the lower crust. If this scenario applies to Venus, then the spacings of small and large scale tectonic features may be controlled by the thicknesses of the strong regions of the upper crust and upper mantle, respectively.

RECENT ACCOMPLISHMENTS

To test the hypothesis that tectonic features on Venus formed in response to multiple scales of extensional and compressional instability, simple models of the Venus lithosphere consisting of two strong or high viscosity layers separated by a weaker layer have been developed. Results show that the lithosphere can be unstable in both extension and compression and that a range of conditions exist for which two scales of deformation will occur. Figure 4 illustrates how the dominant wavelengths are controlled by the thickness of the strong crustal layer (h_1) and some of the physical properties of the medium for both compression and extension. The two lines in each diagram correspond to the short and long wavelengths of deformation. If the width or spacing of a tectonic feature is known, then these diagrams can be used to constrain the thickness of the strong crustal layer. Similar relationships can be established for other physical properties in the problem. Results show that the allowable range of strong crustal layer thicknesses is $3<h_1<20$ km and that total crustal thicknesses fall generally in the range $5<h_c<30$ km. A strong region of the mantle only a few km thick is required to produce a long wavelength instability.

In conclusion, compessional and extensional instability growth is a viable mechanism for the formation of many tectonic features on Venus. The results suggest that at least in some areas, the Venus lithosphere consists of two regions of strength, analogous to the strong upper crust and upper mantle of terrestrial continents.

FUTURE EMPHASIS

Previous analyses (e.g., Smith, 1975) have shown that a compressing layered medium is always unstable (and therefore always deforms at the dominant wavelength) in compression, while in extension deformation may be either unstable or stable (corresponding to uniform thinning of the medium). On Venus it may be possible to define a plausible range of conditions for which the lithosphere is stable in extension. This would place important constraints on the strength of the lithosphere and on the origin of the tectonic features.

REFERENCES

Barsukov, V.L., et al., The geology and geomorphology of the Venus surface as revealed by radar images obtained by Veneras 15 and 16, Proc. Lunar Planet. Sci. Conf. XVI, in press, 1986.

Basilevsky, A.T., et al., Styles of tectonic deformations on Venus: Analysis of Venera 15 and 16 Data, Proc. Lunar Planet. Sci. Conf. XVI, in press, 1986.

Biot, M.A., Folding instability of a layered viscoelastic medium under compression, Proc. Royal Soc. A., 242, 444-454, 1957.

Biot, M.A., Instability of a continuously inhomogeneous viscoelastic half-space under initial stress, Jour. Frank. Inst., 270, 190-201, 1960.

Campbell, D.B., J.W. Head, J.K. Harmon, and A.A. Hine, Venus: Identification of banded terrain in the mountains of Ishtar Terra, Science, 221, 664-674, 1983.

Campbell, D.B., J.W. Head, J.K. Harmon and A.A. Hine, Venus: Volcanism and rift formation in Beta Regio, Science, 226, 167-170, 1984.

Fletcher, R.C., Wavelength selection in the folding of a single layer with power law rheology, Am. Jour. Sci., 274, 1029-1043, 1974.

Head, J.W., Venus global tectonics: Tectonic style and evidence for latitudinal distribution of tectonic features, Lunar Planet Sci. XVII, 325-326, 1986.

Masursky, H., E. Eliason, P.G. Ford, G.E. McGill, G.H. Pettengill, G.G. Schaber, G. Schubert, Pioneer Venus radar results: Geology from images and altimetry, J. Geophys. Res., 85, 8232-8260, 1980.

Smith, R.B., Unified theory of the onset of folding, boudinage, and mullion structure, Geol. Soc. Am. Bull., 86, 1601-1609, 1975.

Pettengill, G.H., E. Eliason, P.G. Ford, G.B. Loriot, H. Masursky, and G.E. McGill, Pioneer Venus radar results: Altimetry and surface properties, J. Geophys. Res., 85, 8261-8270, 1980.

Zuber, M.T., A dynamic model for ridge belts on Venus and constraints on lithospheric structure, Lunar Planet. Sci. Conf. XVII, 979-980, 1986.

Zuber, M.T., and E.M. Parmentier, Lithospheric necking: A dynamic model for rift morphology, Earth Planet. Sci. Lett., in press, 1986.

Zuber, M.T., E.M. Parmentier and R.C. Fletcher, Extension of continental lithosphere: A model for two scales of Basin and Range deformation, J. Geophys. Res., in press, 1986.

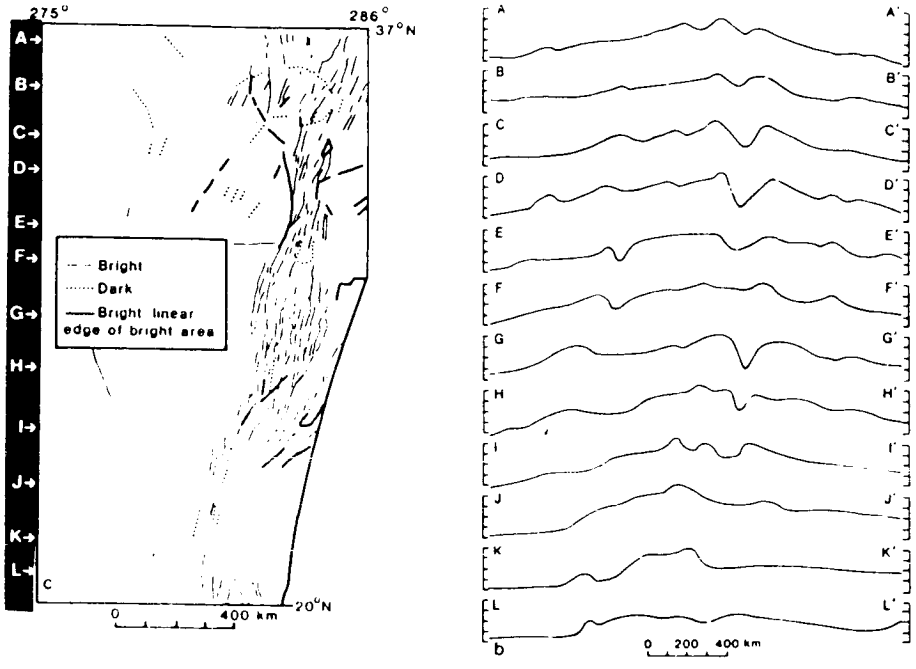

Figure 1. Topographic profiles and sketch map of bright and dark linear features mapped from Arecibo radar image of the Beta Regio Rift (from Campbell et al., 1984). The radar-bright lineations within the central depression of the rift are interpreted as faults. The width of the rift and the spacing of the lineations define two length scales of extensional deformation.

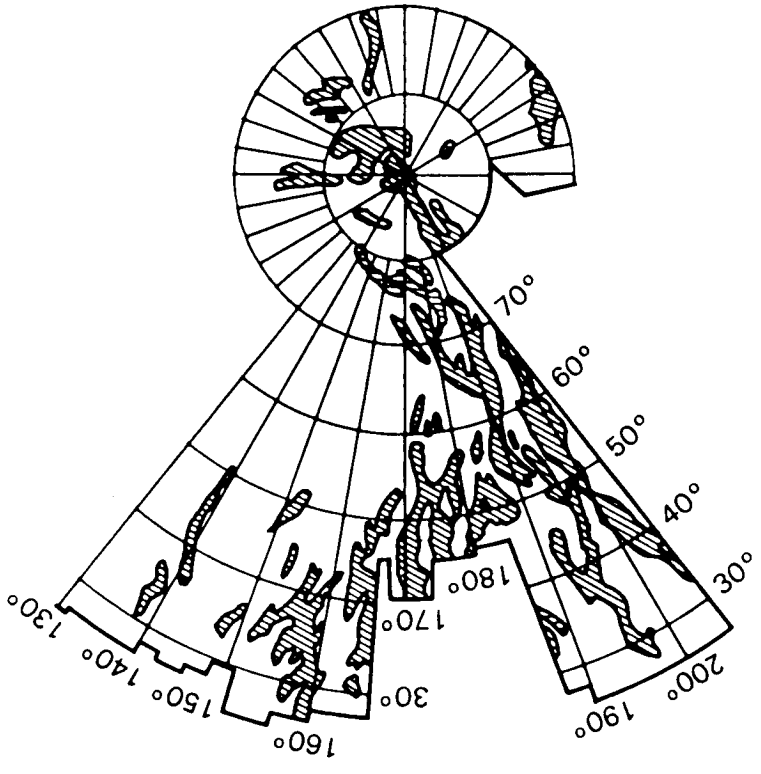

Figure 2. Sketch map showing the distribution of ridge belts in part of the northern hemisphere of Venus (after Barsukov et al., 1986). Within the ridge belts, smaller scale ridges and grooves strike approximately parallel to the belts. The spacings of the ridge belts and the ridges and grooves define two length scales of compressional deformation.

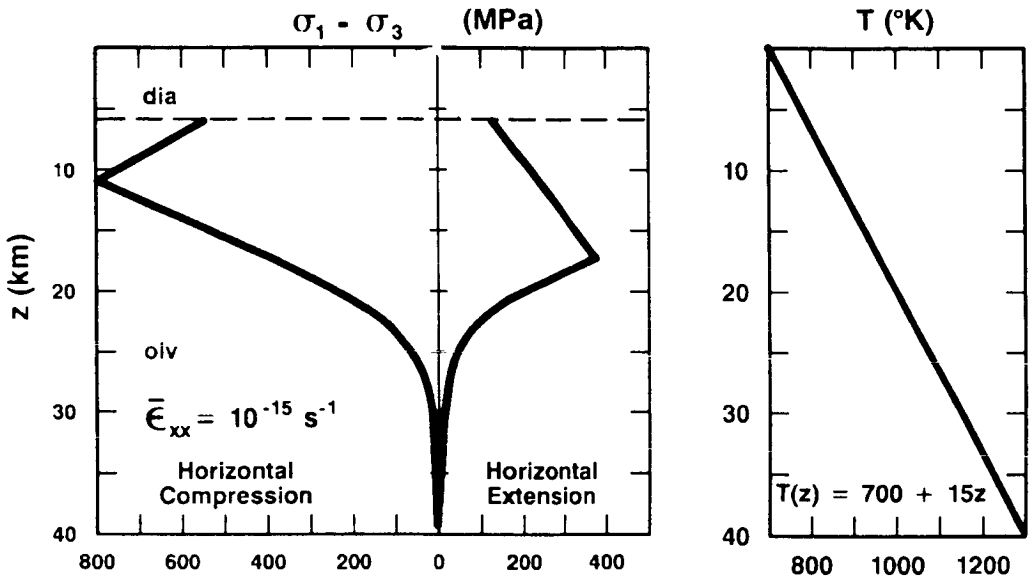

Figure 3. Strength of the Venus lithosphere with depth for compression and extension assuming a crustal thickness and crust and mantle compositions similar to those of terrestrial ocean basin. The strength envelope was constructed for the geothermal gradient shown on the right.

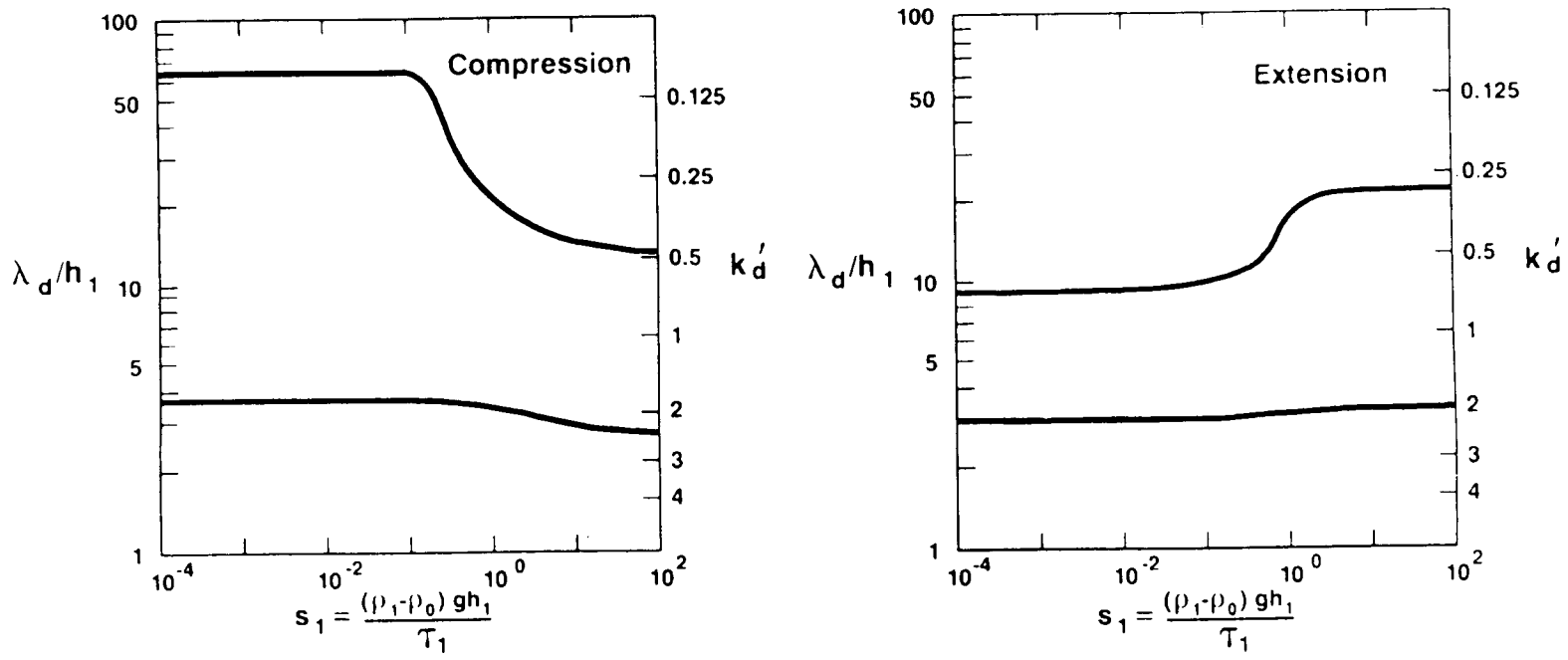

Figure 4. Relationship between dominant wavelength (λ_d) and the dimensionless ratio of the buoyancy force at the surface ($\Delta\varrho gh_1$) to the average strength of the strong crustal layer (τ_1) for compressional and extensional instabilities. The dominant wavelength is normalized to the thickness of the crustal layer h_1. The two lines correspond to short and long wavelength instabilities.

CHAPTER V

GEOPHYSICAL TECHNIQUES DEVELOPMENT

OVERVIEW

This chapter discusses a variety of subjects concerned with measurement system development, computer software development and enhancement, and the development and evaluation of new measurement techniques. Specifically, a detailed discussion is made of the modification, through use of new technology, of the Very Long Baseline Interferometer (VLBI) system, supporting computer software development, and mathematical modeling based on the analysis of VLBI data. A discussion is provided of the calibration procedure used on new Satellite Laser Ranging (SLR) Systems prior to their introduction into the global SLR network used to track the Lageos satellite. Specialized techniques such as computer imaging techniques as applied to ocean topography and geophysical data are described. Analyses to evaluate the capabilities of new measurement techniques such as (1) the direct measurement of the high frequency components of the earth's gravity field through use of a spaceborne gravity gradiometer and (2) the global measurement of crustal deformation, land topography, etc., through the use of a spaceborne geodynamics laser ranging system are both discussed in this chapter. Finally, a discussion of research on soil temperature is included.

Contributors to this chapter are: Thomas A. Clark, Steven C. Cohen, Theodore L. Felsentreger, John M. Gipson, M.W. Hayes, Edwin Himwich, Werner D. Kahn, Ronald Kolenkiewicz, Goran L. Lundqvist, Chopo Ma, Carole Nethery, Barbara H. Putney, James Ray, and Jean E. Welker.

MICROWAVE HOLOGRAPHY

John M. Gipson

OBJECTIVE

During 1984, Very Long Baseline Interferometry (VLBI) was used to measure the complex (amplitude and phase) far field pattern of three antennas used by the Crustal Dynamics Project with the aim of using microwave holography to obtain information about these antennas.

BACKGROUND

Microwave holography is a technique for obtaining information about an antenna from its far field pattern. One can find the far field pattern by modeling the surface of the antenna as a collection of elementary current dipoles. A dipole is a simple kind of antenna whose radiation pattern is known. The strength of the radition pattern is proportional to the dipole current. By adding up the radiation pattern from all of the elementary dipoles one can obtain the far field of the antenna. In microwave holography one inverts this relation to obtain the effective dipole distribution from the far field pattern. This information can be presented in the form of maps which display the strength of the signal on the surface of the antenna (Fig. 1), and deformations of the antenna surface (Fig. 2). One can use this information to improve the performance of an antenna. Ideally, the surface of an antenna should be a perfect parabola. Deviations of the surface from the ideal result in a loss of power while transmitting, and a loss of sensitivity while receiving. An rms deviation of 1/16 of the transmitting (observing) wavelength results in a 50% loss in power (sensitivity). By measuring the surface of an antenna one can determine which areas need adjustment, and by how much.

The measurement of the far field is done with respect to a reference antenna. All-in-all, four experiments were done. Table 1 summarizes these experiments.

During the experiments the reference antenna tracked a celestial source. The antenna to be measured pointed at the celestial source, and at an N-by-N grid of points centered on the source. Both antennas measure and record the strength of the received signal across a broad band of frequencies. These data are subsequently manipulated to obtain the far field of the antenna. This information in turn is used to obtain maps of the antenna.

Table 1.

Date of Experiment	Measured Antenna	Reference Antenna
January 12, 1984	Mojave	Goldstone Venus
August 31, 1984	Gilmore Creek (Fairbanks)	Mojave
October 21, 1984	Mojave	Owens Valley
October 21, 1984	Owens Valley	Mojave

The resolution length R (the size of the minimum observable features) is determined by the antenna size D, the sampling factor f, and by the grid size N:

$$R = D/(N * f).$$

Here f is a number between 0 and 1 which determines how much of the final map the antenna occupies. If f = 1, the antenna just fills the map. In order to clearly define the antenna, a value of f = 0.5 was used. (See figures 1 and 2). In retrospect, this value is excessively conservative. It appears that f = 0.8 would be a good tradeoff between observing efficiency (number of points required to achieve a given image resolution) while avoiding edge effects. An 11 by 11 grid was used in the first experiment, and a 13 by 13 grid in the remaining experiments. The angular spacing Δ between the grid points is relatd to the antenna size D, the observing wavelength λ, and the sampling factor:

$$\Delta = f\ \lambda/D.$$

RECENT ACCOMPLISHMENTS

The analysis of the four experiments summarized in Table 1 is now complete and will come out shortly as a Goddard Technical Memorandum.

Preliminary analysis of the data was done at Haystack, and the results transmitted to Goddard. The far field pattern of the antenna was extracted from the data at Goddard using FRNGE, a program written by Alan Robers of Haystack. The far field pattern was then manipulated to obtain the effective dipole current distribution.

The amplitude of the current distribution is proportional to the strength of the signal on the antenna. By measuring it, one can directly examine the effects of feed and support leg shadowing, areas of low reflectivity, and the aperture illumination function. Fig. 1 shows a plot of the power distribution for the antenna at Gilmore Creek, in Fairbanks, Alaska. Generally, the power peaks in the middle of the antenna and falls off smoothly. Feed box shadowing causes a 4 db drop in the signal strength at the center of the antenna. The legs which support the feed run in the NS and EW directions, and the effects of support leg shadowing are clearly visible. Prior to this experiment, a panel in the SW quadrant of the antenna was removed. Its absence caused a 2.6 dB loss in this area.

The phase of the current distribution yields information about the reflector surface profile and the feed location. In the case of a reflector antenna, the phase of the current distribution is proportional to the distance from the antenna surface to the feed. Deviations of the phase from its expected value indicate areas of the antenna where the distance from surface to feed differs from the ideal case. Such deviations can be due to two effects: a deformed surface, or a misaligned feed.

Surface deformations due to badly formed or aligned panels show up as local deviations in the phase. Large scale surface deformations due to thermal effects or gravitational loading lead to large scale deviations in the phase. Figure 2 shows a map of the surface profile of the Gilmore Creek antenna. The antenna is smooth with a few exceptions. There are sharp gradients at 1 o'clock and at 4 o'clock. There is another sharp gradient at the 7 o'clock position. This is probably connected with the missing panel in this area. The power of the antenna could be improved by about 8% by removing the slight surface deformations.

Feed alignment errors lead to large scale deviations with characteristic signatures. Lateral feed misalignment introduces a phase gradient across the antenna: The feed is closer to one side of the antenna than the other, and hence signals reach one side before they reach the other. A radial feed alignment error causes a phase gradient from the inside of the antenna out. In this case, the feed is closer to (or further from) the inner regions of the antenna than it should be with respect to the outer regions. The characteristic effects of feed alignment errors makes it possible to detect, and compensate for them in the analysis of the phase maps. None of the antennas measured showed significant feed alignment errors.

SIGNIFICANCE

These experiments demonstrated the feasibility of using VLBI to perform microwave holography. In principle, one could use the results of these experiments to adjust the panels and the feeds of the measured antennas to improve their performance. The expected improvements in efficiency range from 5% to 28% at X-band. (The VLBI sensitivity goes as the square root of the single antenna sensitivity, so a great deal of sensitivity is not lost). At higher frequencies the improvement would be more dramatic.

FUTURE EMPHASIS

The analysis of these experiments suggests two other experiments. It would be interesting to make higher resolution maps. It would also be interesting to study the effects of gravity by making maps with the antenna pointing at a number of different directions.

The effects of individual panels are not clearly apparent in any of the maps of this report. For example, in the Gilmore Creek antenna, the resolution length is twice the length of a panel. If f were increased to 0.8 and the grid size to 16 the resolution length would be comparable to the panel size. The increased grid size presents problems with the signal to noise ratio (SNR), and with the time required to acquire the data. For the experiments in this report, the SNR of the on-source points was typically 500, while the SNR of the points at the edge of the grid was about 20. As the grid size increases, the points at the edge are increasingly far away from the beam center. Therefore, to achieve a moderate SNR of 10 one would have to sample for a longer period of time. This increases the time required to acquire data. It may no longer be possible to complete an experiment in a single apparition of a celestial source. However, the data from two or more nights could be combined to make a map with the desired resolution, but with possible contamination from thermal effects.

The second suggested experiment is in some sense the converse of the first. It would be interesting to take 'snapshots' of the antenna at several different positions to study the effects of gravity. By sampling at f = 0.8 on an 8 by 8 grid we obtain a map of the same resolution as those reported here. This can be done in under an hour. One could therefore take several maps during a single apparition of a celestial source.

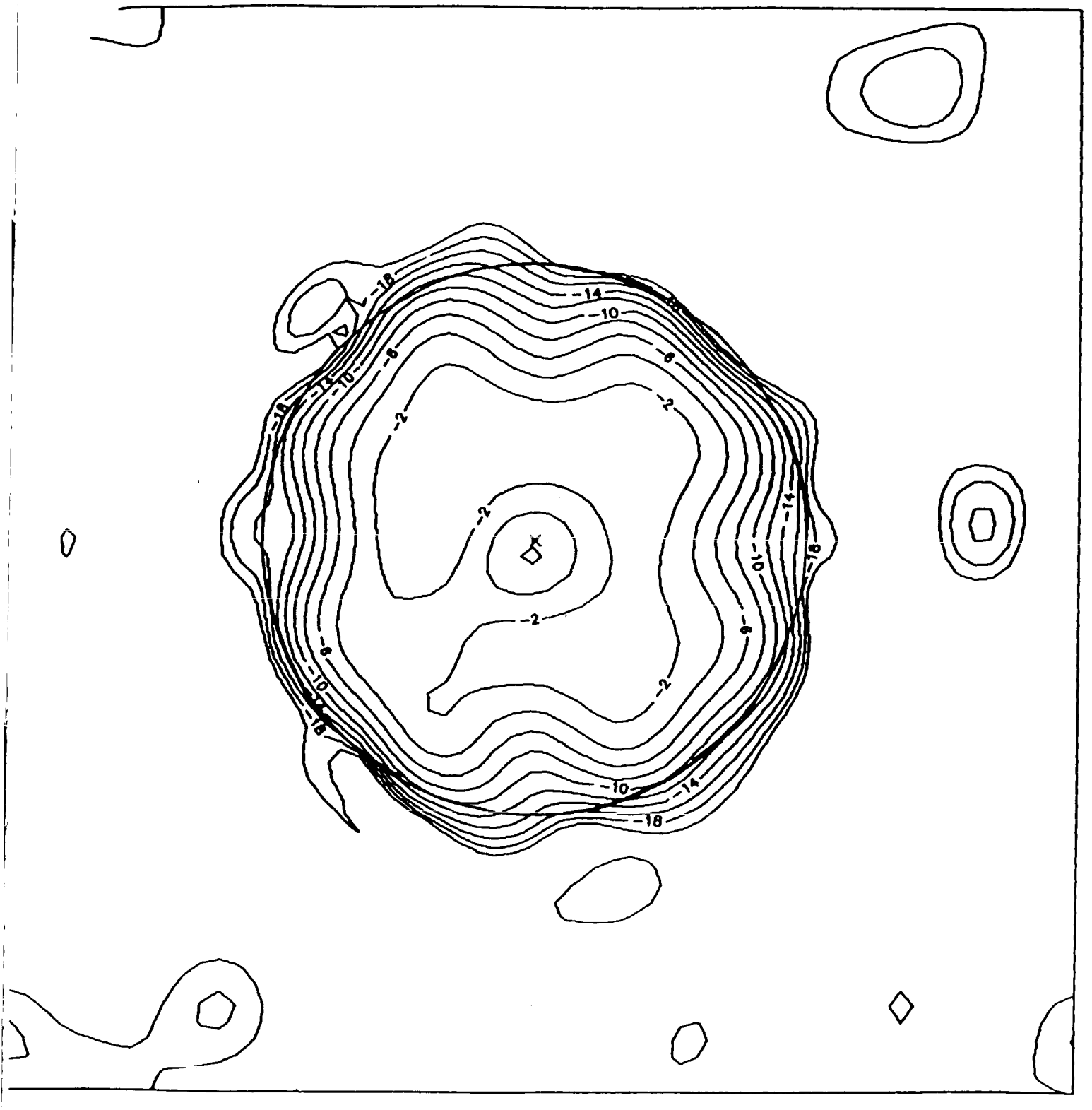

Exp 441. Gilmore Creek. Power Plot.

Figure 1. The center of the antenna is marked with an x. The physical region of the antenna is indicated by the circle. The power is in dB.

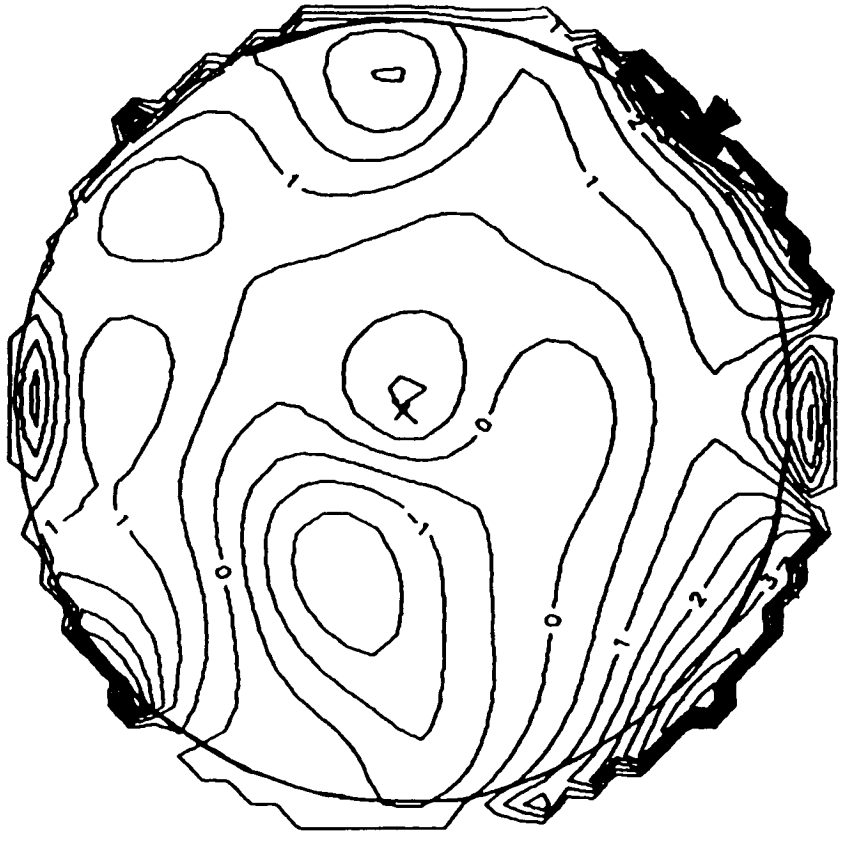

Exp 441. Gilmore Creek. Surface Plot.

Figure 2. The center of the antenna is marked with an x. The physical region of the antenna is indicated by the circle. The surface deviation is in millimeters.

USE OF PHASE DELAY OBSERVATIONS FOR GEODETIC DETERMINATIONS

Jim Ray

OBJECTIVE

Normally geodetic VLBI measurements are made using the group delay observable, the fundamental precision of which is limited by the radio bandwidth that can be synthesized (i.e., spanned using a set of relatively narrow frequency channels). This report summarizes work at GSFC to greatly improve VLBI measurement precision by using the phase delay observable in addition to the group delay.

BACKGROUND

The VLBI geodetic technique uses radio emissions from celestial sources observed simultaneously from two remote sites to determine the phase difference between the relative wavefront arrivals at the two locations. In practice, the phase determination is made relative to stable frequency standards maintained at the sites. The phase difference is a direct and very precise measure of the baseline separating the observing stations projected into the direction to the source. As this measurement can only be made modulo an integral number of wavelengths, interpretation of the observation is inherently ambiguous by an unknown number of wavelengths. If however, phase measurements are made simultaneously at several different frequencies, then the derivative of the phase with respect to frequency will be free of cycle ambiguity problems. This latter data type is known as the group delay. Currently, VLBI geodesy relies almost exclusively upon group delay measurements.

While the frequency derivative of the phase does allow the cycle ambiguity problem to be circumvented, the measurement precision degrades by the ratio of the bandwidth spanned in forming the group delay to the frequency of the band center. For the frequency sequences used by the Crustal Dynamics Project (CDP), the group delay observations are less precise than phase delays by a factor of more than 20.

Observations have been scheduled so as to dwell within each cluster for about 2 hours at a time. This approach of minimizing large angular sweeps should enhance the chance for maintaining phase connection throughout the experiment as well as allow a study of relative phase stability as a function of source-source separation angle.

The CDP experiment of March 8, 1985 produced resolvable S- and X-band phase delays. This was accomplished in a two-step process that first relied upon a very good group delay solution to determine values for the relative site positions, clock behavior, zenith tropospheric delay, and positions for some of the sources. Using the adjusted values for these parameters, resolution of the phase ambiguities was relatively straightforward. The phase delays then gave a solution having a postfit rms residual of 14 ps (4 mm). Comparison of the phase solution with the group solution from the same experiment shows agreement in baseline length within 2 mm. The formal uncertainty on the baseline length from the phase solution is 1 mm (1 sigma). There is, however, a significant difference in the orientation of the two baseline determinations. The reason for this appears to be a low-level phase calibration error in the OVRO receiver system. The problem had not been noticed in the usual group delay solutions, but became evident through close inspection of the phase delay residuals. Both the phase and group solutions from this experiment are consistent with the average result of a group of five mobile experiments also conducted during March 1985, but the formal uncertainty for the mobile experiments is substantially larger.

SIGNIFICANCE

Thus far, the high accuracy of the phase delay measurements has helped to pinpoint non-random variations in instrumental calibration systems that were not detectable using group delays. For the same reason, however, we have not yet established the level of atmospheric phase noise for intermediate length baselines. Apparently, it is low enough, at least some of the time, to permit phase connection over distances of at least 250 km. With continued improvement in instrumental stability, it appears that measurement of California baseline lengths to about the millimeter level should be feasible using phase delays.

FUTURE EMPHASIS

A current goal of this effort is to extend this technique to a three-baseline network by including the Hatcreek Observatory together with Mojave and OVRO. The longest baseline in this example is 729 km. In addition, an attempt will be made to phase

With recent improvements in the CDP receiver technology, frequency standards, calibration techniques, and a priori site and source positions, group delay solutions for many baselines of intermediate length have achieved postfit residual values (rms) of one-quarter X-band wavelength or less (i.e., about 30 ps or 1 cm). In these cases, it is reasonable to expect a group delay solution adjustment for variable parameter values (e.g., site positions, zenith troposphere delay, site clock differences) should be adequate to permit an unambiguous resolution of the phase delay ambiguities. In this bootstrapping approach, the full potential of the precise but ambiguous phase delays may be realized.

While interferometric phase observables are already used routinely for astronomical observations, those measurements are normally made possible by distributing timing signals to all stations from a central facility. The physical links required for such phase-coherent networks necessarily limit their scale to a few tens-of-kilometers, much too small for most applications of interest in the CDP. Demonstration that phase delay observations could be successfully utilized in a VLBI configuration with independent clocks was made in 1978. Results for the 1.24 km baseline between the Haystack and Westford telescopes in Massachusetts showed sub-centimeter repeatability (Rogers et al., 1978).

RECENT ACCOMPLISHMENTS AND RESULTS

Recent efforts at GSFC have attempted to extend the baseline scale over which phase delays can be utilized and to understand the phenomena which limit the application of the technique to still longer baselines. The first step in this effort was a series of experiments to measure the 12.6 km baseline between the Mojave Base Station and the DSS-13 antenna located in the DSN Goldstone complex. Consistency at the sub-centimeter level was achieved in the two horizontal components of the baseline while a roughly 2 cm result was obtained for the vertical component. The poorer quality of the latter component can be attributed to error in the tropospheric calibration, an effect largely independent of the data type used.

The next step has been to attempt to phase connect the Mojave antenna to the 130 foot dish at the Owens Valley Radio Observatory (OVRO), a separation of about 245 km. This much longer baseline represents a formidable challenge to the technique, mostly on account of the greater phase fluctuations due to more highly uncorrelated atmospheric columns over sites widely separated from one another. In an attempt to minimize problems of this type, an innovative schedule has been developed using tight clusters of sources each having internal separations of less than 20 degrees.

connect Hatcreek to a mobile station based at Quincy. While this baseline is considerably shorter than the Mojave-OVRO separation (100 km verus 245 km), the attempt is complicated by the relative insensitivity of the mobile receiving systems compared with the fixed stations. A highly precise determination of the Hatcreek-Quincy baseline is desirable in order to map baseline measurements from one site to the other for the purpose of better estimating tectonic motions between northern and southern California.

REFERENCE

Rogers, A.E.E., C.A. Knight, H.F. Hinteregger, A.R. Whitney, C.C. Counselman III, I.I. Shapiro, S.A. Gourevitch, and T.A. Clark, "Geodesy by Radio Interferometry: Determination of a 1.24-km Base Line Vector with 5-mm Repeatability," J. Geophys. Res., 83, 325-334, 1978.

GLOBL: GLOBAL LEAST-SQUARES SOLUTION SOFTWARE FOR VLBI DATA

Edwin Himwich

OBJECTIVE

Since 1978, the VLBI Data Analysis Team of the Geodynamics Branch has had a continuing task to develop a software system that could be used to analyze the ensemble of geodetic VLBI data to recover estimates of geophysically and astrometrically interesting quantities in an efficient and flexible manner. From the standpoint of the Crustal Dynamics Poject the most important quantities to be extracted are the baseline lengths, that is, the distances between pairs of VLBI stations.

BACKGROUND

The program used for the operational analysis of single VLBI experiments, SOLVE, was written in 1976. A single experiment consists of about 24 hours of data. In order to get good estimates of station positions, SOLVE allows data analysts to study the behavior of the clocks and atmosphere during the experiment.

To analyze data from two or more experiments, a new program, SOLV2 was written in 1981. SOLV2 proved to be very reliable and is extremely useful for comparison with SOLVE for the purpose of verification. The program provided tremendous flexibility in its operation, but at the cost of being extremely cumbersome. It eventually became clear that in order to meet the analysis needs of the project, a new program would have to be developed.

RECENT ACCOMPLISHMENTS AND RESULTS

The program GLOBL has been written to make least squares parameter estimates from several VLBI experiments. It uses the best features of SOLV2 and other programs based on SOLVE to provide a much more efficient and much less cumbersome package than SOLV2. It runs much faster than SOLV2 and requires much less setup.

Figures 1 and 2 show the results from a single GLOBL run to estimate nutation errors. Figure 1 shows daily offset of nutation in longitude; figure 2 shows offset in obliquity. The data used for this solution includes 167 experiments, all of the IRIS and CDP data for 1984 and most of 1985. The most interesting feature of

this data is the apparent annual trend. There are hints of other effects in the data. In particular, there appears to be some small scale structure with a period of about 14 days. A slope appears to be present in the longitude data as well. More analysis will be necessary before precise estimates of these effects can be made.

Some of the more important features of GLOBL are:

A. Saving the Data in a High-Speed Access form (Superfiles)

VLBI data is normally stored in what is known as database form. The database system provides a high level of accountability for the steps taken in processing the data. This self-documenting storage form has a relative low access rate. In GLOBL, advantage is taken of the fact that data is not included in a global solution until its processing has reached a stable point. GLOBL never modifies the data, so the need to update the permanent documentation is avoided. This allows the data to be stored in a higher speed access form, known as Superfile form.

B. Arc-Parameter Elimination

GLOBL, like SOLV2 before it, takes advantage of the large scale structure of the normal equations. A global solution of about half the Mark III data set would use data from about 200 single day experiments. The direct solution of the normal equations for this case would require the inversion of an approximately 10,000 by 10,000 element matrix. Arc-parameter elimination notes that most of this matrix is zero and reduces the matrix inversions to one 120-by-120 and 400 50-by-50 matrices. The time required for matrix inversion goes up roughly as the cube of n for an n-by-n matrix, all other things, such as everything being able to fit in core, being equal. Thus arc-parameter elimination reduces the time spent in matrix inversion processes by a factor of almost 20,000. Without arc-parameter elimination, 2 years would be required for just matrix inversions.

C. Statistics

In order to understand the effect of solving for different parameters or of treating parameters differently, it is useful to have statistics available from the solution. The scaled formal error for each parameter and also residuals by baseline and source are provided. The residual statistics are calculated individually for each experiment as well as for the overall solution.

D. Command File

GLOBL solutions are controlled by a command file. The command file contains all the information that is required to run a solution. This is a fairly small amount of information. In addition to about

two dozen control parameters, the name of each experiment to be processed must be provided. This compares to SOLV2 which required almost two dozen control parameters to be specified for each experiment and required a program to prompt for the values of the parameters. The simplification in GLOBL which reduces the setup burden is to break parameters that can be solved for into different classes. GLOBL than provides control over how each class will be treated. There is a tremendous loss in terms of absolute control of the solution. However, in practice most of that control is not needed. The resulting savings in setup time allows more time to be spent on more important activities, such as interpretation.

E. Archiving of Results

GLOBL makes use of SOLVE's solution archiving system. This allows the results of solutions to be saved for use with the automatic report generator. The report generator will make tables documenting the time evolution of baseline lengths and earth orientation parameters. This will be expanded to include tables of other parameters that can be estimated by GLOBL.

FUTURE EMPHASIS

The goals for the immediate future are to expand the types of parameters that can be solved for and to improve the running speed of the program. The parameters to be solved for can be easily increased to include the coefficients of the nutation and solid-earth tide models. This will allow direct solution for adjustments to both models. A decrease in running time of approximately 33% is anticipated with a straight-forward streamlining of the matrix operations.

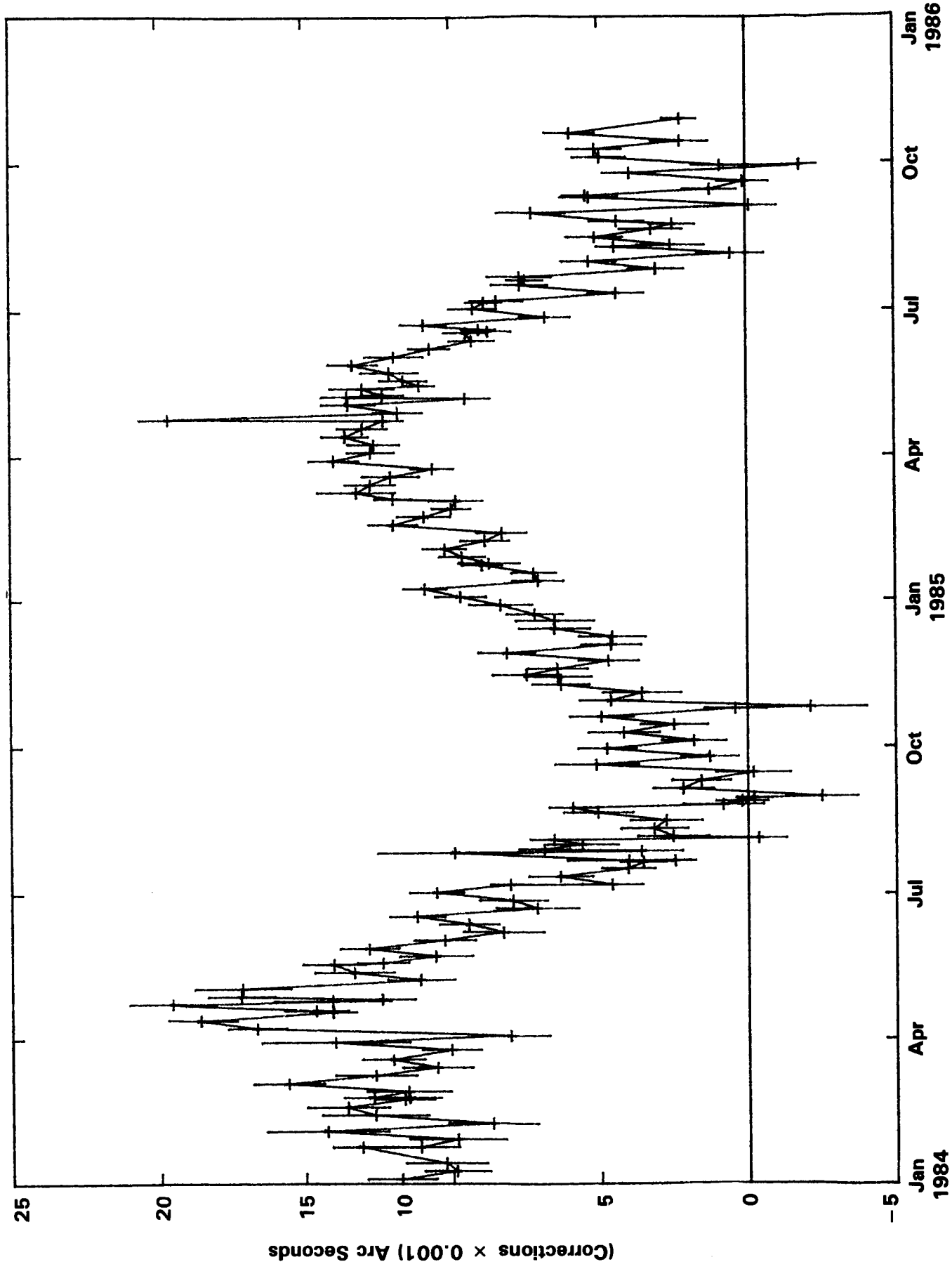

Figure 1. Corrections to Nutation in Longitude from Mark III VLBI Data vs Date

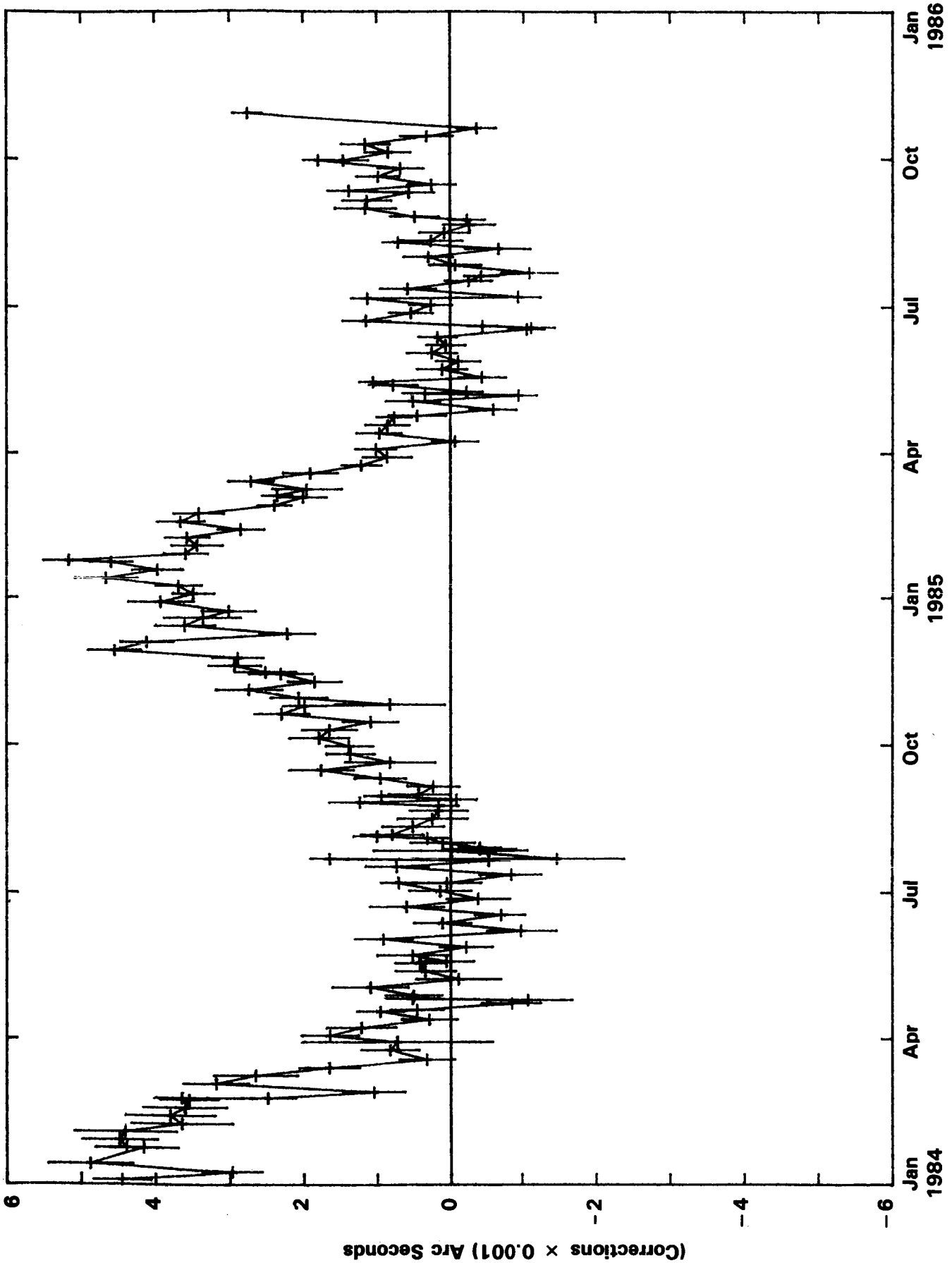

Figure 2. Corrections to Nutation in Obliquity from Mark III VLBI Data vs Date

CREATION OF A GLOBAL GEODETIC NETWORK USING MARK III VLBI

Chopo Ma

OBJECTIVE

For many geodynamic studies it is necessary to have a well-defined, well-controlled terrestrial reference frame of known precision. VLBI is a means for providing such a reference frame.

BACKGROUND

The Mark III VLBI system was developed by NASA to support research in geodynamics and has been used in high precision geodesy since 1979 (Clark, 1979; Rogers et al., 1984; Carter et al., 1985; Clark et al., 1985). By the end of 1984 Mark III data had been acquired from 15 stations which are either dedicated to or available for geodetic measurements. These are listed in table 1. The Haystack Observatory is the site of two stations, the 37-m Haystack antenna and the 18-m Westford antenna. Only Harvard, Haystack, Onsala, Owens Valley and Westford were used before 1983. In addition, five other stations have contributed data on an occasional or one-time basis: Chilbolton, England; Effelsberg, FRG; Maryland Point, Maryland; National Radio Astronomy Observatory, Western Virginia; and Robledo, Spain. Five stations regularly participate in IRIS measurements (Harvard, Richmond, Westford and Wettzell every 5 days; Onsala monthly). Except for Richmond, these stations also participate with the others in observing sessions of the Crustal Dynamics Project.

The status of the stations varies. Kashima, Onsala and Wettzell have permanent VLBI staff and Mark III equipment and are supported by national research agencies. Harvard, Haystack, Mojave, Richmond and Westford likewise have full-time staff and Mark III systems and are funded largely or entirely by NASA and NGS. At Algonquin, Gilmore Creek, Hat Creek, Kauai, Kwajalein, Owens Valley and Vandenberg, Mark III equipment and personnel are made available when required by the Crustal Dynamics Project observing program. Gilmore Creek and Vandenberg are operated solely for the Project while the remainder primarily support other unrelated activites.

The 15 stations form a network whose relative positions are entirely determined by Mark III VLBI data. Since VLBI has no direct tie to the center-of-mass or to the spin axis, the origin and orientation of the network must be defined. The origin is defined by the

adopted Cartesian coordinates of the intersection of axes of the Haystack 37-m antenna. The orientation is defined by the subnetwork in use on October 17, 1980 (Chilbolton, Harvard, Haystack, Onsala and Owens Valley) and the a priori earth orientation parameters used to calculate the theoretical VLBI delays and rates for this observing session. These a priori values were quadratically interpolated from the BIH Circular D to each observation epoch, and the UT1 values were additionally modified to restore the short-period tidal variations. Any errors in Circular D for this period will be directly propagated into the solution and into the overall orientation of the network. The relative orientations of the baselines are not affected by errors in Circular D and would not be altered by a change in the reference day. Likewise, the baselines are not affected by a change in origin.

To add new stations properly to the original network, it is necessary to observe simultaneously with at least four stations of which at least three must be in the original network. From the three or more old stations the complete earth orientation parameters can be estimated simultaneously with the coordinates of the new station(s) in the system of the original network. Thus, for example, Westford was added using the network of Harvard, Haystack, Onsala, Owens Valley and Westford from June 20, 1982. It is desirable to link as many stations as possible through direct simultaneous observations, but practical considerations limit current networks to seven stations. In addition, the requirement of mutual visibility of sources constrains the size of networks. Some of the networks used in 1984 were designated Polar (Haystack, Mojave, Gilmore Creek, Kashima, Wettzell), East Pacific (Mojave, Vandenberg, Gilmore Creek, Kauai, Kwajalein), West Pacific (Mojave, Gilmore Creek, Kauai, Kwajalein, Kashima), and North American Plate Stability (Westford, Algonquin, Harvard, Gilmore Creek). The first three networks were observed twice in 1984, each session lasting 30-56 hours, and all will be repeated regularly for the duration of the Crustal Dynamics Project.

RECENT ACCOMPLISHMENTS AND RESULTS

Data from 16 stations acquired during 1980-84 by the Crustal Dynamics Project and POLARIS/IRIS were combined in a single, sequentially incremented least squares adjustment including 46070 observations, each observation comprising a delay and a delay rate. Most individual data sets spanned 1 day. All data had ionospheric and tropospheric calibration. There were 132 global parameters estimated: all station positions except Haystack and all 44 source positions except the right ascension of 3C273B, whose adopted value defines the right ascension origin. There were 2499 arc parameters including earth orientation parameters from each session except the

reference day, polynomials and sinusoids to model station clock behavior, and zenith tropospheric delays. The models used generally followed the MERIT standards except for the absence of the K1 solid earth tide correction and ocean loading. Details of the data set and the solution are given in Ryan and Ma (1985). The overall fit of the solution was 120 ps in delay and 0.09 ps/s in delay rate.

The distribution of observations by station is given in table 2. The total is twice the number of observations since each observation counts toward two stations. The observations from the POLARIS stations are most numerous, but even the limited use of Algonquin ties it to the network with 416 observations. The theoreticals do not include any a priori station drift because of tectonic plate motion, but the baselines for which data are available over the entire time span are not changing more than 2 cm/yr. The data from the Pacific stations come only from 1984.

SIGNIFICANCE

The adjusted source and station positions can be found in Ryan and Ma (1985). The positions of the 15 permanent VLBI stations are determined with 1-sigma formal statistical errors of less than 5 cm except for three stations in the Pacific. Based on internal and external tests of consistence, the true uncertainties are probably larger by a factor of 2. While the origins of the celestial and terrestrial coordinate systems are specified separately, the source and station positions are not independent. In particular, there is a correlation between the scale of baseline lengths and the declination of the sources. Except for some of the 1984 data from the Pacific, the polar component of baselines is generally much less than the component projected on the equatorial plane. The determination of source declinations, especially for sources near the equator, is correspondingly weak.

FUTURE EMPHASIS

The Crustal Dynamics Project acquires VLBI data from the global network on a regular basis. The quality of the data from more recent years indicates that the network could be tied together at the centimeter level. There are, however, improvements in the application of such models as global plate motions and nutation and in the calibration of the troposphere which must be made before this level of accuracy can be achieved.

REFERENCES

Carter, W.E., D.S. Robertson, J.R. MacKay, (1985), "Geodetic Radio Interferometric Surveying: Applications and Results," J. Geophys. Res., Vol. 90, No. B6, 4577-4587.

Clark, T.A. (1979), "Mark III System Overview," Radio Interferometry Techniques for Geodesy, 285-290, NASA Conf. Pub. 2115, Washington.

Clark, T.A. et al. (1985), "Precision Geodesy Using the Mark-III Very-Long-Baseline Interferometer System," IEEE Trans. on Geoscience and Remote Sensing, Vol. GE-23, No. 4, 438-449.

Rogers, A.E.E. et al. (1983), "Very-Long-Baseline Radio Interferometry: The Mark III System for Geodesy, Astrometry and Aperture Synthesis," Science, Vol. 219, 51-54.

Ryan, J.W. and C. Ma, (1985), "Crustal Dynamics Project Data Analysis: Fixed Station VLBI Geodetic Results," NASA TM 86229, Washington.

Table 1. Global VLBI Network Stations

Algonquin Radio Observatory, Ontario
Gilmore Creek, Alaska
Hat Creek Radio Observatory, California
Harvard Radio Astronomy Station, Texas
Haystack Observatory, Massachusetts
Kashima Space Research Center, Japan
Kokee Park STDN (Kauai), Hawaii
Kwajalein, Marshall Islands
Mojave, California
Onsala Space Observatory, Sweden
Owens Valley Radio Observatory, California
Richmond USNO Timing Station, Florida
Vandenberg, California
Satelitenbeobachtungstation Wettzell, FRG

Table 2. Distribution of Observations by Station

Station	Number of Observations
Algonquin	416
Chilbolton	1973
Gilmore Creek	3276
Hat Creek	708
Harvard	27745
Haystack	5975
Kashima	1819
Kauai	2110
Kwajalein	1185
Mojave	5686
Onsala	5956
Owens Valley	4507
Richmond	1743
Vandenberg	795
Westford	25560
Wettzell	2686

COLLOCATION RESULTS FOR THE NASA AND FRG LASER SYSTEMS

Ronald Kolenkiewicz

OBJECTIVE

An objective of the NASA Crustal Dynamics Project is to obtain Satellite Laser Ranging (SLR) data from the Laser Geodynamics Satellite (LAGEOS). In order to achieve this goal new laser systems must be developed and compared to each other. This process of comparison is called collocation. The standard of measure for the NASA lasers is currently MOBLAS-7, located at the Goddard Space Flight Center in Greenbelt, Maryland. During the summer of 1985 the newly developed laser system, MTLRS-1, owned by the Federal Republic of Germany (FRG), arrived in the USA to perform a collocation with MOBLAS-7. The purpose was to assess the performance and precision of this new laser and to transfer the laser measuring standard to Europe.

BACKGROUND

In April 1985 the German satellite laser ranging system, MTLRS-1, was shipped to the NASA Goddard Space Flight Center in Greenbelt, MD. Here this system was tested by collocating the NASA mobile laser ranging system, MOBLAS-7. The object of a satellite laser ranging system collocation is to place two systems side-by-side, at a known orientation to each other, for the purpose of tracking the same target satellite and to compare the range data obtained. The two systems were precisely surveyed at a distance of 42.37 meters from each other. For the purpose of this experiment the MOBLAS-7 laser was to be considered the standard by which the MTLRS-1 could be evaluated. Satellites to be tracked in order of their priority were LAGEOS, Starlette, and BE-3. The analysis presented here is for the LAGEOS satellite only. This satellite was selected since it is at an altitude which permits laser tracking data to be obtained for a continuous time period as long as 50 minutes, whereas the other lower satellites can only be tracked for a maximum of 15 minutes. In addition, LAGEOS is going to be the prime target of MTLRS-1 when this system participates in the Mediterranean Campaign, conducted by the Working Group of European Geoscientists for the Establishment of Networks for European Research (WEGENER), beginning in 1986.

RECENT ACCOMPLISHMENTS

During the period from May through July 1985, LAGEOS passes were tracked simultaneously at GORF by MOBLAS-7 and MTLRS-1. Using data from these passes as a starting point, a collocation analysis was conducted for the two systems.

The collocation analysis technique uses the precision orbit determination computer program, GEODYN, to obtain a one pass (50 minute maximum) LAGEOS orbit by using the full rate laser ranging data obtained solely by MOBLAS-7. The full rate data obtained during the same pass by MTLRS-1 is superimposed on the orbit, but in no way does it influence the MOBLAS-7 determined orbit. Range residuals to the orbit are thus obtained. Beginning at the first even minute before ranging data for the pass is obtained, 2 minute time intervals are chosen for the entire length of the pass. The mean of the range residuals and their standard deviations are calculated for MOBLAS-7 and MTLRS-1 during each of these 2 minute periods, and their value is considered to be at the time of the midpoint of the interval (the odd minute). In this manner corresponding 2-minute mean residuals from each system can be subtracted, where they exist, and the systematic trends between them may be evaluated.

The first LAGEOS collocation pass candidate was taken on May 10, 1985 at 0600 GMT by MOBLAS-7 and MTLRS-1 and the collocation concluded on July 16, 1985. During this time period 32 LAGEOS passes were tracked simultaneously by both systems. Of these, 13 were selected as having sufficient data to be adequate for a collocation analysis. The selection criteria used to identify these passes follows:

1. Each pass was to have at least five consecutive 2-minute mean points, simultaneously obtained from MOBLAS-7 and MTLRS-1.

2. A valid 2-minute mean point could only be formed if there were at least 300 points from MOBLAS-7 and at least 30 points from MTLRS-1 during the 2-minute period.

This selection criteria resulted in the further consideration of the 13 passes given in Table 1. None of the passes listed in this table were taken during the daylight hours, a condition that is always listed as a requirement for a successful collocation test. All of the passes are on the descending portion of the retrograde LAGEOS orbit, thus passing from northeast to southwest. It is always desirable to track ascending satellite orbits as well during a collocation of systems in order to aid in the determination of any azimuth or orientation related systematic errors that may exist.

Figure 1 shows LAGEOS collocation data for a typical pass taken on June 26, 1985 at 0400 hours GMT. The range residuals are plotted as a function of elapsed time from the beginning of the pass for both the MOBLAS-7 and MTLRS-1 laser systems. These points represent the mean value of the full rate data obtained during a 2-minute period, and the associated one sigma error bars are indicated on each of the 2-minute means. Points which occupy the same 2-minute period are differenced (MOBLAS-7 minus MTLRS-1) and plotted as a function of the elapsed time. The 2-minute overlap geometry, in this example, is designated as 8,3*,7. This implies that eight consecutive 2-minute differences were obtained, followed by three consecutive 2-minute gaps, ending with seven consecutive 2-minute differences. Hence a total of 15 minutes of overlap data was taken during the pass. The weighted mean difference of these points was -1.82 ± 0.11 cm This implies that the MTLRS-1 was measuring short with respect to the MOBLAS-7 laser during the pass. A total of 13 LAGEOS passes was analyzed in a similar manner.

SIGNIFICANCE

Results for the 13 LAGEOS collocation passes analyzed are given in Table 1. In 12 of the passes the MTLRS-1 laser was found to measure short relative to the MOBLAS-7 laser. The weighted mean of the entire data set implies MTLRS-1 is short by 1.94 cm. In addition to this sytematic bias MTLRS-1 data exhibited systematic jumps of as much as 2 centimeters in its range residuals between adjacent 2-minute mean points. Analysis for the possible causes of these systematics is continuing.

FUTURE EMPHASIS

The accuracy of the laser systems being developed continues to improve. New technological developments, such as the Micro Channel Plate (MCP) will be added to the MOBLAS-7 laser system to improve its precision. Preliminary results indicate the rms will improve from 2 1/2 centimeters to 1 centimeter. Several collocations between laser systems are planned for next year.

REFERENCES

Kolenkiewicz, R., V.S. Husson, P.J. Dunn, C.F. Martin, S. Poulose, and M. Abresch, "Recent LAGEOS Satellite Laser Ranging Collocation Analysis," EOS Trans. AGU, Vol. 66, No. 46, November 12, 1985.

Kolenkiewicz, R., "The MTLRS-1 and MOBLAS-7 Collocation," Crustal Dynamics Principal Investigators Meeting, JPL, March 26, 1986.

Table 1. MTLRS-1 Minus MOBLAS-7 Mean Difference

DATE IN 1985	TIME, GMT	TWO MINUTE OVERLAP GEOMETRY*	WEIGHTED MEAN DIFFERENCE, CM
5/10	0934	7	-1.97 ± 0.21
5/15	0612	12	1.46 ± 0.14
5/20	0628	12	-2.00 ± 0.12
5/21	0838	3,1*,6,1*,1	-0.33 ± 0.15
5/30	0704	6,2*,6	-1.15 ± 0.10
6/03	0848	11	-1.52 ± 0.14
6/14	0738	2,1*,10	-2.85 ± 0.11
6/17	0704	2,1*,16	-3.80 ± 0.11
6/26	0520	1,1*,6,6*,3	-3.77 ± 0.18
6/27	0400	8,3*,7	-1.82 ± 0.11
6/27	0732	18	-3.25 ± 0.11
7/04	0838	5	-1.12 ± 0.30
7/14	0530	3,1*,3,2*,5	-0.29 ± 0.21

WEIGHTED MEAN = -1.94 ± 0.04

*NO OVERLAP

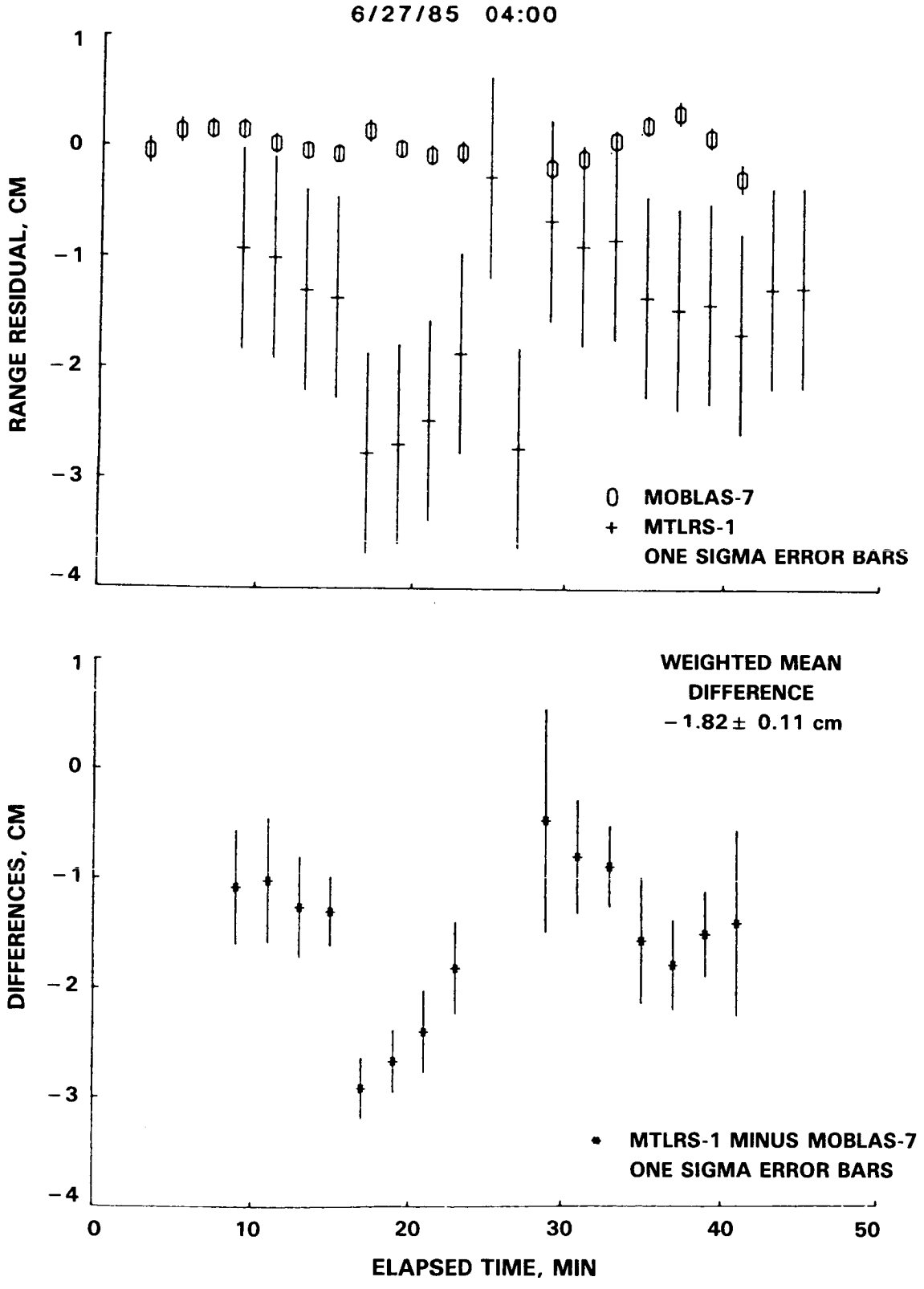

Figure 1. LAGEOS Collocation Data

GEODYN SYSTEMS DEVELOPMENT

Barbara H. Putney

Theodore L. Felsentreger

OBJECTIVES

The purpose of the GEODYN Orbit Determination and Parameter Estimation, the SOLVE, and the ERODYN computer software is to recover and analyze the recovery of geodetic and geophysical parameters from satellite and other data in a state-of-the-art manner and in the most operationally efficient manner.

BACKGROUND

In 1971 the NONAME and GEOSTAR programs were combined to create the GEODYN program. The SOLVE program was created at the same time. A few years later the ERODYN, error analysis program was written. The philosophy of the development of the software system has been maintenance of computer-efficient, well-structured software, with appropriate orbit, earth and numerical models, using precise satellite measurement modeling and efficient numerical models, and performing careful benchmark procedures. This care has paid off in the production of several GEM's (Goddard Earth Models), precision station locations, improved tidal, GM, polar motion and earth rotation values, consistent baselines, and encouraging GRM simulations. Careful usage analysis, and modeling using laser, Doppler, altimeter and other satellite data from LAGEOS, SEASAT, STARLETTE, GEOS and BE-C satellites as well as many others has made these accomplishments possible.

RECENT ACCOMPLISHMENTS AND SIGNIFICANCE

A. Current Software Usage and Development

Continued solutions for gravity field, tides, pole positions, earth rotation, GM, and baselines, and collocation studies has been made as part of the Crustal Dynamics Project. This has been a transition year for the research teams from the GEODYN I to the GEODYN II program.

Using the GSFC TOPEX Gravity Model effort as the goal, the GEODYN II program received its final shakedown, and differences between GEODYN I and GEODYN II were reconciled. Careful comparisons between preprocessing corrections for optical, laser and Doppler satellite data were made. Algorithms such as the expanded tidal model and old TOLS option (using only part of the geopotential in the computation of the variational equations) were modified and incorporated to shorten the required computer time for the GEODYN II program. Detailed timing comparisons were made between GEODYN I and GEODYN II on the Cyber 205 and on the IBM 3081 and Amdahl V7 computers. All-in-all, the software performed to expected timing goals and for normal equation generation far better than anticipated, but showed there is still room for further timing optimization. This is especially true in the IBM version of GEODYN II.

The SOLVE program, which was vectorized a few years ago, continued to perform flexibly to produce the required solutions effectively. The new GEODYN II E-matrix format was incorporated into the software. Optimizing the I/O (input/output) in the system is the logical next step for SOLVE, since on large inversions the I/O takes twice as much time as the CPU time. A technique for doing concurrent I/O has been employed with some success. Master/slave station constraints and a station network constraints are now SOLVE options. Some automatic documentation software have been developed for "flowcharting" the program and cross referencing the subroutines and common blocks. A continued effort to make the program more user-friendly has motivated a change to the program input now allowing ranges of parameters to be suppressed and adjusted, and in the JCL (Job Control Language) section by having the software determine the required size of files and allocating the space from within the program.

The ERODYN program, which was recently converted to the Cyber 205, has been modified to use the GEODYN II E-matrix format. The matrix multiplication and inversion algorithms have been vectorized and the I/O has been modified for the Cyber. Orbit error propagation has been implemented and tested. The software has been updated to include the acceleration parameters now available in GEODYN.

In addition, there were several specialized capabilities requested by users which were incorporated into the ERODYN program. For example, the capability of computing the rms effects of unadjusted parameters and the total rms effects over a whole arc were implemented.

B. GEODYN II Development (Vector GEODYN)

GEODYN II has been designed to run in two parts, GEODYN IIS (starting) and GEODYN IIE (ending). This was done so that the initialization stage of the program, which is sequential in nature, would not waste precious Cyber 205 computer time. Currently, GEODYN IIS runs only on an IBM compatible front end to the Cyber 205. The output of IIS is two files, an interface file and an observation file. The GEODYN IIE program can run on either the IBM compatible computer or the Cyber 205 Vector Processor.

The new software has been designed to process a pass of satellite observations at a time instead of the one observation at a time. This design has produced the vectors that are needed for efficient utilization of the Cyber 205. This required orbit information be stored for the entire pass of data, which implied a rewrite of the software.

Currently, the program can process laser, optical, and Doppler data and all related observation models, which includes biases and center-of-mass offsets and required preprocessing corrections. Still missing are the ocean-loading, and albedo models. Plate motion and GEOPOL (movement of the earth's crust through polar motion in the gravity computation) have been incorporated. The DE 200 JPL Planetary Ephemeris using the Wahr nutation series is now usable by the software.

C. GEODYN II Timings and Their Significance

Figure 1 shows several satellites and the ratio between GEODYN I and GEODYN II Cyber 205 computer charges which is essentially CPU time. The runtime ratios vary from 2.5 to 4.2. This is a good beginning but it is anticipated the ratios could be made significantly higher with efficiency analysis leading to further optimization. The expanded tidal model, not represented in this figure, has been optimized already showing significant improvement.

Figure 2 presents STARLETTE E-MATRIX TIMINGS for various numbers of adjusted parameters and stepsizes. The effect of misuse of computer memory is demonstrated with the first two entries in the figure. By simply adding 12 more large pages (LP is 65000+ words) of memory the STU (System Time Unit-like seconds) drops from 437 to 95. These runs were made with a 2 million words of memory which is in the process of being upgraded to 4 million words. The Cyber is amazingly fast as is shown by the largest of these runs only using 382 STU's. This will allow us to pursue large modeling efforts that were impossible in the past.

Figure 3 graphically demonstrates the relationship between the number of adjusted parameters, STU's required, size of the geopotential, and the effect of tide adjustment on two satellite arcs, GEOS-1 and STARLETTE. The size of the STU's makes it reasonable to do the largest solutions for these satellites. The flatness of the curve is due to vectorization and memory size.

FUTURE EMPHASIS

The final shakedown of GEODYN II has occurred this year for laser, optical and Doppler data. At this point the altimeter model and satellite-to-satellite model are partially implemented. Both will be completed. Generation of normal points will be added directly to the GEODYN program. It is also hoped that some data simulation capability will at least be initiated. Adding models, such as ocean loading, that bring the GEODYN II program up to the capabilities of the GEOYDN I program is another important goal. Continued emphasis on program efficiency and optimization will mold this software into a more useful tool.

The SOLVE program will continue to evolve to maintain capability with the GEODYN program. Further optimization in the arc elimination area has become a necessity with the large number of arc parameters now being used (combining several arcs maintaining the arc parameters). It is still a goal to create a master source file containing both IBM and Cyber programs. This is a time consuming task and is making some progress, but usually gets interrupted for more pressing program modifications.

The ERODYN program will continue to be evolved towards vectorization and compatibility with the new GEODYN. Making the input and output easier to understand for the user, is another goal.

Effort will continue to make the Crustal Dynamics analyses, MARS simulation, and TOPEX gravity model determination as successful as possible. Software will be modified, optimized and created as is required to accomplish these objectives.

Timing Comparison: GEODYN I vs. GEODYN II TVM 09/10/85

SATELLITE	DATA USED	RUN TYPE	CYBER STU's GDYN I	CYBER STU's GYDN II	STU RATIO GDYN I/II
ANNA-1B	OPTICAL	DATA RED	379	130	2.9
TELSTAR	OPTICAL	DATA RED	369	134	2.7
GEOS-1	OPTICAL	DATA RED	487	134	3.6*
GEOS-2	OPTICAL	DATA RED	401	141	2.8
GEOS-1	LASER	DATA RED	257	102	2.5
GEOS-3	LASER	DATA RED	448	170	2.6
LAGEOS	LASER	EMAT	345	105	3.3
STARLETTE	LASER	DATA RED	160/333	66	2.9/6.5**
SEASAT	LAS/USB/DOP	DATA RED	950	229	4.1
OSCAR 14	DOPPLER	DATA RED	328	100	3.3

NOTES: CYBER STU's do not include GEODYN-IIS execution time on Amdahl.

*The GEOS-1 optical run required 5 iterations in GEODYN-I and 4 iterations in GEODYN II.

**The Starlette test case has also been run on the IBM 3081. This was done to give users an idea of how GEODYN-II on the Cyber compares with their previous experience on the IBM 360/95. The results of this timing comparison (GEODYN-I CPU seconds on the 3081 vs. GEODYN-IIE STU's for the GIIE step only, are as follows: GDYN-I (TOLS = 36. Drag On) vs. GDYN-II (TOLS = 48, Drag On) 6.65:1

TVM 09/10/85

Figure 1. Timing comparison: GEODYN I vs. GEODYN II

10/31/85

STARLETTE E-MATRIX TIMINGS

(5 DAYS, 596 OBS 21 STATION COORD, K2, K3, K2
PHASE, H2, L2, ORBIT, SOLRAD, AND DRAG ADJUSTED)
(CYBER 205 HAS 2M WORDS OF MEMORY)

NPARM ADJ	GEOP	STEP SIZE SEC	TIDES MODELED	TIDES ADJ	LP	CPU SEC	STU SEC
1400	36 × 36	45	0	0	15	57	437
1400	36 × 36	45	0	0	27	55	95
1400	36 × 36	45	600	0	27	69	109
1988	36 × 36	45	600	600	27	91	173
1880	42 × 42	38	0	0	27	76	144
1880	42 × 42	38	600	0	27	92	154
2476	42 × 42	38	600	600	27	111	248
2632	50 × 50	30	0	0	27	118	255
2632	50 × 50	30	600	0	27	138	271
3228	50 × 50	30	600	600	27	163	382

Figure 2. Starlette E-Matrix timings

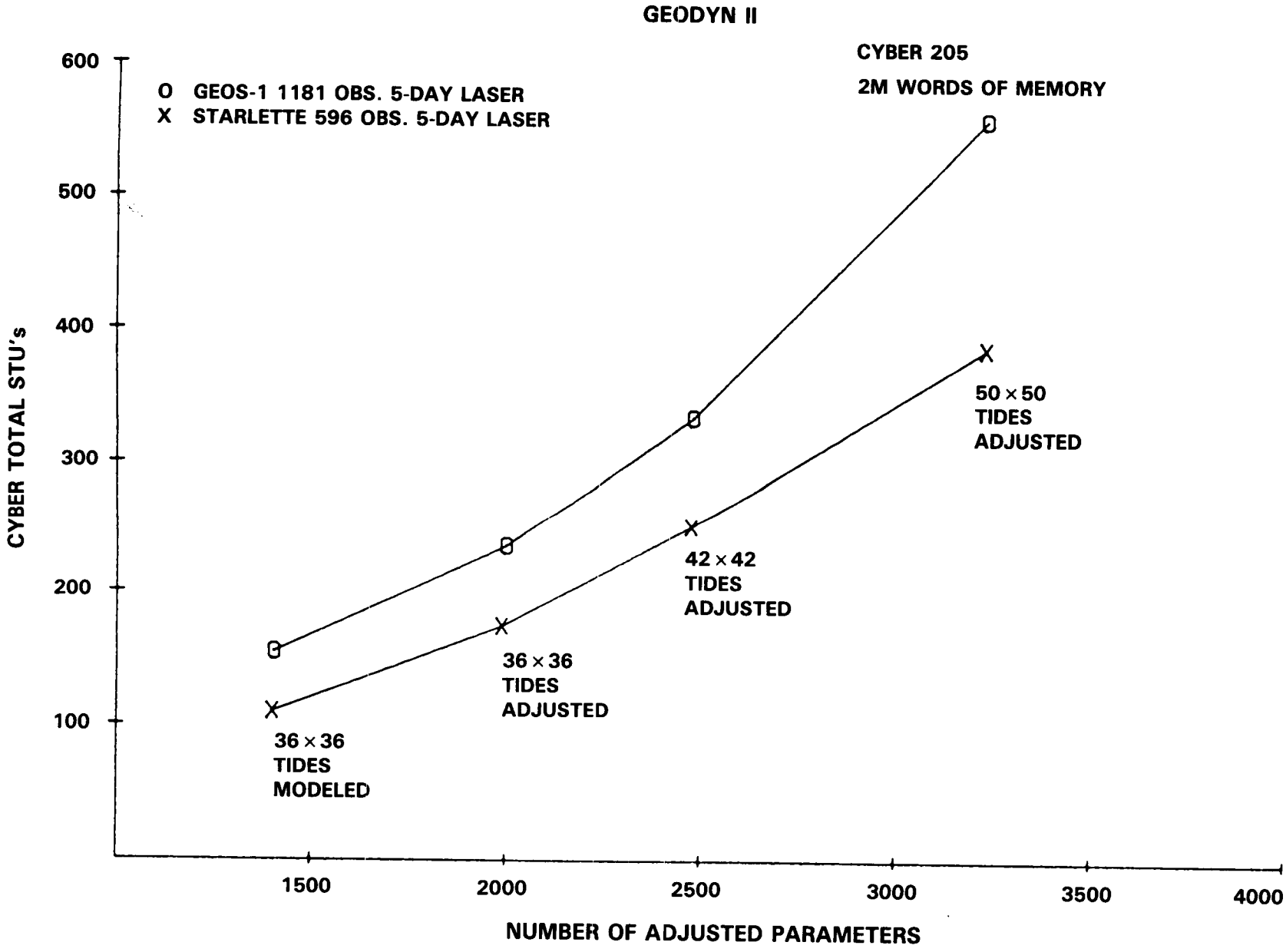

Figure 3. Relationship Between Cyber Total STU's vs. Number of Adjusted Parameters

THE APPLICATION OF COMPUTER IMAGING TECHNIQUES TO OCEAN TOPOGRAPHY AND GEOPHYSICAL DATA

Carole Nethery

OBJECTIVE

Understanding of scientific data may be improved by converting it into an image that may be studied visually. The scientist can identify features, patterns and common elements that would otherwise go unnoticed. The analysis may be done interactively or by viewing photographic copies of the image. Photographs of images provide a means for the scientist to communicate findings to others in his/her professional community. The purpose of this particular set of image analysis programs is to extend the knowledge of the geophysical properties of the oceans. This aim assumes the use of the advanced techniques available at the Goddard Space Flight Center. Mindful of the merits of software sharing and the importance of developing interdisciplinary software, it is also assumed that programs will be designed with generality so that they may be used for a variety of applications.

BACKGROUND

In 1982, several programs were written to convert SEASAT altimeter data describing the ocean surface to images. The software design objectives were: efficient computer use, ease of modification and program generality. After several changes in hardware and user personnel, isolation of hardware-dependent code and facility of user input were given equal consideration. The latter was carried out in part by modifying programs to operate under TAE, (Transportable Applications Executive). Interfaces to the TAE catalog manager were written to simplify user-file interaction.

The programs written handled tape-to-disk transfer, image mapping that allows screening of areas and data ranges, image display, pseudo-coloring of images, calculation of image statistics to aid coloring, and simulation of the illumination of an image by a rotating light source. Procedures were developed for photographing images for publicaiton. The resulting images provided information for publicaitons on mean sea surface and mesoscale ocean surface variability studies.

RECENT ACCOMPLISHMENTS

Mean sea surface data, bathymetry data and gravity field models computed from satellite altimetry have been processed to form photographic images. An example of illuminated topography based on bathymetry data is shown in Figure 1. This image was based upon the 5' x 5' grid of data provided by Washington University in St. Louis. The image will be prepared in poster form as a companion to the mean sea surface maps.

Software has attained production status on the LTP Vax. The versions of the programs installed have improved running times, are easier to use and have produced more consistent photographic generation than in the past. The image terminal interface isolates hardware dependent code. A reasonably efficient procedure for image restoration has been established. Programs have been written to merge files and subset large global files. The tape-to-disk program to read data runs more efficiently. Efforts have been made to make the software easier to use by other applications.

Color enhancement has been improved, particularly for photographic output. The photographic software colors data for the Optronics hardware. Since the eye can see literally millions of colors, color enhancement is complicated and the possible results powerful. The CIE (International Commission of Illumination) System, will be tried as a base. This system describes colors mathemtically and is founded on measurements of color-matching abilities of the average eye. This more logical system might make it easier to handle discrepancies between calculated, screen, and photographic color.

New software is being tested to manage files. Problems with the catalog manager of TAE and unnecessary running time lost has prompted this effort. The management will tailor the file handling to our needs and allow us to bypass those items that we do not use. Groupings of files will be supported and informative listing and selections provided. It is planned that the file selection procedure be available to the IBM PC's. Files foreign to the ocean system, yet appropriate for processing, will be accepted with the user suppling the necessary parameters.

SIGNIFICANCE AND FUTURE EMPHASIS

The programs have provided oceanographers and geophysicists with new information about the oceans and broadened their understanding of the data. Images have appeared in publications and have been presented at scientific meetings and conferences. The image of the global mean sea surface appears in U.S. News and World Report. The image of mesoscale ocean height variability was used for an internationally-distributed NASA Poster. The direction of software development will continue to follow the needs of the scientists in support of their objectives.

The future emphasis will be on image and graphic processing of multiple data sets. Design will lean toward the use of personal computers for software development, with efficient links to the VAX for image display, and MPP (Massive Parallel Processor). The MPP which can handle many calculations at a very high rate, and whose design adapts itself to image processing is almost ready for application. We will be using the MPP, as it becomes available for most image preparation work, remapping and illumination. The new Merlin three-dimensional graphics terminal will be connected to the MPP as well. The Optronics photographic procedure will probably be used initially for the graphics output.

Figure 1. Sea surface topography based on bathymetry.

GEODYNAMICS LASER RANGING SYSTEM FOR AN EARTH OBSERVING SYSTEM SATELLITE

Steven C. Cohen

BACKGROUND

NASA is currently studying the concept of an Earth Observing System (Eos) (NASA, 1984) which involves multisensor satellites making a variety of Earth observations from platforms in near-polar orbits. One of the planned instruments for inclusion on an Eos satellite is the Geodynamics Laser Ranging System (GLRS) (NASA, 1986) GLRS consists of a high precision, low energy, low mass Nd:YAG laser, a precise pointing system, a fast response photodetector and a variety of associated optoelectronic components. GLRS would be used to make very accurate geodetic measurements by ranging to cube corner retroreflectors on the Earth. It could also be used to make land, ice, and ocean altimetric measurements by ranging at nadar. The laser ranging measurements would be made to arrays of targets with nearest neighbors separated by 10-100 km. The measurements would be used to determine target positions and intersite distances and to study regional and local scale crustal movements including strain accumulation and release in seismic zones, strain propagation from plate boundaries into plate interiors, uplift and subsidence associated with both tectonic and nontectonic processes, and regional scale intra- and interplate motions. The positions of the GLRS ground sites could be tied to those of a fiducial network (e.g., the ground-based observatories operated by NASA as part of the Crustal Dynamics Project) to provide a global geodetic network. With targets located on ice sheets, the GLRS measurements could be used to monitor ice velocities and strain. The GLRS measurements would also be used to provide a highly accurate satellite ephemeris for Eos to be used by other precision position devices such as a microwave altimeter. When operated as a short wavelength altimeter GLRS could map the topography of ice sheets and various land forms with higher spatial resolution and accuracy than possible with other techniques. These measurements would be useful to studies of ice dynamics, geomorphology, tectonic plate flexure, and hydrology. Simulation studies have begun to assess the sensitivity of the deduced geodetic parameters from the GLRS ranging measurements (positions, intersite distance, orbital parameters) to noise in the observations and uncertainties in model parameters.

RECENT ACCOMPLISHMENTS AND SIGNIFICANCE

Error analysis and mission simulation studies have begun using GSFC's GEODYN, ERODYN, and SOLVE software programs. The initial studies have focused on determining the precision and accuracy in the deduced intersite distances for an array of cube corner targets located in California as shown in Figure 1. The targets are located every 50 kilometers throughout the state. The parameters used in the study are shown in Table I. Most important are the orbital parameters including an altitude of 800 km (circular orbit) and an inclination of 100 degrees. The laser system has a single shot precision of 1 cm and is pulsed at 10 Hz. Typical results for a 3-day observation period are shown in Table II. Observations are made over 11 orbital passes, each pass being 5-10 minutes long. The orbits are divided into six arcs: five arcs involve two successive passes over the grid and more than one complete revolution of the Earth, while one arc involves a single short pass over the grid. The predicted uncertainties in intersite distances due to laser noise are about 0.2 cm for distances up to 500 km. Predicted uncertainties in the vertical are also well less than 1 centimeter. The absolute accuracy in the deduced parameters depends on the accuracy of the model parameters used in the data reduction. The preliminary analysis has focused on the effects of uncertainties in gravity field, drag, and solar radiation parameters. Results show that the gravity field uncertainties are dominant. Using covariances that are one-quarter that available from the GEM 10B gravity model (a conservative estimate for the Eos era) results in aliases of less than 1 cm (one sigma) for distances up to 100 km and about 2 cm at 500 kilometers. Aliases in the vertical are more severe and can exceed 10 centimeters at 500 km. Further calculations recently obtained suggest that the alias in the vertical measurements (and the cross baseline distance changes) can be reduced by tying GLRS measurements to fiducial points defined by the Crustal Dynamics network.

FUTURE EMPHASIS

A number of effects must be considered to complete the analysis of the GLRS system. Variations in the atmospheric refractive index due to gradients in temperature and pressure can introduce errors into the range measurements if they are not taken into account. The effects of uncertainties in tidal parameters, polar motion, and other geophysical parameters need to be assessed as do the effects of timing and ranging biases. The utility of ties to fiducial points will be considered in more detail. The current error analyses will be augmented by mission studies involving the processing of simulated data. Error analyses and mission simulations for altimetric measurements may also be undertaken.

REFERENCES

NASA, "Earth Observing System Science of Mission Requirement Working Group Report," 1984.

NASA, "LASA Instrument Panel Report," 1985 (in press).

Table I. Simulation Conditions

ORBIT AND MISSION PARAMETERS:
- ALTITUDE: 800 KM
- INCLINATION: 100 DEGREES
- ECCENTRICITY: 0
- TARGET ARRAY: 157 TARGETS (50 KM SPACING)
- SURVEY INTERVAL: 3 DAYS
  11 DATA ACQUISITION ORBITS (20 DEGREE CUTOFF)
  6 ARCS

- APRIORI SATELLITE INFORMATION
  - POSITION: 10 METER (X, Y, Z)
  - VELOCITY: 0.01 METER/SEC (XDOT, YDOT, ZDOT)

- APRIORI TARGET LOCATIONS: 1 METER (X, Y, Z)

SYSTEM PARAMETERS
- RANGE PRECISION: 1 CM
- PULSE RATE: 10 PPS
- ACQUISITION TIME: 10 SECONDS
- DWELL TIME: 0.5 SECONDS
- SLEW TIME: 0.5 SECONDS

OTHER PARAMETERS
- REFERENCE GRAVITY FIELD: GEM10B
- SOLAR RADIATION PRESSURE AND DRAG INCLUDED

Table II. Error Analysis — Baseline Noise & Alias

DISTANCE NORTH (km)	STATION #	(cm) NOISE	ALIAS
50	72	0.2	0.7
100	65	0.2	0.6
150	59	0.2	0.7
200	53	0.2	0.9
250	47	0.2	0.6
300	41	0.2	0.9
350	35	0.2	0.9
400	28	0.2	1.3
450	21	0.2	1.4
500	14	0.1	1.6
(EAST)			
50	80	0.2	0.4
100	81	0.2	1.0
150	82	0.2	1.1
200	83	0.2	1.5
250	84	0.2	2.0

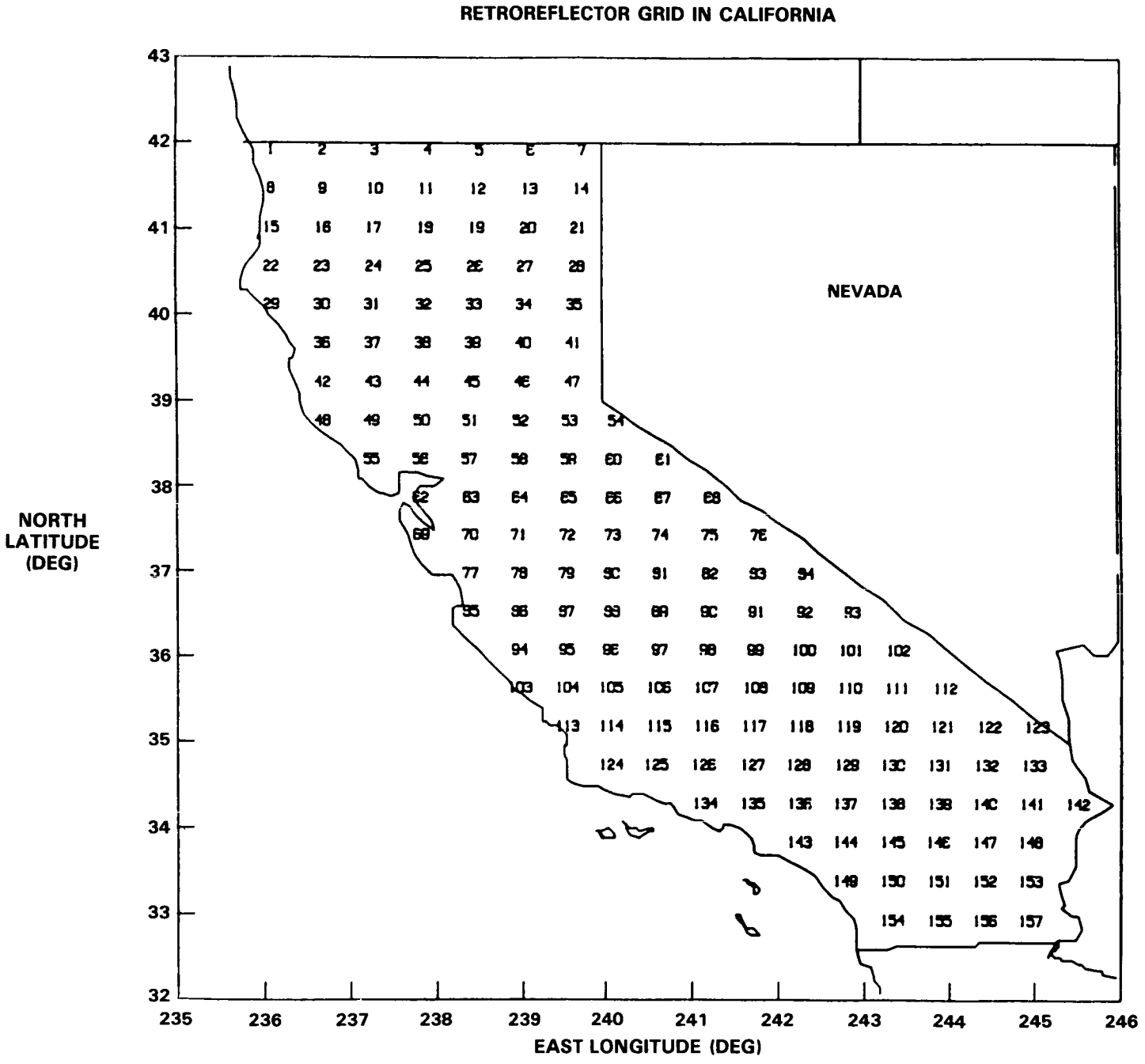

Figure 1. Locations of Ground Targets for GLRS Error Analysis

MARK III VLBI TECHNOLOGY: AN EVALUATION OF THE NEW GENERATION WATER VAPOR RADIOMETERS

G.L. Lundqvist
M.W. Hayes
T.A. Clark

OBJECTIVE

The objective of this task is to evaluate the new generation of water vapor radiometers (WVRs), by data acquisition and analysis, as being capable of measuring the excess microwave path delay due to atmospheric water vapor.

BACKGROUND

The NASA Crustal Dynamics Project has a total of five water vapor radiometers (WVRs) in operation to support VLBI measurements. Four of these are an older JPL design by G. Resch dating from the mid-1970's (the RO series instruments) which have been extensively re-worked by the WVR team at NASA/GSFC, Interferometrics, Inc., and Bendix Field Engineering Corporation. The fifth is the initial prototype of a second-generation instrument developed by M. Janssen and his co-workers at JPL (called the JO series).

The WVRs measure the equivalent sky brightness temperature at 20.7 and 31.4 GHz. The lower frequency is close to the resonant water vapor emission line at 22.235 GHz and is therefore sensitivie to the integrated amount of water vapor along the line of sight. The second frequency is used to measure the amount of liquid water along the same line of sight. By linearly combining the brightness temperatures at these two frequencies, when weighted by properly chosen retrieval coefficients, the microwave excess path delay along the line of sight can be determined.

Typically, the total delay through the troposphere is on the order of 2 meters. Of this, the largest portion is due to the refractive effects of nitrogen and oxygen; this "dry" part can be calibrated by using an accurate barometer to "weigh" the total number of molecules overhead. While the contributions of water vapor are much smaller--typically only about 10% of the total--the variability (both with time and in direction) is quite severe. Since the CDP's precise geodetic measurement programs aim at 1 cm accuracy, the WVRs will play an important part in reaching that goal.

Traditionally the wet part of the excess delay has been determined by using atmospheric models and surface meteorological data. Since the correlation is often very poor between surface and higher layer humidity the surface model tends to give erroneous values for the wet path delay.

RECENT DEVELOPMENTS

The CDP's Mojave Base Station has had one of the upgraded RO-series WVRs, RO7, in operation since December 1984. With this station being located in the California desert, the content of water vapor can be quite low and at times shows little variability from day-to -day. The WVR at Mojave has shown very good long term stability with calibration accuracy typically in the 0.3% range (this reflects an order-of-magnitude improvement over the performance before the upgrade).

As of March 1986 the VLBI facility at the STDN station on the island of Kauai, Hawaii, has the R05 WVR on line. This site has a very interesting local topography. To the east is a mountainous rain forest with the highest annual rainfall on earth; in the opposite direction there exist semi-desert conditions typical of a tropical island. This situation should produce a strong azimuthal dependence in the data.
This is in fact what has been found in the data acquired at this site. Figure 1 shows an example of how quickly the excess path delay can vary although sky conditions and surface humidity showed very little indication of variations during the same period. The upper part of the plot shows the sky brightness temperature (in K) in channel 1 as a function of time and the middle plot shows the corresponding data for channel 2. The lower part is the excess path delay (in cm) as derived from the two channels above. It can be seen that the path delay drops from about 10 cm down to 3-4 cm in only 3 hours and then increases again. Figure 2 shows an example of the azimuthal dependence. The WVR has measured the path delay at 30 degree intervals around the horizon at a constant elevation. The variations in path delay as a function of azimuth can be clearly seen. The variations have a peak value of 4-5 cm. This variation is extreme among the VLBI stations examined so far indicating that the WVR is a necessary part of the Mark III system at that site.

During a recent side-by-side comparison of the RO7 and the J01 WVRs at the Mojave Base Station some interesting results were found. The two WVRs followed the same measurement program on the sky and the output of the two insruments was compared. Figure 3 shows the results of this comparison. The two WVRs measured the sky brightness temperature to within 0.2 K which is a remarkably good result. The two intsruments use very different techniques for the measurements and this indicates that the absolute accuracy of the sky brightness temperatures is on the order of 0.5 K which is close to the goal of the instruments.

SIGNIFICANCE

The significance of these results is that the instruments seem to be capable of measuring excess wet path delay to an accuracy of 0.5 - 1.0 cm. The VLBI data quality has been improved by as much as a factor of 2 on single experiments using path delay corrections from the WVRs.

FUTURE EMPHASIS

By the summer of 1986 the CDP should have WVR's at both Westford and Fort Davis which should provide some very powerful data to apply to the VLBI experiment data sets in order to verify the usefulness of the WVR instruments.

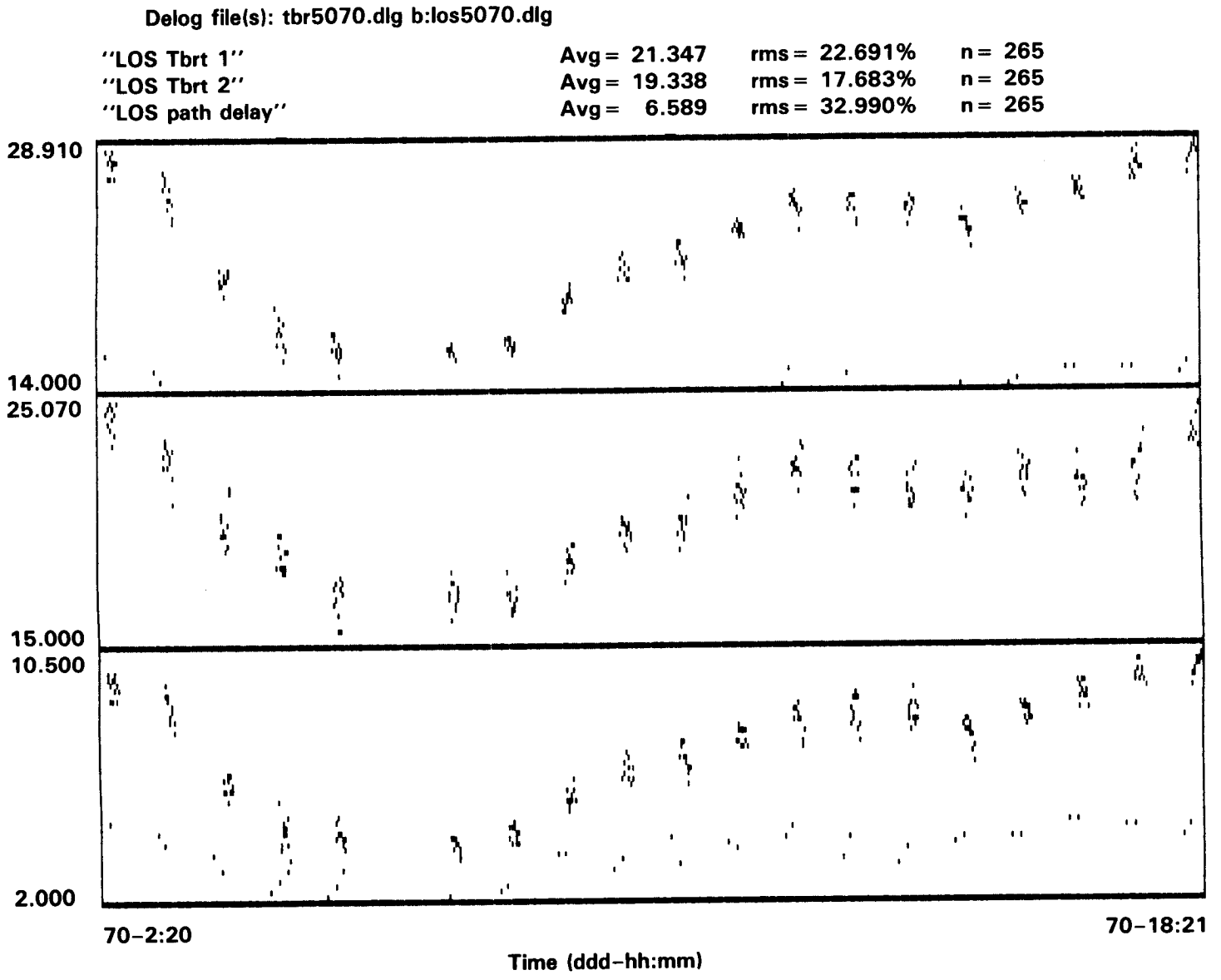
Delog file(s): tbr5070.dlg b:los5070.dlg
"LOS Tbrt 1" Avg = 21.347 rms = 22.691% n = 265
"LOS Tbrt 2" Avg = 19.338 rms = 17.683% n = 265
"LOS path delay" Avg = 6.589 rms = 32.990% n = 265
28.910
14.000
25.070
15.000
10.500
2.000
70-2:20
70-18:21
Time (ddd-hh:mm)

Figure 1

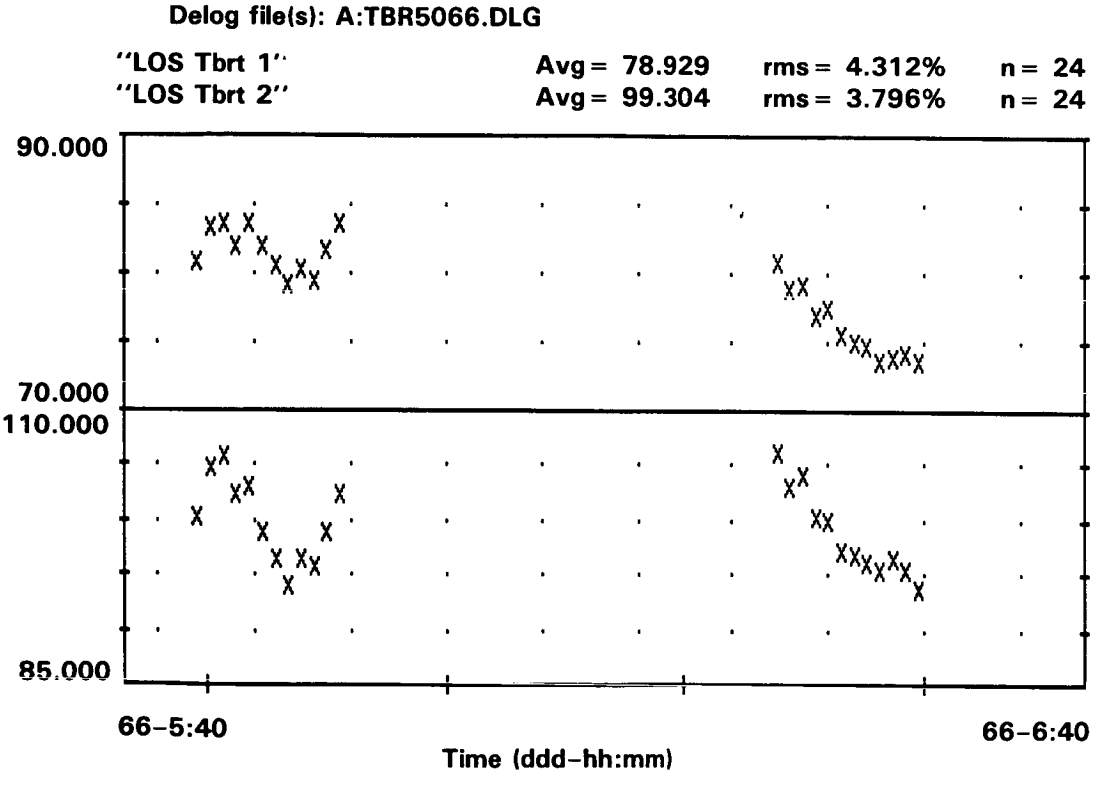
Delog file(s): A:TBR5066.DLG
"LOS Tbrt 1" Avg= 78.929 rms= 4.312% n= 24
"LOS Tbrt 2" Avg= 99.304 rms= 3.796% n= 24
90.000
70.000
110.000
85.000
66-5:40
66-6:40
Time (ddd-hh:mm)

Figure 2

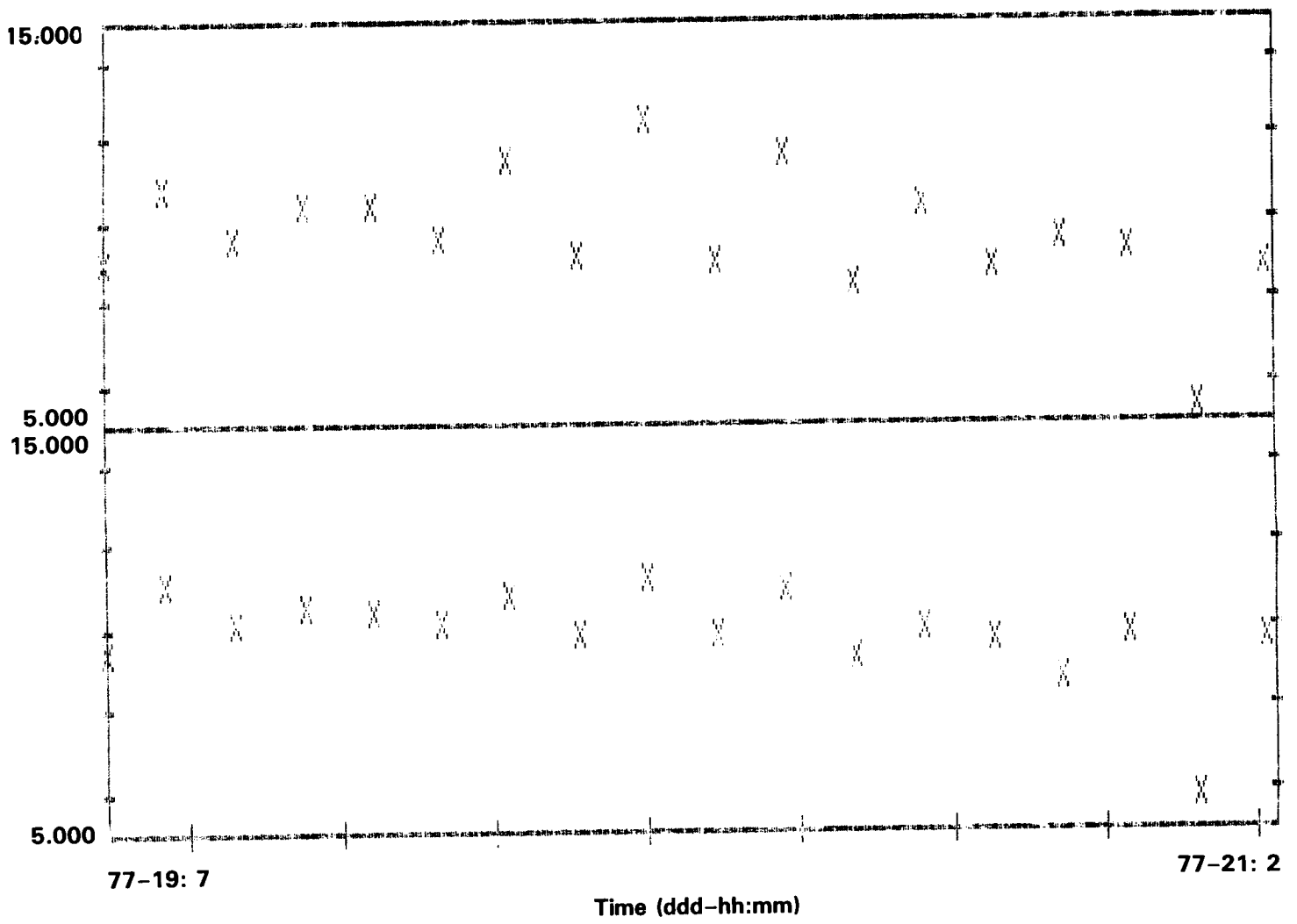
Delog file(s): B:LOS7TST1.dlg B:TIP7TST1.dlg B:TBR7TST1.dlg
"TIP zen tbrt 1" Avg = 9.717 rms = 15.454% n = 18
"TIP zen tbrt 2" Avg = 9.872 rms = 11.656% n = 18
15.000
5.000
15.000
5.000
77-19: 7
77-21: 2
Time (ddd-hh:mm)

Figure 3a

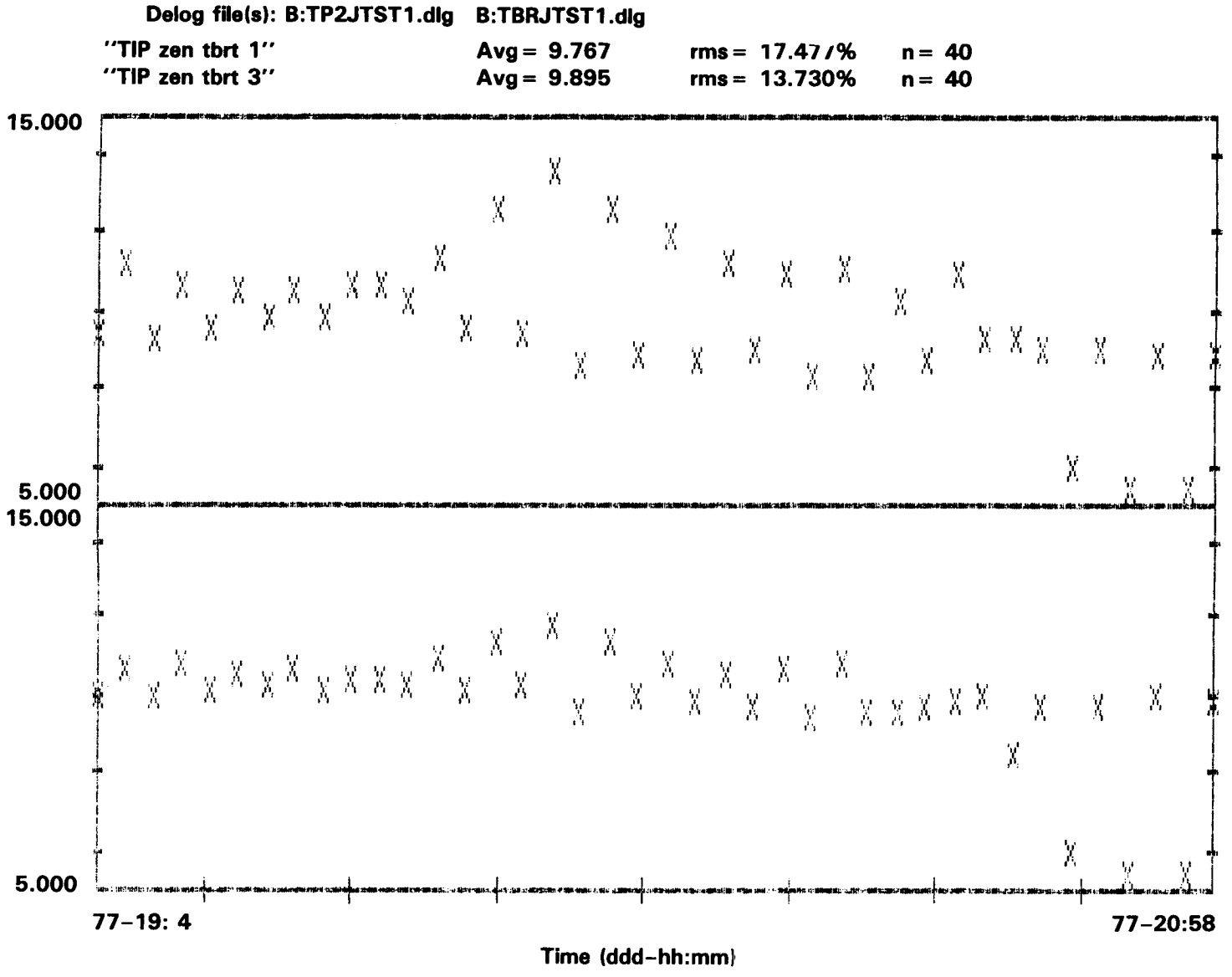
Delog file(s): B:TP2JTST1.dlg B:TBRJTST1.dlg
"TIP zen tbrt 1" Avg = 9.767 rms = 17.47/% n = 40
"TIP zen tbrt 3" Avg = 9.895 rms = 13.730% n = 40
15.000
5.000
15.000
5.000
77-19: 4
77-20:58
Time (ddd-hh:mm)

Figure 3b

HIGH RESOLUTION GRAVITY FIELD MAPPING

WITH A SPACEBORNE GRAVITY GRADIOMETER

Werner D. Kahn

OBJECTIVE

The gravity field of the earth reflects variations in the earth's composition. Knowledge of the earth's gravity field provides information on the density structure of the earth's interior and outer layers from which we can increase our understanding of the formation of geological features, such as mountains and basins, and the mechanisms and scale of processes such as mantle convection. In the area of ocean science, the gravity field is used to construct the reference surface (geoid) for determining the dynamics of the global sea surface. An ultrasensitive gravity gradiometer seems to be a suitable sensor for mapping the fine structure of the earth's gravity field. Studies have thus been undertaken to assess that instrument's capabilities.

BACKGROUND

Covariance error analysis techniques have been used to assess the capabilities of a spaceborne gravity gradiometer to map the fine structure of the earth's gravity field. Since the gradiometer measures the second derivatives of the geopotential field, the gradiometer will be sensitive to the density variations of the earth's outer crust which is the source of the high frequency components of the earth's gravity field. A gravity gradiometer mission would provide in situ measurements on a global scale of the earth's gravity field fine structure. For the covariance error analyses, the effects of orbit altitude, orbit accuracy, and gradiometer precision have been examined.

RECENT ACCOMPLISHMENTS

A computer program has been developed and tested to perform error analysis studies to assess the capabilities of a spaceborne gravity gradiometer. The program was designed to recover gravity or geoid anomalies for the full gravity gradient tensor, the three axes, and the single axis gradiometer configuration. Error sources for the gradiometer studies were instrument precision, orbit position accuracy, satellite attitude and attitude rates. The program provides estimates of high frequency components of the gravity field over a local region. Both mean square gravity and geoid anomalies as the solution parameters were estimated by this program.

The mathematical model for the disturbance potential was derived from Poisson's integral (Heiskanen and Moritz). The components of the gravity tensor were developed by forming the second order partials from the geopotential and a sequential estimator was used to provide estimates of the gravity and geoid anomaly uncertainties based on the modeled error sources. A detailed report describing the mathematical analysis is in preparation. Results of the error analyses to be discussed below assumed the 3-axes gradiometer configuration which in mathematical terms are the diagonal elements of the gravity tensor. They satisfy Laplace's equation (i.e., $\nabla^2 T=0$) and only two of the three components are independent. The 3-axes gradiometer is the configuration now under development by Professor H.J. Paik at the University of Maryland.

Figure 1 shows the evolution of gravity and geoid anomaly uncertainties as a function of resolution. The results depicted are for a orbiting gradiometer in a 160 km and 200 km polar/circular orbit and a mission duration of 180 days. The gradiometer precision of 10^{-3} EOTVOS Units (E)* with, a measurement sampling rate of 1 measurement per 4^s, and a priori knowledge of the gravity field of 9 milligals/1° blk and 50cm/1° blk respectively were also assumed. On the average there are approximately 60 measurements in each 1°x1° blk which corresponds to 16 orbital passes over the block in a 180 day period. Under these assumptions, it can be seen that for the satellite in a 160 km altitude orbit, 1° x 1° gravity and geoid anomalies can be estimated with an accuracy of 0.23 mgals and 1.2 cm respectively. At an orbital altitude of 200 km the above results are 0.45 mgls and 3.5 cm respectively. It can also be seen that the degradation in accuracy is more sensitive to geoid anomalies than to gravity anomalies when increasing the orbit altitude from 160 km to 200 km. The accuracy is thus degraded by a factor of 2 for gravity anomalies and a factor of 3 for Geoid anomalies. The results of Figure 1 show the 3-axes gradiometer to be well suited for mapping the high frequency components of the geopotential. Even at a 200 km orbital altitude, the global gravity field can be very accurately mapped with an orbiting gravity gradiometer having 10^{-3} E system precision.

In Figure 2 the effects of gravity gradiometer system precision is examined for orbit altitudes of 160 km and 200 km, respectively. The results are presented in terms of 1°x1° gravity anomaly accuracy only. It can be seen that the same levels in accuracy due to increase in orbit altitude prevail as those presented in Figure 1. It is interesting to note however, no significant increase in the accuracy of estimated gravity anomalies results from increased gravity gradiometer precision. The curves are relatively flat when the precision in the gradiometer increases from $5\text{x}10^{-3}$E to 10^{-4}E. Large changes do however occur when the precision is increased in the range 10^{-1}E to 10^{-2}E. These results indicate that a spaceborne gravity gradiometer at an orbit altitude of 160 km to 200 km can

* $1E = 10^{-9}/s^2$

with a precision of 10^{-3}E to $6x10^{-4}$E, map the high frequency components of the earth's gravity field to an accuracy better than 1 mgal in terms of gravity anomalies and better than 4 cm in terms of geoid anomalies with a horizontal resolution of 110 km.

FUTURE EMPHASIS

The computer software will be augmented to include the satellite to satellite tracking (SST) measurement data in combination with gravity gradiometer data. Studies will then be performed to evaluate the level of improved accuracy in gravity and geoid anomaly estimation resulting from the combination of these data types.

REFERENCES

Heiskanen, W.A. and H. Moritz, Physical Geodesy, W.H. Freeman and Company, 1967.

Jekeli, C., R.H. Rapp, "Accuracy of the Determination of Mean Anomalies and Mean Geoid Undulations from a Satellite Gravity Field Mapping Mission," The Ohio State University, Department of Geodetic Science Report 307 (August 1980).

Kahn, W.D., F.O. von Bun, "Error Analyses for a Gravity Gradiometer Mission," IEEE Transactions on Geoscience and Remote Sensing, Vol. GE-23, No. 4, July 1985., pp. 527-530.

Reid, G.B., "Application of Kinematical Geodesy for Determining the Short Wavelength Components of the Gravity Field by Satellite Gradiometry," Report 201, Department of Geodetic Science, The Ohio State University, March 1983.

Paik, H.O., "Superconducting Tunable-Diaphragm Transducer for Sensitive Acceleration Measurement," Journ. of Applied Physics, Vol. 47, No. 3, 1168-1178 (March 1976).

Paik, H.O., "Geodesy and Gravity Experiment in Earth Orbit Using a Superconducting Gravity Gradiometer," IEEE Transactions on Geoscience and Remote Sensing, Vol. GE-23, No. 4, July 1985, pp. 524-526.

Lambeck, K., "Methods and Geophysical Applications of Satellite Geodesy," Reports on Progress in Physics 1972, 42, 547-628.

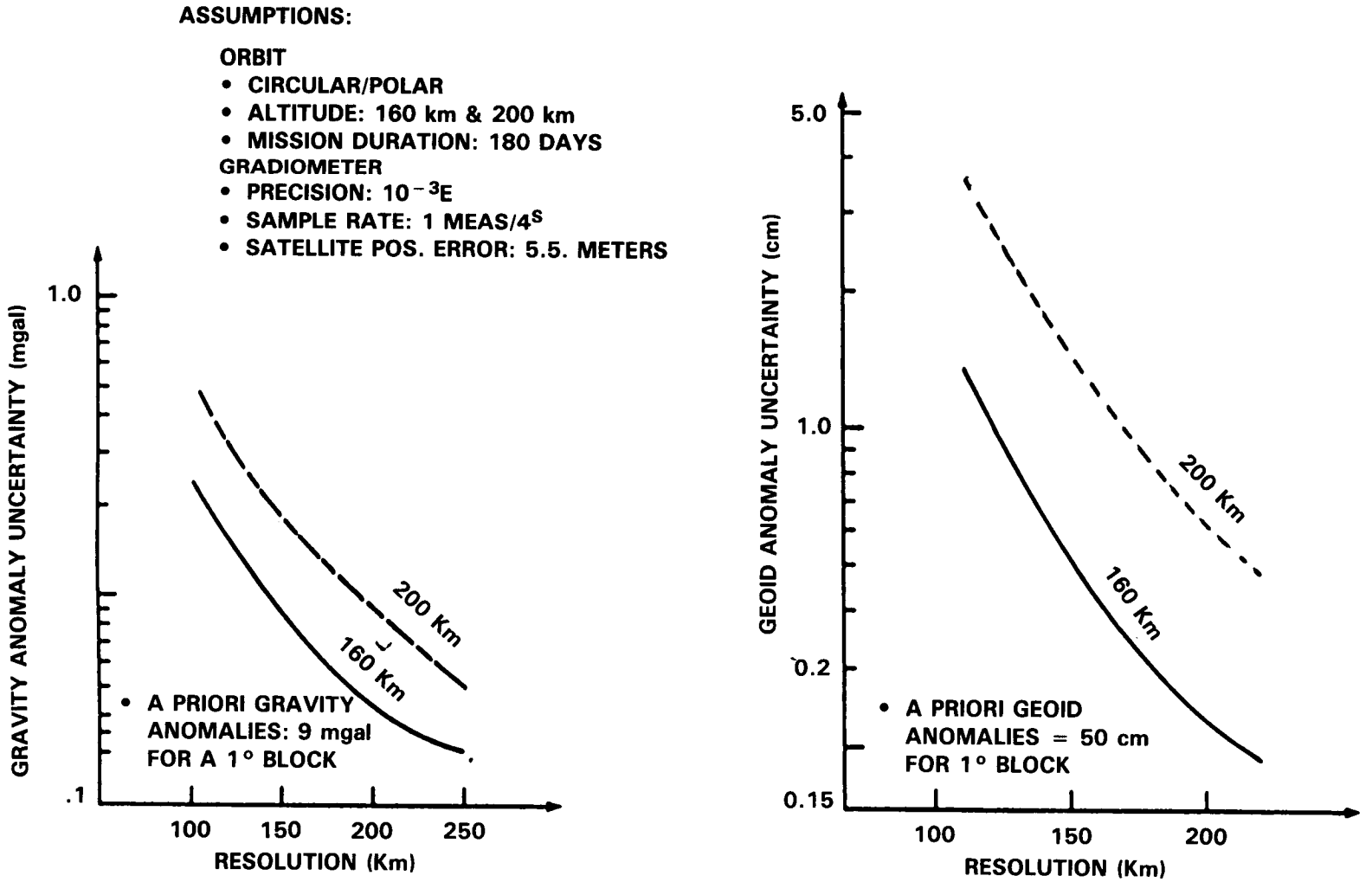

Figure 1. Gravity and Geoid Anomaly Uncertainties vs. Resolution

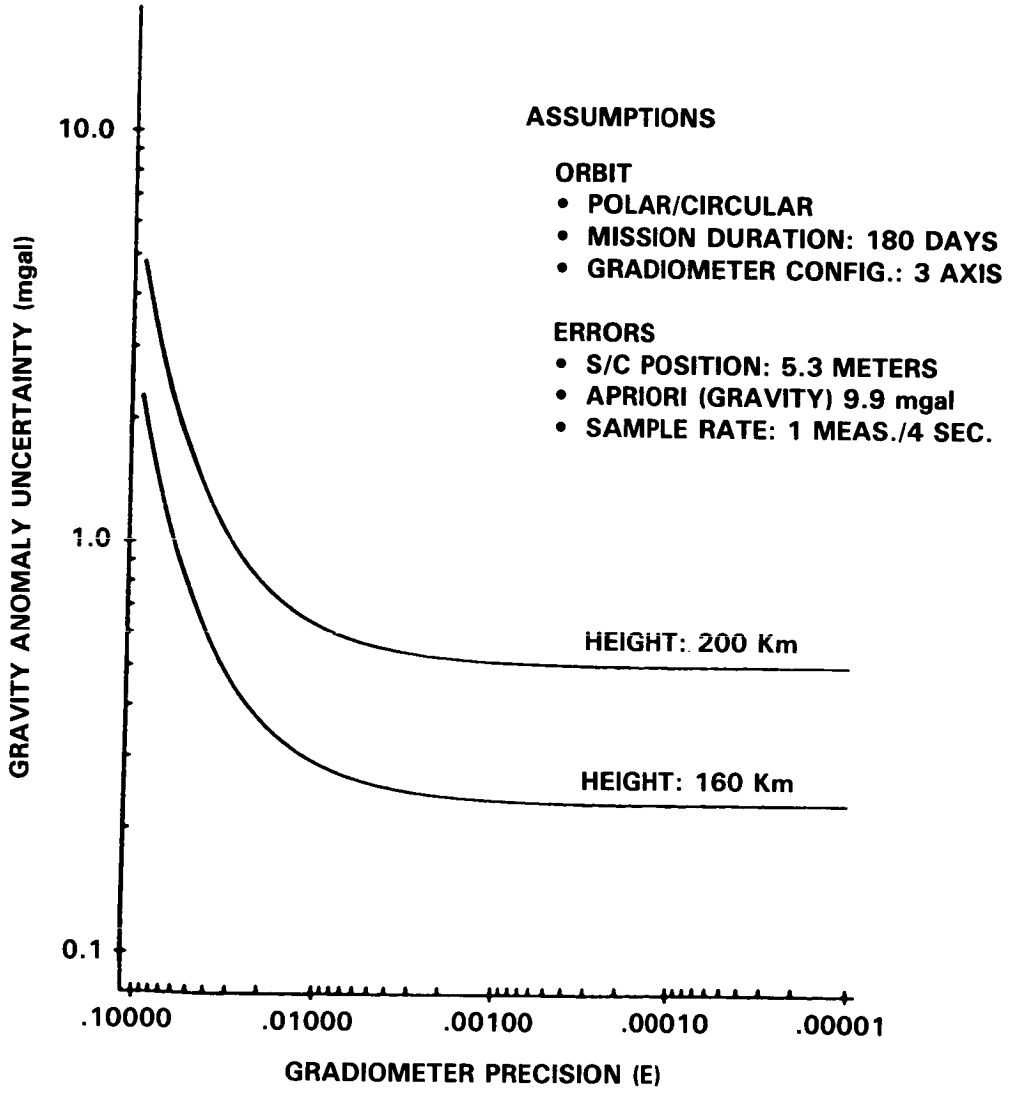

Figure 2. Estimation of 1° × 1° Gravity Anomalies vs. Gradiometer Precision

THE POWER CURVE RECOVERY OF DIURNAL TEMPERATURE EXTREMA

Jean E. Welker

OBJECTIVES

The objectives of this work are: 1) To describe and model the power curve recovery of diurnal temperature extrema, DTE. 2) To discriminate between the different types of precipitation cooling events which cause drops in the diurnal temperature maxima, DTMAX, in soils, air, and shallow pan evaporation water.

BACKGROUND

From a one-dimensional view of temperature alone, variations at the earth's surface manifest themselves in two cyclic patterns of diurnal and annual periods, due principally to the effects of diurnal and seasonal changes in solar heating as well as the gains and losses of available moisture. A related but very different third cycle has been identified, with a variable mesoscale period of from 3 to 14 days. This is the period of recovery or return to the approximate level of original values of a series of 3 to 14 monotonically increasing DTE variables, at 10 cm depth below bare soil after a precipitation-cooling event. An idealized schematic of such an individual cycle is shown in Figure 1, where the recovery leg of 3 to 14 days is represented by 2 , which begins at the minimum value of a. These series of values are obtained from raw data records; a minimum of three consecutive monotonically increasing values is a requirement for these restricted series of values. This third cycle is dependent on the variables of diurnal temperature extrema, DTE, extreme temperature values recorded each day at a test site; the diurnal temperature cycle, on the other hand, is related to the very different variable of temperature readings taken at fixed intervals throughout the day. Although the daily temperature high occurs many times in the afternoon, and the daily temperature low occurs many times shortly after midnight, the DTE variables are not constrained absolutely by a specific time of day, and only are affected by the diurnal cycle in an integrated way. These variables do undergo an annual period by rising in value in the summer and declining in value in the winter. The DTE variables in their dual forms, diurnal temperature maxima, DTMAX, and diurnal temperature minima, DTMIN, each have the peculiar characteristic of recovering from a precipitation-cooling event in a power curve, when the raw data series are a sequence of monotonically increasing values. The DTE recovery clearly depends on solar

heating of the soil with an increased moisture content from precipitation combined with evaporation cooling at soil temperature lowered by precipitation cooling, and many other variables, but is quite regular and universal for vastly different geographical locations, and soil types and structures. The DTE variables gradually rise in value through the summer months from the effects of the alternate heating and cooling of the diurnal period, as seen from the raw data values for the DTMAX variable in Figure 2, for the three soil depths of 5, 10 and 20 cm. This slowly changing growth of DTMAX in a quasi-equilibrium condition is frequently interrupted by a precipitation-cooling event. When a cooling or drop in the value of DTMAX occurs, the initial increments of change are large as the variable recovers and approaches the equilibrium value it had prior to the cooling event. The characteristics of an ascending power curve are also initial large increments of change which become progressively smaller. This recovery occurs slowly over the mesoscale period of 3 to 14 days, so long as another precipitation cooling event does not occur in the meantime, which would restart the recovery cycle after a new minimum DTE value had been achieved. The regularity of the power curve recovery has allowed an accurate power curve fit to the raw DTE data, i.e., each recovery leg, 2, shown in Figure 1, has been fitted with a power curve, for a value of the minimum value, a, and a value for the power exponent, b. From these data fits, a predictive model approach which generalizes the DTE recovery for all precipitation-cooling events has been developed. The generality of the DTMAX power curve recovery for soils was extended by the comparison of its properties with respect to water in evaporation pans and air at the same test sites.

Although the research on the manner of recovery of the DTMAX variable has progressed, a more complete interpretation of the process requires a greater understanding of the initial precipitation cooling process. A precipitation event which cools the soil can affect many variables relating to soil temperature, and the characteristics of the precipitation event are, in themselves, variables. Much of a heavy and intense rainfall over a short duration can run off and not be absorbed in the soil; a slower, longer duration rainfall can have more of its total moisture absorbed in the soil, under the same conditions. The time of the precipitation event is also important, for summer afternoon precipitation on hot soil will differ in effect from the same amount of precipitation on cooler soil in the night. In all cases, the precipitation event occurs over some duration of time relative to the time at which the value of DTMAX in the soil occurs; under ideal conditions, DTMAX occurs sometime in the afternoon.

RECENT ACCOMPLISHMENTS

Recent accomplishments are three-fold: the characteristics of the power curve recovery of the DTE variables are now being considered for soil at different depths, air, and water in evaporation pans. The fact that the power curve recovery occurs in all these substances provides insights as to the energy balance conditions which cause this recovery characteristic. A number of data sets have been entered, analyzed and plotted and have supported initial conclusions. A second approach to the problem is to investigate energy balance experiments which have been conducted for a number of days in order to explain the power curve recovery. One famous experiment conducted in Arizona in the early sixties tracked the energy balance budget both in soil with changing moisture content as well as shallow water and listed recorded value of the DTE variables. For this single example, the reconstructed DTMAX series followed the power curve recovery of the many other examples tested, with the distinct advantage of a detailed description of the energy balance components. (Fritschen and van Bavel, 1962). A third approach has been to assess more detailed precipitation data in order to understand the precipitation cooling process which produced the initial drop in the DTE variables. Precipitation cooling has been perplexing in the past because of a double-valuedness in the amount of precipitation that produces the same drops in the raw DTMAX values. To investigate the problem further, hourly precipitation data have been acquired for one of the station data sets previously considered. After much analysis of the data, it appears that all precipitation data in the 24 hours prior to the recorded drop in the values of DTMAX must be included, and that precipitation values less than or greater than 2.5 cm can produce double-valuedness in the DTMAX values as shown in Figure 3. The implications of these results are being investigated.

SIGNIFICANCE

The regularity of the power curve recovery of the DTMAX variable in soils at different depths, air, and water in evaporation pans allows predictive modeling of the recovery as well as affording an insight into the relevance and the importance of some of the energy balance components and how they affect the DTE variables. Because of the frequency of the DTE drops and recoveries combined with the duration of the mesoscale recovery period, the DTE variables are in the recovery phase a significant portion of the time. For the exceptional data series from the Tifton Experimental Station in Georgia in 1979, the DTMAX variable was in the recovery phase for 69 percent of the March through August period. The power curve recovery is so consistent and regular during this phase that it can be modeled and predicted with varying degrees of accuracy for a number of meteorological stations under a wide variety of conditions.

FUTURE EMPHASIS

The energy balance conditions for soils at different depths, shallow water, and air will continue to be analyzed and appropriate models will be developed. The double-valuedness of the precipitation cooling events have only been characterized for very limited data sets and will be expanded to include others. Further statistical analysis is required to generalize the power curve recovery for a larger number of stations and to further investigate the behavior of the DTMIN variable. A journal article on a portion of the results to date is in preparation. These results had been developed over a period of time in consultation with Professor Helmut Landsberg of the University of Maryland, whose untimely passing in December 1985, is mourned by this author and countless others who have been helped and befriended by this exceptional person.

REFERENCES

Brooks, F.A. and D.G. Rhoades, "Daytime Partition of Irradition and the Evaporation Chilling of the Ground." Trans. Amer. Geophys. Un., 35, No. 1, February 1954, 145-152.

Fritschen, L.J. and C.H. van Bavel, "Energy Balance Components of Evaporating Surfaces in Arid Lands." J. Geophys. Res., 676, No. 13, December 1962, 5179-5185.

Landsberg, Helmut E., "Drought, a Recurring Element of Climate," World Meteorological Organization Special Environmental Report No. 5 Drought WMO No. 403, Geneva, Switzerland, Secretariat of the World Meteorological Organization 1975, 40-61.

Lettau, Heniz, "Improved Models of Thermal Diffusion in the Soil," Trans. Amer. Geophys. Un., 35, No. 1, February 1954, 121-132.

Palmer, W.C., "Meteorological Drought," Washington, D.C., U.S. Department of Commerce, Weather Bureau Research Paper No. 45, February 1965, 55 pp.

Schmugge, T.J., T.J. Jackson and H.L. Kim, "Survey of In-Situ and Remote Sensing Methods for Soil Moisture Determinations," in Deutsch, M., Wiesnet, D.R., and Rango, A., eds. Satellite Hydrology, American Water Resources Association, June 1979.

Vehrencamp, John E., "Experimental Investigations of Heat Transfer at an Air-Earth Interface," Trans. Amer. Geophys. Un., 34, No. 1, February 1953, 22-30.

Welker, J.E., "Thermal Infrared Remote Sensing of Surface Features for Renewable Resource Applications," NASA TM 82106, Greenbelt, MD, Goddard Space Flight Center, January 1981, 26 pp.

Welker, J.E., "Soil Temperature Extrema Recovery Rates after Precipitation Cooling," NASA TM 86163, October 1984, 18 pp.

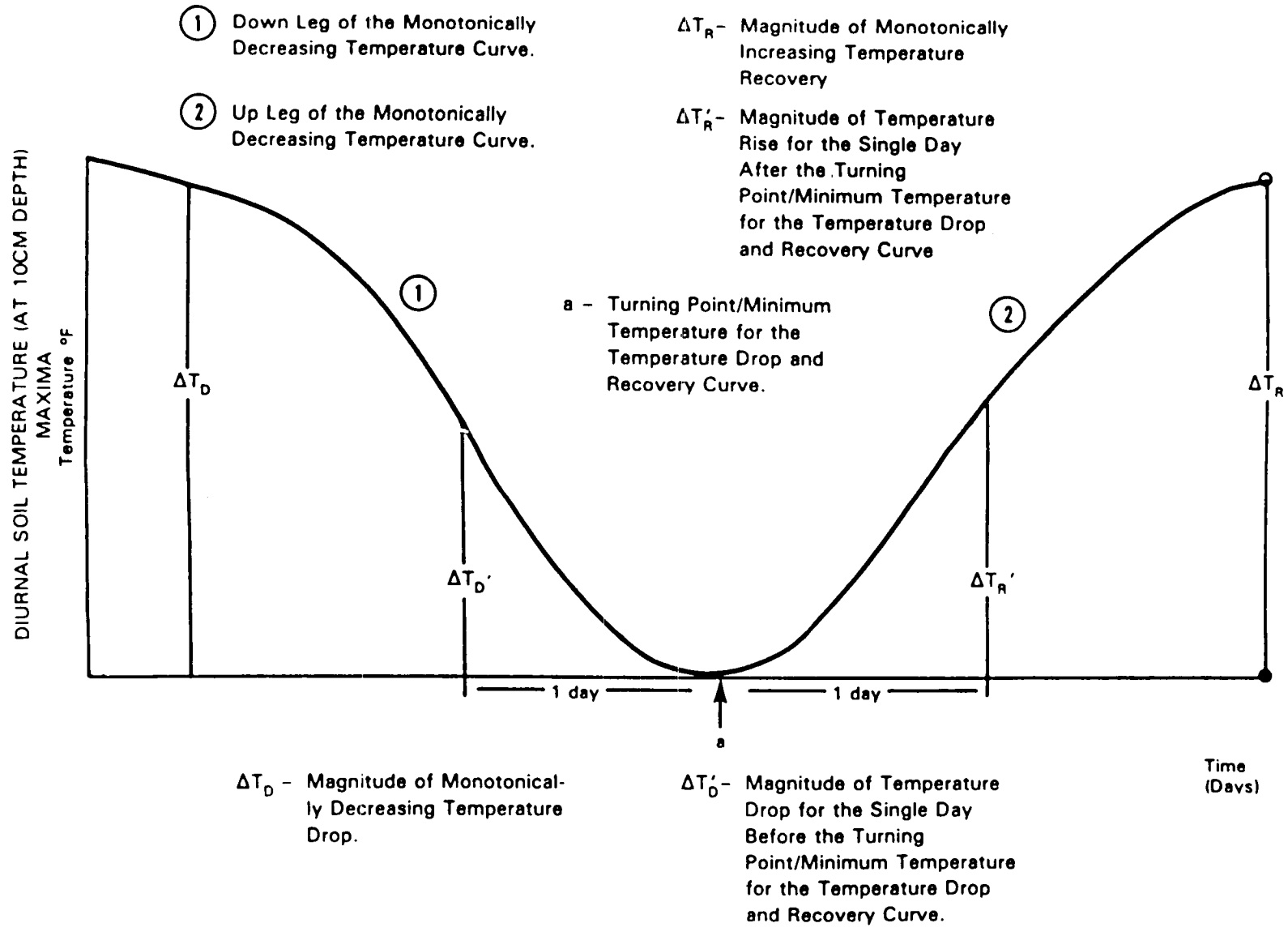

Figure 1. Idealized Schematic of A Single Diurnal Soil Temperature Maximum Drop and Recovery.

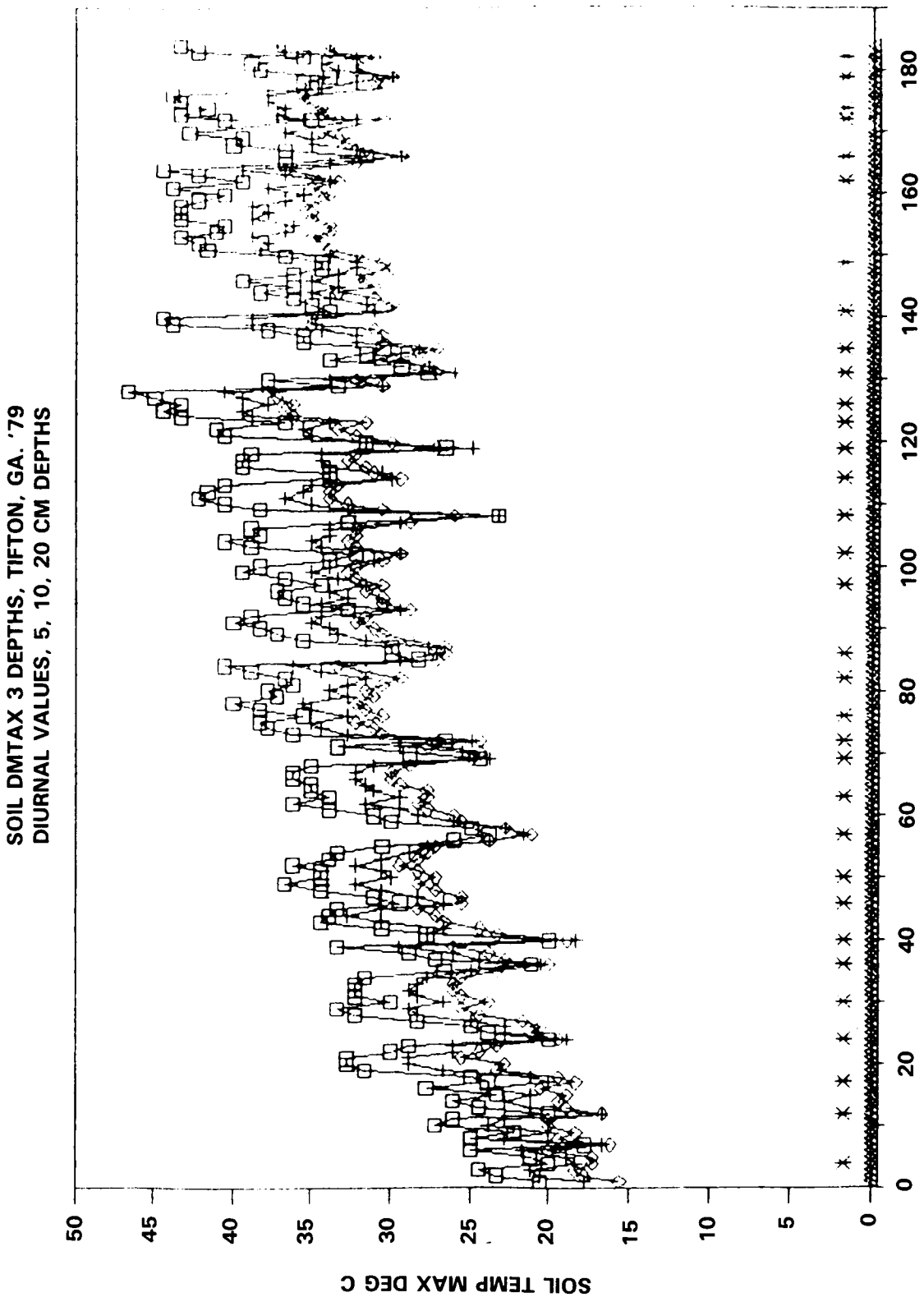
SOIL DMTAX 3 DEPTHS, TIFTON, GA. '79
DIURNAL VALUES, 5, 10, 20 CM DEPTHS
SOIL TEMP MAX DEG C
50
45
40
35
30
25
20
15
10
5
0
0
20
40
60
80
100
120
140
160
180
DAYS FROM MAR1 THRU AUG31
5 CM
10 CM
20 CM

Figure 2

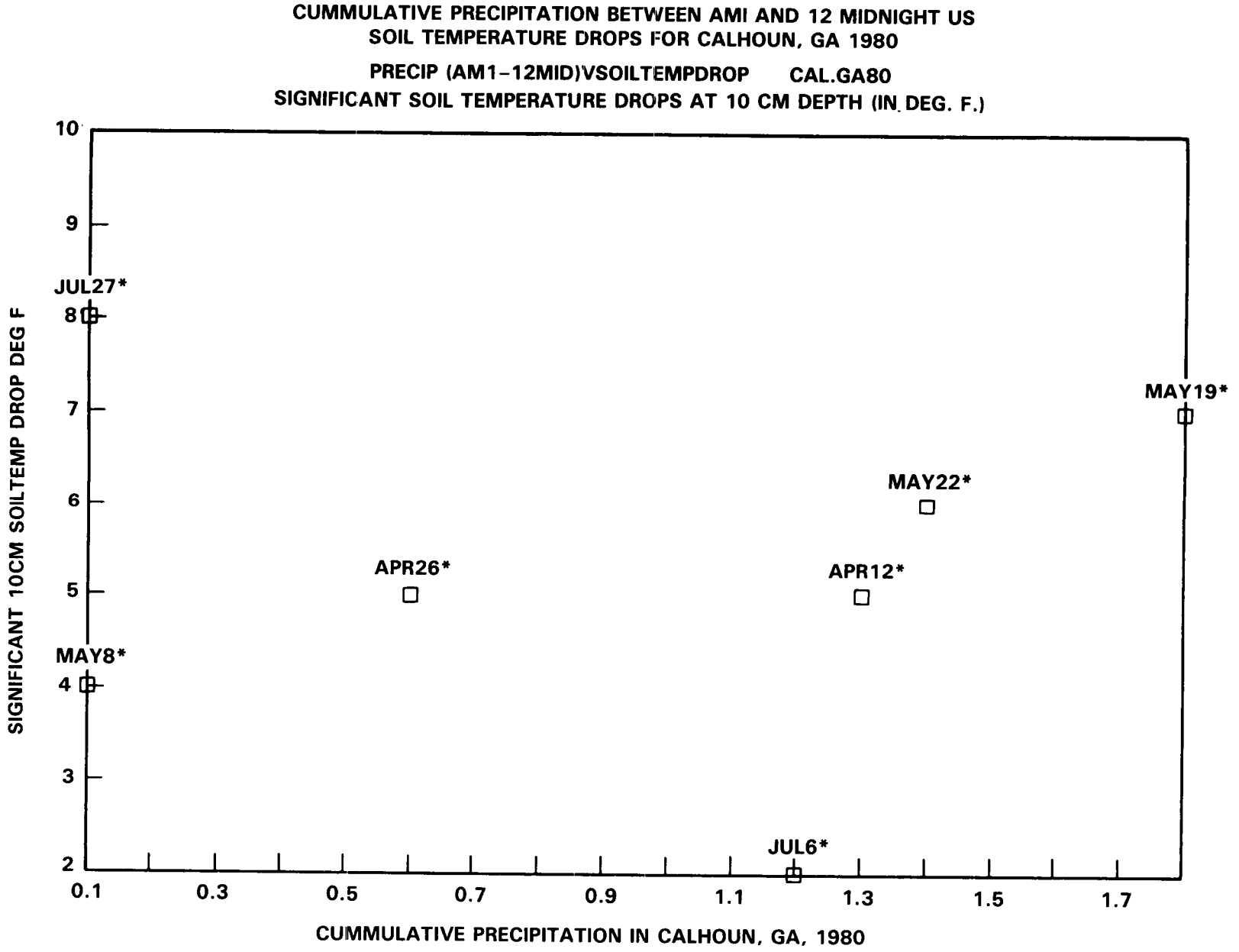
CUMMULATIVE PRECIPITATION BETWEEN AM1 AND 12 MIDNIGHT US
SOIL TEMPERATURE DROPS FOR CALHOUN, GA 1980
PRECIP (AM1-12MID)VSOILTEMPDROP CAL.GA80
SIGNIFICANT SOIL TEMPERATURE DROPS AT 10 CM DEPTH (IN DEG. F.)
SIGNIFICANT 10CM SOILTEMP DROP DEG F
10
9
8
7
6
5
4
3
2
JUL27*
MAY19*
MAY22*
APR26*
APR12*
MAY8*
JUL6*
0.1
0.3
0.5
0.7
0.9
1.1
1.3
1.5
1.7
CUMMULATIVE PRECIPITATION IN CALHOUN, GA, 1980

Figure 3

PUBLICATIONS - 1985

1. Chao, B.F., "Predictability of the Earth's Polar Motion," Bull. Geod., 59, 81-93. Also NASA/GSFC TM 86095.

2. Chao, B.F., "On the Excitation of the Earth's Polar Motion," Geophys. Res. Letters, 12, 526-529.

3. Chao, B.F., R.S. Gross, "Excitation Study of the Lageos-Derived Chandler Wobble," J. Geophys. Res., in press.

4. Christodoulidis, D.C., D.E. Smith, R. Kolenkiewicz, S.M. Klosko, M.H. Torrence and P.J. Dunn, "Observing Tectonic Plate Motions and Deformation from Satellite Laser Ranging," J. Geophys. Res., 4B5142, in print.

5. Christodoulidis, D.C., D.E. Smith, R. Kolenkiewicz, P.J. Dunn, S.M. Klosko, M.H. Torrence, S. Fricke and S. Blackwell, "A Global Geodetic Reference Frame from LAGEOS Ranging (SL5.1AP)," J. Geophys. Res., in print.

6. Christodoulidis, D.C., D.E. Smith, G.H. Wyatt, P.J. Dunn, S.M. Klosko, M.H. Torrence and S. Fricke, "Variations in Length-of-Day and the Atmospheric Angular Momentum," J. Geophys. Res., in print.

7. Christodoulidis, D.C., D.E. Smith, J.B. Minster and T.H. Jordan, "Relative Movement of Tectonic Plates in California Observed by Satellite Laser Ranging," Science, in print.

8. Christodoulidis, D.C., T.H. Jordan, J.B. Minster, and D.E. Smith, "Constraints on Western U.S. Deformation from Satellite Laser Ranging," Science, in print.

9. Cohen, S.C., "Geophysical Interpretation of Satellite Laser Ranging Measurements of Crustal Movement in California," Tectonophysics.

10. Cohen, S.C., and D.E. Smith, "Lageos Scientific Results: Introduction to the Special Issue of the Journal of Geophysical Research," J. Geophys. Res.

11. Felsentreger, T.L., and B.V. Sanchez, "Orbital Computations Using Camera Data," in TOPEX Gravity Model Development Team Activities During Fiscal Year 1984, Technical Memorandum 86208, April 1985.

12. Felsentreger, T.L., and B.V. Sanchez, "Orbital Computations Using Optical Data," in TOPEX Gravity Model Improvement Meeting No. 4 - Minutes, Ed. by J.G. Marsh and G.H. Born, NASA Conference Publication 23801, Austin, Texas, February 1985.

13. Kahn, W.D., F.O. vonBun, "Error Analyses for a Gravity Gradiometer Mission," in publication IEEE Transactions on Geosciences and Remote Sensing, Vol. GE-23, No. 4, July, pp. 527-530.

14. Kahn, W.D., and D.E. Smith, "The Geopotential Research Mission (GRM)," CSTG Bulletin No. 8, in press.

15. Koblinsky, C.J., R.L. Bernstein, W.J. Schmitz, Jr., and P.P. Niiler, "Estimates of the Geostropic Stream Function in the Western North Pacific from XBT Surveys," J. Geophys. Res., 89, 10451-10460.

16. Koblinsky, C.J., A. Badan-Dangon, and T. Baumgartner, "Spring and Summer in the Gulf of California: Observations of Surface Thermal Patterns," Oceanologica Acta, 8, 13-22.

17. Koblinsky, C.J., and P.P. Niiler, "A Local Time-Dependent Sverdrup Balance in the Eastern North Pacific," Science, in press.

18. Kolenkiewicz, R., and C.F. Martin, "Determination of Highly Accurate Orbits for Altimeter Satellites Over Limited Geographic Areas," Adv. Space Res., Vol. 5, No. 2, 169-174.

19. Kolenkiewicz, R., D.E. Smith, D.C. Christodoulidis, M.H. Torrence, S.M. Klosko, and P.J. Dunn, "Geodetic and Geophysical Results from Lageos," Adv. Space Res., 5, 2, 219-228.

20. Kolenkiewicz, R., "A Comparison Between LAGEOS Laser Ranging and Very Long Baseline Interferometry Determined Baseline Lengths," J. Geophys. Res., in press.

21. Kolenkiewicz, R., D.C. Christodoulidis, D.E. Smith, S.M. Klosko, M.H. Torrence and P.J. Dunn, "Observing Tectonic Plate Motions and Deformation from Satellite Laser Ranging," J. Geophys. Res., in press.

22. Kolenkiewicz, R., D.E. Smith, D.C. Christodoulidis, R. Kolenkiewicz, P.J. Dunn, S.M. Klosko, M.H. Torrence, S. Fricke and S. Blackwell, "A Global Geodetic Reference Frame from LAGEOS Ranging (SL5.1AP)," J. Geophys. Res., in press.

23. Lerch, F.J., S.M. Klosko, G.B. Patel, "A Refined Gravity Model from Lageos," NASA TM 48986, February 1983, to be published in Lageos Special Issue of JGR, 1985.

24. Lerch, F.J., S.M. Klosko, C.A. Wagner, and G.P. Patel, "On the Accuracy of Recent Goddard Gravity Models," J. Geophys. Res., in print 1985.

25. Lerch, F.J., S.M. Klosko, and C.A. Wagner, "Comments on Lambeck and Coleman: The Earth's Shape and Gravity Field: A Report of Progress from 1958 to 1982," Geophys. J.R. Astr. Soc., in print 1985.

26. Liu, H.S., "Geodynamical Basis for Crustal Deformation under the Tibetan Plateau, Physics of the Earth and Planetary Interiors, July, in press.

27. Ma, C., T.A. Clark, J.W. Ryan, A.E.E. Rogers, A.R. Whitney, I.I. Shapiro, T.A. Herring, " Precision Geodesy Using the Mark III Very Long Baseline Interferometry System," IEEE Transactions on Geoscience and Remote Sensing, Vol. GE-23, No. 4, 438-449.

28. Ma, C., T.A. Herring, I.I. Shapiro, T.A. Clark, J.W. Ryan, B.R. Schupler, C.A. Knight, G. Lundqvist, D.B. Shaffer, N.R. Vandenberg, H.F. Hinteregger, R.B. Phillips, A.E.E. Rogers, J.C. Webber, A.R. Whitney, G. Elgered, B.O. Ronnang, B.E. Corey, J.L. Davis, "Geodesy by Radio Interferometry: Evidence for Contemporary Plate Motion," submitted to J. Geophys. Res., April.

29. Ma, C., T.A. Clark, J.W. Ryan, "Creation of a Global Geodetic Network Using Mark III VLBI," Proceedings International Conference on Earth Rotation and the Terrestrial Reference Frame, in publication.

30. Ma, C., J.W. Ryan, "Crustal Dynamics Project Data Analysis: Fixed Station VLBI Geodetic Results," NASA TM 86229.

31. Marsh, J.G., A.C. Brenner, B.D. Beckley, T.V. Martin, "Global Mean Sea Surface Based Upon the Seasat Altimeter Data," J. Geophys. Res., in press.

32. Marsh, J.G., F.J. Lerch, R.G. Williamson, "Precision Geodesy and Geodynamics Using Starlette Laser Ranging," J. Geophys. Res., in press.

33. Marsh, J.G., R.G. Williamson, "Starlette Geodynamics: The Earth's Tidal Response," J. Geophys. Res., in press.

34. Rubincam, D.P., and N.R. Weiss, "The Orbit of Lageos and Solar Eclipses," J. Geophys. Res., in press.

35. Ryan, J.W., T.A. Clark, C. Ma, A.E.E. Rogers, A.R. Whitney, I.I. Shapiro, T.A. Herring, "Precision Geodesy Using the Mark III Very Long Baseline Interferometry System," IEEE Transactions on Geoscience and Remote Sensing, Vol. GE-23, No. 4, 438-449.

36. Ryan, J.W., T.A. Clark, "Geodesy by Radio Interferometry: CDP VLBI Measurements for Determination of Tectonic Plate Motion and Plate Stability," EOS, Vol. 66, No. 18, April.

37. Ryan, J.W., T.A. Herring, I.I. Shapiro, T.A. Clark, C. Ma, B.R. Schupler, C.A. Knight, G. Lundqvist, D.B. Shaffer, N.R. Vandenberg, H.F. Hinteregger, R.B. Phillips, A.E.E. Rogers, J.C. Webber, A.R. Whitney, G. Elgered, B.O. Ronnang, B.E. Corey, J.L. Davis, "Geodesy by Radio Interferometry: Evidence for Contemporary Plate Motion," submitted to J. Geophys. Res., April.

38. Ryan, J.W., C. Ma, T.A. Clark, "Creation of a Global Geodetic Network Using Mark III VLBI," Conference on Earth Rotation and the Terrestrial Reference Frame, in publication.

39. Ryan, J.W., and C. Ma, "Crustal Dynamics Project Data Analysis: Fixed Station VLBI Geodetic Results," NASA TM 86229.

40. Sanchez, B.V., D.B. Rao and P.G. Wolfson, "An Objective Analysis Technique for Extrapolating Tidal Fields in a Closed Basin," Marine Geodesy, Vol. 9, No. 1, 71-91, 1985.

41. Smith, D.E., D.C. Christodoulidis, R. Kolenkiewicz, M.H. Torrence, S.M. Klosko, and P.J. Dunn, "Geodetic and Geophysical Results from Lageos," Adv. Space Res., 5, 2, 219-228.

42. Smith, D.E., D.C. Christodoulidis, R. Kolenkiewicz, S.M. Klosko, M.H. Torrence, and P.J. Dunn, "Observing Tectonic Plate Motions and Deformation from Satellite Laser Ranging," J. Geophys. Res., in press.

43. Smith, D.E., and B.D. Tapley, "An Improved Gravity Model for Geosciences: A Status Report," EOS Trans. AGU, 66, 249.

44. Smith, D.E., and W.D. Kahn, "The Geopotential Research Mission (GRM)," CSTG Bulletin No. 8, in press.

45. Smith, D.E., S.C. Cohen, "Lageos Scientific Results: Introduction to the Special Issue of the Journal of Geophysical Research," J. Geophys. Res., in press.

46. Smith, D.E., D.C. Christodoulidis, R. Kolenkiewicz, P.J. Dunn, S.M. Klosko, M.H. Torrence, S. Fricke and S. Blackwell, "A Global Geodetic Reference Frame from LAGEOS Ranging (SL5.1AP)," J. Geophys. Res., in press.

47. Smith, D.E., D.C. Christodoulidis, G.H. Wyatt, P.J. Dunn, S.M. Klosko, M.H. Torrence and S. Fricke, "Variations in Length-of-Day and the Atmospheric Angular Momentum," J. Geophys. Res., submitted for publication.

48. Smith, D.E., S.M. Klosko, M.H. Torrence and P.J. Dunn, "A GSFC Alternative to the SLR MERIT Constants," CSTG Bulletin, submitted for publication.

49. Smith, D.E., D.C. Christodoulidis, M.H. Torrence, S.M. Klosko, and P.J. Dunn, "Polar Motion and Length of Day Determination from Satellite Laser Ranging," CSTG Bulletin, submitted for publication.

50. Zuber, M.T., and E.M. Parmentier, "Ductile Lithosphere Extension: Implications for Rifting on the Earth and Venus," Lunar Planet. Sci. Conf. XVI, 948-949, 1985.

51. Zuber, M.T., and E.M. Parmentier, "Compression of Oceanic Lithosphere: A Model for Intraplate Deformation in the Central Indian Ocean," EOS Trans. Am. Geophys. Un., 66, 360, 1985.

52. Zuber, M.T., and E.M. Parmentier, "Unstable Compression of Oceanic Lithosphere: Application to Intraplate deformation in the central Indian Ocean," EOS Trans. Am. Geophys. Un., 66, 1098, 1985.

53. Zuber, M.T., and E.M. Parmentier, "Ductile Extension of Planetary Lithospheres," Conf. on Heat and Detachment in Crustal Extension on Continents and Planets, 156-159, Sedona, Az., 1985.

ACKNOWLEDGMENTS

We would like to acknowledge the scientific and technical support by the following:

Business & Technological Systems, Inc.

M.D. Schuster
R.C. Morgan
S. Grimes
D. Wildenhaim

EG&G/Washington Analytical Services Center, Inc.

W.T. Wells
C.F. Martin
P.J. Dunn
T.V. Martin
M.H. Torrence
S.M. Klosko
J.J. McCarthy
C. Laferriere
R.G. Williamson
B. Beckley
N.L. Chandler
D.D. Rowlands
D.M. Sevitski
E. Pavlis
J. Robbins
A. Brenner

Interferometrics, Inc.

J.M. Gipson
D. Gordon
M. Hayes
E. Himwich
G. Lundqvist
J. Ray

RMS, Inc.

M.A. Abresch
S. Blackwell
D. Childs
K. Doyle
S.M. Fricke
L. Gehrmann
S.G. Poulose

ACKNOWLEDGMENTS (Continued)

Rochester Institute of Technology

F. Sciremammano

Science Applications Research

R.H. Estes
G.B. Patel
S. Bhati

State University of New York

D. Steinberg

University of Maryland

J. Alexander
T. Carter
B. O'Neel
K. Settle

BIBLIOGRAPHIC DATA SHEET

1. Report No. NASA TM-87801	2. Government Accession No.	3. Recipient's Catalog No.
4. Title and Subtitle Geodynamics Branch Annual Report - 1985		5. Report Date October 1986 6. Performing Organization Code 621
7. Author(s) W. D. Kahn, S. C. Cohen, and B. S. Boccucci, Editors		8. Performing Organization Report No. 87B0017
9. Performing Organization Name and Address Geodynamics Branch Goddard Space Flight Center Greenbelt, Maryland 20771		10. Work Unit No. 11. Contract or Grant No.
12. Sponsoring Agency Name and Address National Aeronautics and Space Administration Washington, D.C. 20546		13. Type of Report and Period Covered Technical Memorandum 14. Sponsoring Agency Code

15. Supplementary Notes

16. Abstract

This report is the Fourth Annual Summary of the Research Program of the Geodynamics Branch. The branch is located within the Laboratory for Terrestrial Physics of the Space and Earth Sciences Directorate of the Goddard Space Flight Center. The research activities of the branch staff cover a broad spectrum of geoscience disciplines including: tectonophysics, space geodesy, geopotential field modeling, and dynamic oceanography. The NASA programs which are supported by the work described in this document include the Geodynamics and Ocean Programs, the Crustal Dynamics Project and the proposed Ocean Topography Experiment (TOPEX). The reports highlight the investigations conducted by the Geodynamics Branch staff during calendar year 1985. The individual papers are grouped into chapters on Crustal Movements and Solid Earth Dynamics, Gravity Field Modeling and Sensing Techniques, and Sea Surface Topography. Further information on the activities of the branch or the particular research efforts described herein can be obtained through the branch office or from individual staff members.

17. Key Words (Selected by Author(s))	18. Distribution Statement
Crustal Dynamics, Gravity, Laser, LAGEOS, Radiometer, Tides	Unclassified - Unlimited Subject Category 42

19. Security Classif. (of this report)	20. Security Classif. (of this page)	21. No. of Pages	22. Price*
Unclassified	Unclassified		

*For sale by the National Technical Information Service, Springfield, Virginia 22161